4-2016

Tadpole orbits in the L4/L5 region: Construction and links to other families of periodic orbits

Alexandre G. Van Anderlecht
Purdue University

Graduate School Form
30 Updated 12/26/2015

PURDUE UNIVERSITY
GRADUATE SCHOOL
Thesis/Dissertation Acceptance

This is to certify that the thesis/dissertation prepared

By Alexandre G Van Anderlecht

Entitled
Tadpole Orbits in the L4/L5 Region: Construction and Links to Other Families of Periodic Orbits

For the degree of Master of Science in Aeronautics and Astronautics

Is approved by the final examining committee:

Kathleen C. Howell
Chair

Carolin E. Frueh

James M. Longuski

To the best of my knowledge and as understood by the student in the Thesis/Dissertation Agreement, Publication Delay, and Certification Disclaimer (Graduate School Form 32), this thesis/dissertation adheres to the provisions of Purdue University's "Policy of Integrity in Research" and the use of copyright material.

Approved by Major Professor(s): Kathleen C. Howell

Approved by: Weinong Wayne Chen 04/18/2016

Head of the Departmental Graduate Program Date

TADPOLE ORBITS IN THE L_4/L_5 REGION: CONSTRUCTION AND LINKS TO OTHER FAMILIES OF PERIODIC ORBITS

A Thesis

Submitted to the Faculty

of

Purdue University

by

Alexandre G. Van Anderlecht

In Partial Fulfillment of the

Requirements for the Degree

of

Master of Science in Aeronautics and Astronautics

May 2016

Purdue University

West Lafayette, Indiana

Dedicated to Mom and Papa.

ACKNOWLEDGMENTS

Without my family, I would not be where I am today. I would like to thank my parents Lana and Luc for providing me with the tools to follow my passions and pursue this challenging and rewarding work. My sister Katya has also given me words of encouragement throughout my time here that I am grateful for. The support given to me by Alexa throughout my most challenging years thus far at Purdue has helped to alleviate any doubts and push forward. I am thankful for the encouragement from my friends at Purdue and those who were present during my undergraduate studies and continue to visit. I would also like to thank Professor Kathleen Howell, my advisor. When I took my first class with her during my junior year of undergraduate studies, I sensed her commitment to teaching and her concern with students understanding the course material to a deeper level. This philosophy extends to her role as my advisor with the questions she asks and suggestions she makes regarding my research, which has challenged me and continues to further develop my understanding of both my work and the fundamentals of astrodynamics. Next, I am gracious for the suggestions provided by the members of the research group. Often their words offer a different approach to a problem that I never considered, and their contributions helped me develop my work to its current point. I am especially thankful to Wayne for generating the orbit convolution maps which have been very useful and for helping to develop my understanding of this work. Thank you to my committee members, Professors Carolin Frueh and James Longuski, who both taught classes that I greatly enjoyed. In addition, I would like to acknowledge Sara Hatch and Ted Sweetser who were my mentors at JPL during my summer internships. Working on a real mission and applying what I have learned has inspired me to continue my graduate studies. Finally, I am thankful for the School of Aeronautics and Astronautics at Purdue for providing me the opportunity to be a teaching assistant.

TABLE OF CONTENTS

Page

LIST OF TABLES

Table Page

LIST OF FIGURES

ABSTRACT

Van Anderlecht, Alexandre G. M.S.A.A., Purdue University, May 2016. Tadpole Orbits in the L_4/L_5 Region: Construction and Links to Other Families of Periodic Orbits. Major Professor: Kathleen C. Howell.

The equations of motion in the Circular Restricted Three-Body Problem (CR3BP) allow five equilibrium solutions, that is, the Lagrange or libration points. Two of the five equilibrium solutions are the triangular or equilateral libration points, L_4 and L_5. As the secondary gravitational body moves in its orbit about the larger mass, L_4 and L_5 lead and trail the secondary by 60 degrees, respectively. This investigation focuses on periodic solutions in the vicinity of the triangular libration points, specifically horseshoe and tadpole orbits. Horseshoe orbits are symmetric periodic solutions in the plane of primary motion encompassing both triangular points, as well as one of the collinear libration points, L_3. As a result of these known properties, it is possible to identify regions bounding the motion of horseshoe orbits. Also planar, tadpole orbits represent stable oscillations about the triangular points, combining a long-period librational motion and a short-period epicyclic motion reflecting the period of the two large gravitational bodies about their barycenter. Different strategies are developed to effectively construct tadpole orbits numerically, since the motion is not symmetrical and cannot be bounded to a limiting region as accomplished with horseshoe orbits. The relationship between tadpole orbits and other periodic orbits in the vicinity of L_4 and L_5 is examined to explore the natural dynamical evolution of motion and produce useful insight for applications.

1. Introduction

Motion in the vicinity of the equilateral Lagrange points is observed to exist in nature and continues to be a focus of analytical and numerical investigations. The asteroid Achilles (588) was discovered by the astronomer Max Wolf in 1906, and as observational techniques have improved, more than one thousand Trojan asteroids have been discovered in the Sun-Jupiter system [1]. The paths followed by these Trojan asteroids appear to be tadpole orbits, which are characterized as stable oscillations about the Lagrangian trianglar equilibrium points, L_4 and L_5 [2]. This motion combines a long-period librational motion and the short-period epicyclic oscillation reflecting the period of the two large gravitational bodies about their barycenter [3]. Tadpole orbits are not limited to the Sun-Jupiter system; other Trojan minor planets have been observed in the Sun-Mars, Sun-Neptune, Sun-Uranus, and Sun-Earth systems. This type of orbit is also present in planet-moon systems, e.g., the Trojan moons Telesto and Calypso in the Saturn-Tethys system as well as Helen and Polydeuces in the Saturn-Dione system. In recently published investigations, Trojan asteroids have been observed on a path that originates in a tadpole orbit around one of the equilateral points and escape this region, to be eventually captured as a tadpole orbit around the opposite equilateral point [4] [5]. This mechanism may possibly be explained by transport via the invariant manifolds associated with the collinear Lagrange point L_3; such manifolds are similar in shape to horseshoe orbits [6]. Murray and Dermott hypothesize that such horseshoe-like motion is directly related to tadpole orbits, resulting from initial conditions with a larger initial radial separation relative to the equilateral point and also representing resonant co-orbital motion [7]. These dynamical relationships describe the motion of some Trojan bodies, but can potentially be exploited in the design of low-cost trajectories. It is apparent from Érdi et al. [1] that substantial anyalysis of the resonant structures surrounding the equilateral points

has been completed and mission design scenarios are offered. Transfer orbits from a circular parking orbit around Earth to the L_4 and L_5 points are available in the Earth-Moon system [8]. In 2008, Irrgang [9] constructed transfer trajectories to and from the equilateral points in the Earth-Moon system. For trajectory design, various researchers now leverage the dynamical environment involving the L_4 and L_5 regions. For example, low-cost trajectories can exploit heteroclinic and homoclinic connections between periodic orbits around L_3, L_4, and L_5 in the Sun-Earth system as well as the invariant manifolds associated with resonant orbits in the Saturn-Titan system to perform transfers [10] [11]. By determining the relationship between tadpole orbits and nearby dynamical structures, low-cost trajectories can also be designed to the L_4/L_5 region or between the equilateral points. The relative locations of the equilateral points with respect to L_3 are advantageous for solar observations, space weather forecasting, and for seeking hidden minor objects. Additionally, serious mission proposals are emerging to explore the Trojan asteroids in the Sun-Jupiter system [5]. Because low-cost trajectories are often examined as end-of life options for spacecraft, such as the Cassini spacecraft in the Saturnian system, tadpole motion is increasingly suggested beyond the systems in which it naturally occurs [12]. In this current investigation, the ability to compute families of tadpole orbits in both the Sun-Jupiter and Saturn-Titan system is demonstrated and trajectories are designed to these orbits by exploiting the related dynamical structures in the region.

1.1 Problem Definition

Alternate strategies for the numerical construction of tadpole orbits are required, since tadpole orbits are not symmetrical and are not bounded as, for example, horseshoe orbits. Because of the known existence of Trojan asteroids, a formulation in terms of the circular restricted three-body problem to model the Sun-Jupiter system is employed in the computation of periodic tadpole orbits. Linear approximations of this motion in systems with higher mass ratios do not accurately predict the non-

linear dynamical behavior. To examine the possible existence of tadpole orbits for other mass ratios, such motion is explored in the Saturn-Titan system as well. The most efficient strategy to construct periodic tadpole orbits depends on the system and orbital characteristics. Given a family of periodic tadpole orbits, a relationship with other periodic solutions in the region is investigated. The characteristics of the families and the dynamical structures in their vicinity offer a framework to explain the migration of the Trojan asteroids originating in tadpole orbits at one triangular point to the vicinity of the opposite triangular point.

1.2 Previous Contributions

Previous investigation in the circular restricted three-body problem has resulted in a better understanding of the system dynamics and the discovery of more periodic solutions. Co-orbital resonant motion continues to be studied extensively, usually in the context of natural bodies in horseshoe and tadpole configurations. Transfer orbits to the equilateral Lagrange points are also a topic of interest for science missions, providing an advantageous location at L_4 and L_5 for certain science missions. Low-cost transfer trajectories are desirable options, as they reduce propellant cost by leveraging the natural dynamics in the system.

1.2.1 Periodic Orbits Near the Triangular Points

The formulation of the n-body problem originated in Newton's *PhilosophiæNaturalis Principia Mathematica*, published in 1687 [13]. He deduced three laws of motion and used these laws to demonstrate that the orbits in Kepler's problem are ellipses. In 1765, Euler derived the three collinear equilibrium points and investigated the motion of the Moon as a test particle in the Sun-Earth system. Then, in 1772, Lagrange proved the existence of Euler's equilibrium points and, additionally, discovered the remaining two equilibrium solutions, known as the equilateral points [4]. In 1889, Poincaré proved that the only integral of motion in the circular restricted three-body

problem is the Jacobi constant and concluded that an infinite number of periodic orbits exist [14]. In 1967, Szebehely, followed by Deprit and Henrard in 1970, present a review of the literature that included the study of periodic motion around the triangular points [15].

1.2.2 Tadpole Orbits

In 1897, Darwin applied a first-order perturbation analysis to objects displaced from the equilateral Lagrange points in the circular restricted three-body problem. He determined that, below a limiting mass of the secondary body, stable librations (which would later be known as tadpole orbits) would result [16]. After Wolf discovered the Trojan asteroid Achilles (588) in 1906, in the vicinity of the L_4 Lagrange point, more asteroids were located including the largest Trojan asteroid Hektor (624) in 1907 by August Kopff. The L_4 group of Trojan asteroids in the Sun-Jupiter system is denoted as the *group of Achilles* and the *Patroclus group* oscillates about L_5 [4]. In 1911, Brown isolated a region where tadpole orbits should exist and extended this analysis to a region that allows horseshoe orbits [17]. The next major results regarding tadpole orbits did not re-emerge until 1961 when Rabe investigated periodic Trojan orbits in the CR3BP for the Sun-Jupiter system; Rabe also determined a region of indefinite stability for these orbits in 1967 [18] [19]. Dermott and Murray examined the dynamics of tadpole and horseshoe orbits in 1981. The general properties of these orbits were described, building upon the previous analytical theory and demonstrating the two types of trajectories through numerical integration [2]. Much of the current analytical framework that serves as the foundation for tadpole orbits was developed by Érdi, who developed a second-order solution for the motion of Trojan asteroids in the elliptical restricted three-body problem. Other authors have offered both analytical and numerical approaches to explore the orbital stability of the Jupiter Trojans [3]. More recently, Barrabés and Ollé demonstrated that the invariant manifolds associated with orbits around the collinear libration point L_3

exhibit motion similar to that of horseshoe orbits for a wide range of mass ratios [6]. Extended by Oshima and Yanao, the 'jumping' phenomenon of Trojan asteroids appears to leverage the L_3 manifolds to move from a tadpole orbit around one of the equilateral points to the opposite triangular point [5].

1.2.3 Transfer Trajectories

Transfer trajectories are designed to deliver a spacecraft to various trajectories including different periodic orbits. Direct transfers may be used, departing from a parking orbit or periodic libration point orbit in the vicinity of the smaller primary. These types of transfer trajectories have been investigated extensively in the Earth-Moon system, beginning with work by D'Amario who specifically investigated transfers from a lunar orbit to a periodic orbit in the vicinity of L_2 [20]. Research on transfers to the triangular points in the Earth-Moon system includes earlier work by Broucke (1979) [21] and more recently by Irrgang (2008) [9]. Direct transfers requires maneuvers to depart or insert into different types of orbits. Low-thrust transfers for Trojan asteroid tours in the Sun-Jupiter system have also been developed [22], [23]. Although they may offer solutions with low propellant cost, low-thrust transfers are excluded in this investigation and may apply to future work. Transfer trajectories to tadpole orbits can be intuitively designed using the dynamics of related nearby motion. This motion includes the invariant manifolds associated with libration point orbits near L_3 and resonant motion such as that of horseshoe orbits. Recently, the invariant manifolds have been used to design low-cost transfer trajectories in the Saturn-Titan system [11].

1.3 Overview of Current Research

This investigation culminates in the design of transfer trajectories between tadpole orbits and other periodic orbits. Background regarding the system model, numerical methods for computing periodic orbits, and techniques for constructing periodic tad-

pole orbits are developed in order to accomplish this task. This work is organized as follows:

Chapter 2: The circular restricted three-body problem is derived, yielding the equations of motion governing the motion as well as the Jacobi constant. Equilibrium solutions and a linear approximation of motion in the vicinity of the Lagrange points are derived. In addition to these linear equations, the zero velocity surfaces offer information that is useful in constructing periodic orbits. Finally, different coordinate transformations are developed to observe the behavior in other frames that may produce additional insight.

Chapter 3: Various numerical methods are available to compute periodic orbits. The state transition matrix is introduced, an essential component for the numerical methods. Single and multiple shooting differential corrections schemes are used to compute both symmetric and asymmetric periodic orbits. Stability analysis adds critical information once the periodic solutions are constructed. Then, continuation schemes are developed to compute families of orbits or to locate other nearby orbits by varying certain system parameters. Poincaré maps are introduced for analyzing the dynamical flow and can be exploited to locate additional periodic orbits. Next, strategies to compute invariant manifolds are introduced, which are essential to develop viable transfers.

Chapter 4: Different techniques for computing periodic tadpole orbits are developed. First, the search and filter method is introduced, beginning with its application to locating near-periodic horseshoe motion. A linear approximation for tadpole motion is then developed, which supplies information that is useful to other techniques in computing tadpole orbits. Poincaré maps representing different surfaces of section are presented to visualize regions where tadpole orbits may exist. Ephemeris data for Trojan asteroids in the Sun-Jupiter system offers an initial guess used to compute periodic solution in the CR3BP. By leveraging these different techniques to find a periodic orbit, families of peri-

odic solutions in the Saturn-Titan and Sun-Jupiter systems are computed. The transition of this type of motion to systems with higher mass ratios is then explored.

Chapter 5: The dynamics governing behavior in tadpole orbits as well as their orbital properties may seed the emergence of other types of trajectories; such an opportunity is investigated in the Saturn-Titan system. Invariant manifolds associated with a L_3 Lyapunov orbit, horseshoe orbit, and resonant orbit are computed for the same value of Jacobi constant as evaluated for a specific tadpole orbit. Links between these trajectories and the tadpole orbit are determined by leveraging the natural dynamics of these manifolds. Finally, transfers from one equilibrium point to the opposite triangular point are developed by also using these manifolds.

2. System Models and Governing Differential Equations

The equations of motion governing the circular restricted three-body problem are derived, along with the only integral of the motion, that is, the Jacobi constant. Equilibrium solutions and the associated linear variational equations that approximate motion in the vicinity of these points are introduced. This background provides the foundation required for constructing periodic orbits.

2.1 The Circular Restricted Three-Body Problem

Motion of a particle under the gravitational forces of n other bodies is known as the general n-body problem. To derive the equations of motion, the appropriate development of the kinematics is critical. Define each particle in the system as P_i, each with mass m_i, where $i = 1, 2, \ldots, n$. To apply Newton's Law of Motion, the base point of the appropriate position vector is fixed in the inertial frame and the derivative as viewed by an inertial observer is required. Consequently, the unit vectors $\hat{X}, \hat{Y}, \hat{Z}$ define the inertial frame I, and the vector $\bar{r}_i$ (where the overbar indicates a vector) locates the position to P_i, with its inertial base point O. The position vector $\bar{r}_{qi}$ orients the particle P_i relative to P_q, as depicted in Figure 2.1. The equation for the total force exerted on P_i is written as

$$\bar{F}_i = -\tilde{G} \sum_{\substack{j=1 \\ j \neq i}}^{n} \frac{m_i m_j}{r_{ji}^3} \bar{r}_{ji} \tag{2.1}$$

where $\tilde{G}$ is the dimensional scalar universal gravitational constant. The expression for the force in equation (2.1) is rewritten as a result of Newton's second law of motion, yielding the differential equation

$$m_i \bar{r}_i'' = -\tilde{G} \sum_{\substack{j=1 \\ j \neq i}}^{n} \frac{m_i m_j}{r_{ji}^3} \bar{r}_{ji} \tag{2.2}$$

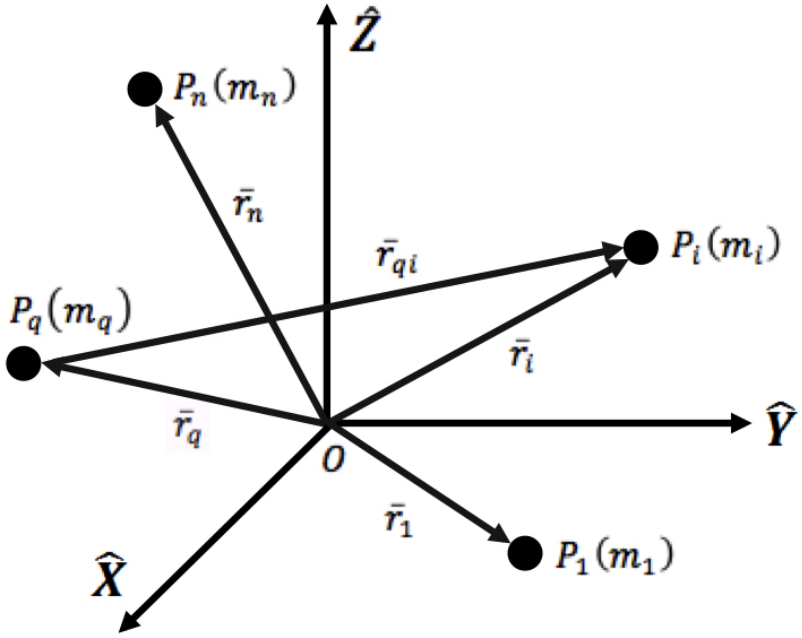

Figure 2.1. Particles in n-Body System

The vector $\bar{r}_i''$ is the acceleration of P_i observed relative to an inertial frame, with the prime indicating a derivative with respect to dimensional time. The equation for this system is then written as

$$\bar{r}_i'' = -\tilde{G} \sum_{\substack{j=1 \\ j \neq i}}^{n} \frac{m_j}{r_{ji}^3} \bar{r}_{ji} \tag{2.3}$$

Reducing equation 2.1 for a system of three bodies P_1, P_2, and P_3, the following differential equation results, describing motion relative to an inertial observer.

$$\bar{r}_3'' = -\tilde{G} \frac{m_1}{{r_{13}}^3} \bar{r}_{13} - \tilde{G} \frac{m_2}{{r_{23}}^3} \bar{r}_{23} \tag{2.4}$$

Solving the differential equation requires a time history for $\bar{r}_1$ and $\bar{r}_2$; however, such information is not available due to the influence of $\bar{r}_3(t)$ on P_1 and P_2. To solve for all three position vectors at the same time requires 18 integrals of the motion, but only 10 constants are known. In the 2-body problem ($n = 2$), the relative motion formulation delivers an analytical solution. However, with the addition of even one additional body ($n = 3$), the relative motion formulation does not reduce to a problem with a closed form solution. But, additional assumptions can produce a representative model that reflects behavior quite accurately in a number of systems.

2.1.1 Assumptions

To gain some useful information regarding a system of only three bodies, some simplifying assumptions are beneficial. Consider the bodies P_1, P_2, P_3 to be particles with masses m_1, m_2, and m_3, respectively. The first two particles P_1 and P_2 are massive bodies denoted the primaries, i.e., a larger primary P_1 and the secondary P_2. If the third body P_3 is modeled as a comet or a spacecraft, it is reasonable to assume that its mass is infinitesimal relative to the primaries. Therefore, the first assumption involves an infinitesimal mass P_3, where $m_3 \ll m_2 < m_1$. With this assumption, the third particle does not influence the motion of the primaries, so the motion of P_1 and P_2 can be represented as an isolated two-body system. Next, assume that the primaries move on circular orbits relative to each other, about their barycenter. As a result, the barycenter is inertially fixed, and the origin of the inertial frame can be defined by B.

Now, the circular restricted three-body problem can be properly defined, with the system and its coordinate frames depicted in Figure 2.2. The inertial frame with the unit vectors $\hat{X}, \hat{Y}, \hat{Z}$ has its origin at the barycenter B. Since P_1 and P_2 are assumed to be on conic paths, their mutual plane of motion is fixed, defined by the $\hat{X} - \hat{Y}$ plane. It is useful however to define a rotating coordinate frame R that moves with the primaries, with unit vectors $\hat{x}, \hat{y}, \hat{z}$. The $\hat{x}$ direction is representative of a line

directed from P_1 to P_2 on which the bodies are fixed in this rotating frame. Because the unit vectors form an orthonormal triad, the $\hat{y}$ direction is perpendicular to the $\hat{x}$ direction, and the $\hat{z}$ direction is parallel to the angular momentum vector of the primary system, aligned with the inertial $\hat{Z}$ unit vector. A rotation through the angle θ relates the rotating and inertial frames.

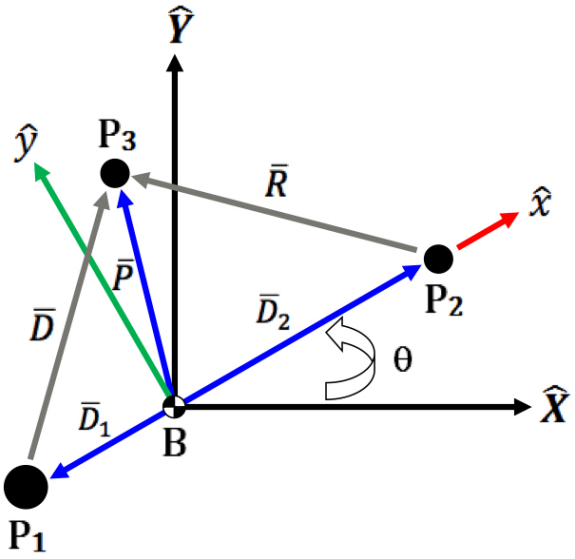

Figure 2.2. Coordinate Frame Definitions in the CR3BP

2.1.2 Differential Equations of Motion

In order to derive the equations of motion for the CR3BP, begin with equation (2.4) which describes the motion of P_3 with respect to an inertial observer, and use the vector definitions seen in Figure 2.2.

$$\bar{P}'' = -\tilde{G}\frac{m_1}{D^3}\bar{D} - \tilde{G}\frac{m_2}{R^3}\bar{R} \tag{2.5}$$

The vector $\bar{P}$ can be defined in terms of its rotating coordinates with dimensional units.

$$\bar{P} = \tilde{x}\hat{x} + \tilde{y}\hat{y} + \tilde{z}\hat{z} \tag{2.6}$$

The derivative of $\bar{P}$ is taken in its rotating coordinates fixed in frame R but with respect to the inertial frame I as

$$\bar{P}' = \frac{^R d\bar{P}}{dt} + ^I\bar{\omega}^R \times \bar{P} \tag{2.7}$$

where the angular velocity $^I\bar{\omega}^R = \theta'\hat{z}$. Through this expression, the derivative of $\bar{P}$ is evaluated to be

$$\bar{P}' = \left(\tilde{x}' - \tilde{y}\theta'\right)\hat{x} + \left(\tilde{y}' + \tilde{x}\theta'\right)\hat{x} + \tilde{z}\hat{z} \tag{2.8}$$

The second derivative of $\bar{P}$ with respect to the inertial frame can then be taken. Because the motion involves circular orbits, the angular velocity is constant and can be defined as $\theta' = N$.

$$\bar{P}'' = \left(\tilde{x}'' - 2\tilde{y}'N - \tilde{x}N^2\right)\hat{x} + \left(\tilde{y}'' + 2\tilde{x}'N - \tilde{y}N^2\right)\hat{y} + \tilde{z}''\hat{z} \tag{2.9}$$

The $\hat{x}, \hat{y}, \hat{z}$ components of this differential equation can now be equated to the related components in equation (2.5), where $\bar{P}''$ is initially defined. First, some characteristic quantities can be defined in order to simplify the expressions by nondimensionalizing the relevant quantities. The characteristic length l^* represents the distance between the two primaries and remains constant and the characteristic mass m^* is equivalent to the total mass of the system, being only the mass of the primaries due to the negligible mass of the third body. The characteristic time is defined such that the gravitational constant is made nondimensional and equal to unity.

$$l^* = D_1 + D_2 \tag{2.10}$$

$$m^* = m_1 + m_2 \tag{2.11}$$

$$t^* = \sqrt{\frac{(l^*)^3}{\tilde{G}m^*}} \tag{2.12}$$

The mass parameter (used to nondimensionalize the primary masses) and nondimensional time are defined as

$$\mu = \frac{m_2}{m^*} \tag{2.13}$$

$$\tau = \frac{t}{t^*} \tag{2.14}$$

Upon nondimensionalizing the relevant quantities by using these characteristic quantities, three scalar second order nondimensional differential equations for the motion of P_3 result, which are the equations of motion governing the CR3BP.

$$\ddot{x} - 2\dot{y} - x = -\frac{(1-\mu)(x+\mu)}{d^3} - \frac{\mu(x-1+\mu)}{r^3} \tag{2.15}$$

$$\ddot{y} + 2\dot{x} - y = -\frac{(1-\mu)y}{d^3} - \frac{\mu y}{r^3} \tag{2.16}$$

$$\ddot{z} = -\frac{(1-\mu)z}{d^3} - \frac{\mu z}{r^3} \tag{2.17}$$

These equations are written in a simplified form, using the magnitudes d and r of the position vectors that define the location of the third body with respect to the two primaries.

$$d = \sqrt{(x+\mu)^2 + y^2 + z^2} \tag{2.18}$$

$$r = \sqrt{(x-1+\mu)^2 + y^2 + z^2} \tag{2.19}$$

Now the equations of motion governing the circular restricted three-body problem are developed, and useful properties about the motion in this system can be investigated.

2.1.3 Integral of Motion

The equations of motion for the CR3BP are coupled and nonlinear, so no general closed-form solution is known. If integrals of the motion exist, they may give useful

information regarding the motion of the spacecraft. An expression for the gravitational potential associated with the differential equations that represents the system model can be expressed in terms of a pseudo-potential function.

$$U^* = \frac{1-\mu}{d} + \frac{\mu}{r} + \frac{1}{2}\left(x^2 + y^2\right) \tag{2.20}$$

The equations of motion can now be rewritten in terms of the pseudo-potential function as

$$\ddot{x} - 2\dot{y} = \frac{\partial U^*}{\partial x} \tag{2.21}$$

$$\ddot{y} + 2\dot{x} = \frac{\partial U^*}{\partial y} \tag{2.22}$$

$$\ddot{z} = \frac{\partial U^*}{\partial z} \tag{2.23}$$

An energy integral is then computed by first evaluating the dot product of the velocity of the third body in the rotating frame with the equations of motion written in equations (2.21) - (2.23), and taking the summation of these scalar energy quantities to be

$$\dot{x}\ddot{x} + \dot{y}\ddot{y} + \dot{z}\ddot{z} = \frac{\partial U^*}{\partial x}\dot{x} + \frac{\partial U^*}{\partial y}\dot{y} + \frac{\partial U^*}{\partial z}\dot{z} \tag{2.24}$$

After integrating equation (2.24), Jacobi's integral results as

$$\dot{x}^2 + \dot{y}^2 + \dot{z}^2 = 2U^* - C \tag{2.25}$$

The equation defining the Jacobi constant can be written in a more compact form, noting that v defines the velocity relative to the rotating frame.

$$v^2 = 2U^* - C \tag{2.26}$$

This energy constant is a quantity that can be used to help determine where orbital motion may exist.

2.2 Equilibrium Solutions

The Jacobi constant is a quantity that provides useful information on the system, but finding particular solutions may also give insight into the motion of a spacecraft. Because U^* is only a function of position and independent of velocity and time, P_3 will theoretically remain at particular locations indefinitely with no initial velocity or accelerations with respect to the rotating frame. These locations are the equilibrium solutions, also known as libration or Lagrange points, and their locations are determined by solving

$$\frac{\partial U^*}{\partial x}\dot{x} = \frac{\partial U^*}{\partial y}\dot{y} = \frac{\partial U^*}{\partial z}\dot{z} = 0 \tag{2.27}$$

Because the velocity and acceleration in the rotating frame are zero at these equilibrium points, the gradient of the pseudo-potential function can be simplified by eliminating these values. Each of the Lagrange points L_i can be determined numerically by solving the following set of equations

$$-\frac{(1-\mu)\,(x_{L_i}+\mu)}{d_{L_i}^3} - \frac{\mu\,(x_{L_i}-1+\mu)}{r_{L_i}^3} + x_{L_i} = 0 \tag{2.28}$$

$$-\frac{(1-\mu)\,y_{L_I}}{d_{L_i}^3} - \frac{\mu y_{L_i}}{r_{L_i}^3} + y_{L_i} = 0 \tag{2.29}$$

$$-\frac{(1-\mu)\,z_{L_I}}{d_{L_i}^3} - \frac{\mu z_{L_i}}{r_{L_i}^3} = 0 \tag{2.30}$$

where $\bar{d}_{L_i}$ and $\bar{r}_{L_i}$ are the position vectors at each L_i that define the location of the third body with respect to the two primaries. Solving equations (2.28) - (2.30) results in five equilibrium solutions. All of the points reside in the plane of motion of the primaries, with no $\hat{z}$-component. Three of the solutions are located on the $\hat{x}$-axis, and known as the collinear points. They are arbitrarily labeled with the first point L_1 and second point L_2 on the left and right of the secondary, respectively, and the third point L_3 to the left of the larger primary, as seen in Figure 2.3. The two remaining Lagrange points form two complete equilateral triangles with the primaries, giving

them their name of the equilateral or triangular points. It is determined that the equilateral points L_4 and L_5 are located at the following coordinates

$$L_4 = \left(\frac{1}{2} - \mu\right)\hat{x} + \frac{\sqrt{3}}{2}\hat{y} \tag{2.31}$$

$$L_5 = \left(\frac{1}{2} - \mu\right)\hat{x} - \frac{\sqrt{3}}{2}\hat{y} \tag{2.32}$$

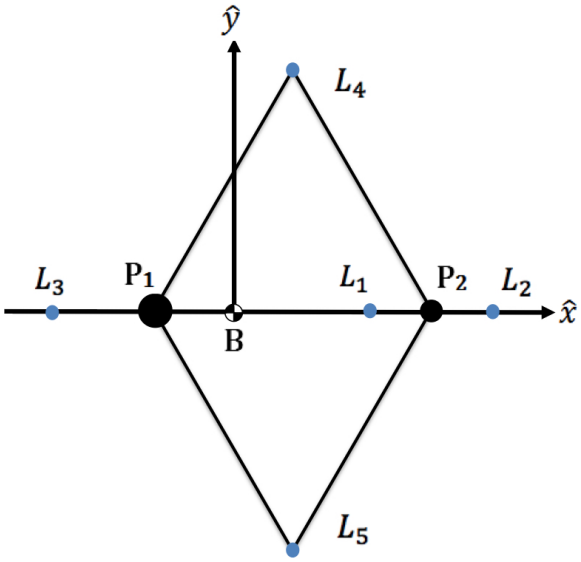

Figure 2.3. Lagrange Point Locations in the CR3BP

The focus of this investigation involves motion in the vicinity of the triangular Lagrange points.

2.2.1 Linear Variational Equations

Particles placed at the five equilibrium points are stationary with respect to the rotating frame. In order to evaluate the stability of the Lagrange points, the equations of motion are linearized relative to these particular solutions. During analysis, it is expected that motion which remains in the vicinity of an equilibrium point after being perturbed will be stable. The equilibrium solutions are perturbed by variations in position ξ, η, ζ

$$x = x_{L_i} + \xi \tag{2.33}$$

$$y = y_{L_i} + \eta \tag{2.34}$$

$$z = z_{L_i} + \zeta \tag{2.35}$$

The time derivatives of the state variables are expressed in terms of the variation.

$$\dot{x} = \dot{\xi} \tag{2.36}$$

$$\dot{y} = \dot{\eta} \tag{2.37}$$

$$\dot{z} = \dot{\zeta} \tag{2.38}$$

$$\ddot{x} = \ddot{\xi} \tag{2.39}$$

$$\ddot{x} = \ddot{\eta} \tag{2.40}$$

$$\ddot{x} = \ddot{\zeta} \tag{2.41}$$

The equations of motion written in terms of the pseudo-potential function are expanded about the equilibrium solutions using a Taylor series expansion. After neglecting the higher-order terms and linearizing, the linear variational equations result

$$\ddot{\xi} - 2\dot{\eta} = U^*_{xx}\xi + U^*_{xy}\eta + U^*_{xz}\zeta \tag{2.42}$$

$$\ddot{\eta} + 2\dot{\xi} = U^*_{yx}\xi + U^*_{yy}\eta + U^*_{yz}\zeta \tag{2.43}$$

$$\ddot{\zeta} = U^*_{zx}\xi + U^*_{zy}\eta + U^*_{zz}\zeta \tag{2.44}$$

where the subscripts in each U^* term are representative of partial derivatives evaluated at L_i. These partial derivatives are determined to be

$$U_x^* = x - \frac{(1-\mu)}{d^3}(x+\mu) - \frac{\mu}{r^3}(x-1+\mu) \tag{2.45}$$

$$U_y^* = y - \frac{(1-\mu)}{d^3}y - \frac{\mu}{r^3}y \tag{2.46}$$

$$U_z^* = -\frac{(1-\mu)}{d^3}z - \frac{\mu}{r^3}z \tag{2.47}$$

$$U_{xx}^* = 1 - \frac{(1-\mu)}{d^3} - \frac{\mu}{r^3} + \frac{3(1-\mu)(x+\mu)^2}{d^5} + \frac{3\mu(x-1+\mu)^2}{r^5} \tag{2.48}$$

$$U_{yy}^* = 1 - \frac{(1-\mu)}{d^3} - \frac{\mu}{r^3} + \frac{3(1-\mu)y^2}{d^5} + \frac{3\mu y^2}{r^5} \tag{2.49}$$

$$U_{zz}^* = -\frac{(1-\mu)}{d^3} - \frac{\mu}{r^3} + \frac{3(1-\mu)z^2}{d^5} + \frac{3\mu z^2}{r^5} \tag{2.50}$$

$$U_{xy}^* = U_{yx}^* = \frac{3(1-\mu)(x+\mu)y}{d^5} + \frac{3\mu(x-1+\mu)y}{r^5} \tag{2.51}$$

$$U_{xz}^* = U_{zx}^* = \frac{3(1-\mu)(x+\mu)z}{d^5} + \frac{3\mu(x-1+\mu)z}{r^5} \tag{2.52}$$

$$U_{yz}^* = U_{zy}^* = \frac{3(1-\mu)yz}{d^5} + \frac{3\mu yz}{r^5} \tag{2.53}$$

Because all of the Lagrange points are in-plane, the partial derivatives containing z-components are evaluated to be zero. As a result, equations (2.42) - (2.44) can be reduced and written as

$$\ddot{\xi} - 2\dot{\eta} = U_{xx}^*\xi + U_{xy}^*\eta \tag{2.54}$$

$$\ddot{\eta} + 2\dot{\xi} = U_{yx}^*\xi + U_{yy}^*\eta \tag{2.55}$$

$$\ddot{\zeta} = U_{zz}^*\zeta \tag{2.56}$$

The in-plane and out-of-plane motion linear for these equations is decoupled, so that each type of motion can be investigated independently. For this investigation, planar motion of P_3 is of interest. Begin by defining the the variational equations relative to each L_i in first-order state space form for planar motion.

$$\bar{x} = \begin{bmatrix} \xi & \eta & \dot{\xi} & \dot{\eta} \end{bmatrix}^T \tag{2.57}$$

$$\dot{\bar{x}} = A\bar{x} \tag{2.58}$$

$$A = \begin{bmatrix} \mathbf{0}_{2\times 2} & \mathbf{I}_{2\times 2} \\ \mathbf{U}_{xx} & \mathbf{\Omega}_{2\times 2} \end{bmatrix} \tag{2.59}$$

$$\mathbf{U}_{xx} = \begin{bmatrix} U^*_{xx} & U^*_{xy} \\ U^*_{yx} & U^*_{yy} \end{bmatrix} \tag{2.60}$$

$$\mathbf{\Omega} = \begin{bmatrix} 0 & 2 \\ -2 & 0 \end{bmatrix} \tag{2.61}$$

To find the roots or eigenvalues, the determinant $\|(\lambda I - A)\| = 0$ must be evaluated. The characteristic equation becomes

$$\lambda^4 + \left(4 - U^*_{xx} - U^*_{yy}\right)\lambda^2 + \left(-2U^*_{xy} - 2U^*_{yx}\right)\lambda + \left(U^*_{xx}U^*_{yy} - U^*_{xy}U^*_{yx}\right) = 0 \tag{2.62}$$

The eigenvalues of the A matrix can give insight into the linear stability of the equilibrium solutions. The following table summarizes Lyapunov stability in terms of the eigenvalues.

Table 2.1. Lyapunov Stability

Condition	Stability
$\Re(\lambda_i) > 0$ for any λ_i	unstable
$\Re(\lambda_i) < 0$ for all λ_i	asymptotically stable
$\Re(\lambda_i) \leq 0$ for all λ_i	marginally stable

By using this Lyapunov stability criteria, it is determined that the collinear Lagrange points L_1, L_2, and L_3 are linearly unstable. For systems with a large enough mass ratio (such as the Saturn-Titan system), the triangular points L_4 and L_5 are marginally stable in the linear system.

2.2.2 Motion Near the Collinear Lagrange Points

The collinear Lagrange points are located on the $\hat{x}$-axis, and this information is useful in simplifying the solution for the linear motion in the vicinity of L_1, L_2, and L_3. Because $y_{L_i} = z_{L_i} = 0$ for these points, the characteristic equation can be rewritten as

$$\lambda^4 + \left(4 - U^*_{xx} - U^*_{yy}\right)\lambda^2 + U^*_{xx}U^*_{yy} = 0 \tag{2.63}$$

The roots of the characteristic equation are found to be

$$\lambda_{1,2} = \pm\sqrt{-\beta_1 + (\beta_1^2 + \beta_2^2)^{\frac{1}{2}}} \tag{2.64}$$

$$\lambda_{3,4} = \pm\sqrt{-\beta_1 - (\beta_1^2 + \beta_2^2)^{\frac{1}{2}}} \tag{2.65}$$

where the constants in each expression β_i are functions of the pseudo-potential evaluated at each L_i

$$\beta_1 = 2 - \frac{U^*_{xx} + U^*_{yy}}{2} \tag{2.66}$$

$$\beta_2^2 = -U^*_{xx}U^*_{yy} > 0 \tag{2.67}$$

$$\beta_3 = \frac{s^2 + U^*_{xx}}{2s} \tag{2.68}$$

$$s = \sqrt{\beta_1 + (\beta_1^2 + \beta_2^2)^{\frac{1}{2}}} \tag{2.69}$$

The solutions to the linear variational equations can be written as

$$\xi = \sum_{i=1}^{4} A_i e^{\lambda_i t} \tag{2.70}$$

$$\eta = \sum_{i=1}^{4} \lambda_i A_i e^{\lambda_i t} \tag{2.71}$$

where each A_i is a coefficient. The goal is to result in periodic motion by exciting the oscillatory mode, so the conditions $A_1 = A_2 = 0$ are set. By selecting these initial

conditions, the unstable frequencies are removed so that motion will remain near the Lagrange point. Now the variations and their derivatives can be defined as

$$\xi = \xi_0 \cos\left(s\left(\tau - \tau_0\right)\right) + \frac{\eta_0}{\beta_3} \sin\left(s\left(\tau - \tau_0\right)\right) \tag{2.72}$$

$$\eta = \eta_0 \cos\left(s\left(\tau - \tau_0\right)\right) - \beta_3 \xi_0 \sin\left(s\left(\tau - \tau_0\right)\right) \tag{2.73}$$

$$\dot{\xi} = -\xi_0 s \sin\left(s\left(\tau - \tau_0\right)\right) + \frac{\eta_0}{\beta_3} s \cos\left(s\left(\tau - \tau_0\right)\right) \tag{2.74}$$

$$\dot{\eta} = -\eta_0 s \sin\left(s\left(\tau - \tau_0\right)\right) - \beta_3 \xi_0 s \cos\left(s\left(\tau - \tau_0\right)\right) \tag{2.75}$$

where the initial positions and velocities at initial time τ_0 are (ξ_0, η_0) and $(\dot{\xi}_0, \dot{\eta}_0)$, respectively. The period is computed to be

$$P = \frac{2\pi}{s} \tag{2.76}$$

This information from the linear motion is useful in predicting the nature of motion near the collinear Lagrange points in the nonlinear system.

2.2.3 Motion Near the Equilateral Lagrange Points

Next, the solution of the linear motion relative to the L_4 and L_5 is investigated. Understanding this motion will provide the foundation for describing tadpole orbits. Planar motion is of interest, so the characteristic equation takes the form

$$\lambda^4 + \left(4 - U^*_{xx} - U^*_{yy}\right)\lambda^2 + \left(U^*_{xx} U^*_{yy} - U^{*\,2}_{yy}\right) = 0 \tag{2.77}$$

Evaluating the partial derivatives of the pseudo-potential function at the location of the equilateral Lagrange points results in

$$U^*_{xx} = \frac{3}{4} \tag{2.78}$$

$$U^*_{yy} = \frac{9}{4} \tag{2.79}$$

$$U^*_{xy} = \pm\frac{3\sqrt{3}}{2}\left(\mu - \frac{1}{2}\right) \tag{2.80}$$

Substituting the values in from equations (2.78) - (2.80), the characteristic equation can be rewritten as

$$\lambda^4 + \lambda^2 + \frac{27}{4}\mu\left(1-\mu\right) = 0 \tag{2.81}$$

The roots of the fourth order characteristic equation are determined, using the quantities defined in equations (2.84) - (2.86) to simplify the expression.

$$\lambda_{1,2} = \pm j s_1 \tag{2.82}$$

$$\lambda_{3,4} = \pm j s_2 \tag{2.83}$$

$$g = 1 - 27\mu\left(1-\mu\right) \tag{2.84}$$

$$j s_1 = \sqrt{\left(\frac{1}{2}\left(-1+\sqrt{g}\right)\right)} \tag{2.85}$$

$$j s_2 = \sqrt{\left(\frac{1}{2}\left(-1-\sqrt{g}\right)\right)} \tag{2.86}$$

The expression defining the variable g defined in equation (2.84) can be used to find the critical value of the mass ratio μ for which the triangular points are stable in the linear system. By defining $\Lambda = \lambda^2$, the characteristic equation can be written in a simpler form and the root Λ can be evaluated in terms of g.

$$\Lambda^2 + \Lambda + \frac{27}{4}\mu\left(1-\mu\right) = 0 \tag{2.87}$$

$$\Lambda = \frac{1}{2}\left(-1 \pm \sqrt{g}\right) \tag{2.88}$$

The equilateral points will be marginally stable from a linear perspective if $0 < g \leq 1$. It is determined that the critical value of mass ratio $\mu_0 = 0.03852$. For values less than this, the triangular points become unstable. Assuming the value of mass ratio results in marginal stability, the motion is bounded and the superposition of two harmonic oscillations with different frequencies, including a long and short period motion. Because there are no real components of the roots, the motion of the linear system relative to the equilateral points has marginal stability. The equations for the variations and their derivatives can be written as

$$\xi = \alpha_1 \cos s_1\tau + \alpha_2 \sin s_1\tau + \alpha_3 \cos s_2\tau + \alpha_4 \sin s_2\tau \tag{2.89}$$

$$\eta = \beta_1 \cos s_1\tau + \beta_2 \sin s_1\tau + \beta_3 \cos s_2\tau + \beta_4 \sin s_2\tau \tag{2.90}$$

$$\dot{\xi} = -\alpha_1 s_1 \sin s_1\tau + \alpha_2 s_1 \cos s_1\tau - \alpha_3 s_2 \sin s_2\tau + \alpha_4 s_2 \cos s_2\tau \tag{2.91}$$

$$\dot{\eta} = -\beta_1 s_1 \sin s_1\tau + \beta_2 s_1 \cos s_1\tau - \beta_3 s_2 \sin s_2\tau + \beta_4 s_2 \cos s_2\tau \tag{2.92}$$

where α_i and β_i are coefficients that can be selected. To find initial conditions of the equations for the variations, it is necessary to determine the relationship between these coefficients. First, the second derivatives of the variations are computed.

$$\ddot{\xi} = -\alpha_1 s_1^2 \cos s_1\tau - \alpha_2 s_1^2 \sin s_1\tau - \alpha_3 s_2^2 \cos s_2\tau - \alpha_4 s_2^2 \sin s_2\tau \tag{2.93}$$

$$\ddot{\eta} = -\beta_1 s_1^2 \cos s_1\tau - \beta_2 s_1^2 \sin s_1\tau - \beta_3 s_2^2 \cos s_2\tau - \beta_4 s_2^2 \sin s_2\tau \tag{2.94}$$

Next, the equations for the variations and their first and second derivatives are substituted in to the original differential equation for the variations defined in equations (2.54) - (2.55). By solving the system of equations, the relationships between the coefficients α_i and β_i are determined.

$$\alpha_1 = \frac{-2\beta_2 s_1 - U^*_{xy}\beta_1}{U^*_{xx} + s_1^2} \tag{2.95}$$

$$\alpha_2 = \frac{-2\beta_1 s_1 + U^*_{xy}\beta_2}{U^*_{xx} + s_1^2} \tag{2.96}$$

$$\alpha_3 = \frac{-2\beta_4 s_2 - U^*_{xy}\beta_3}{U^*_{xx} + s_2^2} \tag{2.97}$$

$$\alpha_4 = \frac{-2\beta_3 s_2 + U^*_{xy}\beta_4}{U^*_{xx} + s_2^2} \tag{2.98}$$

The terms corresponding to the long period motion in equations (2.89)-(2.90) contain the coefficients $\alpha_1, \alpha_2, \beta_1$ and β_2, and the short period motion contains $\alpha_3, \alpha_4, \beta_3$ and β_4. To eliminate the long period terms, the related coefficients must be set to zero, resulting in the linear short period motion. The opposite procedure is used to compute the linear long period motion. By keeping all of the coefficients, combined short and long period motion results, which can provide a linear approximation of tadpole orbits.

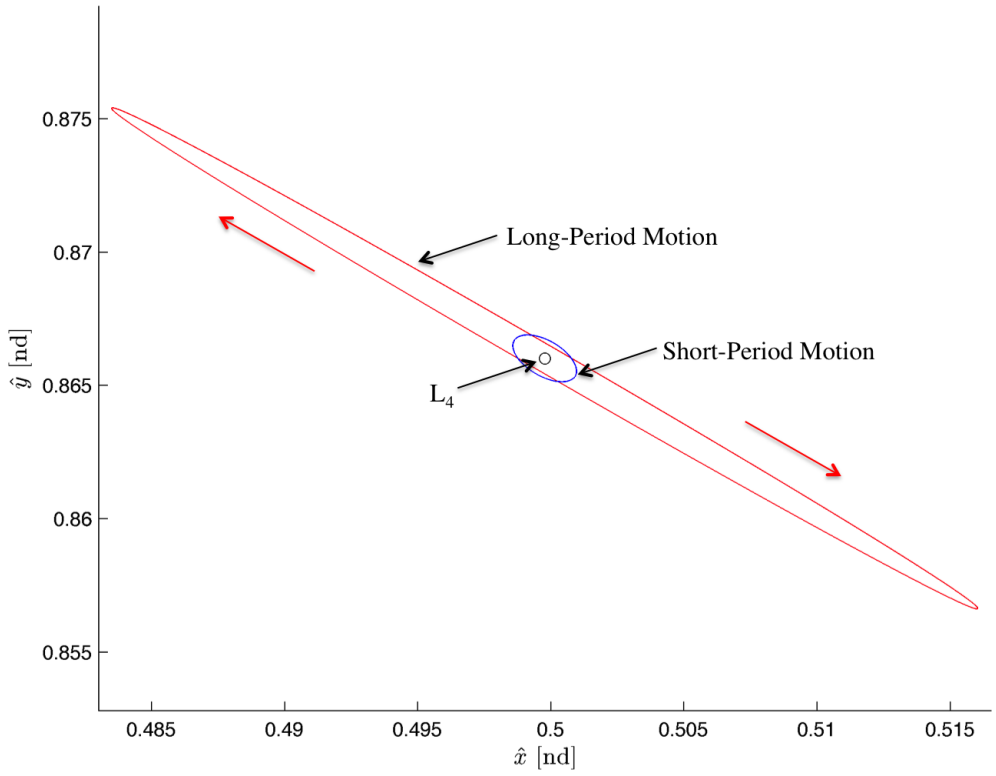

Figure 2.4. Short and Long Period Linear Motion in the Saturn-Titan System

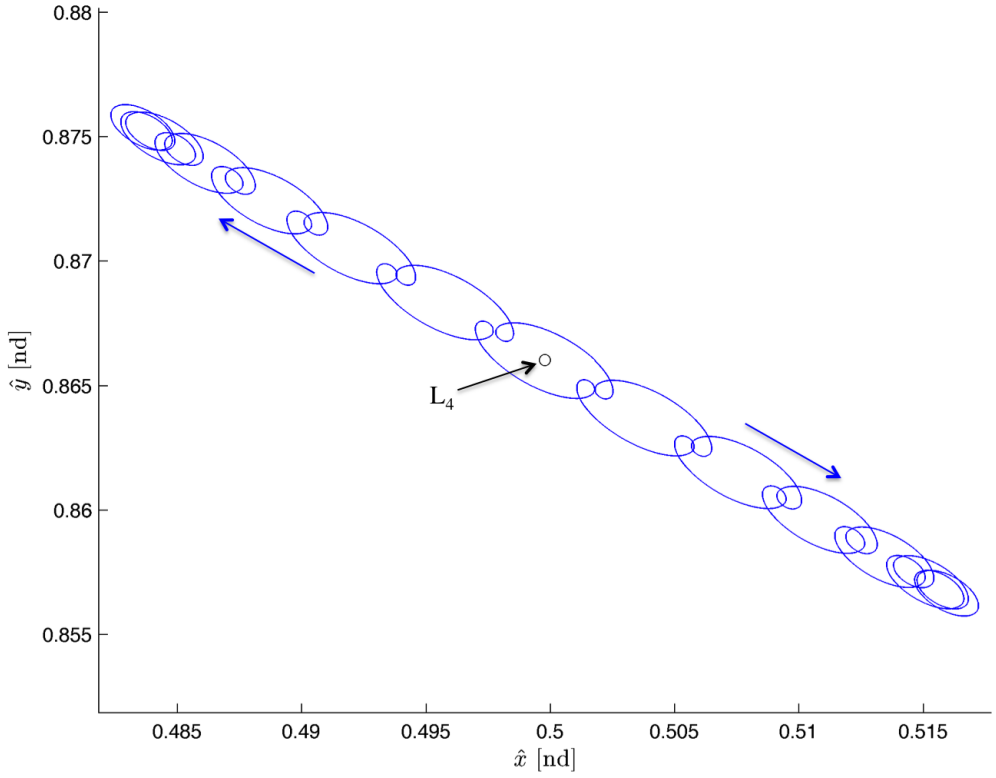

Figure 2.5. Combined Short and Long Period Linear Motion in the Saturn-Titan System

2.3 Zero Velocity Surfaces

Equilibrium solutions and the Jacobi constant lead to another important concept that can be used to bound the region where motion can occur in the system. If the relative velocity $v = 0$, then the expression for the Jacobi constant can be reduced to

$$\dot{x}^2 + \dot{y}^2 + \frac{2\left(1-\mu\right)}{d} + \frac{2\mu}{r} = C \tag{2.99}$$

An infinite variety of (x, y, z) combinations satisfy equation (2.99), generating a surface of solutions in three dimensions. The Lagrange points also satisfy the requirement of zero relative velocity and additionally have zero relative acceleration. Examining each term in the expression defining the zero-velocity surface, it is determined that the sign of each term is positive, so C must always be positive. Additional information can be found from the surfaces when evaluating the expression for the Jacobi constant, with the velocity term included.

$$v^2 = 2U^* - C \tag{2.100}$$

For points lying along the zero-velocity surfaces, this velocity term is zero by definition. The acceleration however will be nonzero, so the third body will move on the surface. In order for motion between two surfaces to occur, the evaluation of v^2 would have to be negative, indicating imaginary velocity. As a result, a third body cannot move between two surfaces because an imaginary velocity is not physically possible. Any motion outside of a surface results in a positive v^2 term, and in this region orbital motion can occur. The zero-velocity surfaces are a function of the mass parameter of the system μ, and they evolve as the Jacobi constant decreases. These surfaces can be viewed as curves for planar motion, and Figure 2.6 shows how the zero-velocity curves change for the Saturn-Titan system.

In Figure 2.6(a), the value of C is set to that of L_1, and this Jacobi constant represents the critical value before the gateway opens to allow motion in the vicinity of this Lagrange point. In Figure 2.6(b) $C = C_{L_2}$, and the general structure of the

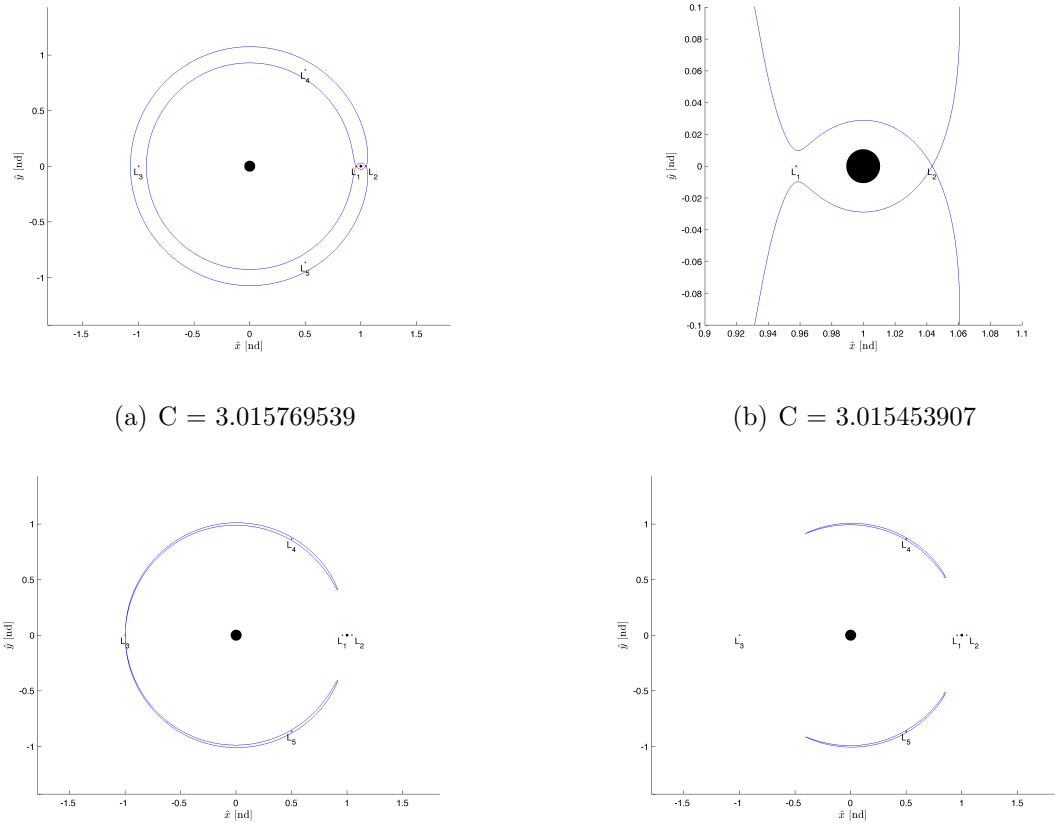

(a) C = 3.015769539

(b) C = 3.015453907

(c) C = 3.000236693

(d) C = 3.000000027

Figure 2.6. Zero-Velocity Curves in the Saturn-Titan System

curve is similar to the previous figure; however, this view is zoomed to show that the L_1 gateway is clearly open. The following two figures are representative of the zero-velocity curves for the critical value of L_3 and the average Jacobi constant of L_3 and L_4, respectively. Once the Jacobi constant of the triangular points is reached, the curve disappears. It is important to note that surfaces bounding the motion will still exist outside of the $\hat{x} - \hat{y}$ plane.

2.4 Coordinate Frame Transformations

The CR3BP uses a coordinate frame that rotates with the two primaries and by observing motion in this frame, periodic orbits and other useful trajectories can be found that are not apparent in the inertial frame. Ephemeris data describing the motion of real spacecraft and small bodies may only be available in an inertial frame, so methods must be developed in order to convert this state information to the rotating frame. Additionally, a trajectory analyst may have a conic two-body approximation of an orbit, and converting this information so that it can be integrated in the three-body problem demonstrates how the inclusion of a secondary body affects the motion.

2.4.1 Relating the Inertial and Rotating Frames

In order to convert a trajectory from the inertial to the rotating frame, recall the diagram of the CR3BP in Figure 2.2. The angle θ relates the rotating and inertial frame. If the ephemeris states of a spacecraft or small body are available relative to an inertial frame fixed in the larger primary, the angle θ can be approximated by the orbit of the secondary relative to the primary. This approximation can be made assuming the orbit of the secondary is nearly circular and that this ephemeris data is available at the same time of the spacececraft or small body. The direction cosine matrix (DCM) used to convert between the inertial and rotating frames is defined as

$$ {}^{I}C^{R} = \begin{bmatrix} cos(\theta) & sin(\theta) & 0 \\ -sin(\theta) & cos(\theta) & 0 \\ 0 & 0 & 1 \end{bmatrix} \tag{2.101} $$

The transformation for a position vector fixed in the inertial frame to the rotating frame can be performed as follows.

$$ {}^{I}\bar{r}_{1\times 3} = {}^{R}\,\bar{r}_{1\times 3}\,{}^{I}C^{R} \tag{2.102} $$

The inertial velocity cannot be directly transformed to the rotating frame using the same method as the position vector transformation. Instead, the angular velocity of the inertial frame relative to the rotating frame must be accounted for such that the velocity to be computed is relative to the rotating frame. This angular velocity is simply the mean motion of the system about its barycenter.

$$\frac{^R d\bar{r}}{dt} = \frac{^I d\bar{r}}{dt} + {}^R\bar{\omega}^I \times {}^I\bar{r} \tag{2.103}$$

$$^R\bar{\omega}^I = -\dot{\theta}\hat{z} = \frac{1}{t^*} \tag{2.104}$$

After the velocity has been computed relative to an observer fixed in the rotating frame, it is still expressed in terms of inertial coordinates. The transformation to the rotating frame can now be performed using the DCM in equation (2.101).

2.4.2 Polar Coordinates in the Rotating Frame

Sometimes expressing the motion in terms of the rotating coordinates does not always give all of the information required to describe the characteristics of a trajectory. The path that the third body follows can be complex and better understood by converting to polar coordinates. Although the location of the larger primary and barycenter of the primary system are usually very close in most systems, it may also be desirable to observe how P_3 moves relative to the larger primary in polar coordinates. The radius r can then be representative of the distance from the third body to the larger primary, with θ defining the location of the spacecraft with respect to the $\hat{x}$-axis. In order to give both options of defining the radius with respect to the barycenter or the larger primary, introduce the variable x^*, where $x^* = x$ for the first case. If the distance of P_3 from P_1 is desired, then $x^* = x + \mu$. The conversion to polar coordinates from a state expressed in the rotating frame can be computed using the following equations.

$$\theta = tan^{-1}\frac{y}{x^*} \tag{2.105}$$

$$r = \sqrt{(x^*)^2 + y^2} \tag{2.106}$$

$$\dot{\theta} = \left(\frac{\dot{y}}{x^*} - \frac{y\dot{x}}{(x^*)^2}\right) cos^2\theta \tag{2.107}$$

$$\dot{r} = \frac{(x^*)\,\dot{x} + y\dot{y}}{\sqrt{(x^*)^2 + y^2}} \tag{2.108}$$

By performing this change of coordinates, additional frequencies in the motion of periodic orbits may be discovered. This investigation may provide information that relates an orbit to related motion or characteristics of the system itself. If information is instead available in terms of polar coordinates (for example if range measurements are given), the rotating frame Cartesian coordinates may be of interest. This conversion is performed using the following equations.

$$x = r\cos\theta \tag{2.109}$$

$$y = r\sin\theta \tag{2.110}$$

$$\dot{x} = \dot{r}\cos\theta - r\dot{\theta}\sin\theta \tag{2.111}$$

$$\dot{y} = \dot{r}\sin\theta - r\dot{\theta}\cos\theta \tag{2.112}$$

The equations are the same for motion relative to the barycenter or P_1 (assuming θ accounts for this choice), except that μ must be subtracted from (2.109) for the latter.

3. Numerical Methods for Computing Periodic Orbits

Now that the equations of motion and linear approximations of the motion around the Lagrange points have been developed for the CR3BP, periodic orbits can be searched for in the nonlinear system. Using numerical integration, initial state conditions can be propagated. Even though the desired orbit may be nearby, the resulting motion is almost certainly not the actual periodic orbit in the nonlinear system. Instead of varying initial conditions randomly until desired motion is achieved, an intuitive approach can be developed that may result in the desired motion.

3.1 The State Transition Matrix

A standard method exists to obtain information about trajectories nearby the integrated motion that helps determine how the initial state should be changed in order to achieve the desired end solution. This method relies on the variational equations and the State Transition Matrix (STM). The STM is the derivative of the state solution at time t with respect to initial conditions at time t_0. Beginning with initial conditions $\bar{x}^*(t_0)$, the final trajectory $\bar{x}^*(t)$ results. A nearby trajectory with isochronous correspondence can be determined by perturbing the state as

$$\bar{x}(t) = \bar{x}^*(t) + \delta\bar{x}(t) \tag{3.1}$$

The nearby trajectory defined by equation (3.1) can be substituted into the system equation of motion written as

$$\dot{\bar{x}} = \bar{f}(\bar{x}, t) \tag{3.2}$$

Using a Taylor series expansion, the first order linear and time-varying variational equation results, where $\bar{x}^*$ is a solution of equation (3.2).

$$\delta\dot{\bar{x}} = \frac{\partial \bar{f}}{\partial \bar{x}}\Big|_{\bar{x}^*} \delta\bar{x} \tag{3.3}$$

The general solution for $\delta\bar{x}$ is determined to be

$$\delta\bar{x} = \phi\left(t, t_0\right) \delta\bar{x}\left(t_0\right) \tag{3.4}$$

where $\phi\left(t, t_0\right)$ is the STM. The differential equation that governs the STM and its initial conditions are defined as

$$\dot{\phi}\left(t, t_0\right) = A\left(t\right) \phi\left(t, t_0\right) \tag{3.5}$$

$$\phi\left(t_0, t_0\right) = I \tag{3.6}$$

where I is the identity matrix. The matrix $A\left(t\right)$ is defined as

$$A\left(t\right) = \begin{bmatrix} \mathbf{0}_{3\times3} & \mathbf{I}_{3\times3} \\ \mathbf{U}_{xx} & \mathbf{\Omega}_{3\times3} \end{bmatrix} \tag{3.7}$$

$$\mathbf{U}_{xx} = \begin{bmatrix} U^*_{xx} & U^*_{xy} & U^*_{xz} \\ U^*_{yx} & U^*_{yy} & U^*_{yz} \\ U^*_{zx} & U^*_{zy} & U^*_{zz} \end{bmatrix} \tag{3.8}$$

$$\mathbf{\Omega} = \begin{bmatrix} 0 & 2 & 0 \\ -2 & 0 & 0 \\ 0 & 0 & 0 \end{bmatrix} \tag{3.9}$$

Numerically integrating the STM is required in order to solve for for $\delta\bar{x}$. The variational equations can then be solved for using the STM, which is defined as

$$\phi(t,t_0) = \begin{bmatrix} \frac{\partial x}{\partial x_0} & \frac{\partial x}{\partial y_0} & \frac{\partial x}{\partial z_0} & \frac{\partial x}{\partial \dot{x}_0} & \frac{\partial x}{\partial \dot{y}_0} & \frac{\partial x}{\partial \dot{z}_0} \\ \frac{\partial y}{\partial x_0} & \frac{\partial y}{\partial y_0} & \frac{\partial y}{\partial z_0} & \frac{\partial y}{\partial \dot{x}_0} & \frac{\partial y}{\partial \dot{y}_0} & \frac{\partial y}{\partial \dot{z}_0} \\ \frac{\partial z}{\partial x_0} & \frac{\partial z}{\partial y_0} & \frac{\partial z}{\partial z_0} & \frac{\partial z}{\partial \dot{x}_0} & \frac{\partial z}{\partial \dot{y}_0} & \frac{\partial z}{\partial \dot{z}_0} \\ \frac{\partial \dot{x}}{\partial x_0} & \frac{\partial \dot{x}}{\partial y_0} & \frac{\partial \dot{x}}{\partial z_0} & \frac{\partial \dot{x}}{\partial \dot{x}_0} & \frac{\partial \dot{x}}{\partial \dot{y}_0} & \frac{\partial \dot{x}}{\partial \dot{z}_0} \\ \frac{\partial \dot{y}}{\partial x_0} & \frac{\partial \dot{y}}{\partial y_0} & \frac{\partial \dot{y}}{\partial z_0} & \frac{\partial \dot{y}}{\partial \dot{x}_0} & \frac{\partial \dot{y}}{\partial \dot{y}_0} & \frac{\partial \dot{y}}{\partial \dot{z}_0} \\ \frac{\partial \dot{z}}{\partial x_0} & \frac{\partial \dot{z}}{\partial y_0} & \frac{\partial \dot{z}}{\partial z_0} & \frac{\partial \dot{z}}{\partial \dot{x}_0} & \frac{\partial \dot{z}}{\partial \dot{y}_0} & \frac{\partial \dot{z}}{\partial \dot{z}_0} \end{bmatrix} \tag{3.10}$$

Each element of the STM predicts how each component of the final state will change based on a change in each component of the initial state. It is useful in the targeting problem which is the foundation of numerically computing periodic orbits in the CR3BP.

3.2 Differential Corrections

In order to solve a targeting problem, a numerical technique must be employed that will iteratively use the information from the STM and a baseline trajectory in order to achieve a desired result. The initial guess must be updated until certain convergence criteria are met by minimizing the error between the desired and actual final state. A convenient way to define this problem is through the constraints and free-variables formulation. First, consider a design variable vector $\bar{X}$ of n free-variables subject to m constraint equations

$$\bar{X} = \begin{bmatrix} X_1 \\ X_2 \\ \vdots \\ X_n \end{bmatrix} \tag{3.11}$$

$$\bar{F}\left(\bar{X}\right) = \begin{bmatrix} F_1\left(\bar{X}\right) \\ F_2\left(\bar{X}\right) \\ \vdots \\ F_m\left(\bar{X}\right) \end{bmatrix} = \bar{0} \tag{3.12}$$

In a targeting problem, the goal is to find a solution $\bar{X}^*$ that satisfies the constraints $\bar{F}\left(\bar{X}^*\right) = \bar{0}$. Usually if the number of free variables is greater than or equal to the number of constraints, a solution can be obtained. By supplying an initial guess $\bar{X}^i$, the constraint vector can be approximated with a Taylor series expansion. The following relationship between each iteration can be defined, where $D\bar{F}\left(\bar{X}^i\right)$ is the Jacobian matrix of dimensions $m \times n$.

$$\bar{F}\left(\bar{X}^j\right) + D\bar{F}\left(\bar{X}^j\right) \cdot \left(\bar{X}^{j+1} - \bar{X}^j\right) = \bar{0} \tag{3.13}$$

$$D\bar{F}\left(\bar{X}^i\right) = \begin{bmatrix} \frac{\partial F_1}{\partial X_1} & \frac{\partial F_1}{\partial X_2} & \cdots & \frac{\partial F_1}{\partial X_n} \\ \frac{\partial F_2}{\partial X_1} & \frac{\partial F_2}{\partial X_2} & \cdots & \frac{\partial F_2}{\partial X_n} \\ \vdots & \vdots & \ddots & \\ \frac{\partial F_m}{\partial X_1} & \frac{\partial F_m}{\partial X_2} & & \frac{\partial F_m}{\partial X_n} \end{bmatrix} \tag{3.14}$$

If the number of free-variables and constraints are equivalent ($n = m$), then one unique solution exists to equation (3.13). This solution is known as Newton's Method and can be written as

$$\bar{X}^{j+1} = \bar{X}^j - D\bar{F}\left(\bar{X}^j\right)^{-1} \bar{F}\left(\bar{X}^j\right) \tag{3.15}$$

If the number of free-variables is greater than the number of constraints, then infinite solutions exist. Because one unique solution must be selected, the solution

$\bar{X}^{j+1}$ closest to $\bar{X}^{j}$ is selected because it inherits the most characteristics of the previous iteration. This selection yields the minimum error for the achieved evaluation of the desired constraints. The update equation for the minimum-norm solution is formulated as

$$\bar{X}^{j+1} = \bar{X}^{j} - D\bar{F}\left(\bar{X}^{j}\right)^{T}\left[D\bar{F}\left(\bar{X}^{j}\right)D\bar{F}\left(\bar{X}^{j}\right)^{T}\right]^{-1}\bar{F}\left(\bar{X}^{j}\right) \tag{3.16}$$

The update equation for either Newton's Method or the minimum-norm solutions is iterated until the magnitude of the constraint vector is less than some error ϵ. Generally, the error at each iteration should decrease until this condition is met.

3.2.1 Single Shooting

The single shooting method is a simple way to solve a targeting problem. It is commonly used to find the initial state required in order to achieve a desired final state. For a general formulation, consider a baseline trajectory with initial state $\bar{x}_0$ at time t_0 and final state $\bar{x}_f$. The goal is to compute the solution $\bar{x}_0^*$ such the desired final state $\bar{x}_f^*$ at time t_f is achieved.

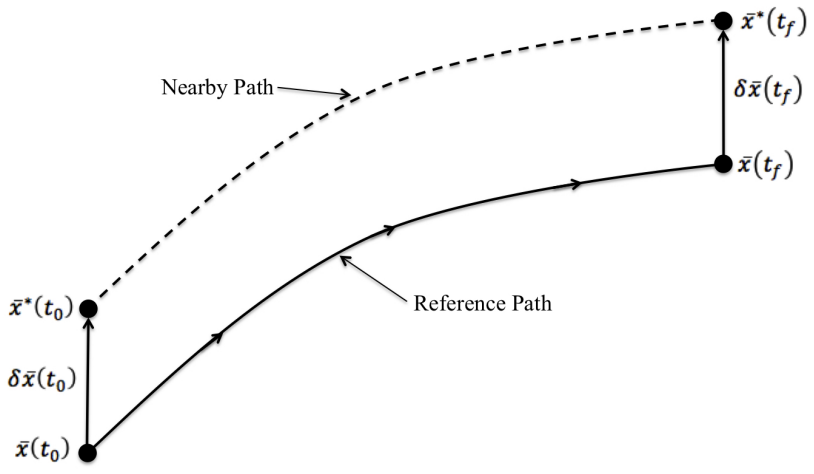

Figure 3.1. Single Shooting Targeting Scheme

Modifications can then be made to the general formulation for specific applications. Common problems include computing the ΔV maneuver applied at a fixed initial position to insert a spacecraft in to a specific orbit at a later time. If the mission constraints require a specific final time, this variable can also be fixed.

3.2.2 Multiple Shooting

The single shooting method provides a versatile framework that can be changed to satisfy different needs; however, due to the nonlinearities of the CR3BP, it has difficulty converging for some trajectories. Because the STM provides a linear approximation of the variation, error in predicting the final state increases for baselines with longer integration times. Orbits with complicated geometry also prove difficult to converge due to their highly nonlinear motion. By approximating a trajectory by a set of n discrete patch points instead of integrating only one trajectory leg, the multiple shooting method can be used to solve targeting problems. Let each of the patch points along the trajectory be defined by $\bar{x}_1, \bar{x}_2, \ldots, \bar{x}_{n-1}, \bar{x}_n$, with each point (except for the final one) integrated for times $t_1, t_2, \ldots, t_{n-1}$, respectively. Each iteration, a new set of points that is close as possible to the old set is generated, until a continuous trajectory is formed such that each $\bar{x}_{i+1}^t(\bar{x}_i) = \bar{x}_{i+1}$.

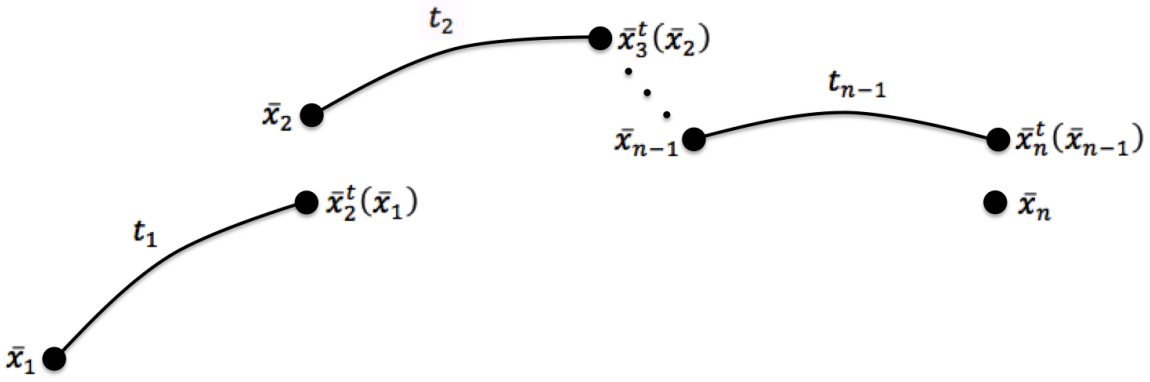

Figure 3.2. Multiple Shooting Targeting Scheme

Multiple shooting is advantageous in many scenarios where single shooting may have difficulty finding a solution. Often times only an approximate solution of a trajectory is available and the goal is a nearby solution that inherits the characteristics of the approximate solution. For example, a two-body Keplerian orbit may be of interest. The conic approximation may still provide an adequate initial guess that converges using the shooting method in the CR3BP, but some of the geometry may be lost is only the single shooting method is used. Multiple shooting accounts for sensitives of not only the first point along the trajectory but the intermediate points as well.

3.3 Computing Periodic Orbits

Now that different differential corrections methods have been determined, these strategies can be employed to find periodic orbits in the CR3BP. Because the equations of motion represent a time-invariant Hamiltonian system, periodic motion can exist, and this motion can be found through numerical integration. A two-point boundary value problem is presented, as the final and initial state of a periodic orbit must be the same. Periodic motion can be found near the Lagrange points, with some motion being more complex than other. Different strategies can be used depending on the type of orbit.

3.3.1 Symmetric Orbits

The process for computing periodic orbits can be simplified in the case of trajectories that are symmetric. According to the *Mirror Theorem*, if at two separate times a mirror configuration occurs, then an orbit is periodic [24]. In the CR3BP, symmetry about the $\hat{x}$-axis can be exploited. By propagating the equations of motion in backwards time, a mirror image trajectory across the $\hat{x}$-axis exists for every trajectory. This motion can be achieved through the following transformation, where derivatives are taken with respect to $\tau' = -\tau$.

$$x' = x \tag{3.17}$$

$$y' = -y \tag{3.18}$$

$$z' = z \tag{3.19}$$

$$\dot{x}' = -\dot{x} \tag{3.20}$$

$$\dot{y}' = \dot{y} \tag{3.21}$$

$$\dot{z}' = -\dot{z} \tag{3.22}$$

As a result, determining symmetric periodic orbits only requires integration for one-half period. When determining planar libration point orbits in the vicinity of the collinear points, periodic solutions can be found simply by setting the initial conditions at one of the perpendicular $\hat{x}$-axis crossings. To achieve this result, the conditions $\dot{x}_0 = y_0 = 0$ are set on the initial state $\bar{x}_0$ such that the only unknowns are then x_0 and $\dot{y}_0$. After propagating for a half-period $\frac{P}{2}$, the final state $\bar{x}_f$ is targeted to also have a perpendicular $\hat{x}$-axis crossing resulting in $\dot{x}_f = y_f = 0$. For these simple Lyapunov orbits, usually the single shooting method is sufficient to converge on a solution. An initial guess for the baseline trajectory can be determined by the linear variational equations for motion near the collinear equilibrium points.

Other types of symmetric orbits exist that have longer periods or more complex geometry where multiple shooting may be required to converge on a solution or reduce computation time by finding a solution more easily. Examples of these orbits may include horseshoe orbits that encompass the two triangular points and L_3 or some other resonant orbits.

3.3.2 Asymmetric Orbits

Not all periodic orbits in the CR3BP are symmetric about the $\hat{x}$-axis, so a more versatile technique must be used that can also find asymmetric orbits. In order to create a robust correction scheme that can handle orbits that may be difficult to

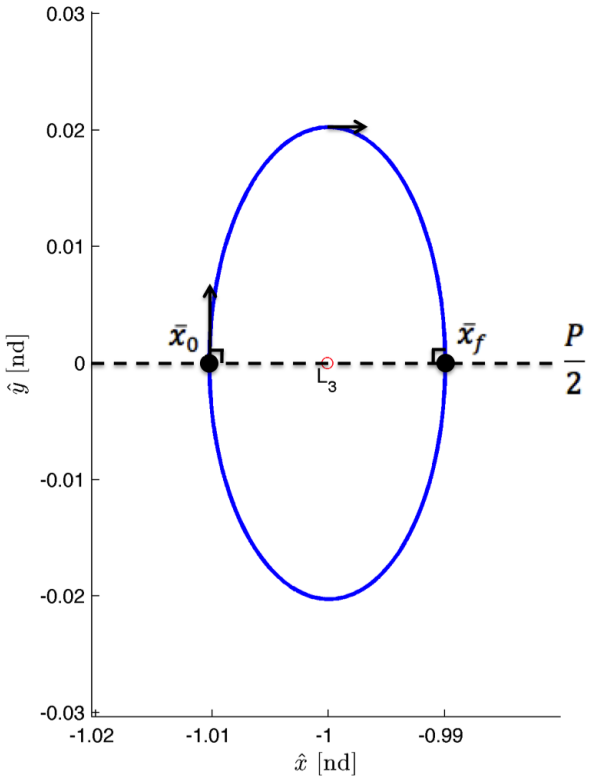

Figure 3.3. L_3 Lyapunov Orbit

converge, a multiple shooting targeter is developed. Let each of the patch points along the trajectory be defined by $\bar{x}_1, \bar{x}_2, \ldots, \bar{x}_{n-1}, \bar{x}_n$, with the total integration time of all segments defined by T. The complete variable vector of length $6n+1$ contains the state at each of the n patch points and this total time.

$$\bar{X} = \begin{bmatrix} \bar{x}_1 \\ \bar{x}_2 \\ \vdots \\ \bar{x}_n \\ T \end{bmatrix} \tag{3.23}$$

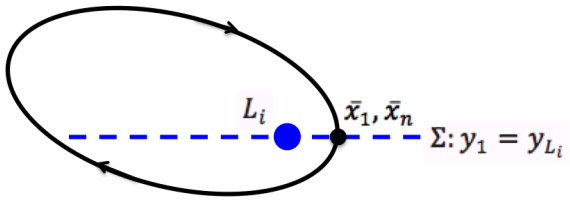

Figure 3.4. Diagram of Asymmetric Orbit Corrections Scheme

Each of the patch points (except for the final one) are integrated for time $\frac{T}{n-1}$ to the points $\bar{x}_2^t, \bar{x}_3^t, \ldots, \bar{x}_n^t$. Because a continuous trajectory is desired, the first set of constraints F_C of length $6\,(n-1)$ requires the condition that $\bar{x}_{i+1}^t\,(\bar{x}_i) = \bar{x}_{i+1}$. The second set of constraints F_P of length five requires that a periodic orbit is obtained, such that the final and initial states coincide. In order to guarantee that motion remains in the vicinity of a libration point, a final constraint F_L is required. The $\hat{y}$ component of the position vector for the initial point is constrained to a hyperplane fixed at the $\hat{y}$ coordinate of the Lagrange point of interest L_i. Using this constraint creates a robust framework that can be used to find solutions in the vicinity of both the collinear and triangular equilibrium points for asymmetric and symmetric orbits. The constraint vector $\bar{F}\left(\bar{X}\right)$ of length $6n$ is defined as

$$\bar{F}\left(\bar{X}\right) = \begin{bmatrix} F_C \\ F_P \\ F_L \end{bmatrix} = \bar{0} \tag{3.24}$$

$$F_C = \begin{bmatrix} \bar{x}_2^t - \bar{x}_2 \\ \bar{x}_3^t - \bar{x}_3 \\ \vdots \\ \bar{x}_n^t - \bar{x}_n \end{bmatrix} \tag{3.25}$$

$$F_P = \begin{bmatrix} x_n^t - x_1 \\ y_n^t - y_1 \\ z_n^t - z_1 \\ \dot{x}_n^t - \dot{x}_1 \\ \dot{z}_n^t - \dot{z}_1 \end{bmatrix} \tag{3.26}$$

$$F_L = y_1 - y_{L_i} \tag{3.27}$$

Note that one of the state components is removed in the set of periodicity constraints because it is redundant with only five of the states required to guarantee a periodic orbit. In this case, the constraint regarding the $\hat{y}$ velocity component is selected; however, this choice is arbitrary. The resulting Jacobian matrix $D\bar{F}\left(\bar{X}\right)$ is of dimension $6n \times 6\left(n-1\right)$.

$$D\bar{F}\left(\bar{X}\right) = \begin{bmatrix} \mathbf{\Phi}_{1(6\times6)} & -\mathbf{I}_{6\times6} & \mathbf{0}_{6\times6} & \cdots & \cdots & \mathbf{0}_{6\times6} & \frac{1}{n-1}\dot{\bar{x}}_2^t \\ \mathbf{0}_{6\times6} & \ddots & \ddots & \ddots & & \vdots & \vdots \\ \vdots & \ddots & \ddots & \ddots & \ddots & \vdots & \vdots \\ \vdots & & \ddots & \ddots & \ddots & \mathbf{0}_{6\times6} & \vdots \\ \mathbf{0}_{6\times6} & \cdots & \cdots & \mathbf{0}_{6\times6} & \mathbf{\Phi}_{n-1(6\times6)} & -\mathbf{I}_{6\times6} & \frac{1}{n-1}\dot{\bar{x}}_n^t \\ \frac{\partial F_P}{\partial \bar{x}_1} & \mathbf{0}_{5\times6} & \cdots & \mathbf{0}_{5\times6} & \frac{\partial F_P}{\partial \bar{x}_{n-1}} & \mathbf{0}_{5\times6} & \frac{\partial F_P}{\partial T} \\ \frac{\partial F_L}{\partial \bar{x}_1} & \mathbf{0}_{1\times6} & \cdots & \cdots & \cdots & \mathbf{0}_{1\times6} & 0 \end{bmatrix} \tag{3.28}$$

$$\frac{\partial F_P}{\partial \bar{x}_1} = \begin{bmatrix} -1 & 0 & 0 & 0 & 0 & 0 \\ 0 & -1 & 0 & 0 & 0 & 0 \\ 0 & 0 & -1 & 0 & 0 & 0 \\ 0 & 0 & 0 & -1 & 0 & 0 \\ 0 & 0 & 0 & 0 & 0 & -1 \end{bmatrix} \tag{3.29}$$

$$\frac{\partial F_P}{\partial \bar{x}_{n-1}} = \begin{bmatrix} \frac{\partial x_n^t}{\partial x_{n-1}} & \frac{\partial x_n^t}{\partial y_{n-1}} & \frac{\partial x_n^t}{\partial z_{n-1}} & \frac{\partial x_n^t}{\partial \dot{x}_{n-1}} & \frac{\partial x_n^t}{\partial \dot{y}_{n-1}} & \frac{\partial x_n^t}{\partial \dot{z}_{n-1}} \\ \frac{\partial y_n^t}{\partial x_{n-1}} & \frac{\partial y_n^t}{\partial y_{n-1}} & \frac{\partial y_n^t}{\partial z_{n-1}} & \frac{\partial y_n^t}{\partial \dot{x}_{n-1}} & \frac{\partial y_n^t}{\partial \dot{y}_{n-1}} & \frac{\partial y_n^t}{\partial \dot{z}_{n-1}} \\ \frac{\partial z_n^t}{\partial x_{n-1}} & \frac{\partial z_n^t}{\partial y_{n-1}} & \frac{\partial z_n^t}{\partial z_{n-1}} & \frac{\partial z_n^t}{\partial \dot{x}_{n-1}} & \frac{\partial z_n^t}{\partial \dot{y}_{n-1}} & \frac{\partial z_n^t}{\partial \dot{z}_{n-1}} \\ \frac{\partial \dot{x}_n^t}{\partial x_{n-1}} & \frac{\partial \dot{x}_n^t}{\partial y_{n-1}} & \frac{\partial \dot{x}_n^t}{\partial z_{n-1}} & \frac{\partial \dot{x}_n^t}{\partial \dot{x}_{n-1}} & \frac{\partial \dot{x}_n^t}{\partial \dot{y}_{n-1}} & \frac{\partial \dot{x}_n^t}{\partial \dot{z}_{n-1}} \\ \frac{\partial \dot{z}_n^t}{\partial x_{n-1}} & \frac{\partial \dot{z}_n^t}{\partial y_{n-1}} & \frac{\partial \dot{z}_n^t}{\partial z_{n-1}} & \frac{\partial \dot{z}_n^t}{\partial \dot{x}_{n-1}} & \frac{\partial \dot{z}_n^t}{\partial \dot{y}_{n-1}} & \frac{\partial \dot{z}_n^t}{\partial \dot{z}_{n-1}} \end{bmatrix} \tag{3.30}$$

$$\frac{\partial F_P}{\partial T} = \frac{1}{n-1}\begin{bmatrix} \dot{x}_n^t \\ \dot{y}_n^t \\ \dot{z}_n^t \\ \ddot{x}_n^t \\ \ddot{z}_n^t \end{bmatrix} \tag{3.31}$$

$$\frac{\partial F_L}{\partial \bar{x}_1} = \begin{bmatrix} 0 & 1 & 0 & 0 & 0 & 0 \end{bmatrix} \tag{3.32}$$

Each $\mathbf{\Phi}_i$ in the Jacobian matrix is representative of the STM for each segment of the trajectory, where $\mathbf{\Phi}_i = \phi\left(t_{i+1}, t_i\right)$. Note that equation (3.30) actually contains the elements of the state transition matrix relating the integrated state $\bar{x}_n^t$ to the patch

point $\bar{x}_{n-1}$, with the row related to the $\hat{y}$ velocity for periodicity missing due to the initial decision of removing this constraint.

An example of this correction scheme is its application to tadpole orbits. Due to the complex motion of tadpole orbits and long integration time in some systems, multiple shooting is required to converge on a solution or even to find a solution that resembles the desired motion. In Figure 3.5, a nearly periodic trajectory near L_4 is used to generate the initial patch points, represented by red stars. For the converged periodic tadpole orbit, the final nodes (blue stars) moved to satisfy all of the constraints within some tolerance level of error. The final solution clearly differs; however, the tadpole motion is preserved and the solution remains in the vicinity of the initial guess. With fewer patch points or a single shooting scheme, the complex desired motion would likely not be found.

Although the *Mirror Theorem* was previously used to simplify the computation of symmetric periodic orbits, its general application is not only limited to this case. Motion near one of the triangular points can also be related to a partner motion around the other point. As a result, a mirror version of this tadpole motion also exists around L_5.

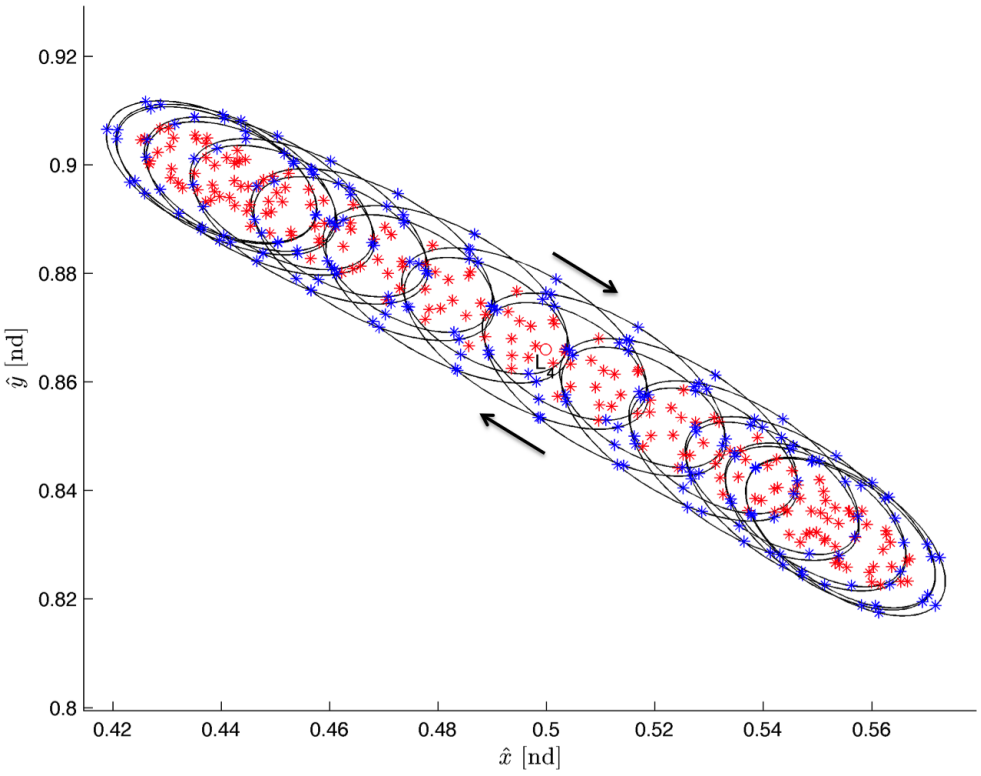

Figure 3.5. Periodic Tadpole Orbit Computation with Multiple Shooting

3.4 Stability Analysis of Periodic Orbits

Now that periodic orbits can be computed in the CR3BP, it is important to analyze the solutions. Four types of steady-state behavior exist in nonlinear systems: equilibrium points, periodic orbits, quasi-periodic solutions, and chaos. According to Lyapunov stability, it was determined that the collinear points are unstable and the triangular points are marginally stable for the linear system. It can be predicted that motion near the collinear points in the nonlinear system will diverge with a perturbation, while motion near the equilateral points might remain bounded with a small perturbation. Even so, stability analysis for motion in the nonlinear system requires a different approach to evaluate the actual behavior. It is important to note that the equilibrium points are constant solutions and that the A matrix is constant for this linear system.

Periodic orbits in the nonlinear system are particular solutions of the differential equations, but the state varies with time. Accordingly, the invariant A matrix from the linearized system cannot be used to evaluate the stability of these solutions. The STM can be used to assess stability, but it also changes with time. After one full cycle of the motion over time T, the monodromy matrix $\phi(T, 0)$ can be defined as a special form of the state transition matrix. After one full period of the motion, the eigenvalues or characteristic multipliers λ_i of the monodromy matrix can be evaluated for stability analysis. Because the motion is periodic, the monodromy matrix is evaluated at a fixed point where the final state meets the initial state after one full cycle. The location of the characteristic multipliers in the complex plane determine the stability of the fixed point and consequently the stability of the periodic orbit.

Because the CR3BP is a Hamiltonian time-invariant system, the eigenvalues of the monodromy matrix for periodic orbits come in reciprocal pairs. For a full six-dimensional state, often two of the three eigenvalue pairs are equal to unity. One of the pairs is indicative of a Hamiltonian system with the other pair indicating that the solution is a member of a family of orbits. Because the eigenvalues come in pairs, the

Table 3.1. Periodic Orbit Stability

Condition	Stability
$\|\lambda_i\| > 1$ for any λ_i	unstable
$\|\lambda_i\| < 1$ for all λ_i	asymptotically stable
$\|\lambda_i\| \leq 1$ for all λ_i	marginally stable

stability index ν for a pair of the non-unity eigenvalues λ_i, λ_j can be used to evaluate the stability of a periodic orbit.

$$\nu = \frac{1}{2}\left(\|\lambda_i\| + \|\lambda_j\|\right) \tag{3.33}$$

If the magnitude of this value is less than or greater than one, the orbit is stable or unstable respectively.

3.5 Continuations Schemes

After computing one periodic orbit in the vicinity of an equilibrium point, it is possible to find nearby solutions with related characteristics. These solutions form a family of orbits containing infinite members that are sometimes bounded to a certain region. The Jacobi constant and orbital period are examples of characteristics that can be used to parameterize a family of periodic orbits. Different numerical continuation techniques can be used to find nearby solutions that are members of family. Depending on the complexity of the motion and the existence of various types of other motion in the vicinity of an orbit, the type of algorithm used can vary.

3.5.1 Natural Parameter Continuation

For simple cases, natural parameter continuation can be used to compute families of orbits. This algorithm is an adaptation of the iterative solver to a parameterized

problem. It only requires an initial solution to seed the initial guess of another family member. A parameter is selected, and a step in this parameter from the initial guess is taken at each iteration. Because the remaining variables are unmodified, this method does not predict how the rest of the solution space will change after varying the selected parameter. As a result, often small steps must be taken to converge on another family member. Because this algorithm is easy to implement, it is a useful tool to quickly see how other variables evolve while varying different parameters.

3.5.2 Pseudo-Arclength Continuation

In order to predict how all of the variables evolve when computing members across an orbit family, pseudo-arclength continuation can be used. It is an approximation of the arclength in the tangent space of a curve that represents the family of orbits. Contrary to natural parameter continuation where only one parameter is varied in the initial guess, this method takes a linear step in the entire solution space to predict the next family member. Although it is still a linear approximation for a nonlinear system, this method provides an initial guess that is usually much closer to the actual solution. This method requires additional information than only the previous solution, but it is not required to know how the family evolves if this information can be obtained.

Assume that an initial solution for a periodic orbit exist $\bar{X}^*_{i-1}$ satisfying the constraints $\bar{F}\left(\bar{X}^*_{i-1}\right) = \bar{0}$. The next family member $\bar{X}_i$ can be approximated by shifting the previous solution by a step Δs along the family tangent vector. Define the null vector of the Jacobian matrix for the previously converged solution as $\Delta\bar{X}^*_{i-1} = \mathcal{N}\left(D\bar{F}\left(\bar{X}^*_{i-1}\right)\right)$. An augmented constraint vector $\bar{G}\left(\bar{X}_i\right)$ contains the constraints used in the targeter $\bar{F}\left(\bar{X}_i\right)$ as well as an additional constraint enforcing that the next family member exists in a direction tangent to the solution space.

$$\bar{G}\left(\bar{X}_i\right) = \begin{bmatrix} \bar{F}\left(\bar{X}_i\right) \\ \left(\bar{X}_i - \bar{X}^*_{i-1}\right)^T \Delta\bar{X}^*_{i-1} - \Delta s \end{bmatrix} = \bar{0} \tag{3.34}$$

The Jacobian matrix of the augmented system contains the matrix $D\bar{F}\left(\bar{X}_i\right)$ as well as an additional row containing the null space of the previous solution.

$$D\bar{G}\left(\bar{X}_i\right) = \begin{bmatrix} D\bar{F}\left(\bar{X}_i\right) \\ \Delta\bar{X}_{i-1}^{*\,T} \end{bmatrix} \tag{3.35}$$

It is important that the length of the constraint vector $\bar{F}\left(\bar{X}_i\right)$ is one less than that of the free variable vector $\bar{X}_i$, such that the Jacobian matrix $D\bar{F}\left(\bar{X}_i\right)$ will have one less row than column. As a result, the null space for the converged current family member $\Delta\bar{X}_i^*$ will only contain one vector spanning the solution space. Because the augmented constraint vector $\bar{G}\left(\bar{X}_i\right)$ is the same length as $\bar{X}_i$, the Jacobian matrix $D\bar{G}\left(\bar{X}_i\right)$ is square and can be inverted. Consequently, Newton's method can be used numerically to iterate and find a unique solution for the current family member $\bar{X}_i^*$.

$$\bar{X}_{i+1} = \bar{X}_i - D\bar{G}\left(\bar{X}_i\right)^{-1}\bar{G}\left(\bar{X}_i\right) \tag{3.36}$$

Because the null vector $\Delta\bar{X}_{i-1}^*$ forms an orthonormal basis for the solution space, it is a unit vector representing the direction of the family tangent vector. In order to seed the initial guess used to compute a new family member, a step from the previous solution is taken in the null direction. The size of this step can be modified by multiplying the unit vector by a scalar Δs.

$$\bar{X}_i = \bar{X}_{i-1}^* + \Delta s\Delta\bar{X}_{i-1}^* \tag{3.37}$$

As an example, the L_3 Lyapunov orbit family in the Saturn-Titan system is computed using pseudo-arclength continuation and the multiple shooting correction scheme developed previously, constraining the initial point along the orbit to the hyperplane $\Sigma : y = 0$. The step size Δs is varied using a line search such that the initial error from the magnitude of the constraint vector is within some tolerance. The family evolves from the small elliptical curve near L_3 into the bean shape that also encompasses the triangular points. It does not necessarily end here, but new solutions take

a longer time to converge when they approach the secondary body due to increased sensitivity in this region.

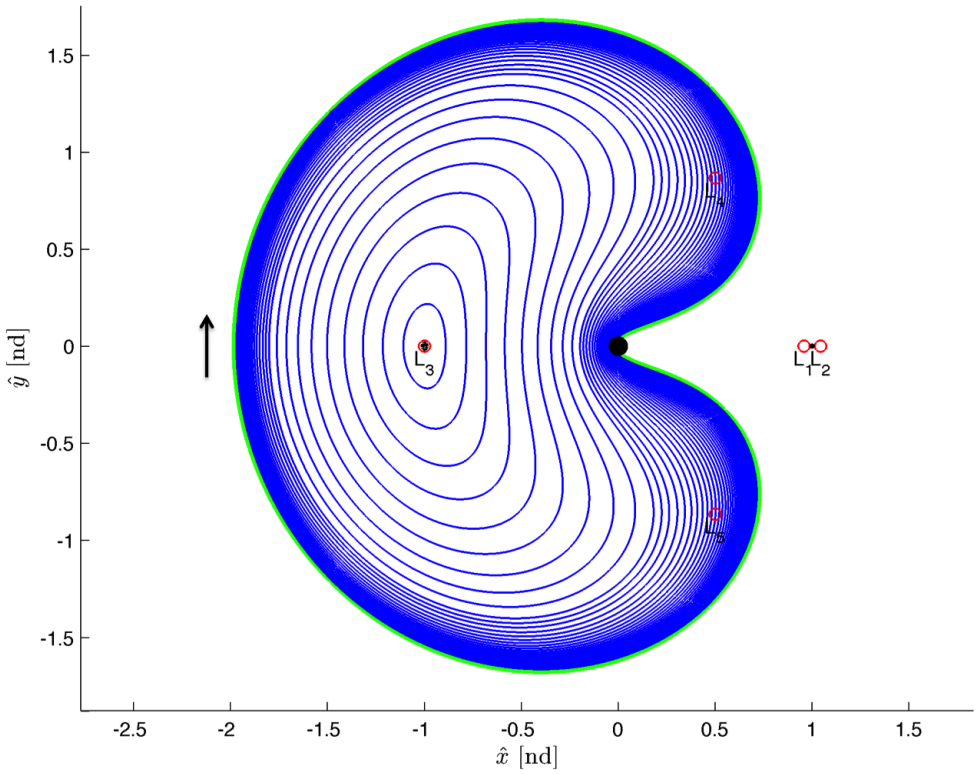

Figure 3.6. L_3 Lyapunov Orbit Family in the Saturn-Titan System

3.5.3 Continuation in System Parameters

Alternative problem formulations can be used to compute families of orbits by varying model-specific parameters. The evolution of periodic orbits based on changing a specific parameter may be desirable rather than stepping along the family tangent vector where this parameter may not change at all or change with a certain progression. A similar structure to pseudo-arclength continuation can be used to perform this numerical continuation, where a prediction is made on how the remaining variables should change after a step from the previous solution is taken.

Continuation in Mass Ratio

Periodic orbits may be more difficult to compute in systems with certain mass ratios, or initial conditions for periodic solutions may be available for a system other than the one being investigated. In order to solve this problem, a robust continuation method can be developed to find solutions parameterized by μ. First, begin with the free variables vector $\bar{X}$ and constraints vector $\bar{F}\left(\bar{X}\right)$ defined in the multiple shooting scheme in equations (3.23) - (3.24), respectively. Define the new free variable vector $\bar{Y}$, also containing the mass ratio μ. The constraint vector $\bar{G}\left(\bar{Y}\right)$ is equivalent to $\bar{F}\left(\bar{X}\right)$, and does not contain the additional constraint used in pseudo-arclength continuation.

$$\bar{Y} = \begin{bmatrix} \bar{X} \\ \mu \end{bmatrix} \tag{3.38}$$

$$\bar{G}\left(\bar{Y}\right) = \bar{F}\left(\bar{X}\right) \tag{3.39}$$

The new Jacobian matrix then becomes the following augmented matrix.

$$D\bar{G}(\bar{Y}) = \begin{bmatrix} D\bar{F}(\bar{X}) & \frac{\partial \bar{F}(\bar{X})}{\partial \mu} \end{bmatrix} \tag{3.40}$$

The partial derivatives of the constraints with respect to the mass ratio are evaluated as

$$\frac{\partial \bar{F}(\bar{X})}{\partial \mu} = \begin{bmatrix} \frac{\partial \bar{x}_2^t}{\partial \mu} - \frac{\partial \bar{x}_2}{\partial \mu} \\ \frac{\partial \bar{x}_3^t}{\partial \mu} - \frac{\partial \bar{x}_3}{\partial \mu} \\ \vdots \\ \frac{\partial \bar{x}_n^t}{\partial \mu} - \frac{\partial \bar{x}_n}{\partial \mu} \\ \frac{\partial \bar{x}_n^t}{\partial \mu} - \frac{\partial \bar{x}_1}{\partial \mu} \\ \frac{\partial y_1}{\partial \mu} - \frac{\partial y_{L_i}}{\partial \mu} \end{bmatrix} = \begin{bmatrix} \frac{\partial \bar{x}_2^t}{\partial \mu} \\ \frac{\partial \bar{x}_3^t}{\partial \mu} \\ \vdots \\ \frac{\partial \bar{x}_n^t}{\partial \mu} \\ \frac{\partial \bar{x}_n^t}{\partial \mu} \\ 0 \end{bmatrix} \tag{3.41}$$

Because the state is not an explicit function of the mass ratio, the partial derivatives in equation (3.41) cannot be evaluated directly and variation principles are required. The state time derivatives can be expressed as a function $\dot{\bar{x}} = \bar{f}\left(t, \bar{x}, \mu\right)$ which includes this additional parameter. The equation representing the derivative relationship between the state and the mass parameter can be written as

$$\frac{d}{dt}\left(\frac{d\bar{x}}{d\mu}\right) = \frac{\partial \bar{f}}{\partial \bar{x}}\frac{d\bar{x}}{d\mu} + \frac{\partial \bar{f}}{\partial \mu} \tag{3.42}$$

The term $\frac{\partial \bar{f}}{\partial \bar{x}}$ is actually the definition of the $A\left(t\right)$ matrix from the variational equations and can be substituted into equation (3.42).

$$\frac{d}{dt}\left(\frac{d\bar{x}}{d\mu}\right) = A(t)\frac{d\bar{x}}{d\mu} + \frac{\partial \bar{f}}{\partial \mu} \tag{3.43}$$

The final term relating $\bar{f}\left(t, \bar{x}, \mu\right)$ can be written in terms of its vector components.

$$\frac{d\bar{f}}{d\mu} = \begin{bmatrix} \frac{\partial \dot{x}}{\partial \mu} \\ \frac{\partial \dot{y}}{\partial \mu} \\ \frac{\partial \dot{z}}{\partial \mu} \\ \frac{\partial \ddot{x}}{\partial \mu} \\ \frac{\partial \ddot{y}}{\partial \mu} \\ \frac{\partial \ddot{z}}{\partial \mu} \end{bmatrix} \tag{3.44}$$

Each of the components in equation (3.44) can be evaluated analytically.

$$\frac{\partial \dot{x}}{\partial \mu} = \frac{\partial \dot{y}}{\partial \mu} = \frac{\partial \dot{z}}{\partial \mu} = 0 \tag{3.45}$$

$$\begin{aligned}\frac{\partial \ddot{x}}{\partial \mu} = &\frac{3\mu(m+x-1)^2}{\left((\mu+x-1)^2+y^2+z^2\right)^{5/2}} - \frac{\mu+x-1}{\left((\mu+x-1)^2+y^2+z^2\right)^{3/2}} \\ &- \frac{\mu}{\left((\mu+x-1)^2+y^2+z^2\right)^{3/2}} - \frac{1-\mu}{\left((\mu+x)^2+y^2+z^2\right)^{3/2}} \\ &+ \frac{\mu+x}{\left((\mu+x)^2+y^2+z^2\right)^{3/2}} + \frac{3(1-\mu)(\mu+x)^2}{\left((\mu+x)^2+y^2+z^2\right)^{5/2}}\end{aligned} \tag{3.46}$$

$$\begin{aligned}\frac{\partial \ddot{y}}{\partial \mu} = &-\frac{y}{\left((\mu+x-1)^2+y^2+z^2\right)^{3/2}} + \frac{y}{\left((\mu+x)^2+y^2+z^2\right)^{3/2}} \\ &+ \frac{3\mu y(\mu+x-1)}{\left((\mu+x-1)^2+y^2+z^2\right)^{5/2}} + \frac{3(1-\mu)y(\mu+x)}{\left((\mu+x)^2+y^2+z^2\right)^{5/2}}\end{aligned} \tag{3.47}$$

$$\begin{aligned}\frac{\partial \ddot{z}}{\partial \mu} = &-\frac{z}{\left((\mu+x-1)^2+y^2+z^2\right)^{3/2}} + \frac{z}{\left((\mu+x)^2+y^2+z^2\right)^{3/2}} \\ &+ \frac{3\mu z(\mu+x-1)}{\left((\mu+x-1)^2+y^2+z^2\right)^{5/2}} + \frac{3(1-\mu)z(\mu+x)}{\left((\mu+x)^2+y^2+z^2\right)^{5/2}}\end{aligned} \tag{3.48}$$

In order to solve for the partial derivative terms in equation (3.41), equation (3.43) can be integrated numerically, using the following initial conditions.

$$\frac{d\bar{x}}{d\mu}(0) = \bar{0} \tag{3.49}$$

Now, change in the states can be predicted with change in the mass parameter. For the augmented system, the Jacobian matrix $D\bar{G}\left(\bar{Y}\right)$ has two less rows than columns. As a result, the null space is spanned by two vectors ν_X and ν_μ, where ν_μ corresponds with the null space direction that has a non-zero value in the μ component. Define the null vector of the previously converged family member as

$$\Delta\bar{Y}^*_{i-i} = \begin{bmatrix} v_X & v_\mu \end{bmatrix} \tag{3.50}$$

The next family member can be predicted by taking a step in the direction of this null vector, and scaled by the mass parameter. With this formulation, the scalar $\Delta\mu$ can be used to define the size of the step in μ.

$$\bar{Y}_i = \begin{bmatrix} \bar{X}_i \\ \mu_i \end{bmatrix} = \begin{bmatrix} \bar{X}^*_{i-i} \\ \mu^*_{i-1} \end{bmatrix} + \Delta\mu \frac{v_\mu}{v_\mu \cdot \hat{\mu}} \tag{3.51}$$

This new guess is a linear projection of what the new solution should be with a change in μ, and thus, corrections will be required to compute the actual value that converges the constraints $\bar{F}\left(\bar{X}\right)$ to $\bar{0}$ at the new value of mass parameter.

Continuation in Jacobi Constant

In some mission design scenarios, an orbit existing at a specific Jacobi constant is desired in order to design a low-energy transfer. A catalog of periodic orbits may also exist for a certain type of motion, but none of the family solutions may be at the required energy level. In order to solve this problem, a robust continuation method can be developed to find solutions parameterized by C. First, begin with the free variables vector $\bar{X}$ and constraints vector $\bar{F}\left(\bar{X}\right)$ defined in the multiple shooting scheme in equations (3.23) - (3.24), respectively. The constraint vector $\bar{G}\left(\bar{X}\right)$ contains an additional constraint requiring the Jacobi constant of the first patch point to be equal to the desired value C_d.

$$\bar{G}(\bar{X}) = \begin{bmatrix} \bar{F}(\bar{X}) \\ C_{\bar{x}_1} - C_d \end{bmatrix} \tag{3.52}$$

The new Jacobian matrix then becomes the following matrix with an additional row.

$$D\bar{G}(\bar{X}) = \begin{bmatrix} & D\bar{F}(\bar{X}) & \\ \frac{\partial\left(C_{\bar{x}_1} - C_d\right)}{\partial \bar{x}_1} & 0 & \dots \quad 0 \end{bmatrix} \tag{3.53}$$

The partial derivatives associated with the Jacobi constant constraint in (3.53) are evaluated as

$$\frac{\partial C}{\partial x} = -\frac{2\mu(\mu+x-1)}{((\mu+x-1)^2+y^2+z^2)^{3/2}} - \frac{2(1-\mu)(\mu+x)}{((\mu+x)^2+y^2+z^2)^{3/2}} + 2x \tag{3.54}$$

$$\frac{\partial C}{\partial y} = -\frac{2\mu y}{((\mu+x-1)^2+y^2+z^2)^{3/2}} + \frac{2(\mu-1)y}{((\mu+x)^2+y^2+z^2)^{3/2}} + 2y \tag{3.55}$$

$$\frac{\partial C}{\partial z} = -\frac{2\mu z}{((\mu+x-1)^2+y^2+z^2)^{3/2}} - \frac{2(1-\mu)z}{((\mu+x)^2+y^2+z^2)^{3/2}} \tag{3.56}$$

$$\frac{\partial C}{\partial \dot{x}} = -2\dot{x} \tag{3.57}$$

$$\frac{\partial C}{\partial \dot{y}} = -2\dot{y} \tag{3.58}$$

$$\frac{\partial C}{\partial \dot{z}} = -2\dot{z} \tag{3.59}$$

Because the augmented constraint vector $\bar{G}\left(\bar{X}_i\right)$ is the same length as $\bar{X}_i$, the Jacobian matrix $D\bar{G}\left(\bar{X}_i\right)$ is square and can be inverted. Consequently, Newton's method can be used numerically to iterate and find a unique solution for the current orbit $\bar{X}_i^*$ as computed in equation (3.36). In order to set this method up as a continuation scheme, now introduce the augmented system $\bar{Y}$ that contains the desired value of Jacobi constant and the associated augmented constraint vector.

$$\bar{Y} = \begin{bmatrix} \bar{X} \\ C_d \end{bmatrix} \tag{3.60}$$

$$D\bar{G}\left(\bar{Y}\right) = \begin{bmatrix} D\bar{G}\left(\bar{X}\right) & \frac{\partial \bar{F}\left(\bar{X}\right)}{\partial C_d} \end{bmatrix} \tag{3.61}$$

$$\frac{\partial \bar{F}\left(\bar{X}\right)}{\partial C_d} = \begin{bmatrix} 0 \\ \vdots \\ 0 \\ -1 \end{bmatrix} \tag{3.62}$$

The null space of the previously converged orbit $\Delta\bar{Y}_{i-1}^* = \mathcal{N}\left(D\bar{G}\left(\bar{Y}_{i-1}^*\right)\right)$ contains two vectors ν_X and ν_C, where ν_C corresponds with the null space direction that has a non-zero value in the C component. An initial guess for the next family member can be computed by taking a linear step from the previous solution.

$$\bar{Y}_i = \bar{Y}^*_{i-i} + \Delta C \frac{v_C}{v_C \cdot \hat{C}} \tag{3.63}$$

If the null vector is scaled by the component corresponding to the Jacobi constant $\hat{C}$, this step can be scaled such that it is defined by a scalar change in C defined by ΔC.

3.6 Poincaré Maps

Poincaré sections are useful in discovering periodic and quasiperiodic orbits in the CR3BP. An analytical solution to the problem does not exist, due to the known existence of only one integral of the motion, the Jacobi constant. By slicing the solution space, the behavior of certain variables can be examined. Dynamical systems can be expressed by systems of differential equations expressed in equation (3.64) or by maps defined in equation (3.65).

$$\dot{\bar{x}} = \bar{f}\left(\bar{x}, t\right) \tag{3.64}$$

$$\bar{x}_{n+1} = \bar{f}\left(\bar{x}_n\right) \tag{3.65}$$

A continuous time system can be reduced to an associated discrete time system through the study of maps. Using maps is advantageous as it reduces the dimension of the system by eliminating at least one variable in the problem. This reduction can be performed strategically by fixing certain variables to achieve a specific characteristic for a set of initial conditions (such as initial conditions with the same value of Jacobi constant). Poincaré maps can also provide insight into the system global dynamics and help to describe why certain types of behavior exist. Constructing maps requires knowledge of the geometrical structure of the phase space for the ordinary differential equations and insight into the type of information that is desired. In the CR3BP, Poincaré maps are commonly used to determine orbit structure near periodic orbits and to find periodic orbits.

Consider an autonomous system defined in n-dimensional phase space, with vector field $\bar{f}$ generating a flow $\bar{x}\left(\bar{x}_0, t\right) = \varphi_t\left(\bar{x}_0\right)$. This flow is representative of a trajectory that corresponds to the initial conditions $\bar{x}_0$ for the differential equations governing the system. Because this point $\bar{x}_0$ varies within the phase space, a set of solutions are generated for a variety of trajectories. Consider the hyperplane Σ that exists in phase space of dimension $n-1$, defined such that the flow is transverse with at least one component normal to the plane for a trajectory.

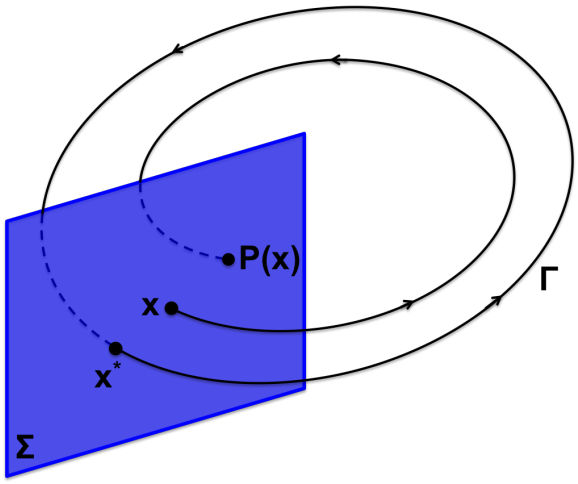

Figure 3.7. Poincaré Map

Assume that a cycle Γ exists, which is representative of a periodic orbit. The point x^* is along Γ and as a result, the hyperplane Σ is transversal to Γ at this point. During each time interval of one period T, the trajectory through x^* intersects the hyperplane at this same point. Because the flow is continuous, trajectories with initial conditions along Σ nearby x^* will intersect the hyperplane again in approximately time T, returning in the vicinity of x^*. The flow φ_t and hyperplane Σ can then define a Poincaré map P of the autonomous system. The first return of a trajectory passing through Σ with the normal component parallel to that of the initial intersection defines a nonlinear map P. The flow from one iteration of the map can be represented as

$$P\left(\bar{x}_0\right) = \bar{x}\left(\bar{x}_0\right) \tag{3.66}$$

where $\bar{x}$ is the state vector resulting from the nonlinear map with initial conditions $\bar{x}_0$. If the trajectory is periodic, then the map P repeatedly maps the fixed point $\bar{x}^*$ on to itself. Consequently, one limit cycle becomes a point on the map. In order to observe one cycle, it is useful to produce a one-sided map which examines the flow as the trajectory returns to the hyperplane in one direction. The Poincaré map reduces a continuous time to a discrete time system, and stability properties of the fixed point can be analyzed by linearizing the map relative to the fixed point.

3.7 Numerical Computation of Invariant Manifolds

Analyzing the stability properties of a fixed point can be accomplished using a Poincaré map. As a result, the stability properties of a periodic orbit can also be analyzed by using the STM, which is a stroboscopic map. A stroboscopic map is a map sampled at specific time intervals, which are usually defined by the period T defining a cycle. The STM is a linear stroboscopic map which is used to examine local stability of periodic solutions. By linearizing the Poincaré map relative to a fixed point, the Floquet Theorem and Lyapunov's Theorem are connected. Before discussing invariant manifold theory, it is important to discuss some properties of the STM. First, because the CR3BP is a time-invariant system, λ and λ^{-1} are both eigenvalues of the monodromy matrix $\phi(T, t_0)$. Second, the eigenvalues of the monodromy matrix are independent of the starting point for a periodic solution. With both of these conditions met, the eigenvectors of the monodromy matrix can be transitioned by using the STM. If a fixed point x^* on a map P is being considered, then changing the location of the stroboscopic map should not change the eigenvalues of the monodromy matrix; however, the eigenvectors will change. Therefore, it is convenient that for a periodic solution the eigenvectors of the monodromy matrix $\bar{v}_i(t_i)$ can be transitioned using the following equation.

$$\bar{v}_i(t_i) = \phi(t_i, t_0)\,\bar{v}_i(t_0) \tag{3.67}$$

The eigenvalues for the fixed point x^* are indicative of the rates of expansion or contraction from the point, with the eigenvectors indicating the direction that motion departs and arrives. By using this information, the computation of invariant manifolds can be used to approximate how motion will naturally approach and depart a periodic orbit. Let $W^S(\Gamma)$ and $W^U(\Gamma)$ be the global stable and unstable manifolds of a periodic orbit Γ, with $W^S_{loc}(\Gamma)$ and $W^U_{loc}(\Gamma)$ representing the local stable and unstable manifolds. These global manifolds can be defined by propagating the local stable and unstable flow backwards and forwards in time, respectively. The global stable and unstable manifolds are tangent to the stable and unstable subspaces $E^S(\Gamma)$ and $E^U(\Gamma)$ at the fixed point x^*.

Consider that the fixed point $\bar{x}^*$ is an $(n-1)$-dimensional representation of Γ which is a periodic orbit. The monodromy matrix associated with $\bar{x}^*$ contains stable, unstable, and center subspaces with dimensions n_S, n_U, and n_C. The stable manifold $W^S(\Gamma)$ and unstable manifold $W^U(\Gamma)$ are then of dimension (n_S+1) and (n_U+1), respectively. These manifolds are tangent to the stable and unstable subspaces, so the eigenvectors of the mondromy matrix can be used to approximate the directions which the manifolds depart and approach a periodic orbit. Define the components of an eigenvector contained within the stable and unstable subspace as

$$\bar{v}_S = \begin{bmatrix} x_S & y_S & z_S & \dot{x}_S & \dot{y}_S & \dot{z}_S \end{bmatrix}^T \tag{3.68}$$

$$\bar{v}_U = \begin{bmatrix} x_U & y_U & z_U & \dot{x}_U & \dot{y}_U & \dot{z}_U \end{bmatrix}^T \tag{3.69}$$

Two half-manifolds span each of the stable and unstable subspaces, corresponding to positive and negative eigenvector directions. A state along each half-manifold can be approximated by taking a step d from a fixed point $\bar{x}^*$ in both directions defined by the stable and unstable eigenvectors.

$$\bar{x}_S = \bar{x}^* \pm d \cdot \bar{V}^{W^S} \tag{3.70}$$

$$\bar{x}_U = \bar{x}^* \pm d \cdot \bar{V}^{W^U} \tag{3.71}$$

The eigenvectors are normalized by the position components, such that d is scalar defining the distance magnitude of this step from the fixed point.

$$\bar{V}^{W^S} = \frac{\bar{v}_S}{\sqrt{x_S^2 + y_S^2 + z_S^2}} \tag{3.72}$$

$$\bar{V}^{W^U} = \frac{\bar{v}_U}{\sqrt{x_U^2 + y_U^2 + z_U^2}} \tag{3.73}$$

The states $\bar{x}_S$ and $\bar{x}_U$ are then integrated in backwards and forwards time, respectively. If the step-off distance is selected to be too small, trajectories will take an infinite amount of time to depart the orbit; however, if this values is too large, then the state does not accurately approximate the stable and unstable manifolds. Different manifold arcs can be computed by varying the value of d at the same $\bar{x}^*$ or by fixing d and selecting a different hyperplane Σ for various locations along the periodic orbit.

4. Tadpole Orbits

With the numerical tools developed to find periodic solutions, periodic tadpole orbits in the circular restricted three-body problem can be computed. Different approaches used to construct these orbits numerically are discussed. Once a periodic solution is obtained, families of periodic orbits are computed in the Saturn-Titan and Sun-Jupiter systems and their orbital characteristics are analyzed.

4.1 Computing Periodic Tadpole Orbits

Different approaches can be used to tadpole orbits, and choosing a method depends on the system and orbit characteristics. Linear approximations made by Dermott and Murray can be used to define regions where horseshoe and tadpole orbits are expected to exist [2]. These approximations are only beneficial when the mass of the secondary is much smaller than the mass of the primary. When this mass ratio is increased, other techniques must be employed, especially for tadpole orbits due to their asymmetry.

4.1.1 Search and Filter Techniques

If prior knowledge is known about the desired type of motion, initial conditions can be selected and propagated that may lead to near-periodic solutions. Tadpole and horseshoe orbits are both representative of resonant co-orbital motion that exists in the vicinity of the triangular Lagrange points. Horseshoe orbits are symmetric about the $\hat{x}$-axis and contain both of these equilateral points as well as the collinear point L_3. These properties reflect motion that is similar to that of the zero velocity curves for energy levels between that of L_2 and L_3 for simple horseshoe orbits. Additionally, horseshoe orbits will have at least two perpendicular $\hat{x}$-axis crossings. With this

information known about the motion, near-periodic solutions representative of this motion can be obtained by propagating a set of initial conditions that meet the criteria bounding the horseshoe region. Then, trajectories that are likely candidates for horseshoe motion can be selected using a search and filter technique used in previous investigations [25] [26].

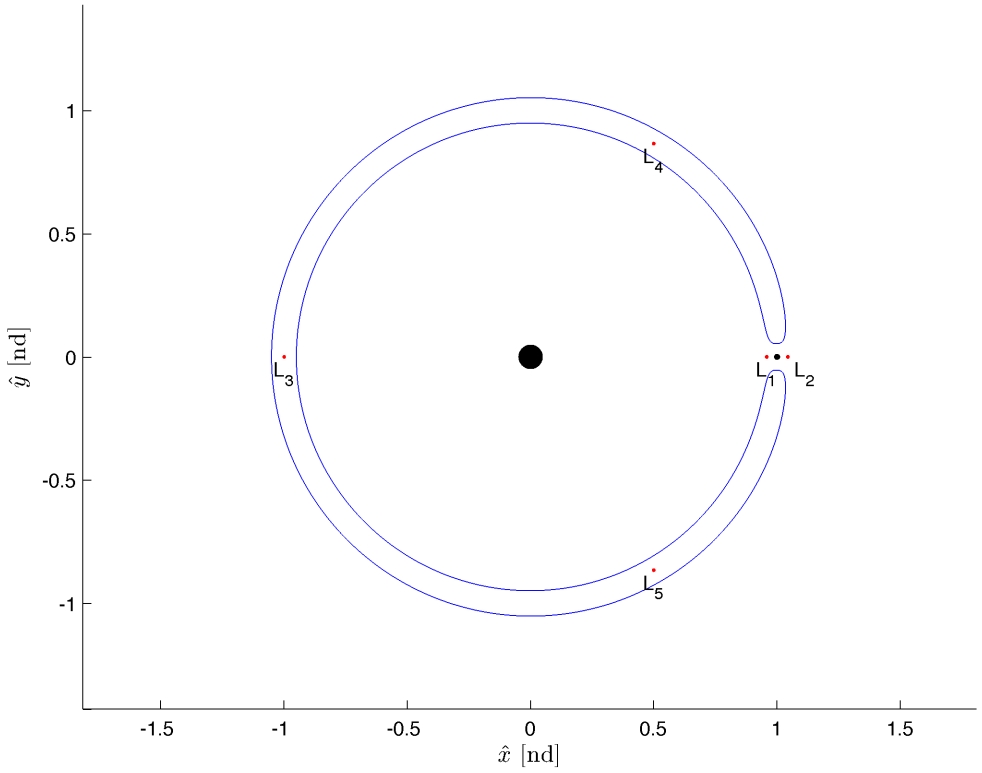

Figure 4.1. ZVC for C = 3.007845 in Saturn-Titan System

Because simple horseshoe orbits have two perpendicular $\hat{x}$-axis crossings and pass through L_3, it is convenient to select initial conditions that lie along this axis. Begin with the a state vector satisfying these conditions, which is reduced to only two free-variables for planar motion.

$$\bar{x}_0 = \begin{bmatrix} x_0 & 0 & 0 & 0 & \dot{y}_0 & 0 \end{bmatrix}^T \tag{4.1}$$

The position component x_0 is varied for points beginning near the left side of L_3 where one of the perpendicular crossings is expected to occur. Because simple horseshoe orbits usually follow the motion of zero-velocity curves similar to the one depicted in Figure 4.1, the initial conditions can be limited by the Jacobi constant of the triangular points. As the value of x_0 is decreased, a new set of values for $\dot{y}_0$ are selected such that the Jacobi constant remains less than C_{L_4}. Each of these initial states are propagated until the next $\hat{x}$-axis crossing, with the velocity $\dot{x}_f$ recorded. Because a perpendicular crossing is of interest, a zero-valued $\dot{x}_f$ is desired. If a large set of data is generated, an initial value of $\dot{y}_0$ can be interpolated for an associated $\dot{x}_0$ that gives a perpendicular crossing. If the trajectory is propagated for two $\hat{x}$-axis crossings, some near-periodic orbits may be obtained. In order to reduce the set of initial conditions to possible horseshoe orbit candidates, the data is filtered to obtain trajectories that satisfy the following conditions.

1. The first $\hat{x}$-axis crossing must not extend past the $\hat{x}$-coordinate of L_4
2. The trajectory propagated for two $\hat{x}$-axis crossing must extend past the $\hat{x}$-coordinate of L_4

As an example of this technique, nearly 10,000 initial conditions are propagated in the Saturn-Titan system. In Figure 4.2, the velocity at the first crossing $\dot{x}_f$ is plotted against the initial velocity $\dot{y}_0$ before any filtering.

It appears that many possible candidates for horseshoe orbits may exist with zero-valued $\dot{x}_f$. Not only does this require analyzing a large set of initial conditions, but some of these trajectories may not even pass by the triangular points or return to a viable location for the second crossing. The filtering process is applied to remove any conditions that will not yield horseshoe-like motion, and the set of initial conditions is reduced to half as many states. In Figure 4.3, the filtered data is plotted in blue.

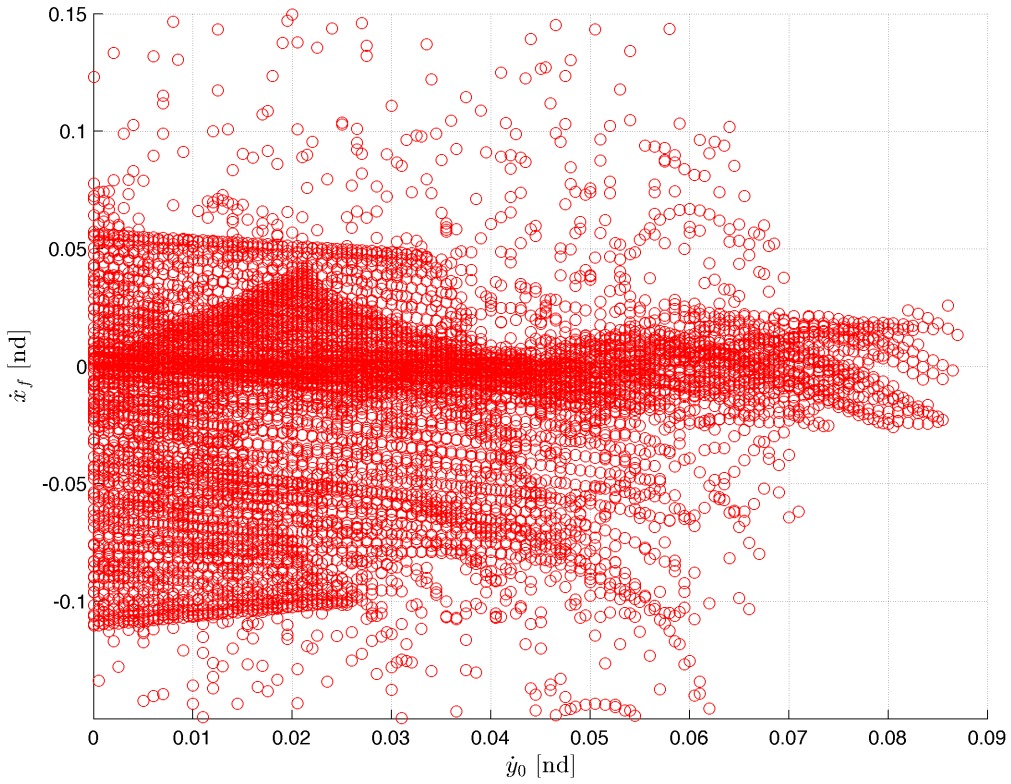

Figure 4.2. Horseshoe Orbit Search in Saturn-Titan System

This data is also smoothed (indicated by a green line), so that an initial value of $\dot{y}_0$ can be interpolated for an associated $\dot{x}_0$ that gives a perpendicular crossing.

Although the amount of candidate initial conditions is greatly reduced, it appears that many choices are available as a guess for a near-periodic horseshoe orbit. By examining the smoothed data closer, it is easier to identify initial conditions that yield nearly perpendicular $\hat{x}$-axis crossings.

With the initial conditions selected from the zoomed image in Figure 4.4, the trajectory can be propagated to see if it yields motion representative of a horseshoe orbit. In Figure 4.5, the trajectory is plotted in the rotating frame, matching the desired

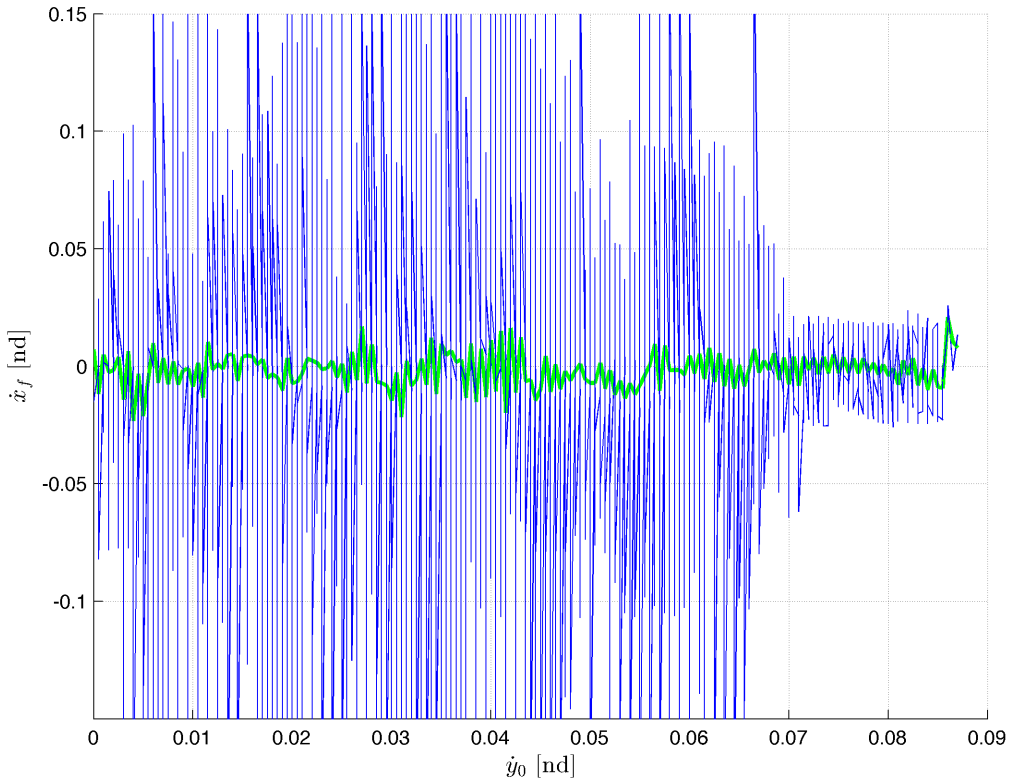

Figure 4.3. Horseshoe Orbit Search With Filtering in Saturn-Titan System

behavior. These initial conditions can be used in a targeting algorithm to compute the periodic horseshoe orbit in the vicinity of this trajectory.

Searching for tadpole orbits using the search and filter technique is also possible but more trivial because they are asymmetric and cannot be universally bounded by Jacobi constant. Because tadpole orbits exist in the vicinity of the triangular Lagrange points, it is convenient to generate initial conditions such that the $\hat{y}$-position is located at the coordinates of one of these points. For a small displacement ϵ from the Lagrange point, tadpole motion can be found, so the initial coordinate x_0 satisfies

$$\theta = \frac{\pi}{3} + \epsilon \tag{4.2}$$

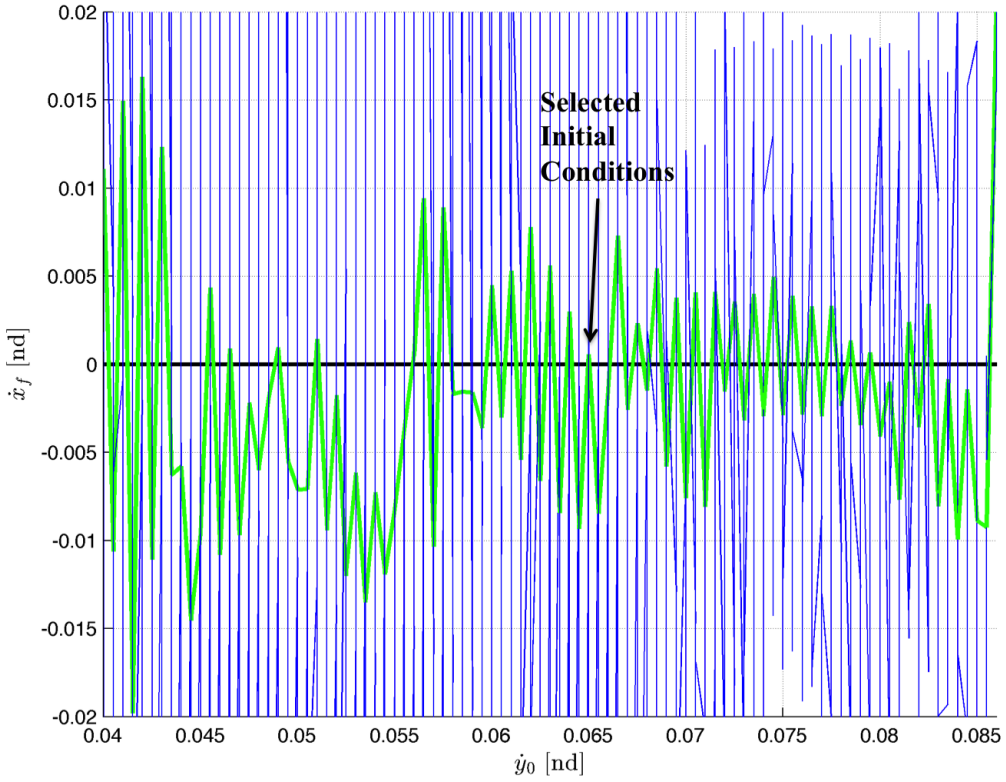

Figure 4.4. Horseshoe Orbit Search Initial Conditions in Saturn-Titan System

where θ is the angle between the $\hat{x}$-axis and the initial position.

The initial velocities $\dot{x}_0$ and $\dot{y}_0$ are varied for each point, but the range of these values cannot be definitely bounded by the Jacobi constant. Even so, it is expected that small tadpole orbits should exist for a value of Jacobi constant that is near that of L_4. Because the type of resulting motion cannot be fully predicted, a technique such as ending propagation at an axis crossing as was done for the horseshoe orbit is not possible. For small displacements from the triangular Lagrange point, a tadpole orbit should have the same period as the long period linear motion.

A set of about 5000 initial conditions propagated for one long period is investigated for a range of Jacobi constant down to a value that is slightly less than C_{L_4}, with the

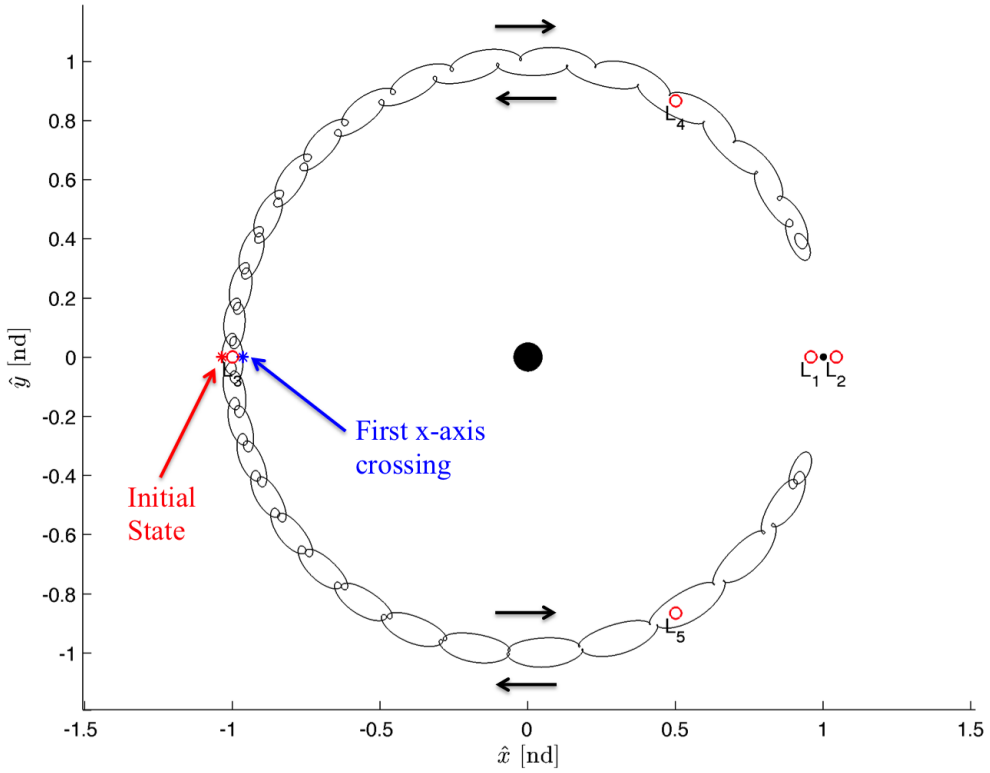

Figure 4.5. Near-Periodic Horseshoe Orbit from Search and Filter

magnitude of the difference between the final state $\bar{x}_f$ and $\bar{x}_0$ plotted against values of $\dot{y}_0$. This generates a stroboscopic map where periodic trajectories should exist near points with a small value for this error. A large collection of possible near-periodic tadpole orbits can be seen in Figure 4.8. It is difficult to define specific filtering criteria to reduce the set of initial conditions; however, it is clear that solutions with the minimum state error are desirable. These conditions are also grouped with more structure than the horseshoe search, most likely because the trajectories do not diverge far from L_4 due to the small initial displacement from the Lagrange point. As a result, filtering is not necessary in this process.

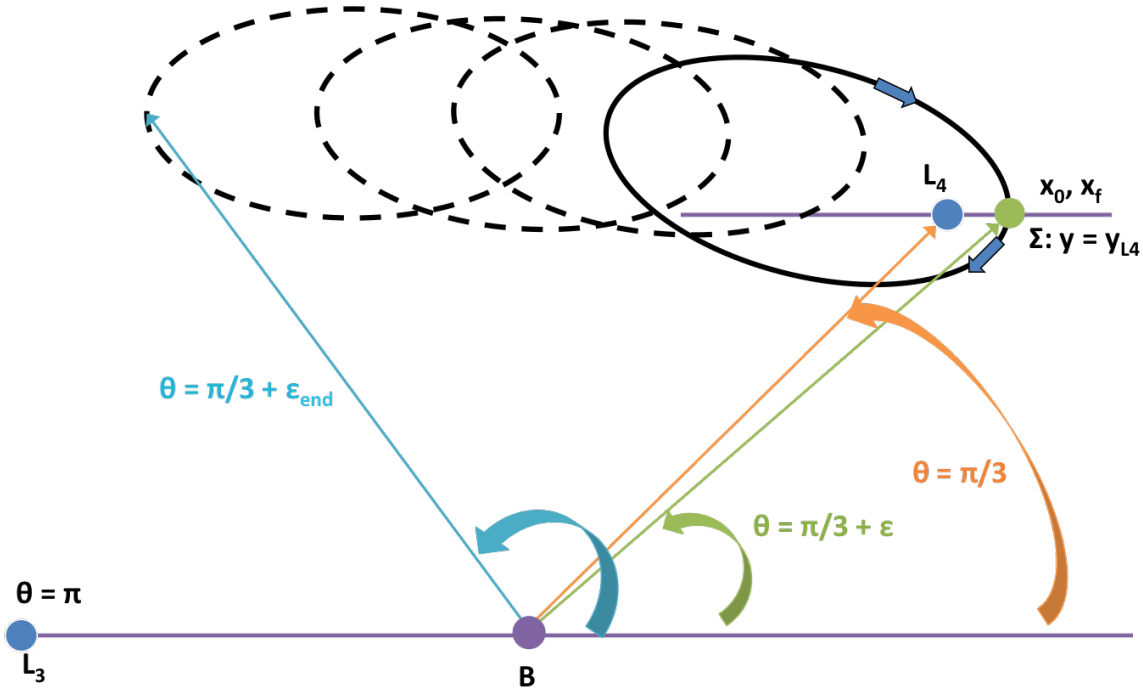

Figure 4.6. Tadpole Orbit Initial Conditions

These initial conditions can be used in a targeting algorithm to compute the periodic tadpole orbit in the vicinity of this trajectory.

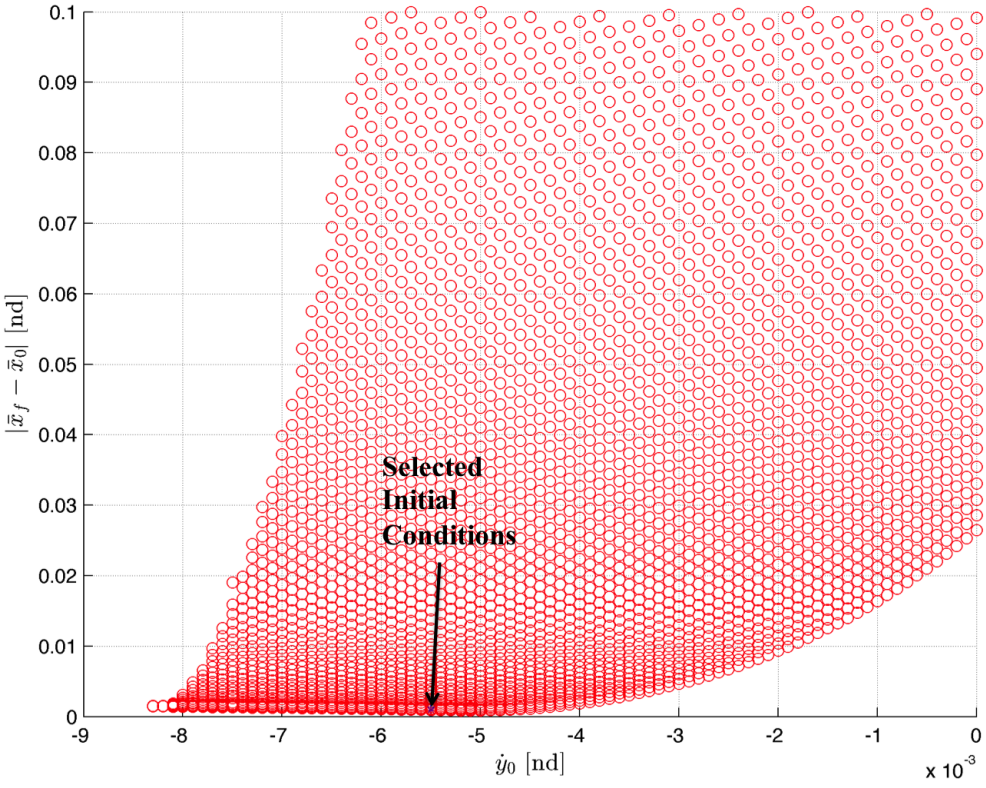

Figure 4.7. Tadpole Orbit Search

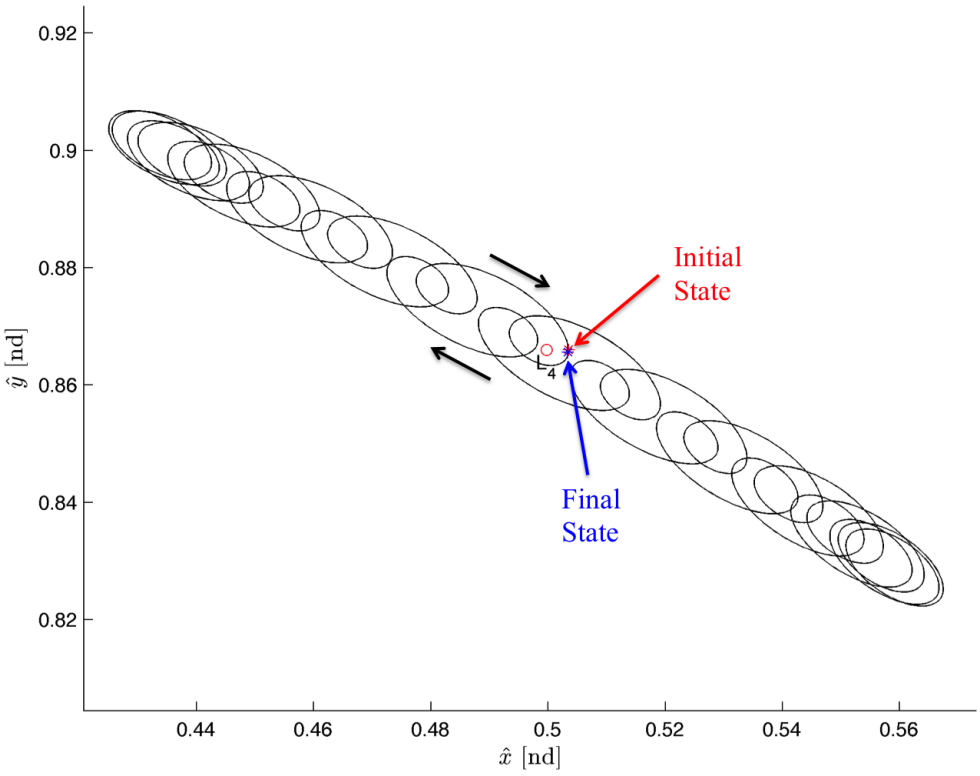

Figure 4.8. Near-Periodic Tadpole Orbit from Search

4.1.2 Linear Approximation of the Motion

Because tadpole orbits cannot be universally bounded by Jacobi constant and defined by an exact geometry, examining a linear approximation of the motion may give insight into nearly periodic trajectories. Often elements of the linear approximation are required to find tadpole orbits using the other methods discussed. The search and filter technique uses the linear long period to estimate the length of one period. The diagram in Figure 4.6 can be used to illustrate the linear approximation of a tadpole orbit, where the initial conditions are displaced by a small amount from the triangular point.

In order to make linear approximations of tadpole orbits using a method common among Dermott and Murray [2] and other authors, first assume that the mass of the secondary m_2 is much less than that of the primary mass m_1, such that the mass ratio μ is infinitesimal. Define r and θ as polar coordinates defining the distance from the barycenter (of the primary system) to the spacecraft and the angle defining the spacecraft position with respect to the $\hat{x}$-axis. The distance Δ is defined as

$$\Delta = 1 - r \ll 1 \tag{4.3}$$

Because the linear approximation of a small tadpole orbit is valid for a small displacement from L_4, requiring Δ to be a very small value indicates that $r \approx 1$, which is the distance from the barycenter to the triangular point for an infinitesimal value of μ. The relationship between r (defined within Δ) and θ can be written as

$$\Delta^2 + \frac{4}{3}\mu\left(\frac{1}{\sin\frac{\theta}{2}} + 4\sin^2\frac{\theta}{2}\right) = 4\mu\beta \tag{4.4}$$

where β is a constant of integration from the equations of motion written in terms of the polar coordinates. Tadpole motion should exist in the vicinity of L_4 and should not pass through L_3, so it is important to develop a relationship between β and the polar coordinates defining these Lagrange points.

$$\Delta_{L_4} = 0 \tag{4.5}$$

$$\theta_{L_4} = \frac{\pi}{3} \tag{4.6}$$

$$\beta_{L_4} = 1 \tag{4.7}$$

$$\Delta_{L_3} = 0 \tag{4.8}$$

$$\theta_{L_3} = \pi \tag{4.9}$$

$$\beta_{L_3} = \frac{5}{3} \tag{4.10}$$

From this information, it can be determined that for the linear system with infinitesimal mass ratio, $\beta = \frac{5}{3}$ is the maximum value for tadpole motion. Tadpole orbits combine a long period librational and short period epicyclic motion, which can be defined for the current assumptions as

$$\mathcal{P}_{long} = \frac{2\pi}{\sqrt{\frac{27}{4}\mu}} \tag{4.11}$$

$$\mathcal{P}_{short} = \frac{2\pi}{\sqrt{1 - \frac{27}{8}\mu}} \tag{4.12}$$

Resulting from the combination of short and long period motion, the trajectory may change directions many times in a complex motion. The conditions defining where these turning points occur can be related to the polar coordinates defined in equations

$$\Delta = 0 \tag{4.13}$$

$$\dot{\theta} = 0 \tag{4.14}$$

As performed in the search and filter technique in equation (4.2), initial conditions can be selected for a small displacement ϵ from the triangular point that should result in a small tadpole orbit. The analytical limit for tadpole motion for the assumptions of this linear approximation can be defined by a maximum value of ϵ.

$$\epsilon_{end} = \sqrt{\frac{4\left(\beta - 1\right)}{3}} \tag{4.15}$$

Because the linear approximation assumes an infinitesimal mass ratio, using this technique to find tadpole orbits can usually only find near-periodic motion for systems with a small value of μ. Finding tadpole orbits in the Saturn-Titan system is possible but more challenging than other systems, as the mass ratio is relatively large. Even with the information from the linear approximation, an infinite number of initial conditions are possible, and not all may lead to near-periodic motion in the nonlinear system. The search and filter technique sweeps through a large set of initial conditions displaced by ϵ from the triangular point for a limited range of Jacobi constant where tadpole motion is expected to occur. This method generates many trajectories only requiring knowledge of the linear long period of the system. Initial conditions can also be generated more intuitively by combining the linear long and short period motion derived previously in the variational equations. This method also relies on initial conditions with a small displacement ϵ from the triangular point.

4.1.3 Poincaré Maps

Poincaré maps can be used to help visualize regions where tadpole orbits may exist by propagating many initial conditions. They may also depict the dynamics of nearby motion, giving insight into the global dynamics of the system. A one-sided map would likely give insight into the system dynamics, but due to the sensitivity of the region where tadpole motion is expected to occur, a standard puncture plot may not yield any near-periodic tadpole orbits without densely populated initial conditions. The *orbit convolution* technique developed by Schlei et al. generates a scalar field depiction of the dynamics associated with a particular Poincaré map [27]. An image with a resolution of $N \times M$ is generated, with the map computed for n iterates (returns to the surface of section) at each pixel. Because computing many intersections can be computationally expensive, convolutions passes K can be applied to reduce

this computational time. Using this method more clearly defines quasi-periodic and chaotic regions. The chaotic regions appear in grey, with each distinct color usually representing a specific orbital structure. Because tadpole orbits are surrounded by quasiperiodic motion, they are likely to appear within island chains. These structures often clearly emerge when using the orbit convolution method, making it a suitable choice for finding tadpole orbits.

Often the Jacobi constant is fixed when generating Poincaré maps. Because tadpole orbits cannot be universally bounded by C, it is convenient to have some insight into the energy that these orbits exist at. Otherwise, many different maps for a range of Jacobi constant could be created, with the results investigated in search of structures representative of tadpole orbits. Because near-periodic orbits can be found in the Saturn-Titan system using a linear approximation, the Jacobi constant of one of these previously computed orbits can be selected for generating initial conditions for trajectories. A map can be created using the knowledge that tadpole motion will pass through the y-coordinate of L_4. As a result, the hyperplane defining the Poincaré section is defined as $\Sigma : y = y_{L_4}$. The following table summarizes the parameters for the orbit convolution map in Figure 4.9, where the velocity $\dot{x}$ is plotted on the y-axis against the position x for each crossing of the hyperplane.

Table 4.1. Orbit Convolution Map Conditions for Saturn-Titan System

Parameter	Value
μ	0.00023669
C	2.99965918
x (nd)	$\begin{bmatrix} 0.4 & 0.6 \end{bmatrix}$
$\dot{x}$ (nd)	$\begin{bmatrix} -0.1 & 0.1 \end{bmatrix}$
Resolution	512×512
Iterates	$n = 50$
Convolutions	$K = 5$

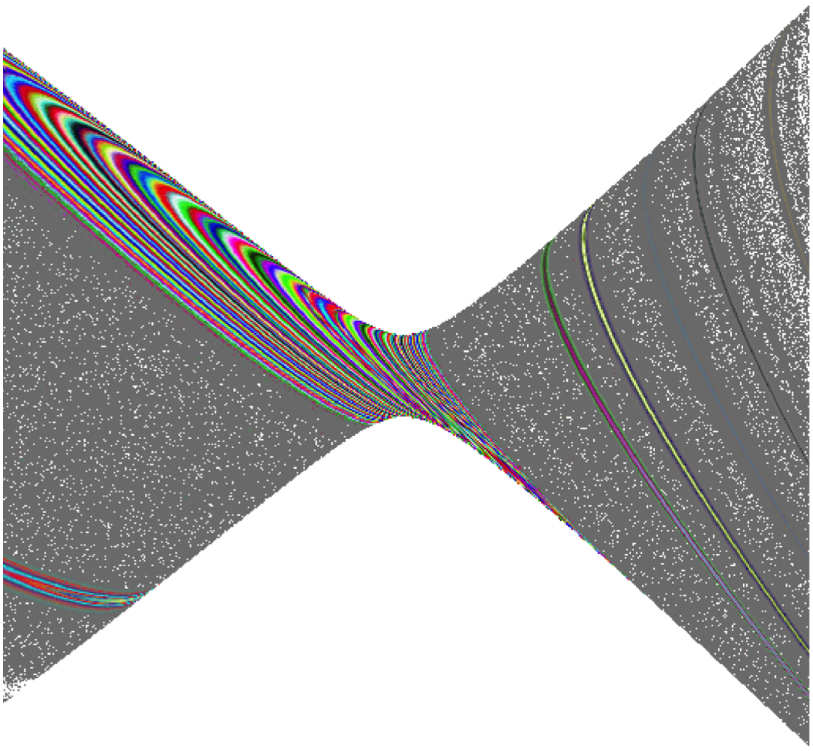

Figure 4.9. Orbit Convolution Map for Saturn-Titan System (Figure created by W. Schlei, 2016)

Because small tadpole orbits originate from small displacements from L_4, it is expected that an orbit will be found near the center of this map. This position approximately indicates the location of L_4, with a small velocity. This region is investigated more closely in Figure 4.10. The tadpole orbit is expected to be represented by a point in the middle of a saddle-center island chain, indicative of a periodic orbit.

In Figure 4.11, the initial conditions selected from the point in Figure 4.10 are propagated. The initial velocity $\dot{y}$ is selected such that the Jacobi constant of the initial state equals the desired value for the map. Because the period of the orbit is unknown, and the trajectory begins as a small displacement from L_4, the linear long period is a suitable estimate for the period of the nonlinear periodic orbit. The final and initial state are very similar after this time, and a targeting scheme can be used

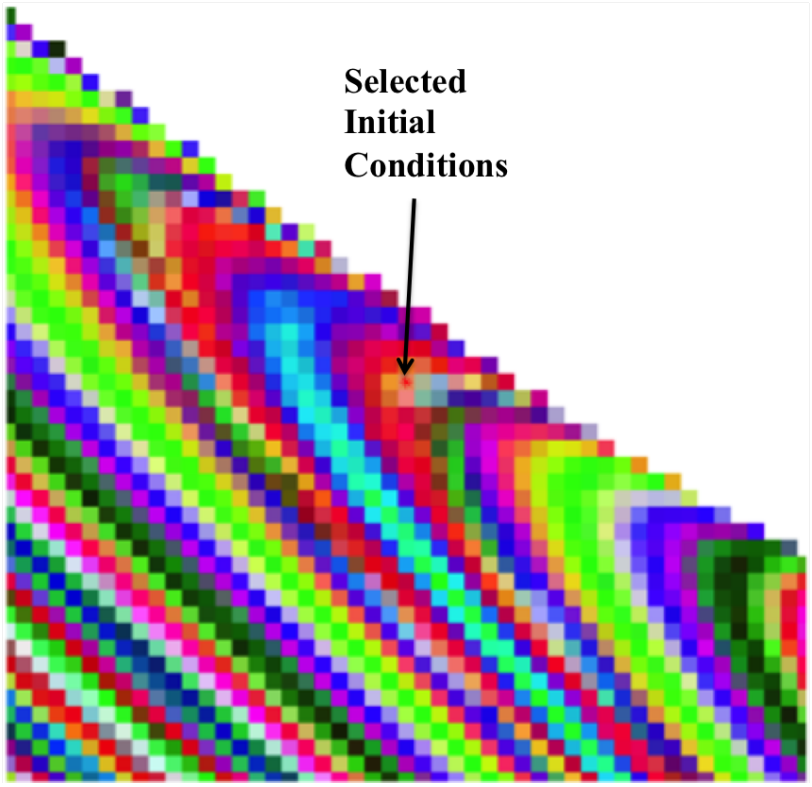

Figure 4.10. Zoomed View of Orbit Convolution Map for Saturn-Titan System

to compute the periodic orbit using this trajectory as an initial baseline. This orbit resembles the one found earlier using the search and filter technique.

Although this map provides some information about the system, using a different surface of section may give more information. Using polar coordinates relative to the barycenter, define the hyperplane $\Sigma : \theta = \theta_{L_4}$. The Saturn-Titan system is still investigated, using the same value of Jacobi constant as the previous map. The following table summarizes the parameters for the orbit convolution map in Figure 4.12, where the velocity $\dot{r}$ is plotted on the y-axis against the radius r for each crossing of the hyperplane where $r\dot{\theta} \geq 0$. The range of r is selected such that the middle of the map approximately indicates the distance to L_4.

It also is expected that an orbit will be found near the center of this map, because small tadpole orbits originate from small displacements from L_4. Initial conditions

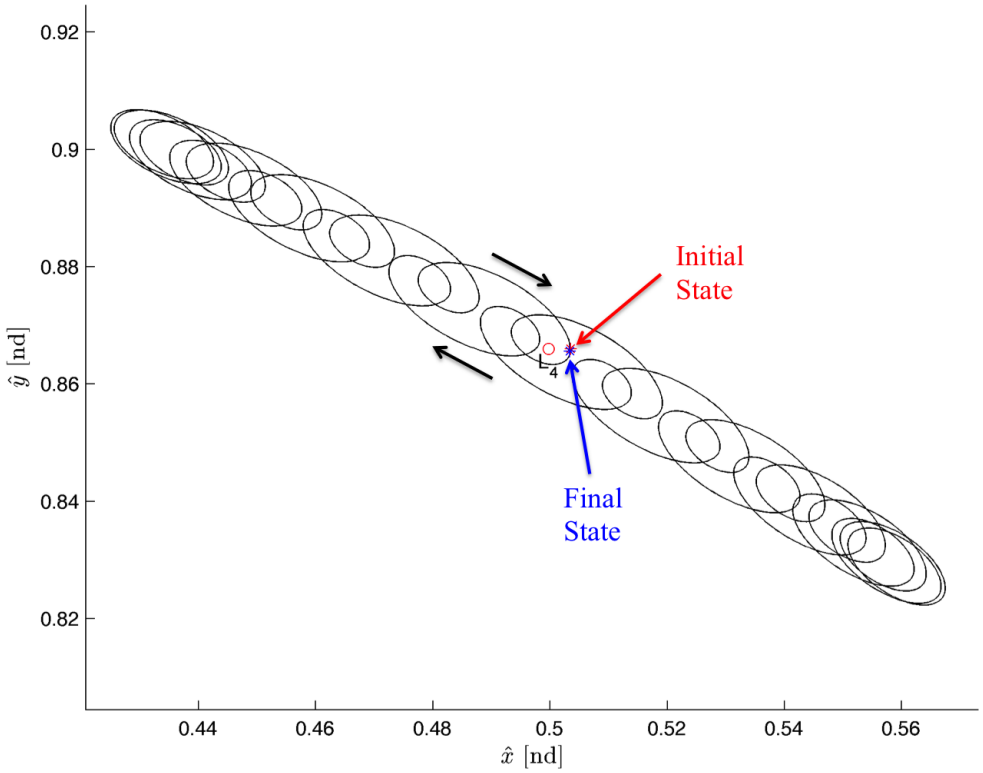

Figure 4.11. Propagated Trajectory from Orbit Convolution Map

are selected near the center of the map where a tadpole orbit may be found. This region is investigated more closely in Figure 4.13.

The polar coordinates from the map must be converted to Cartesian coordinates to integrate the equations of motion and use other numerical tools that use these coordinates. Because the value of r can be extracted and the surface of section is fixed at $\theta = \theta_{L_4}$, the values of x and y can be directly computed.

$$x = r\cos\theta_{L_4} \tag{4.16}$$

$$y = r\sin\theta_{L_4} \tag{4.17}$$

Table 4.2. Orbit Convolution Map Conditions for $\Sigma : \theta = \theta_{L_4}$

Parameter	Value
μ	0.00023669
C	2.99965918
r (nd)	$\begin{bmatrix} 0.9 & 1.05 \end{bmatrix}$
$\dot{r}$ (nd)	$\begin{bmatrix} -0.2 & 0.2 \end{bmatrix}$
Resolution	1024×1024
Iterates	$n = 50$
Convolutions	$K = 6$

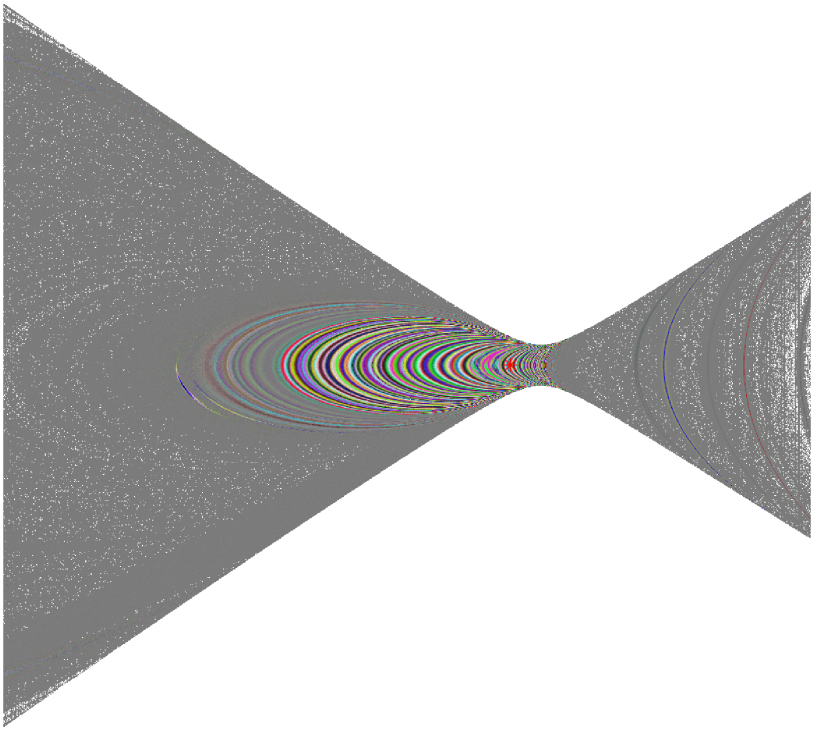

Figure 4.12. Orbit Convolution Map for $\Sigma : \theta = \theta_{L_4}$ (Figure created by W. Schlei, 2016)

The value of $\dot{\theta}$ must be computed before the Cartesian velocities, such that the resulting initial state has a Jacobi constant equal to the desired value.

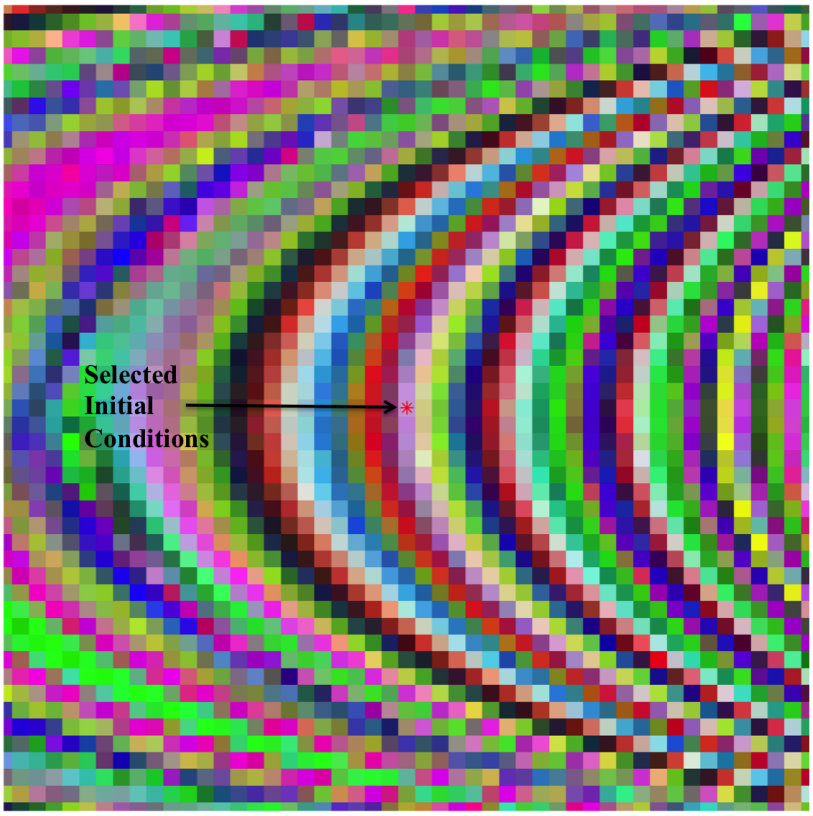

Figure 4.13. Zoomed View of Orbit Convolution Map for $\Sigma : \theta = \theta_{L_4}$

$$\dot{\theta} = \sqrt{\frac{-\dot{r}^2 \cos^2\theta - \dot{r}^2 \sin^2\theta - C + 2U^*}{r^2}} \tag{4.18}$$

Now the Cartesian velocities can be computed using the polar coordinate transformation developed earlier.

In Figure 4.11, the initial conditions selected from the point in Figure 4.13 are propagated in the nonlinear system for the length of the linear long period. A targeting scheme can likely be used to compute the nearby periodic orbit because the final and initial states are close. The same tadpole orbit as the one using the $\Sigma : y = y_{L_4}$ is found, but the structure of this map appears to be more orderly which may help find additional information about the dynamics in this region that may be more difficult to determine using the other map. Other tadpole-like motion exists nearby, and this

map can be used to find other tadpole orbits and study the relationship between these orbits and other orbits at this energy level.

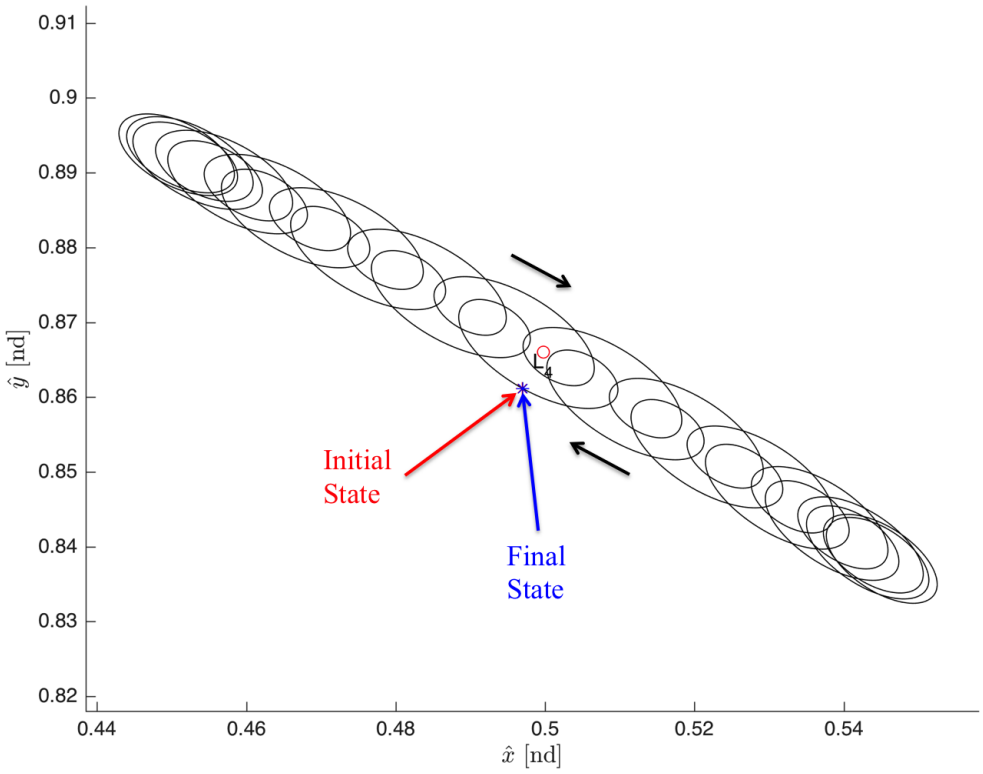

Figure 4.14. Propagated Trajectory from $\Sigma : \theta = \theta_{L_4}$ Map

4.1.4 Observations of Trojan Asteroids

Periodic tadpole orbits in the CR3BP can also be computed numerically by using information from orbits that appear in nature. The discovery of many Trojan asteroids in the Sun-Jupiter system provide many different orbits available for investigation. Ephemerides for many Trojan asteroids and other small bodies are available through the JPL HORIZONS system [28]. By using this information and propagating to generate initial conditions in the CR3BP, periodic motion for 3D orbits may be found. Additionally, these solutions can be compared to the actual ephemeris motion to see if the behavior of the resulting orbits is similar and if the shape is maintained. In order to investigate the motion of the Trojan asteroids in the Sun-Jupiter system, the states in the Sun-fixed inertial frame must be computed first. Using the SPICE system [29], ephemerides of Jupiter and the asteroid of interest can be computed relative to the Sun. The ephemeris Trojan asteroids are not planar or exactly periodic as the tadpole orbits computed in previous sections. In order to simplify the analysis and provide initial conditions that may be easier to correct in the CR3BP, Trojan asteroids with low inclination are selected. The first asteroid investigated is Eurymedon, which resides in the L_4 region in the *greek camp* of Trojan Asteroids. The approximate Keplerian orbital elements and additional information used to catalog the orbit can be found in Table 4.3.

In Figure 4.15, the ephemeris state of Eurymedon and Jupiter is computed relative to the Sun, such that it is plotted in a Sun-centered inertial frame. The state is propagated for 190 years, with an initial epoch of March 1, 1900. Because the period of tadpole orbits are typically similar to the linear long period of the system, it is expected that in order for the geometry of the orbit to nearly repeat in the Sun-Jupiter system, at least 148 years of data must be analyzed.

This ephemeris inertial state is then converted to the Sun-Jupiter rotating frame. Jupiter's actual orbit is not circular; however, its eccentricity is small enough that it can be approximated as such. This rotating frame is computed by determining the

Table 4.3. Eurymedon Data from JPL Solar System Dynamics Group

Parameter	Value
IAU Name	Eurymedon
Primary Designation	5012
SPK-ID	2005012
e (nd)	0.0851
a (AU)	5.272
i (deg)	5.00
Ω (deg)	34.83
ω (deg)	333.56
Period (year)	12.1

angle Θ that locates Jupiter relative to the inertial $\hat{X}$-axis. An initial state from this orbit is selected such that is begins near L_4 on the hyperplane $\Sigma : y = y_{L_4}$, which will be a convenient location for the targeter used later to find a periodic orbit.

The ephemeris state in the Sun-Jupiter rotating frame offers insight into how the motion may look in the CR3BP. Useful information about the orbit is difficult to obtain due to the complex motion, so using polar coordinates may retrieve additional properties about dominant frequencies in the motion. Because the ephemeris orbit is 3D, it is useful to add an additional component z representing the position in the $\hat{z}$ direction, which is independent of the in-plane motion. This addition generates a set of cylindrical coordinate r, θ, z that describe the motion. The radius r (in the $\hat{x} - \hat{y}$ plane) and angle θ describe the in-plane motion of the orbit.

In Figure 4.17, three dominant frequencies emerge. Motion repeats in intervals of 12 and 6 years, commensurate with the linear short period and half of this time for the Sun-Jupiter system. The librational period appears to be approximately 148 years which is comparable to the linear long period. In order to compute a periodic tadpole orbit, the ephemeris state must be transitioned to the CR3BP. The initial conditions

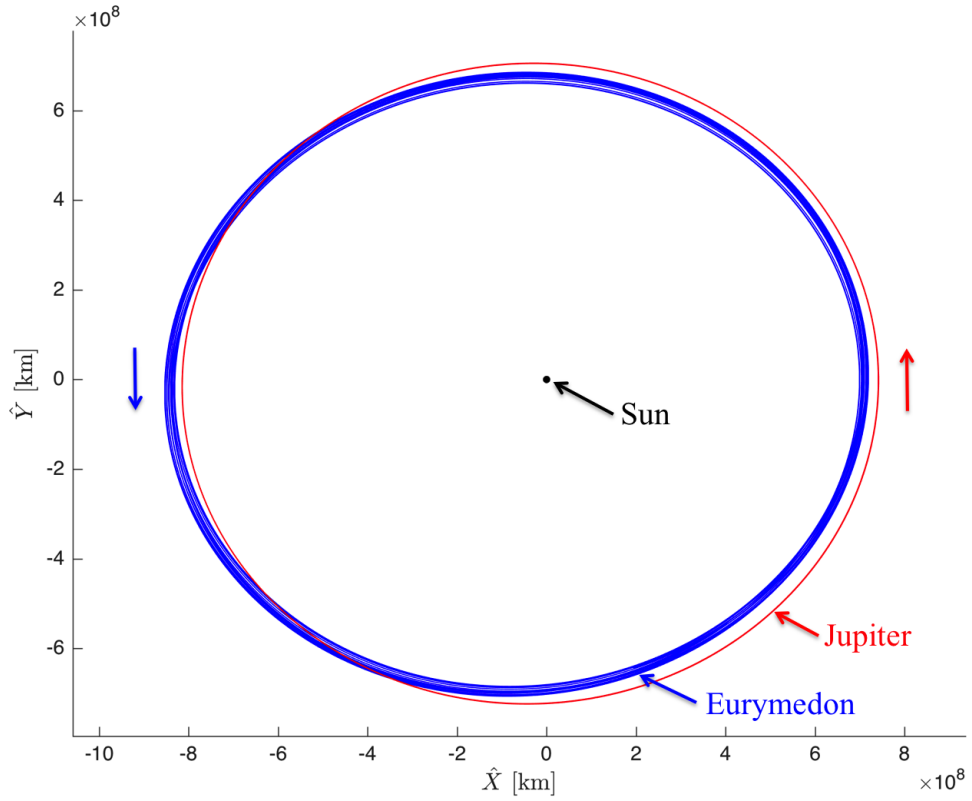

Figure 4.15. Eurymedon Ephemeris Orbit (Sun-Centered Inertial Frame)

selected in Figure 4.16 are integrated with the CR3BP equations of motion until the trajectory returns near the initial state, and the planar motion is shown in Figure 4.18. Although the out-of-plane component from the ephemeris state is expected to be small due to the small inclination of the orbit, it cannot be ignored if a periodic solution of the full librational motion is to be computed by using this ephemeris state to generate initial conditions in the CR3BP. The projection of the orbit in the $\hat{x} - \hat{y}$ plane is useful in demonstrating the epicyclic and librational motion; however, an additional epicyclic motion is observed when viewing the 3D orbit.

This motion differs slightly from the ephemeris orbit, but the overall structure is maintained. Because the CR3BP models a circular orbit of the Sun and Jupiter about

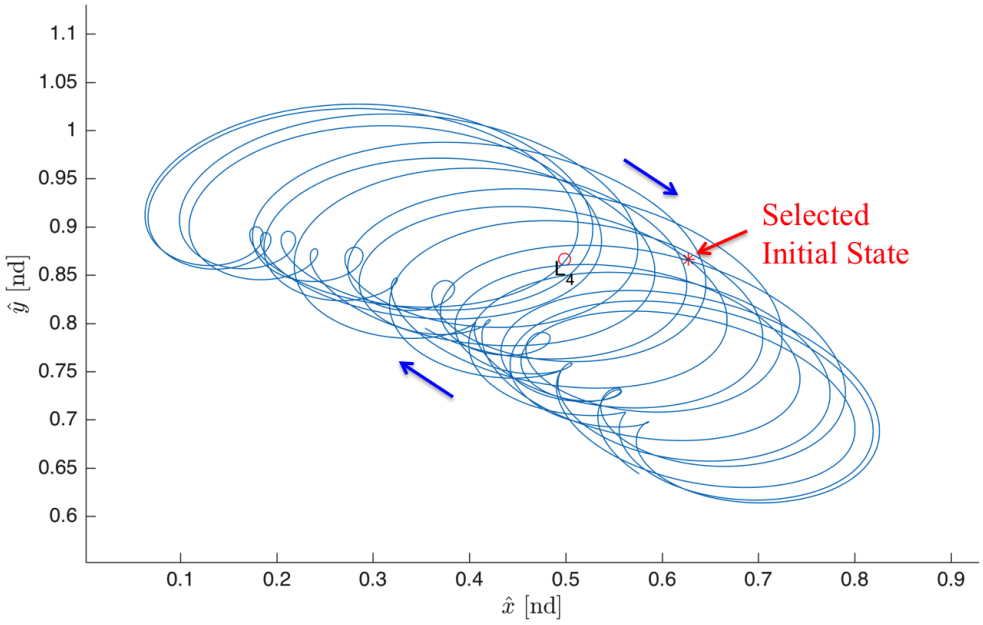

Figure 4.16. Eurymedon Ephemeris Orbit (Sun-Jupiter Rotating Frame)

their barycenter, the CR3BP rotating frame and approximated ephemeris frame differ, which is a possible explanation for the apparent difference between the two orbits. The difference between the ephemeris orbit and that propagated in the CR3BP is obvious in the inertial frame.

Although differences from the ephemeris motion in both the rotating and inertial frames are apparent, using cylindrical coordinates in the CR3BP rotating frame can show how significant these differences are. The frequencies representative of the short period epicyclic motion are maintained in all three cylindrical components, with the most significant difference from the ephemeris motion appearing in the θ term. This result is expected again due to the approximation of a circular Jupiter orbit. The

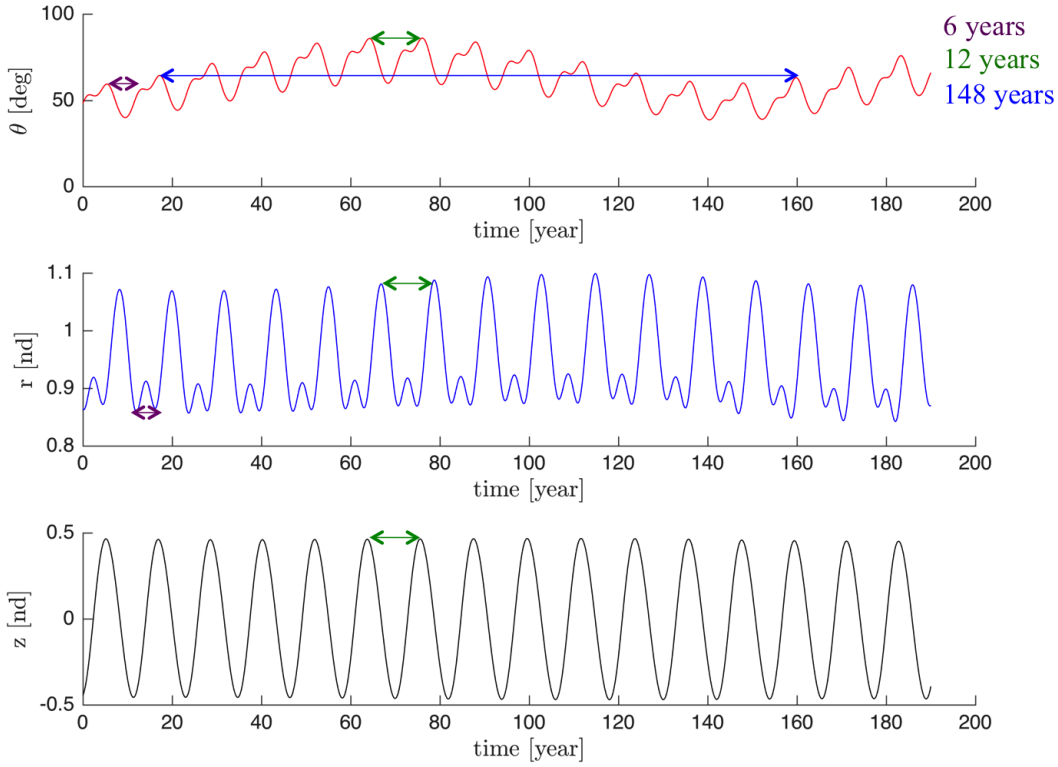

Figure 4.17. Polar Components for Eurymedon Ephemeris Orbit

in-plane geometry in the CR3BP repeats after 154 years, which is 6 years longer than the linear long period and the time it takes for the geometry to approximately repeat for the ephemeris state. This periodic orbit is in 1:13 resonance with the Sun-Jupiter system, such that it takes 13 revolutions of the Sun-Jupiter system about its barycenter for the orbit to complete one full cycle.

Now that information about the geometry of the nearly-periodic orbit for the CR3BP is available, the nearby periodic solution can be found using a targeting scheme. The tadpole region is sensitive, especially due to the long period of these orbits in the Sun-Jupiter system. As a result, the periodic orbit obtained may maintain similar characteristics to the initial guess but have some differences. The resulting

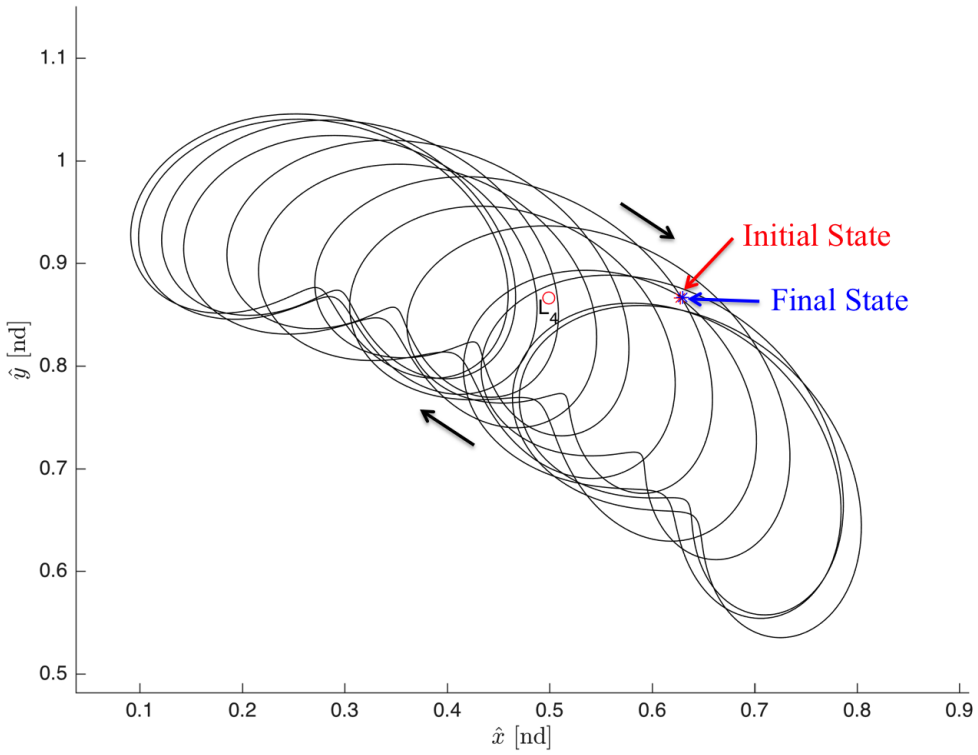

Figure 4.18. Eurymedon CR3BP Orbit (Rotating Frame $\hat{x} - \hat{y}$ Plane)

periodic tadpole orbit both with planar and 3D views can be seen in Figures 4.22 - 4.23.

Clearly, the resulting trajectory differs from the initial guess. In Figure 4.22, the planar motion remains in the vicinity of the initial trajectory; however, the looping structure appears to have significantly changed. In the 3D view of the orbit in Figure 4.23, the out-of-plane structure appears similar to the initial guess. Now this motion appears to have some similarity to the L_4 vertical family of orbits. Again, the cylindrical coordinates offer a more useful depiction of the frequencies of the orbit.

For the corrected periodic tadpole orbit, the two frequencies for the in-plane motion are eliminated, leaving epicyclic motion with the period of approximately 6 years

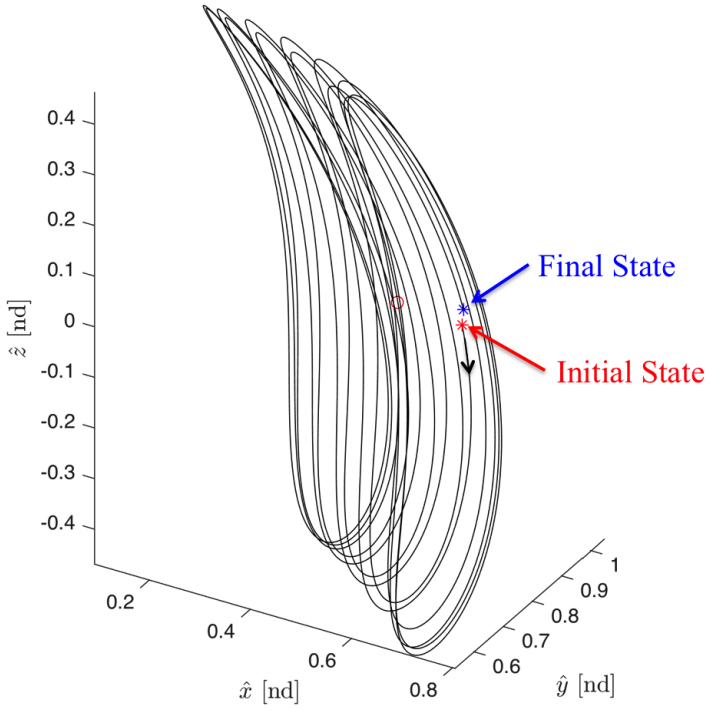

Figure 4.19. Eurymedon CR3BP Orbit (3D View)

representative of half the linear short period. The 12 year epicylic motion is maintained in the out-of-plane motion. Although the properties of the epicyclic motion is changed for the solution, the long period librational motion is maintained. The resulting orbit maintains the period of the initial guess, but the looping structure is changed. A solution closer to the initial guess may be obtained, as infinite periodic tadpole orbits exist; however, it may be difficult to find due to the sensitivity of the initial conditions.

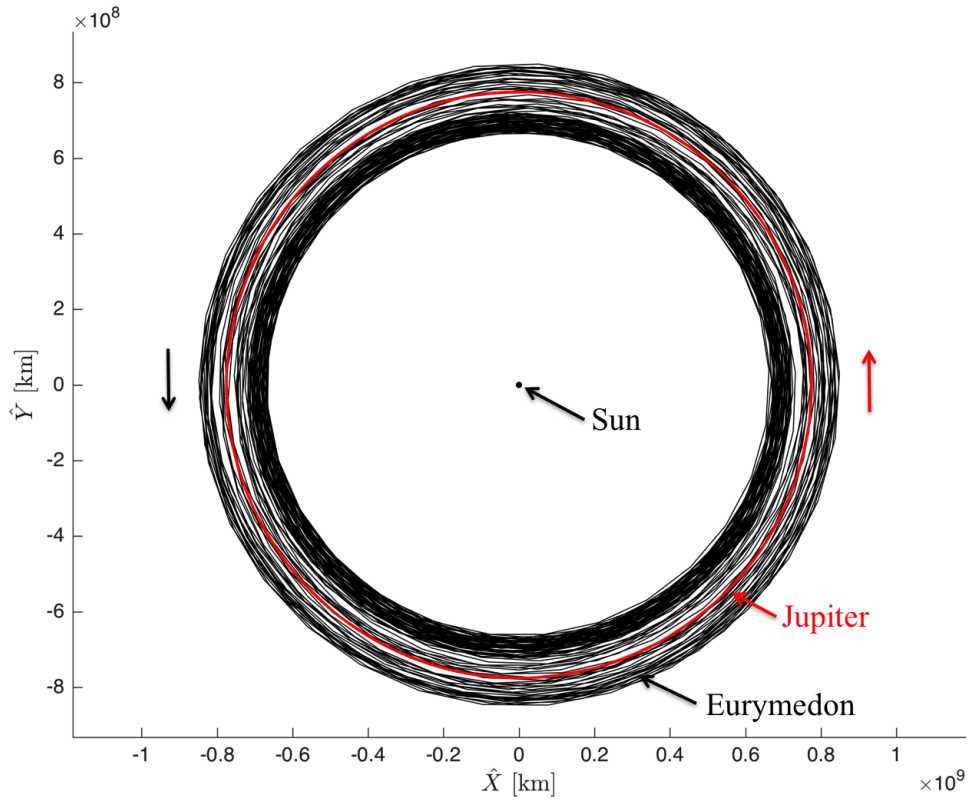

Figure 4.20. Eurymedon CR3BP Orbit (Inertial Frame)

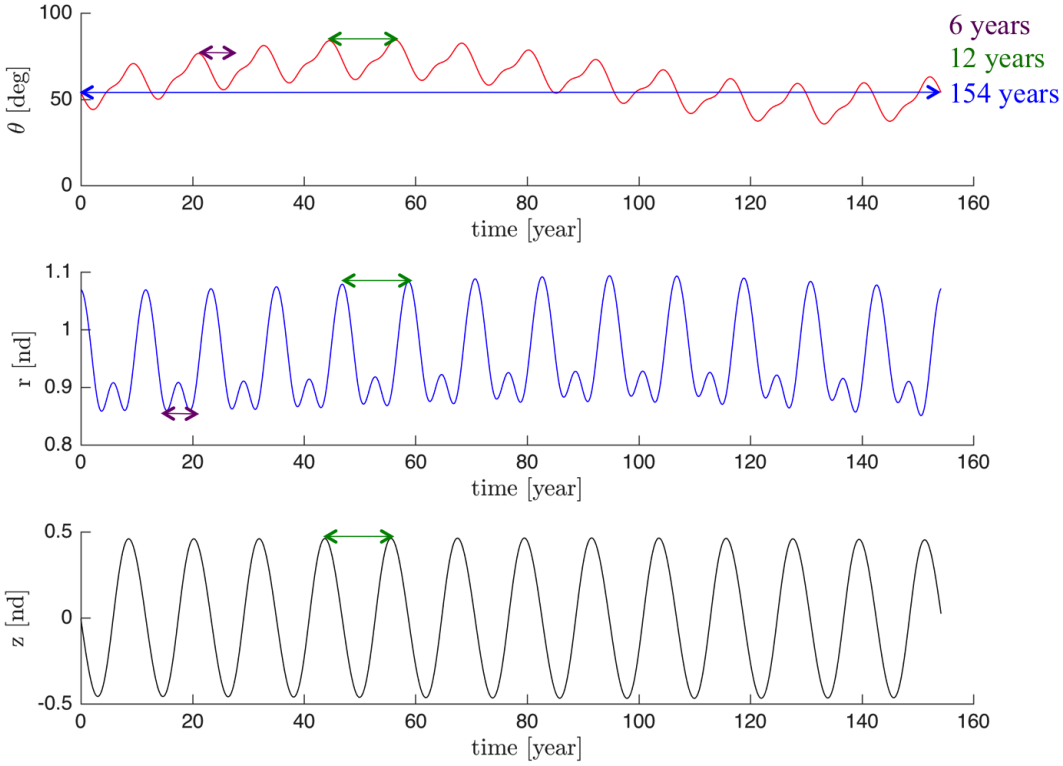

Figure 4.21. Polar Components for Eurymedon CR3BP Orbit

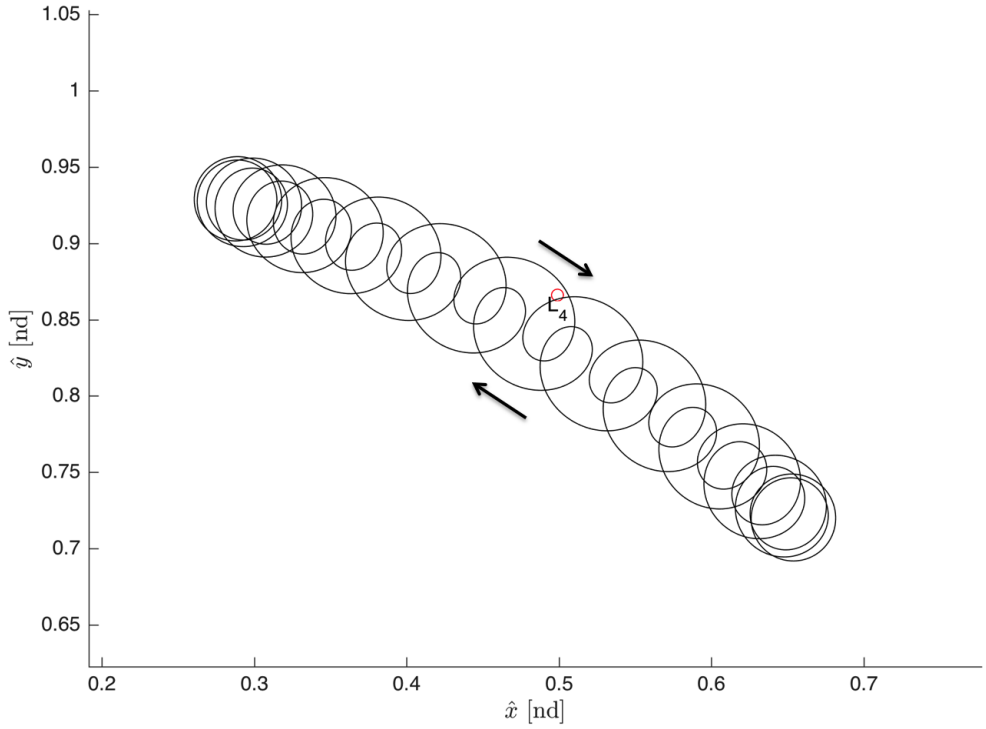

Figure 4.22. Corrected Eurymedon CR3BP Orbit (Rotating Frame $\hat{x} - \hat{y}$ plane)

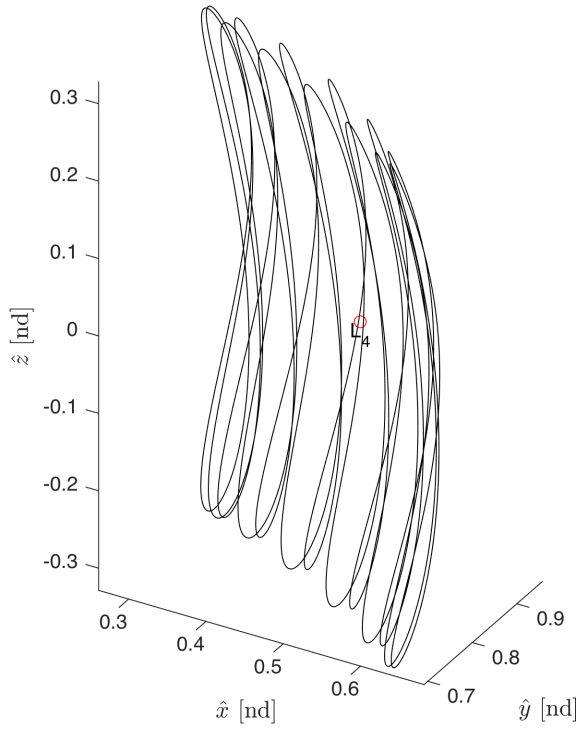

Figure 4.23. Corrected Eurymedon CR3BP Orbit (3D View)

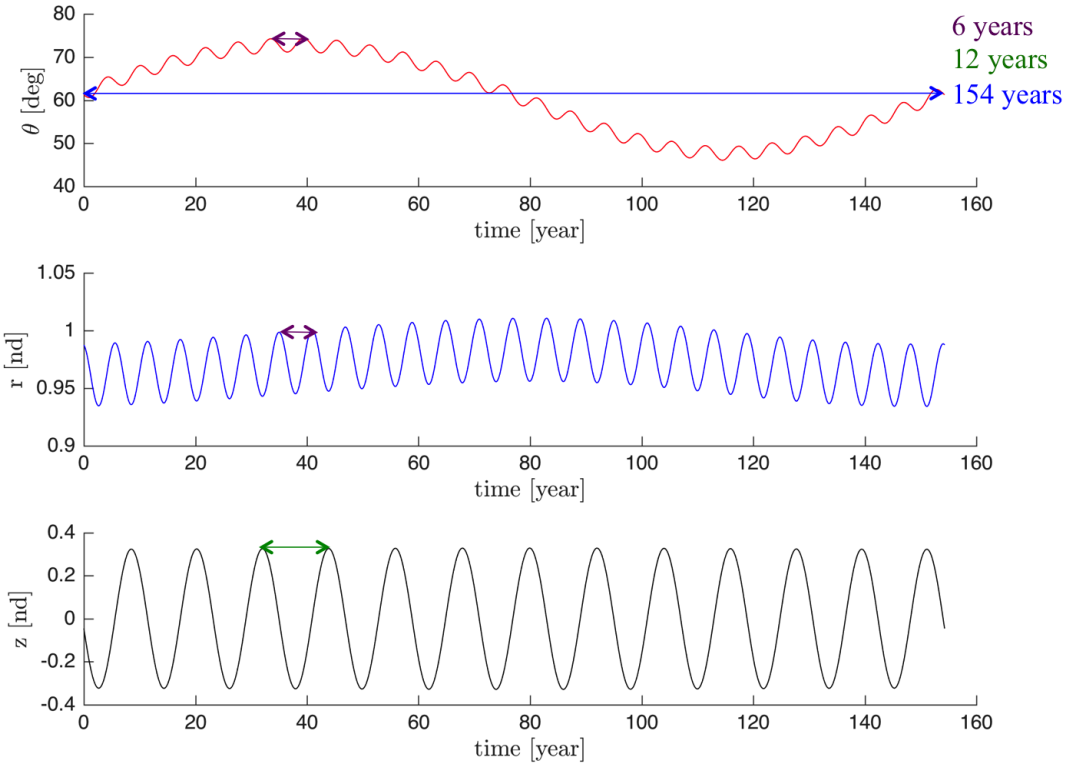

Figure 4.24. Polar Components for Corrected Eurymedon CR3BP Orbit

4.2 Families of Orbits

Periodic tadpole orbits exist in families, and once a solutions is obtained, other family members with similar properties can be computed. By finding these other orbits, different properties such as the period and Jacobi constant can be examined to see how they change as the family evolves. It is desirable to find a range of orbits with different energy levels to offer a variety of choices for mission design scenarios. The stability may also be investigated to see if larger tadpole orbits that deviate further from the triangular point remain stable. In addition, by evolving the families, the influence of other nearby motion may be observed. Because it is difficult to compute larger tadpole orbits and initial conditions are sensitive to find periodic solutions, a continuation scheme is used to continue the family by supplying an initial periodic solution. For this investigation, tadpole orbits are computed in the Saturn-Titan and Sun-Jupiter systems. Useful characteristics for these systems are defined in Tables 4.4 - 4.5.

Table 4.4. Saturn-Titan System Parameters

Parameter	Value
μ	$2.366943848017401 \times 10^{-4}$
l^* (km)	1221865
t^* (day)	2.537963230502414
$\mathcal{P}_{long}$ (day)	398.9507907593953
$\mathcal{P}_{short}$ (day)	15.952866475339174
C_{L_1}	3.015769539429093
C_{L_2}	3.015453907344979
C_{L_3}	3.000236693214998
$C_{L_{4,5}}$	2.999763361639430

Table 4.5. Sun-Jupiter System Parameters

Parameter	Value
μ	$9.533559933579646 \times 10^{-4}$
l^* (km)	778340821
t^* (day)	689.4736106457045
$\mathcal{P}_{long}$ (year)	147.9534904459595
$\mathcal{P}_{short}$ (year)	11.887881479380388
C_{L_1}	3.038747339060641
C_{L_2}	3.037475944677899
C_{L_3}	3.000953336886087
$C_{L_{4,5}}$	2.999047552894292

4.2.1 Tadpole Orbits in the Saturn-Titan System

Periodic tadpole orbits in the Saturn-Titan system can be obtained by various techniques discussed previously. Usually the periodic orbits found by using these techniques are small and the motion resides near the triangular point. Although tadpole orbits cannot be definitely bounded by Jacobi constant or by shape, it is expected that as the family evolves, the orbits will grow in size and extend towards L_3. Due to the nonlinear looping nature of tadpole motion, continuation in a specific parameter cannot be easily predicted, so using pseudo-arclength continuation is desirable. The following family of 200 planar periodic L_4 tadpole orbits is computed in the Saturn-Titan system, beginning with a small orbit and increasing in size as the orbits deviate further from the triangular point.

From Figure 4.25, it is difficult to see how the family evolves as the orbits overlap and the looping structure changes between family members. Additionally, the family does not end at the final computed member. The family likely continues to extend towards L_3; however, as the members grow large, converging to a solution becomes

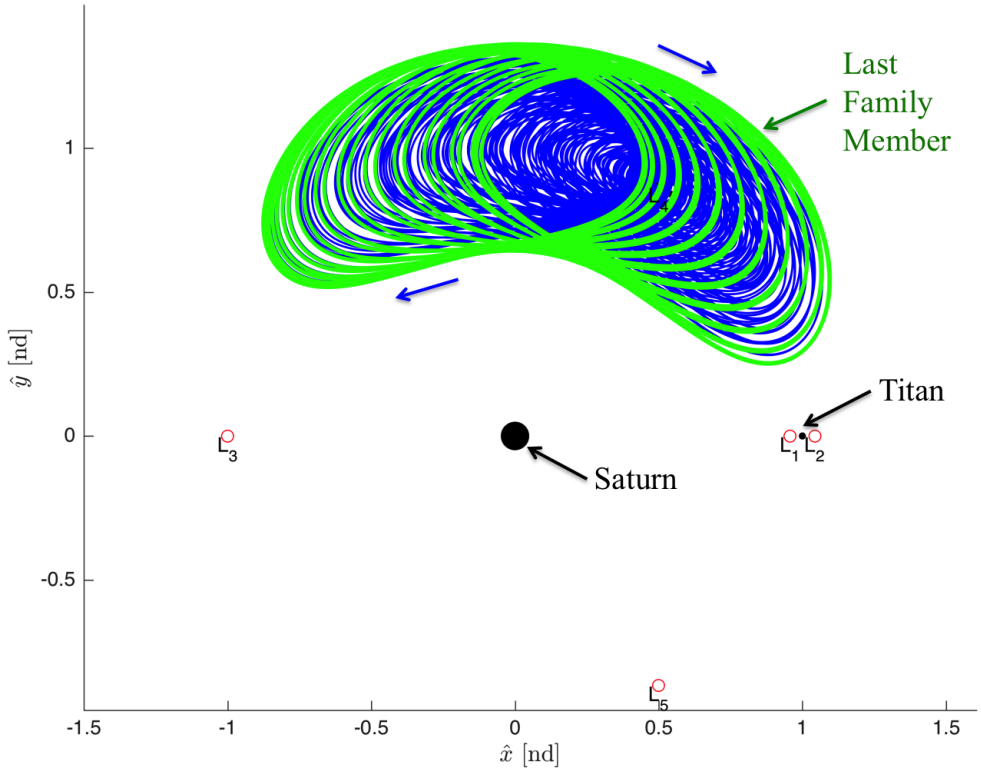

Figure 4.25. Planar L_4 Tadpole Family in Saturn-Titan System (Rotating Frame)

more difficult and smaller steps along the family tangent vector must be taken. In Figure 4.26, the period and Jacobi constant of each family member is plotted. The period slightly decreases, but it remains close to 399 days which is comparable to the linear long period of the Saturn-Titan system. The Jacobi constant begins slightly below that of L_4 for the first family member and decreases significantly. This variety of orbits provides many options that can be matched with other orbits at similar energy levels for a mission design scenario.

The stability index of the pair of eigenvalues λ_1, λ_2 of the monodromy matrix can be used to evaluate the stability of the tadpole orbits, and the other two pairs of eigenvalues across the family are unity. For the smaller tadpole orbits, the stability

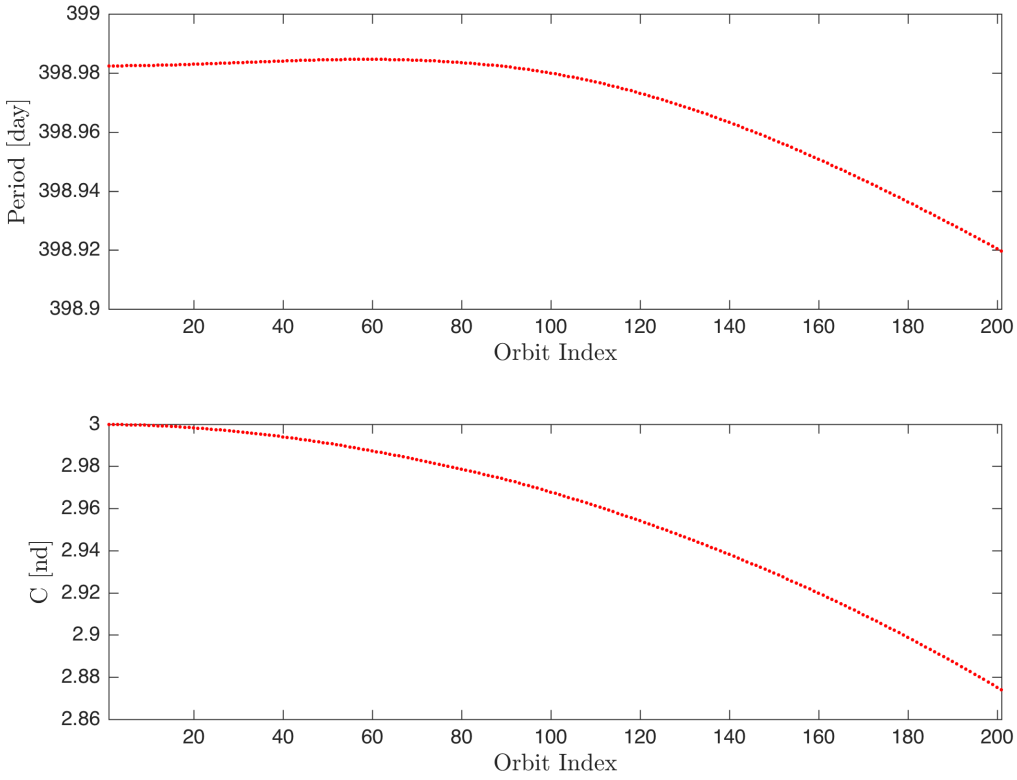

Figure 4.26. Planar L_4 Tadpole Family Characteristics

index $\nu = 1$, indicating that the orbit is stable. These orbits will have no invariant manifolds as they do not contain a stable/unstable subspace. As the family evolves, the stability index increases slightly. These values remain near one, indicating that the orbits are insignificantly unstable and that motion with a slight perturbation should still remain near the nominal solution. Additionally, a large step-off distance would be required to depart or arrive at these orbits using invariant manifolds in a reasonably amount of time. This large step-off distance would result in an approximation of the invariant manifolds with a significant amount of error. Because it is difficult to see how the family evolves in Figure 4.25, different members of the family are plotted. The initial conditions for each member are listed in Table 4.6.

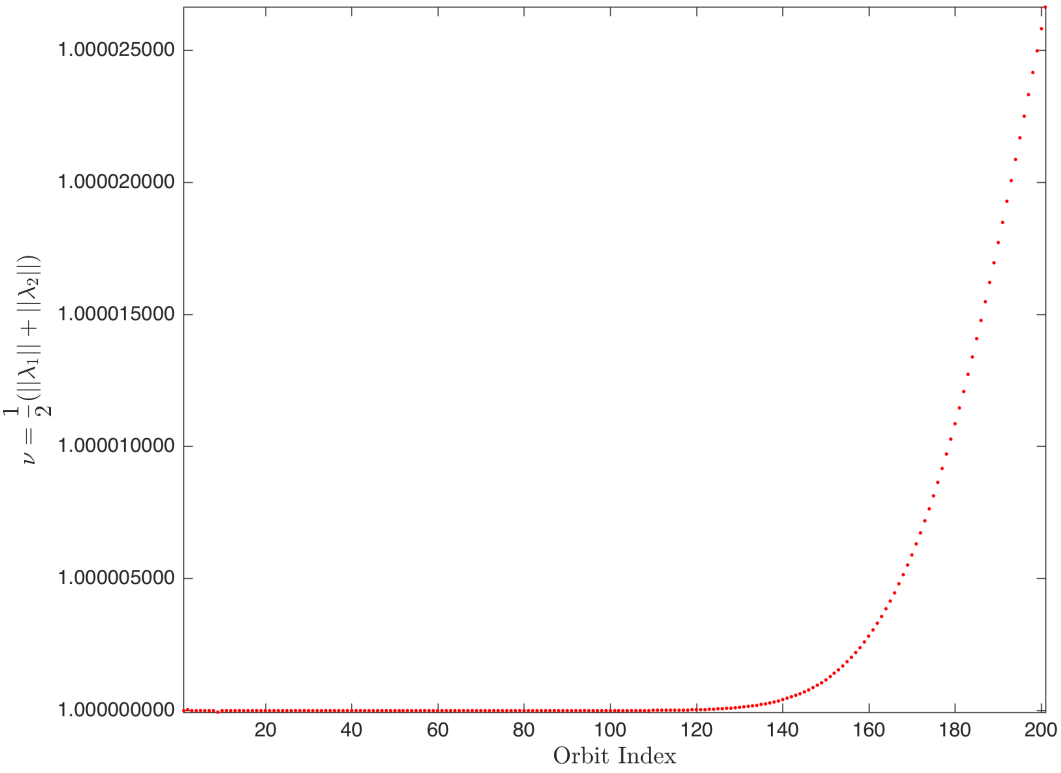

Figure 4.27. Planar L_4 Tadpole Family Stability Index

The first tadpole family member can be seen in Figure 4.28. It is not necessarily the smallest tadpole orbit in the entire orbit family, but it is the smallest member (also with the highest Jacobi constant) that is computed in this set. The orbit begins near L_4 with small velocity components in both the $\hat{x}$ and $\hat{y}$ directions. Because the Jacobi constant is slightly less than that of the triangular points, the motion is not bounded by a ZVC in the plane. The small loops indicative of the short period epicyclic motion are apparent, and these loops do not appear to be the same size throughout the orbit. Although the direction of the complex looping motion is difficult to describe at all points along the orbit, the flow of the epicyclic motion moves in a clockwise direction around the triangular point similar to that of the short period orbits.

Table 4.6. Planar L_4 Tadpole Family Members in the Saturn-Titan System

Orbit	x_0 (nd)	y_0 (nd)	$\dot{x}_0$ (nd)	$\dot{y}_0$ (nd)	P (day)	C
1	0.5006453	0.8660254	-0.0015819	-0.0028112	398.98241	2.9997535
20	0.5145889	0.8660254	-0.0072946	-0.0407063	398.98296	2.9982208
40	0.5080839	0.8660254	-0.0301217	-0.0703856	398.98405	2.9939543
60	0.4882363	0.8660254	-0.0611736	-0.0940484	398.98460	2.9872743
80	0.4461267	0.8660254	-0.1051902	-0.1101190	398.98351	2.9785902
100	0.4093155	0.8660254	-0.1409712	-0.1326200	398.97996	2.9677537
120	0.4010802	0.8660254	-0.1555316	-0.1669582	398.97313	2.9541090
140	0.4022849	0.8660254	-0.1625141	-0.2036145	398.96326	2.9381601
160	0.4124825	0.8660254	-0.1629569	-0.2419097	398.95079	2.9197877
180	0.4313037	0.8660254	-0.1575447	-0.2816297	398.93633	2.8988498
200	0.4581910	0.8660254	-0.1467875	-0.3228505	398.92054	2.8752160

As the family evolves as seen in Figure 4.29, the amplitude of the orbit increases in both its length and width as the motion displaces further from L_4. The epicyclic loops also increase in size, and the orbit seems to have a relatively symmetric structure. Although the initial position is still close to the triangular points, the increase in the amplitude of the motion can be attributed to the larger initial velocity magnitude. When examining members further along the family, the amplitude of the motion continues to increase with an increase in initial velocity magnitude. Additionally, the Jacobi constant decreases, indicative of an increase in energy resulting from the increase in velocity. In Figure 4.30, the asymmetry of the orbit is much more obvious than the previous smaller tadpole orbits.

The final computed family member is plotted in Figure 4.31, although it is not necessarily the boundary of where this family ends. Due to the complexity of tadpole orbits and long integration time, computing larger periodic tadpole orbits is nontrivial. The range of members computed does provide adequate information on how this

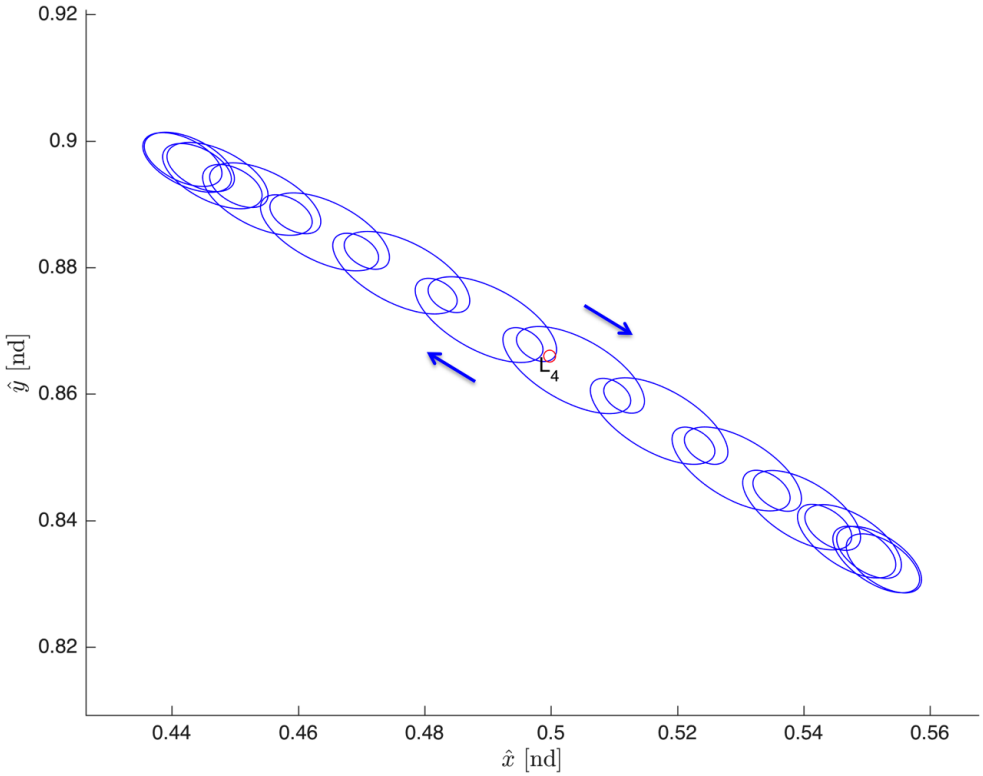

Figure 4.28. Planar L_4 Tadpole Family Member 1

family of tadpole orbits evolves, as seen by the consistent decrease in Jacobi constant across the family.

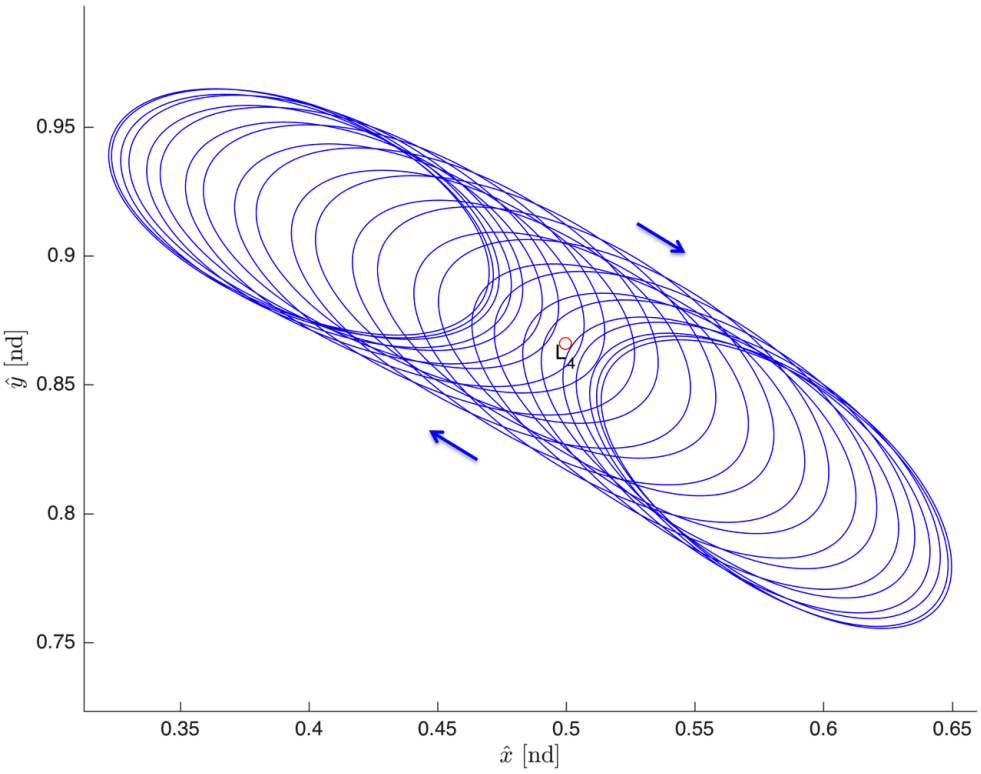

Figure 4.29. Planar L_4 Tadpole Family Member 20

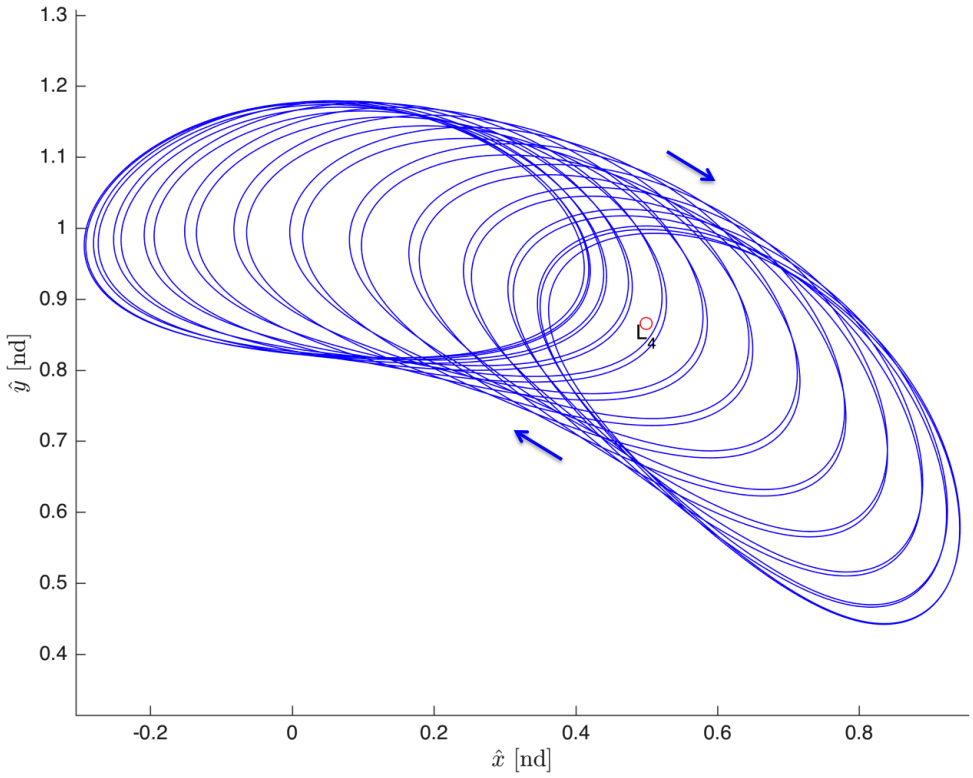

Figure 4.30. Planar L_4 Tadpole Family Member 100

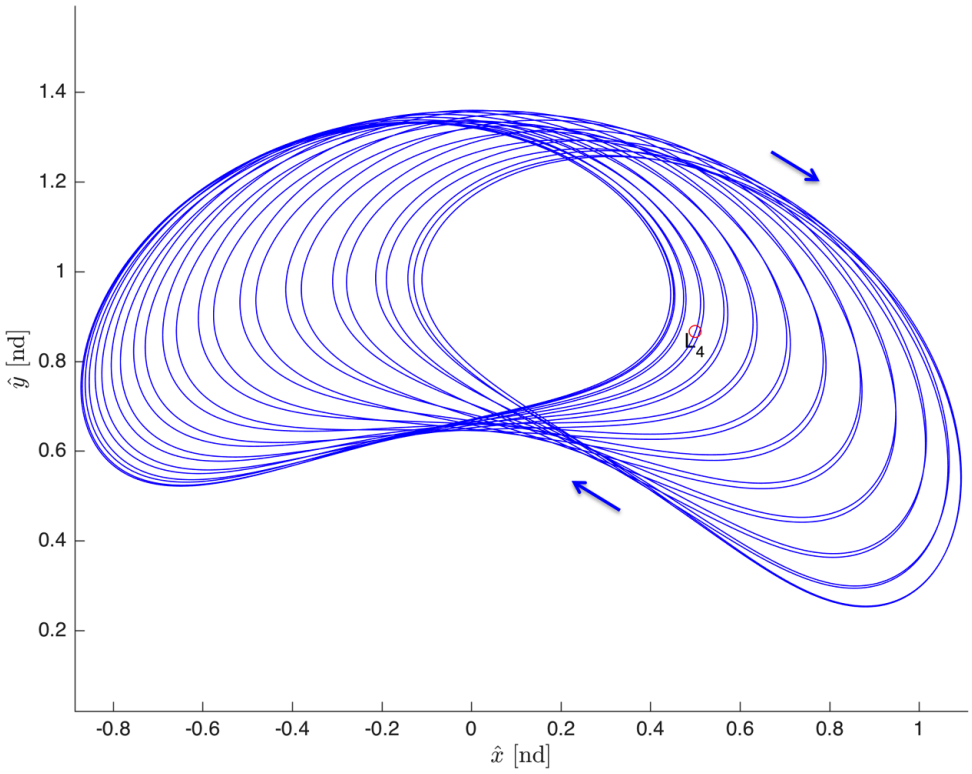

Figure 4.31. Planar L_4 Tadpole Family Member 200

4.2.2 Tadpole Orbits in the Sun-Jupiter System

The motion of ephemeris Trojan orbits in the Sun-Jupiter system can provide a suitable initial guess for obtaining 3D periodic motion in the CR3BP. Although the converged solution may or may not be the closest periodic solution in the CR3BP that is representative of the actual Trojan asteroid motion, it may be desirable to compute other orbits in the vicinity that have similar characteristics. By computing different orbits in the same family, more information about the dynamics in the region can be obtained. Additionally, these orbits can provide a variety of options for different mission design scenarios. It is expected that as the family evolves, the orbits will grow in size and extend towards L_3, and pseudo-arclength continuation is used due to the complex tadpole motion. The following family of 64 periodic L_4 tadpole orbits with 3D motion is computed in the Sun-Jupiter system, beginning with a small orbit orbit and increasing in size as the orbits deviate further from the triangular point. A planar view of the family is shown in Figure 4.32, where the looping due to the short period epicylic motion is apparent. Because the family is 3D, it is important to also include the out-of-plane motion, as seen in Figure 4.33.

From Figure 4.32, it is difficult to see how the family evolves; however, it is clear that the amplitude of the orbit increases across the family. The family does not necessarily end at the final computed member and likely continues to extend towards L_3. As the members increase in size, converging to a solution becomes more difficult and smaller steps along the family tangent vector must be taken. In addition, the targeter may converge to the nearby long period orbit due to the sensitivity of initial conditions. In Figure 4.34, the period and Jacobi constant of each family member is plotted. The period slightly decreases, but it remains close to 154 years which is 6 years longer than the linear long period of the Sun-Jupiter system. The Jacobi constant increase until it is slightly below that of L_4. The stability index across all the members computed in this family is equal to unity, indicating that each of the

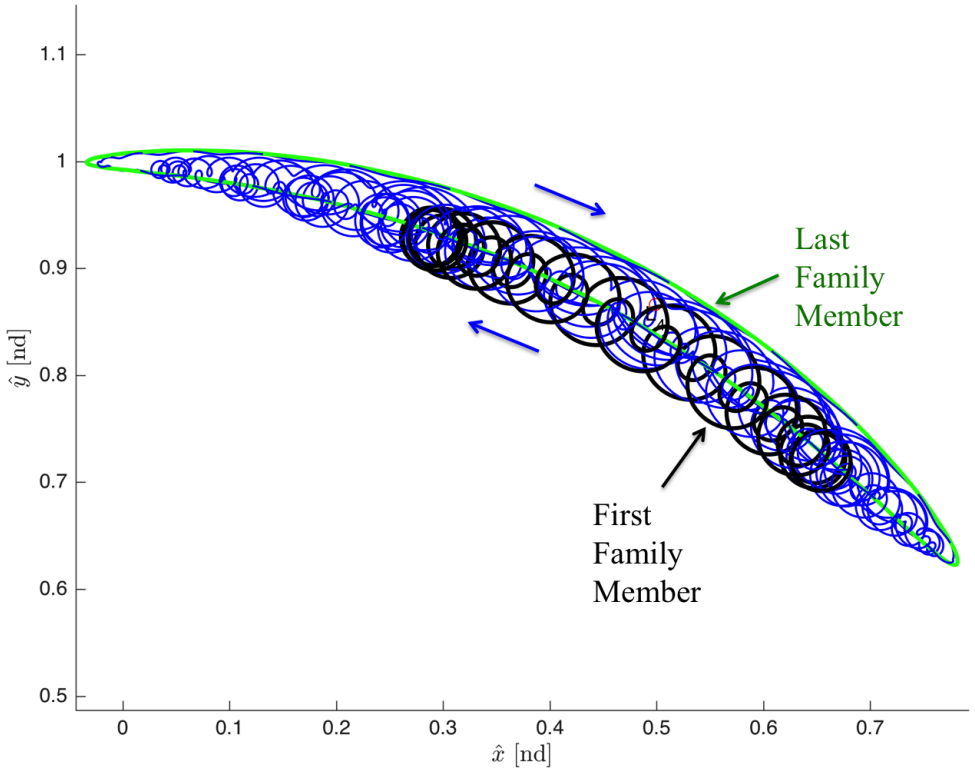

Figure 4.32. L_4 Tadpole Family in Sun-Jupiter System (Rotating Frame $\hat{x} - \hat{y}$ Plane)

members are marginally stable solutions. The initial conditions for each member are listed in Table 4.6.

The first tadpole family member can be seen in Figure 4.35. It is not necessarily the tadpole orbit with the smallest amplitude in the $\hat{x} - \hat{y}$ plane in the entire orbit family, but it is the smallest member (also with the lowest Jacobi constant) that is computed in this set. The orbit begins near L_4 with velocity components in both the $\hat{x}$ and $\hat{y}$ directions and a large velocity component in the $\hat{z}$ direction. As a result of the large out-of-plane velocity component, periodic motion with a large amplitude in this direction occurs. Because the Jacobi constant is slightly less than that of the

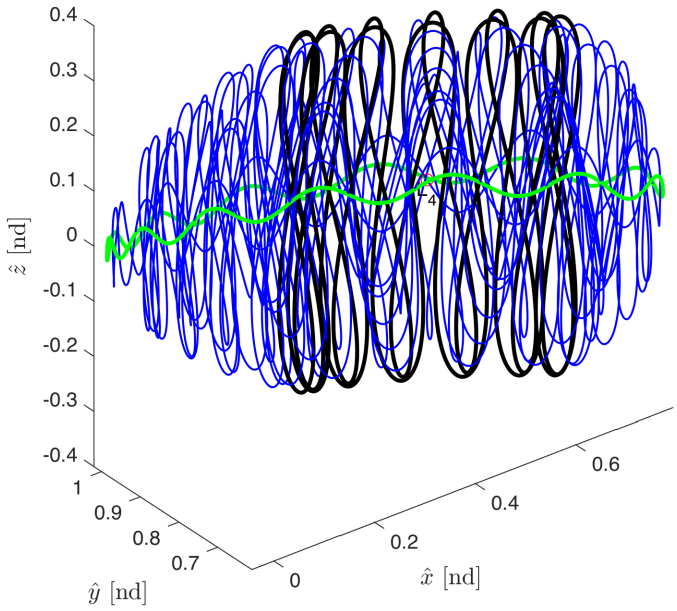

Figure 4.33. L_4 Tadpole Family in Sun-Jupiter System (3D View)

triangular points, the motion is not bounded by a ZVC in the plane. The small loops indicative of the epicyclic motion are apparent, and these loops do not appear to be the same size throughout the orbit.

As the family evolves as seen in Figure 4.36, the amplitude of the orbit increases in both its length and width in the $\hat{x} - \hat{y}$ plane as the motion displaces further from L_4. The in-plane epicyclic loops decrease in size, and the amplitude of the out-of-plane motion also decreases.

The final computed family member is plotted in Figure 4.37, although it is not necessarily the boundary of where this family ends. This orbit has the largest in-plane displacement from the triangular point and has the smallest out-of plane motion in

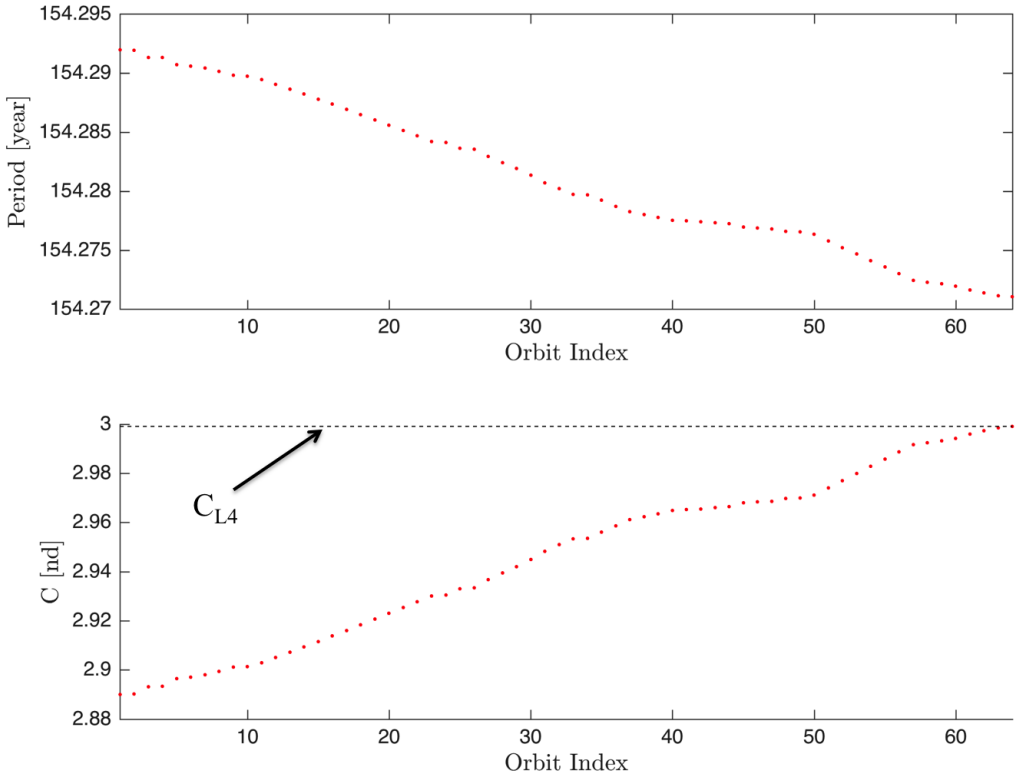

Figure 4.34. L_4 Tadpole Family Characteristics in Sun-Jupiter System

the family. It appears to have motion very similar to that of a long period orbit, which explains the difficulty in continuing the family without using a very small step size due to the influence of this other nearby orbit family. The range of members computed does provide adequate information on how this family of tadpole orbits evolves and provides a variety of options at different energy levels with varying amplitudes of out-of-plane behavior.

Table 4.7. L_4 Tadpole Family Members in the Sun-Jupiter System

Orbit	x_0 (nd)	y_0 (nd)	z_0 (nd)	$\dot{x}_0$ (nd)	$\dot{y}_0$ (nd)	$\dot{z}_0$ (nd)	P (yr)	C
1	0.47455	0.86603	-0.04569	0.02492	-0.03060	-0.32514	154.292	2.89005
5	0.47171	0.86603	-0.04913	0.02002	-0.02857	-0.31526	154.291	2.89648
10	0.46990	0.86603	-0.04949	0.01687	-0.02652	-0.30775	154.290	2.90141
15	0.46771	0.86603	-0.03691	0.01341	-0.01954	-0.29358	154.288	2.91158
20	0.46485	0.86603	-0.03084	0.00783	-0.01378	-0.27505	154.286	2.92298
25	0.46226	0.86603	-0.03044	0.00211	-0.00993	-0.25676	154.284	2.93301
30	0.45915	0.86603	-0.03394	-0.00524	-0.00609	-0.23220	154.281	2.94498
35	0.45686	0.86603	-0.03163	-0.01092	-0.00159	-0.20775	154.279	2.95597
40	0.45328	0.86603	-0.05098	-0.01877	-0.00053	-0.18028	154.278	2.96490
45	0.44409	0.86603	-0.10219	-0.03031	-0.00128	-0.14514	154.277	2.96796
50	0.43452	0.86603	-0.13566	-0.03874	0.00462	-0.09673	154.276	2.97114
55	0.44242	0.86603	-0.09354	-0.03514	0.01077	-0.06912	154.274	2.98573
55	0.44242	0.86603	-0.09354	-0.03514	0.01077	-0.06912	154.274	2.98573
60	0.44837	0.86603	-0.04431	-0.03182	0.01375	-0.05805	154.272	2.99417
64	0.44948	0.86603	-0.01281	-0.03179	0.01647	-0.01722	154.271	2.99903

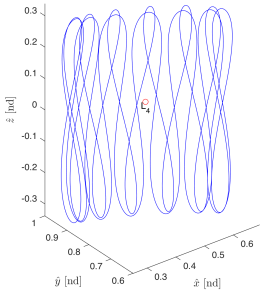

(a) Tadpole Family Member 1 (3D View)

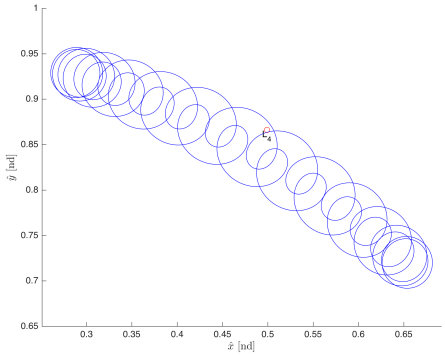

(b) Tadpole Family Member 1 ($\hat{x} - \hat{y}$ Plane)

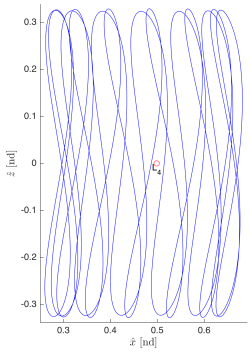

(c) Tadpole Family Member 1 ($\hat{x} - \hat{z}$ Plane)

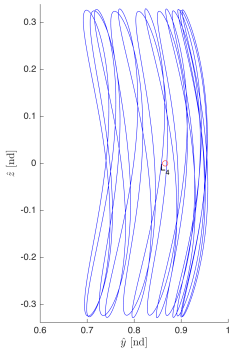

(d) Tadpole Family Member 1 ($\hat{y} - \hat{z}$ Plane)

Figure 4.35. L_4 Tadpole Family Member 1

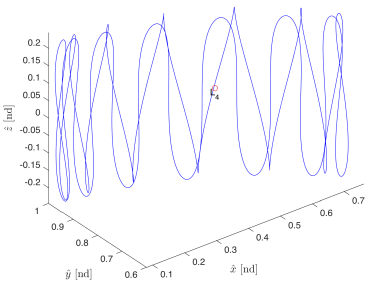

(a) Tadpole Family Member 30 (3D View)

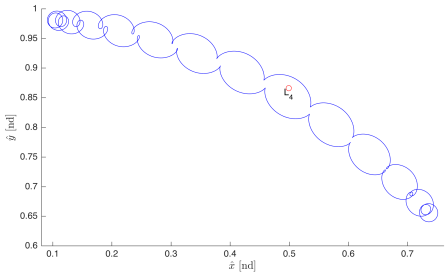

(b) Tadpole Family Member 30 ($\hat{x}-\hat{y}$ Plane)

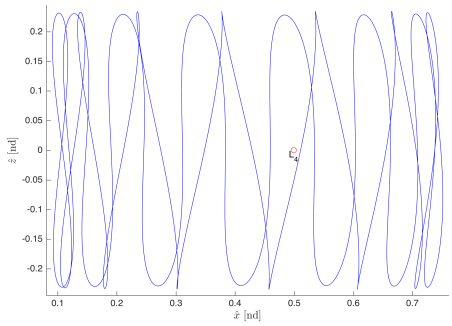

(c) Tadpole Family Member 30 ($\hat{x}-\hat{z}$ Plane)

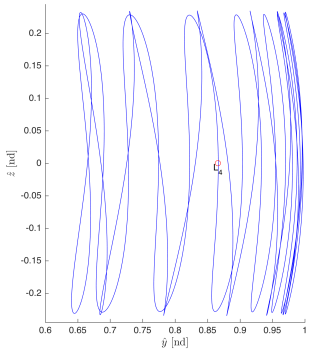

(d) Tadpole Family Member 30 ($\hat{y}-\hat{z}$ Plane)

Figure 4.36. L_4 Tadpole Family Member 30

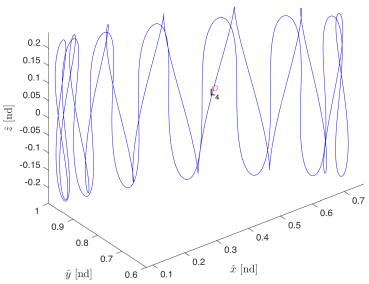

(a) Tadpole Family Member 64 (3D View)

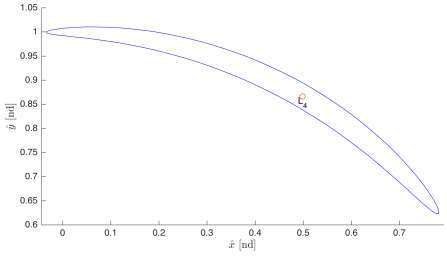

(b) Tadpole Family Member 64 ($\hat{x} - \hat{y}$ Plane)

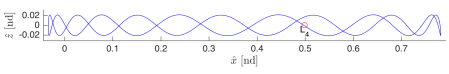

(c) Tadpole Family Member 64 ($\hat{x} - \hat{z}$ Plane)

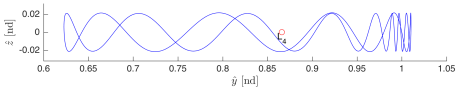

(d) Tadpole Family Member 64 ($\hat{y} - \hat{z}$ Plane)

Figure 4.37. L_4 Tadpole Family Member 64

4.2.3 Tadpole Orbits in High Mass Ratio Systems

Using different strategies, it is possible to compute tadpole orbits in different systems. For systems with a low enough mass ratio, finding these orbits is easier because the liner approximation of the motion can provide useful information used to find periodic solutions in the nonlinear system. As the mass ratio is increased, the assumptions used in the linear approximation are violated. Because periodic tadpole orbits can be obtained in systems with small mass ratios, it is possible to use these solutions as an initial guess in a continuation scheme where the mass ratio μ is increased. A set of these planar periodic solutions for a range of mass ratio is computed, with the first orbit computed in the Saturn-Titan system. Twelve of these orbits are plotted in Figure 4.38, with the initial conditions for each orbit listed in Table 4.8. It is important to note that the Lagrange point locations will slightly change as the mass ratio increases, and they are plotted where they reside in the Saturn-Titan in Figure 4.38.

The first tadpole orbit computed in the μ-continuation scheme can be seen in Figure 4.39, and it is the orbit with the smallest mass ratio (equal to that of the Saturn-Titan system) that is computed in this set. The orbit begins near L_4 with small velocity components in both the $\hat{x}$ and $\hat{y}$ directions. Because the Jacobi constant is slightly less than that of the triangular points, the motion is not bounded by a ZVC in the plane. The small loops indicative of the short period epicyclic motion are apparent, and the motion along these loops moves in a clockwise direction around the triangular point.

As the mass ratio increases, the orbit becomes more asymmetric and extends further toward L_3. This orbit in Figure 4.40 is still stable and the period and Jacobi constant remain nearly the same as the first orbit.

In Figure 4.41, the orbit is now slightly unstable and the motion extends even closer to L_3. The period is maintained and the looping structure is still very similar to the orbit in Figure 4.40.

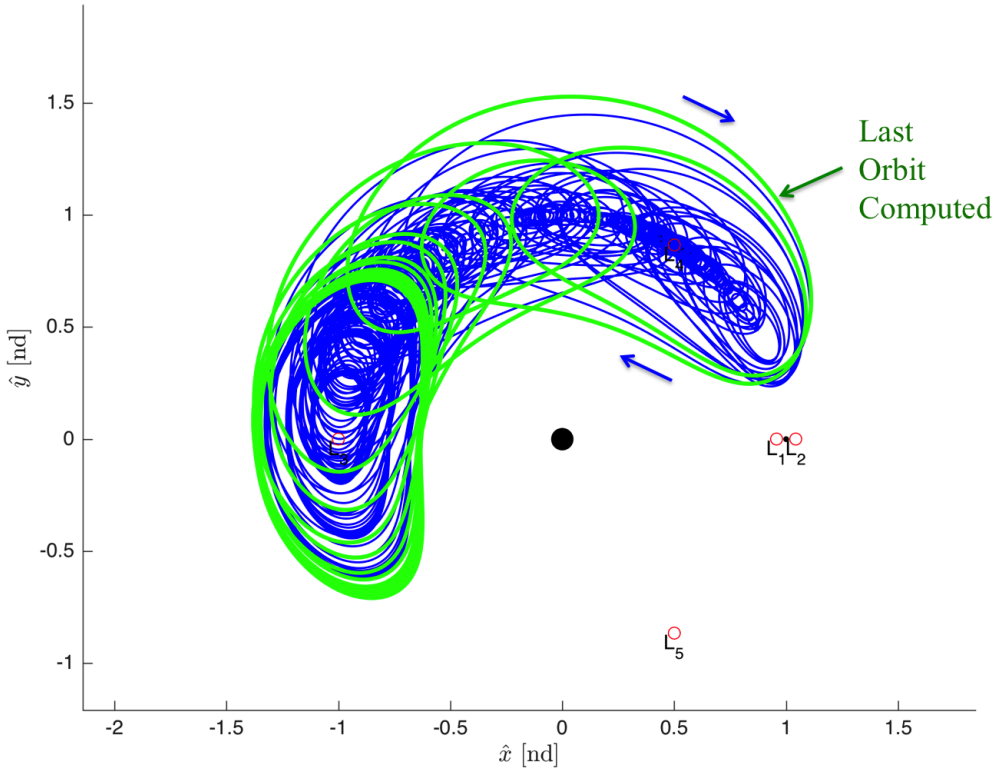

Figure 4.38. Planar L_4 Tadpole Orbit Continuation in Mass Ratio (Rotating Frame)

The instability significantly increases for the orbit plotted in Figure 4.42, and the orbit now extends past L_3. This type of motion violates the classical definition of a tadpole orbit due to both the instability and large variation from the triangular point. The period is maintained, and the Jacobi constant remains close to that of the first orbit computed.

The orbit in Figure 4.43 is the final solution computed using mass ratio continuation. Although more orbits could be computed for an increasing mass ratio, the initial conditions become more sensitive such that converging to a solution is more trivial. In addition, the instability is now so large and expected to continue increas-

Table 4.8. L_4 Tadpole Orbit Continuation in Mass Ratio

Orbit	x_0 (nd)	y_0 (nd)	$\dot{x}_0$ (nd)	$\dot{y}_0$ (nd)	P (nd)	C	ν	μ
1	0.5036	0.8660	-0.0026	-0.0104	157.21	2.9997	1.0000	2.37×10^{-4}
2	0.5582	0.8660	0.0351	-0.0523	157.21	2.9985	1.0000	2.40×10^{-4}
3	0.5577	0.8660	0.0418	-0.0381	157.22	2.9992	1.0000	2.45×10^{-4}
4	0.5945	0.8660	0.0733	-0.0560	157.24	2.9987	1.0000	2.69×10^{-4}
5	0.5332	0.8660	0.0172	-0.0155	157.29	3.0000	1.0002	3.27×10^{-4}
6	0.4298	0.8660	-0.0912	-0.0063	157.33	2.9946	1.1532	4.02×10^{-4}
7	0.2329	0.8660	-0.2371	-0.0231	157.34	2.9770	10.083	5.30×10^{-4}
8	-0.0861	0.8660	-0.2696	-0.1234	157.38	2.9670	328.36	9.01×10^{-4}
9	-0.4422	0.8660	-0.0127	-0.1253	157.49	2.9866	6968.1	1.70×10^{-4}
10	-0.6095	0.8660	0.2259	-0.1034	157.39	2.9490	5.88×10^{5}	2.94×10^{-3}
11	-0.6397	0.8660	0.3254	-0.1273	157.22	2.8959	2.21×10^{7}	4.58×10^{-3}
12	-0.6731	0.8660	0.3922	-0.1131	157.06	2.8615	4.16×10^{8}	6.40×10^{-3}

ing. Orbits that are this unstable would not be useful in a mission design scenario, as small perturbations would cause the motion to diverge rapidly from the periodic orbit. The period is still maintained, indicating that the same type of librational motion is maintained across all the orbits. In the Saturn-Titan system, the time is nearly equivalent to the long period linear motion; however, this time will vary for different systems. As a result, it is expected that by increasing the mass ratio, true stable tadpole orbits will not be computed using this method if the period remains nearly the same.

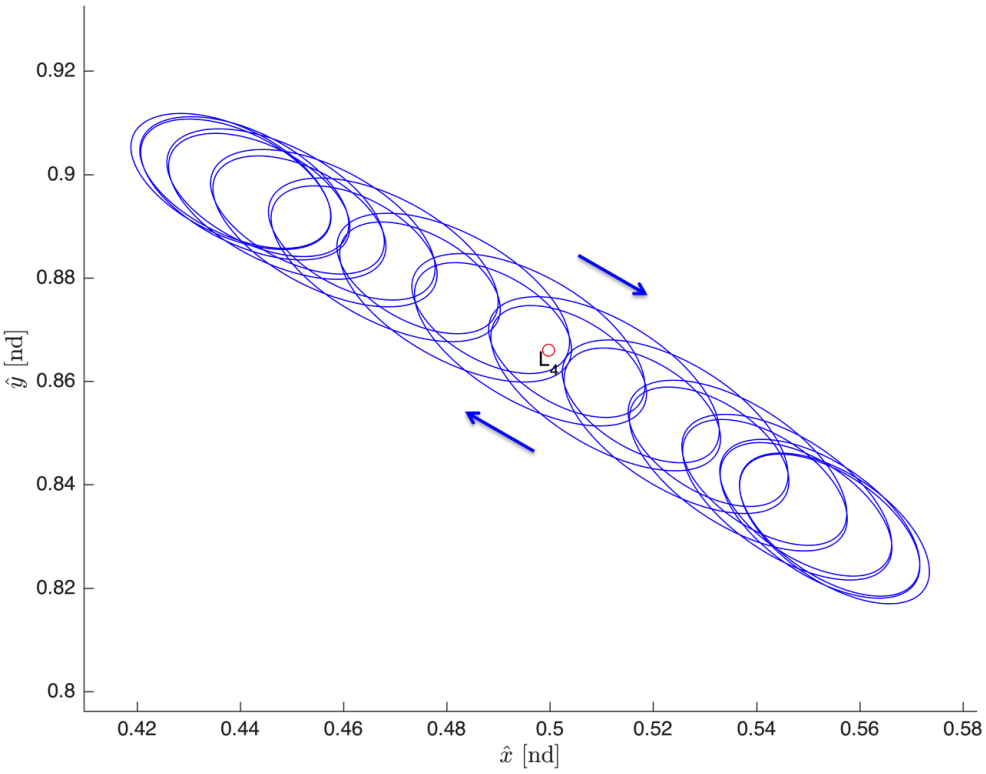

Figure 4.39. L_4 Tadpole Continuation in Mass Ratio Orbit 1

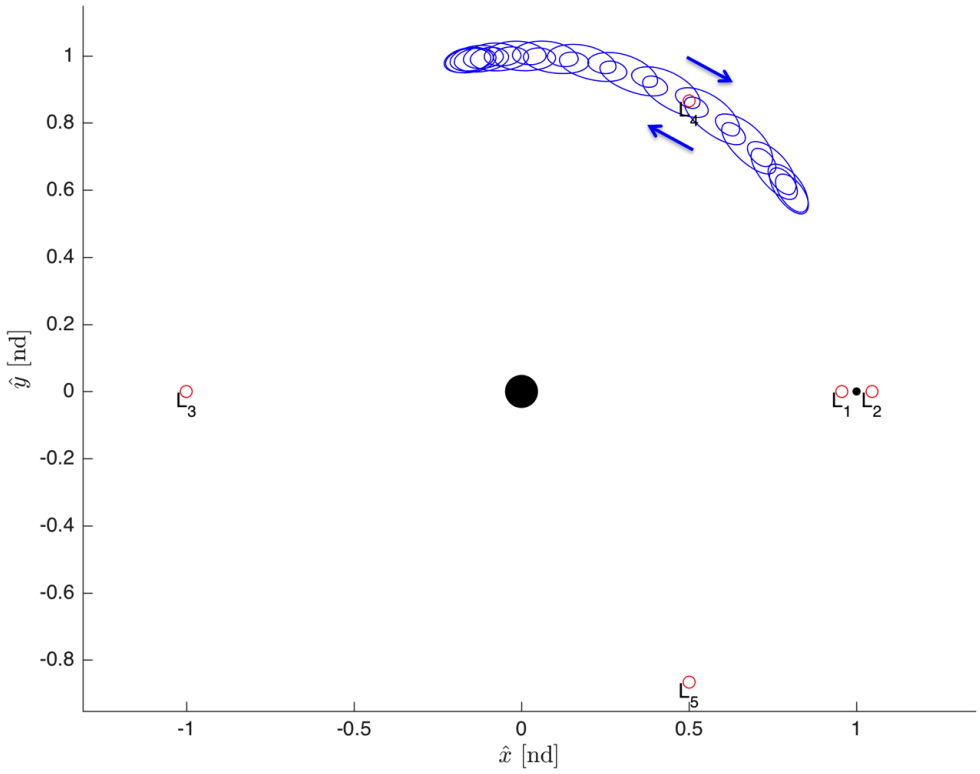

Figure 4.40. L_4 Tadpole Continuation in Mass Ratio Orbit 4

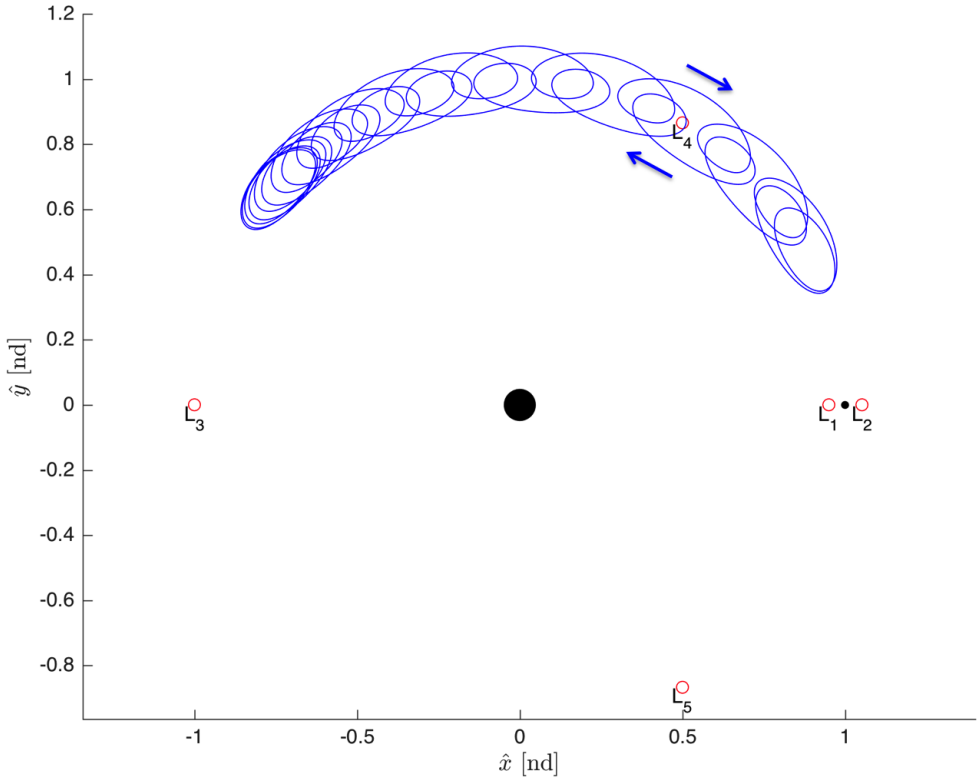

Figure 4.41. L_4 Tadpole Continuation in Mass Ratio Orbit 6

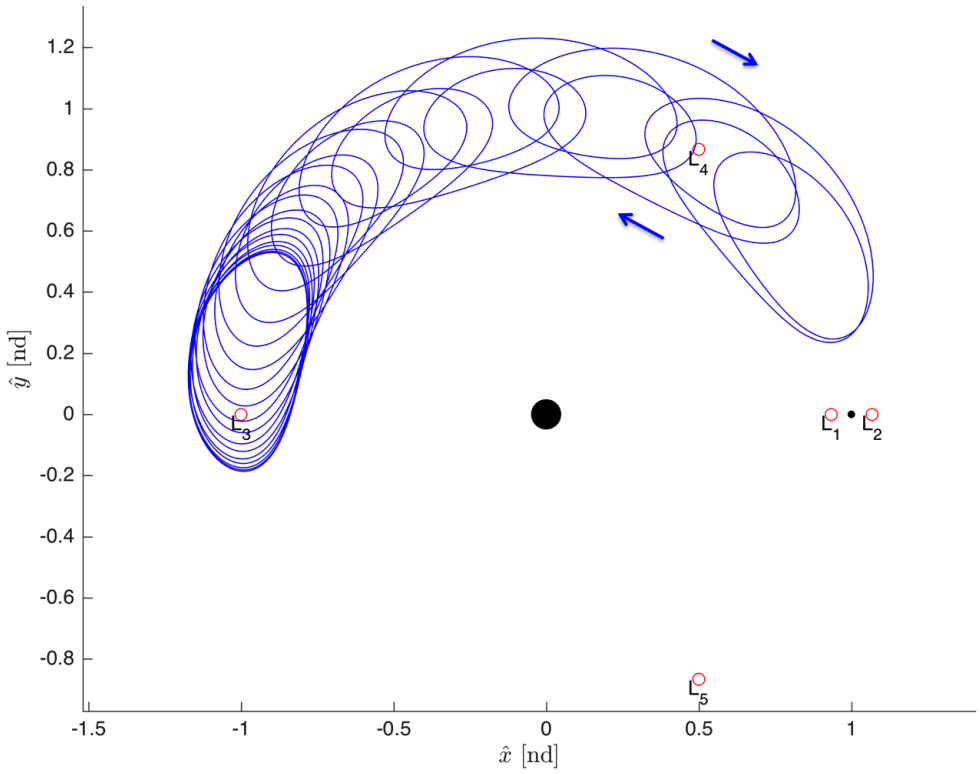

Figure 4.42. L_4 Tadpole Continuation in Mass Ratio Orbit 8

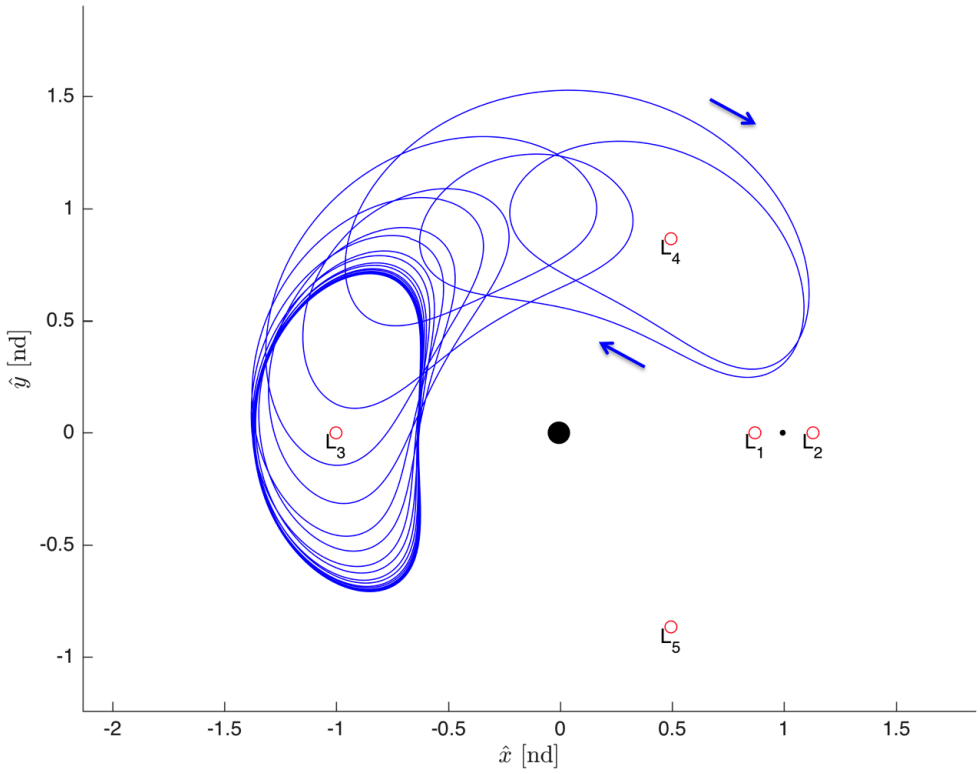

Figure 4.43. L_4 Tadpole Continuation in Mass Ratio Orbit 12

5. Trajectory Design Incorporating Dynamics Related to Tadpole Orbits

5.1 Dynamics of Related Orbits

Investigating other periodic orbits related to tadpole orbits provides a better understanding of tadpole motion. Some periodic orbits are directly related with motion representative of the frequencies observed in tadpole motion. By considering the dynamical structures associated with these periodic solutions, the natural flow can be leveraged to provide low-cost transfer trajectories.

5.1.1 Long and Short Period Triangular Point Orbits

Tadpole orbits combine a long period librational and short period epicyclic motion. The long and short period motion in the nonlinear system can be approximated by the linear motion, and these frequencies appear in the associated tadpole orbits. By investigating the families of long and short period orbits, insight about tadpole orbits can be gained. Although the evolution of these families is well known in the Earth-Moon system, less information is known for other systems including the Saturn-Titan system. Periodic long and short periodic orbits in the Saturn-Titan system can be obtained by using a linear approximation of the motion for a small displacement from the triangular point. Subsequent family members can then be computed by using pseudo-arclength continuation, which is desirable due to the asymmetry of these orbits.

Saturn-Titan L_4 Short Period Family

The following family of 1000 planar periodic L_4 short period orbits is computed in the Saturn-Titan system, beginning with a small orbit orbit from the linear approximation of the motion.

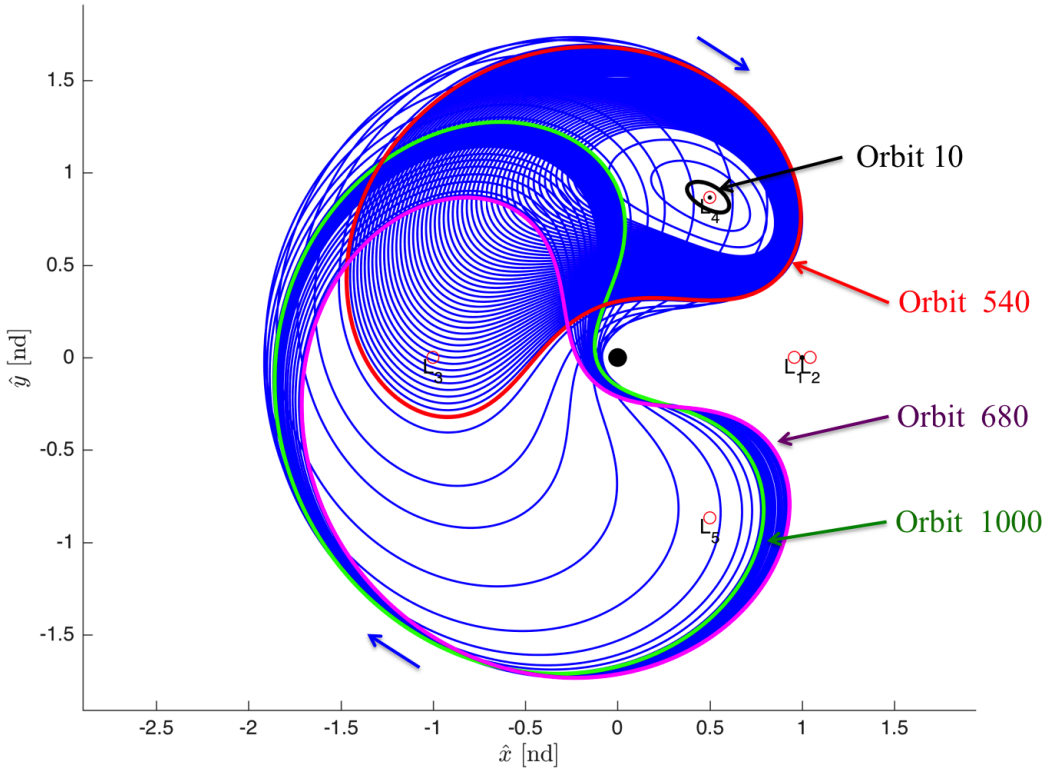

Figure 5.1. L_4 Short Period Family in Saturn-Titan System (Rotating Frame)

In Figure 5.1, every tenth computed orbit is plotted. The family begins with a small elliptical motion around L_4 and continues to move towards L_3, until this collinear point is contained in the orbit. As the family continues to evolve, the motion no longer contains L_4 and only moves around the collinear point and L_5, indicating that the L_4 and L_5 short period family are likely related. The evolution of the period and

Jacobi constant across the family is depicted in Figure 5.2. The stability index for all pairs of eigenvalues $\nu = 1$ for all members across the family, indicating that the short period orbits in the Saturn-Titan system are stable. As a result, these orbits will have no invariant manifolds as they do not contain a stable/unstable subspace. The first and last orbits computed are not necessarily the limiting boundaries of the family; however, this set of solutions gives insight into how the family evolves with orbits spanning a large range of Jacobi constant.

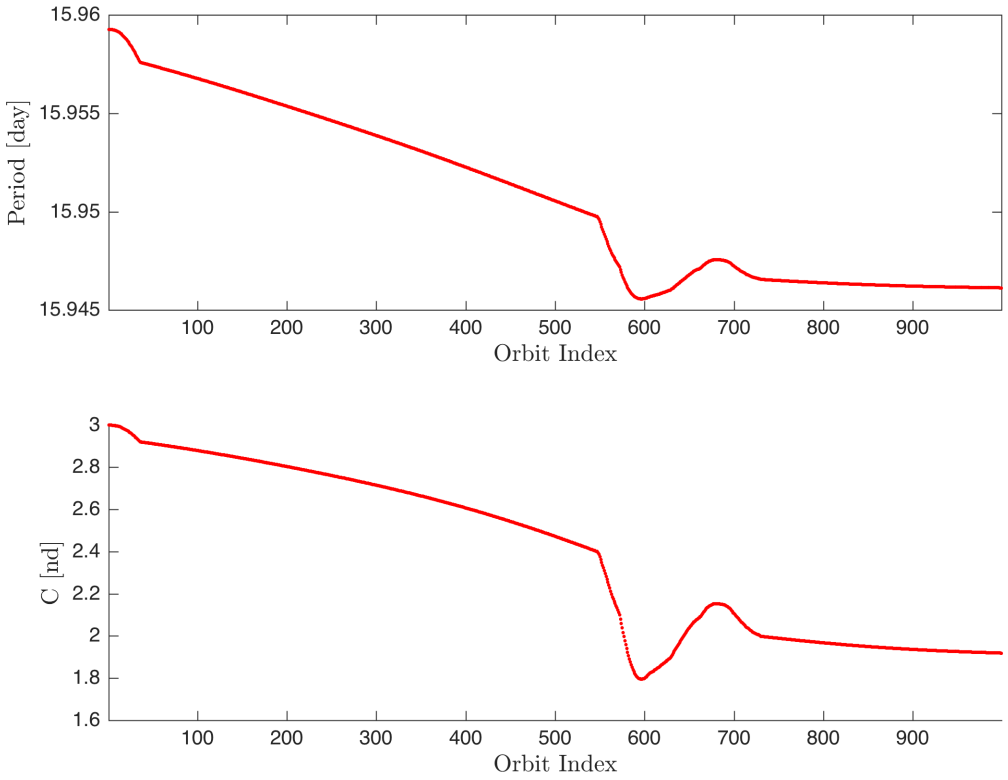

Figure 5.2. L_4 Short Period Family Characteristics

Saturn-Titan L_4 Long Period Family

The following family of 535 planar periodic L_4 long period orbits is computed in the Saturn-Titan system, beginning with a small orbit orbit from the linear approximation of the motion.

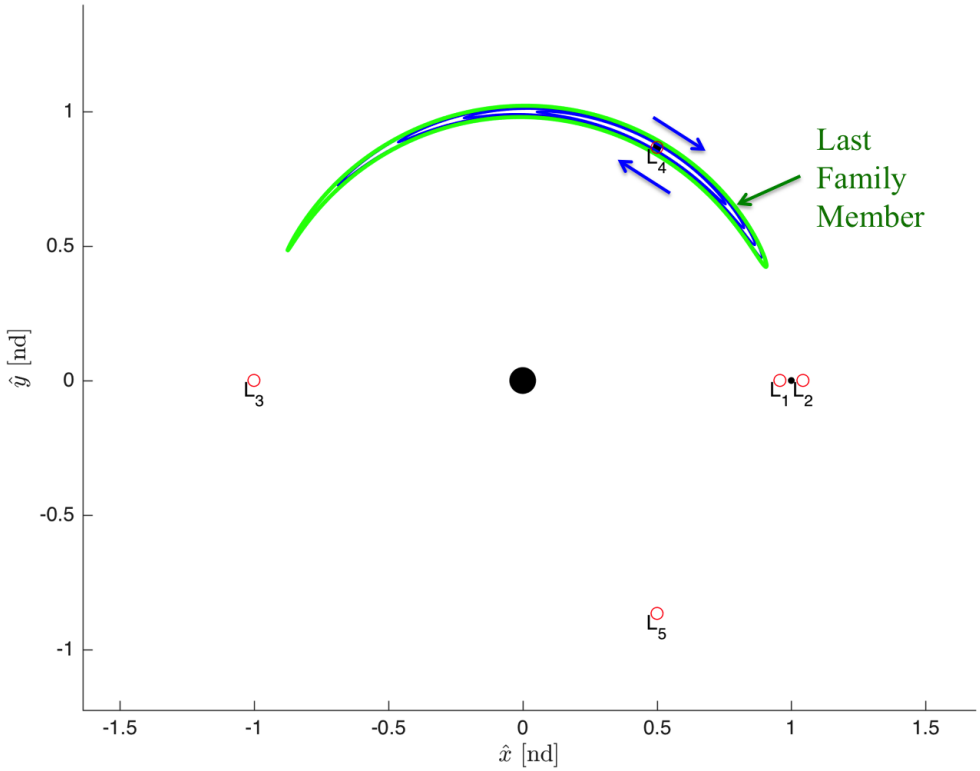

Figure 5.3. L_4 Long Period Family in Saturn-Titan System (Rotating Frame)

In Figure 5.3, every hundredth family member is plotted. The family begins with an elliptical motion around L_4 with a large amplitude along its long axis and a very small width. As the family continues to evolve, the orbits extend towards L_3, similar to that of the tadpole family. The evolution of the period and Jacobi constant across the family is depicted in Figure 5.4. The Jacobi constant remains slightly above that

of L_4, indicating that the in-plane motion is bounded by a zero-velocity curve at this energy level. The stability index for all pairs of eigenvalues $\nu = 1$ for all members across the family, indicating that the long period orbits in the Saturn-Titan system are stable. As a result, these orbits will have no invariant manifolds as they do not contain a stable/unstable subspace.

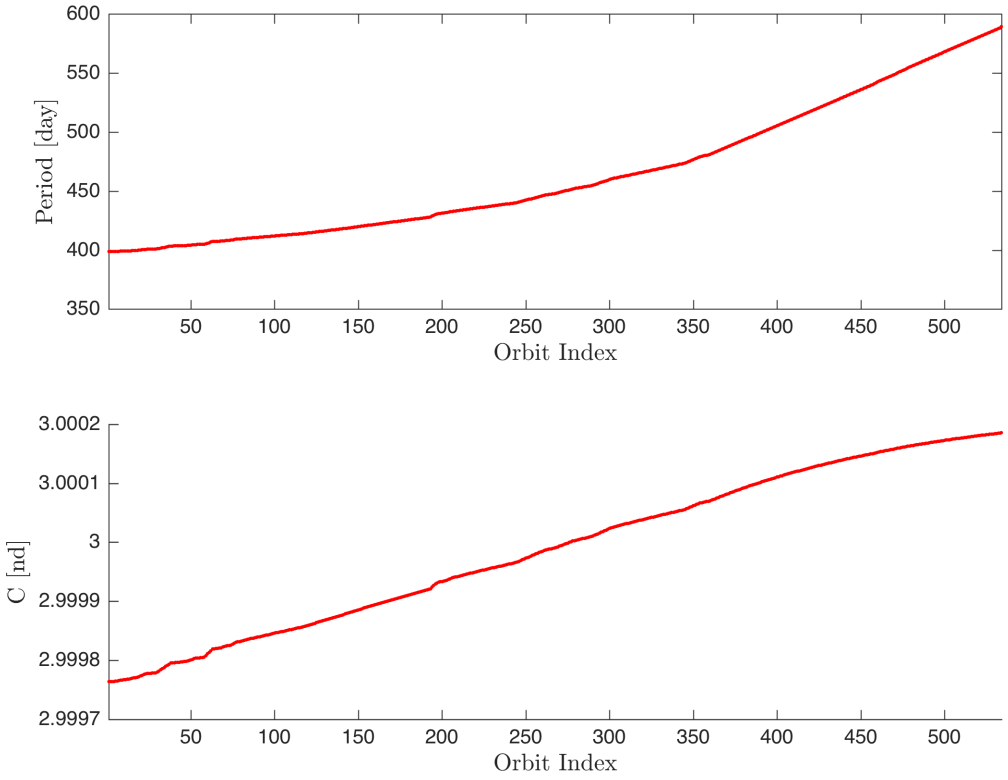

Figure 5.4. L_4 Long Period Family Characteristics

5.1.2 L_3 Lyapunov Orbits

The L_3 Lyapunov orbits can be related to the motion of tadpole orbits through its invariant manifolds. Because members of the L_3 Lyapunov orbit family are unstable

in the Saturn-Titan system, natural motion arrives and departs these orbits by means of their stable and unstable manifolds, respectively. In order to compare motion at the same energy level, orbits with a similar Jacobi constant must exist. Figure 5.6 shows the Jacobi constant of different members of L_3 Lyapunov and tadpole orbit family members. From this plot, it is apparent that a L_3 Lyapunov orbit with a matching Jacobi constant exists for all possible tadpole family members.

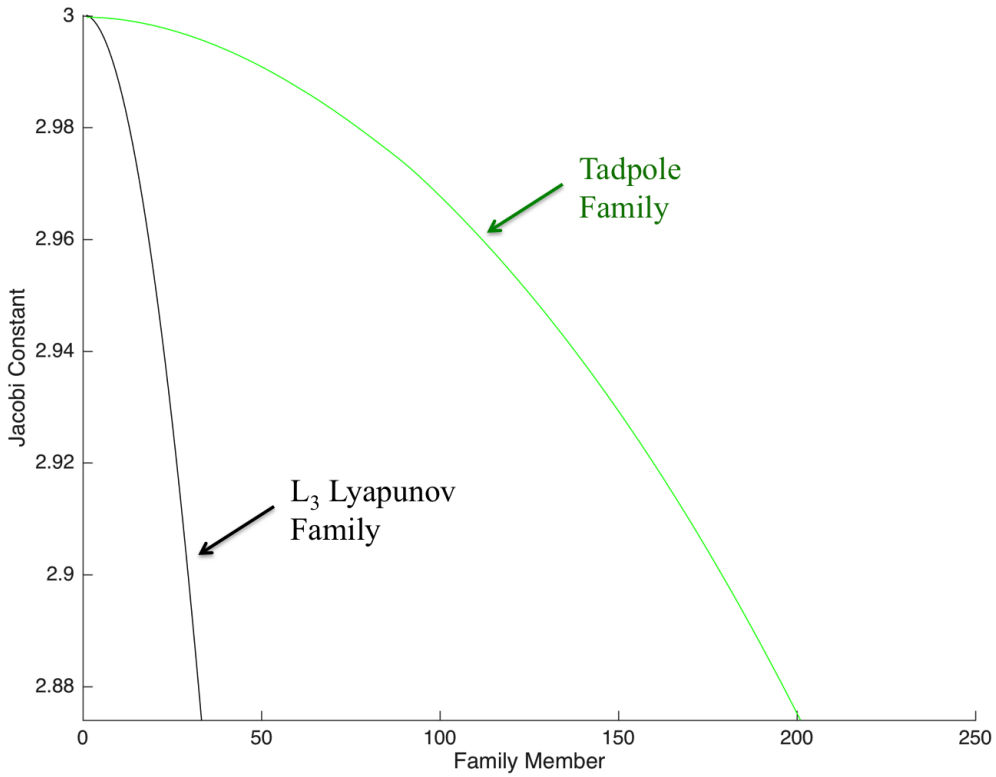

Figure 5.5. Tadpole and L_3 Lyapunov Family Jacobi Constant

Tadpole family member 152 is selected as it is large and extends closer to L_3 than some of the other family members. The L_3 Lyapunov family member with the closest Jacobi constant to this tadpole orbit is selected; however, an exact match in energy does not exist because of the step size used in computing the family members.

Because the behavior of the L_3 Lyapunov manifolds are of interest, an exact match for the two different types of orbits is actually not desirable. The invariant manifolds are approximated by taking a small step d off of the orbit in the direction of the stable/unstable eigenvectors, so the resulting trajectory will have a Jacobi constant that is slightly different than that of the originating Lyapunov orbit. Thus, a Lyapunov orbit with a Jacobi constant slightly different than that of the tadpole orbit is desired such that the step d can be selected such that the invariant manifold and tadpole orbit match in Jacobi constant. The nearest matching L_3 Lyapunov orbit is used as an initial guess in a Jacobi constant targeter such that the solution differs by 2×10^{-5} from the tadpole orbit. Table 5.1 shows the selected tadpole and L_3 Lyapunov orbit as well as characteristics defining these orbits. The resonance with the period of the Saturn-Titan system about its barycenter is also computed, where this value represents the number of the revolutions of the Saturn-Titan system during one period of the orbit.

Table 5.1. Selected Tadpole and L_3 Lyapunov Orbit

Orbit	Jacobi Constant (nd)	Period (day)	System Resonance	ν
Tadpole	2.927436457	398.95604852	25.01841888	1
L_3 Lyapunov	2.927456457	15.943335091	0.999801951	1.011644962

For the Lyapunov orbit, 200 manifold arcs are computed for each subset of stable manifolds W^{S^+}, W^{S^-} and unstable manifolds W^{U^+}, W^{U^-}. These manifolds are computed by selecting a different hyperplane Σ across the entire orbit, such that each of these fixed points are evenly distributed in time for one period of the orbit. The step d is computed such that the manifold and tadpole orbit match in Jacobi constant. If the step is more than 2000 km, the trajectory is discarded, because taking a step that is too large results in an inaccurate approximation of the invariant manifolds. The step must also be large enough so that the manifold departs the Lyapunov orbit in a reasonable amount of time due to the small stability index of the orbit. As an

additional consequence, these trajectories take a long time to reach the tadpole orbit so they are propagated for 60 revolutions of the Lyapunov orbit. In Figure 5.6, ten of the manifold trajectories in each subset of stable manifolds W^{S+}, W^{S-} and unstable manifolds W^{U+}, W^{U-} distributed across the orbit are plotted.

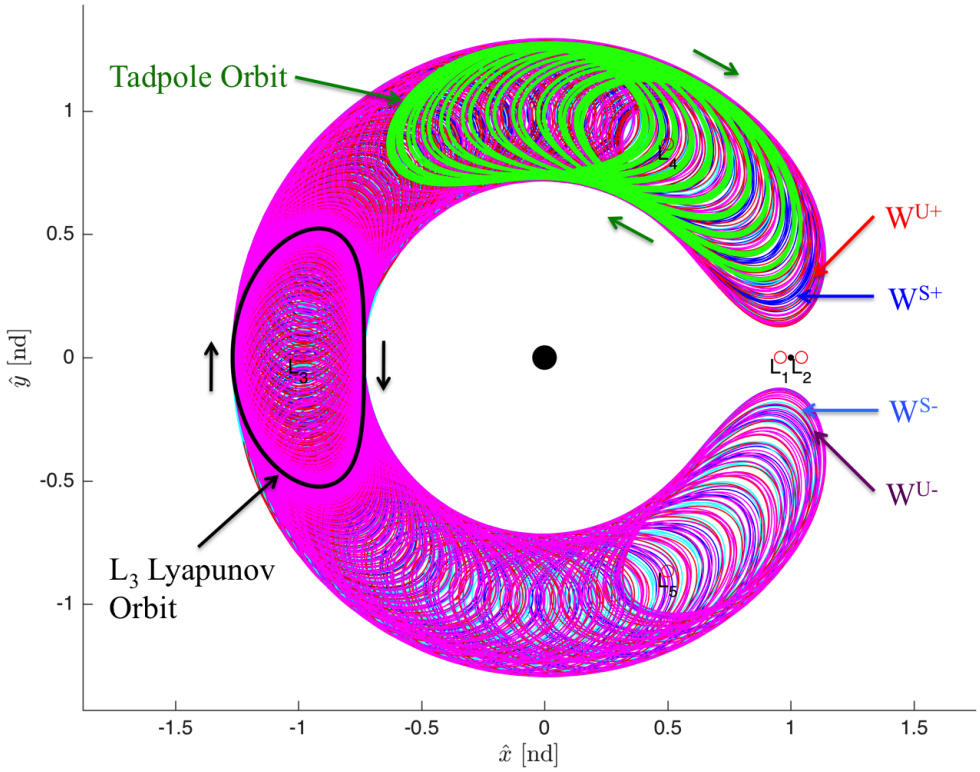

Figure 5.6. Tadpole and L_3 Lyapunov Orbit with Invariant Manifolds

From Figure 5.6, the manifold trajectories resemble the structure of a horseshoe orbit. Manifolds of each type extend towards L_4 and past the tadpole orbit. In addition, they also extend toward L_5 and would reach a mirror tadpole orbit around this triangular point. The relationship between all of the manifold arcs computed and the tadpole orbit is difficult to analyze due to the complex looping motion. The looping motion of both the tadpole orbit and L_3 Lyapunov orbit manifolds is also

advantageous because the trajectories change direction many times. A *loop map* can be investigated, similar to the method used by Oshima and Yanao [5]. The polar coordinates r and θ are computed each time the trajectory changes direction, when $\dot{\theta} = 0$. At each of these instances, points intersecting in position can be found, and the velocity difference between the manifolds and tadpole orbit can be approximated by only a change in $\dot{r}$. In Figure 5.7, the loop map is plotted for the L_3 Lyapunov manifolds and the tadpole orbit. Points corresponding to the condition $\dot{r} > 0$ are indicated by an asterisk and those for $\dot{r} < 0$ indicated by a triangle. It is important to differentiate these points because intersecting trajectories may be moving in opposite directions, resulting in a large velocity difference.

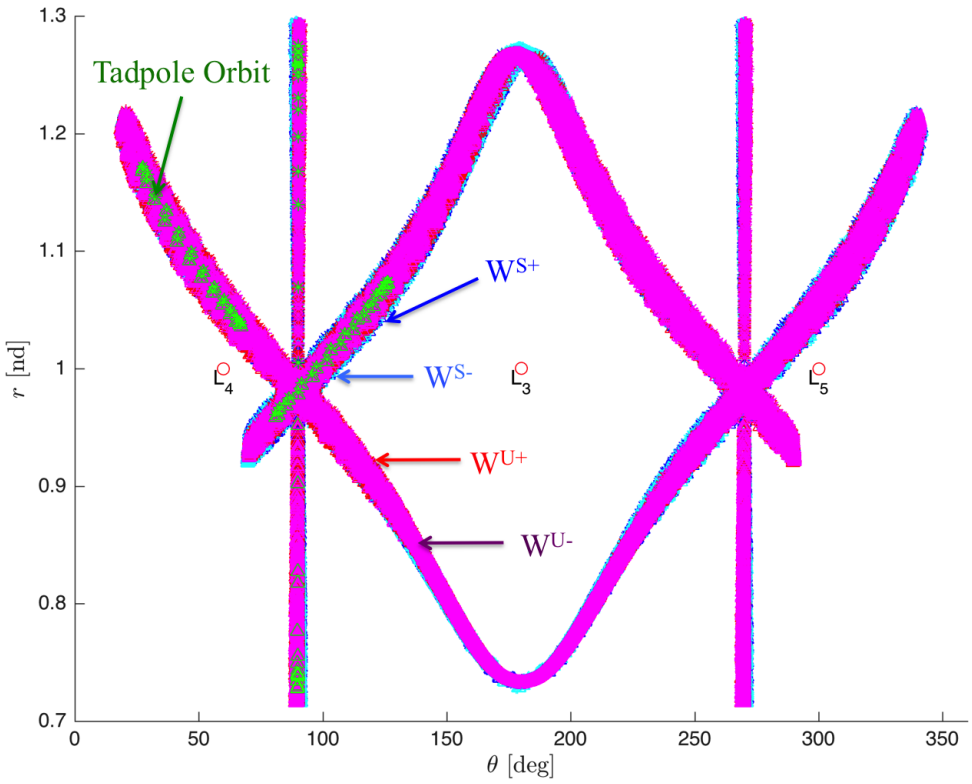

Figure 5.7. Tadpole and L_3 Lyapunov Orbit Manifolds Loop Map

In Figure 5.7, it is difficult to differentiate between the manifold map crossings due to the density of points on the map from the large amount of manifolds propagated. However, it is clear that the manifolds circulate around the triangular points and L_3, providing a network of options connecting these regions. In addition, the tadpole orbit clearly overlaps the region where some of the manifolds intersect the map. Because the region near L_4 is of interest for this example, a zoomed image is presented in Figure 5.8.

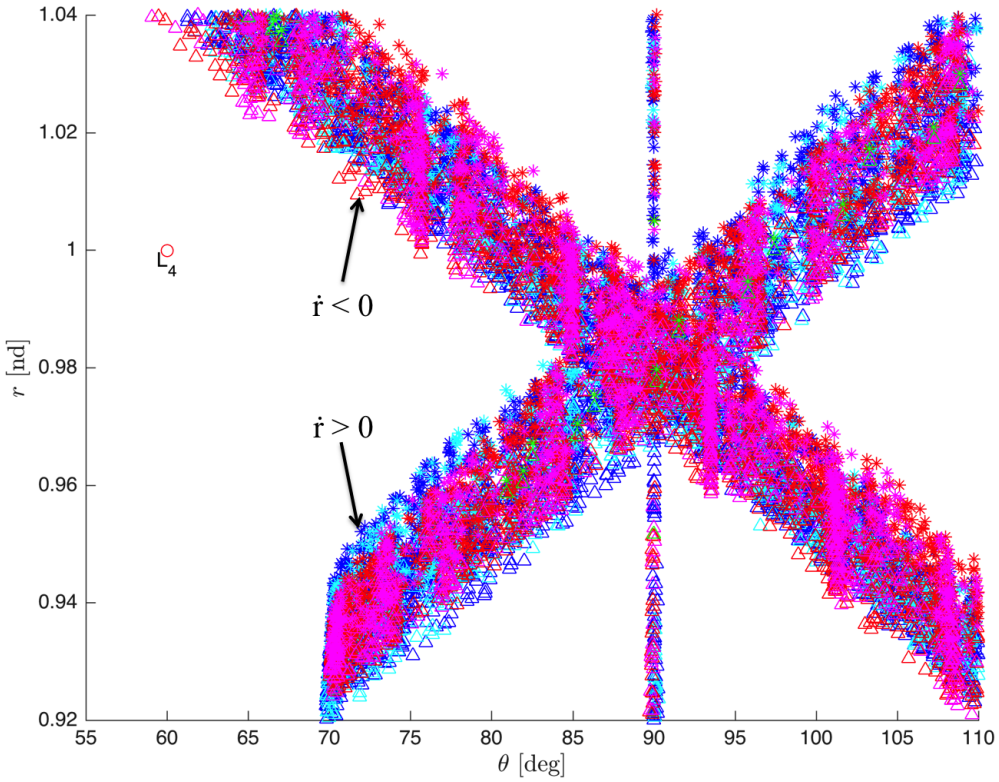

Figure 5.8. Tadpole and L_3 Lyapunov Orbit Manifolds Loop Map (Zoomed View)

5.1.3 Horseshoe Orbits

The horseshoe orbit can be related to the motion of tadpole orbits through its invariant manifolds, because members of the horseshoe orbit family are unstable in the Saturn-Titan system. Figure 5.10 shows the Jacobi constant of different members of the horseshoe and tadpole orbit family members. From this plot, it is apparent that a horseshoe orbit with a matching Jacobi constant exists for all possible tadpole family members.

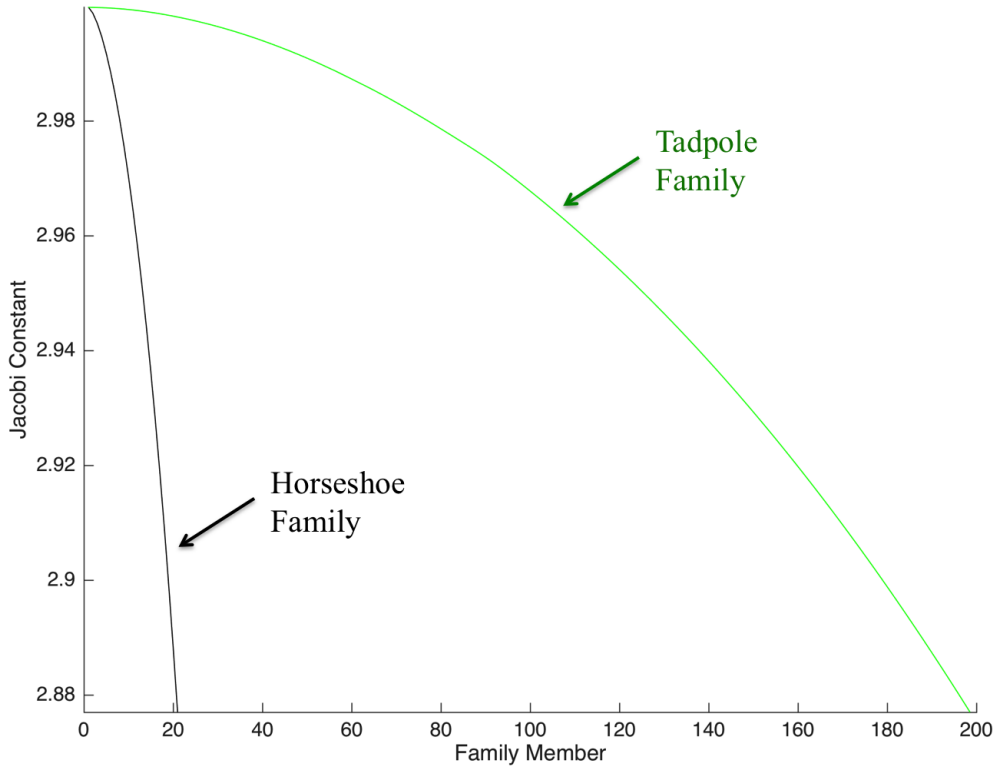

Figure 5.9. Tadpole and Horseshoe Orbit Family Jacobi Constant

Tadpole family member 152 is selected so that the same orbit is used as the one in the L_3 Lyapunov orbit example. The horseshoe orbit family member with the closest

Jacobi constant to this tadpole orbit is selected. This solution is used as an initial guess in a Jacobi constant targeter such that the solution differs by 2×10^{-6} from the tadpole orbit. This orbit is offset by a smaller difference in Jacobi constant than the L_3 Lyapunov orbit example because the stability index is much higher. As a result, the required step-off distance to depart the orbit will be smaller which corresponds to a smaller change in Jacobi constant. Due to the long orbital period and complexity of the horseshoe orbit, a continuation scheme is required to find this orbit even though the Jacobi constant is only changed slightly. Table 5.2 shows the selected tadpole and horseshoe orbit as well as characteristics defining these orbits.

Table 5.2. Selected Tadpole and Horseshoe Orbit

Orbit	Jacobi Constant (nd)	Period (day)	System Resonance	ν
Tadpole	2.927436457	398.95604852	25.01841888	1
Horseshoe	2.927438457	973.51183884	61.04864698	453.6270387

For the horseshoe orbit, 75 manifold arcs are computed for each of the subsets of stable manifolds W^{S^+}, W^{S^-} and unstable manifolds W^{U^+}, W^{U^-}. Fewer arcs are computed than the L_3 Lyapunov orbit example due to the much longer period of these orbits which is computationally expensive. These manifolds are computed by selecting a different hyperplane Σ across the entire orbit, such that each of these fixed points are evenly distributed in time for one period of the orbit. The step d is computed such that the manifold and tadpole orbit match in Jacobi constant, and the trajectory is discarded if the step is more than 2000 km. These manifolds arcs are propagated for 3 revolutions of the horseshoe orbit; however, propagation is stopped when the trajectories move far away from the system. In Figure 5.10, ten manifold arcs in each of the subsets of stable manifolds W^{S^+}, W^{S^-} and unstable manifolds W^{U^+}, W^{U^-} distributed across the orbit are plotted.

From Figure 5.10, most of the manifold trajectories maintain the structure of the originating horseshoe orbit. The relationship between all of the manifolds computed

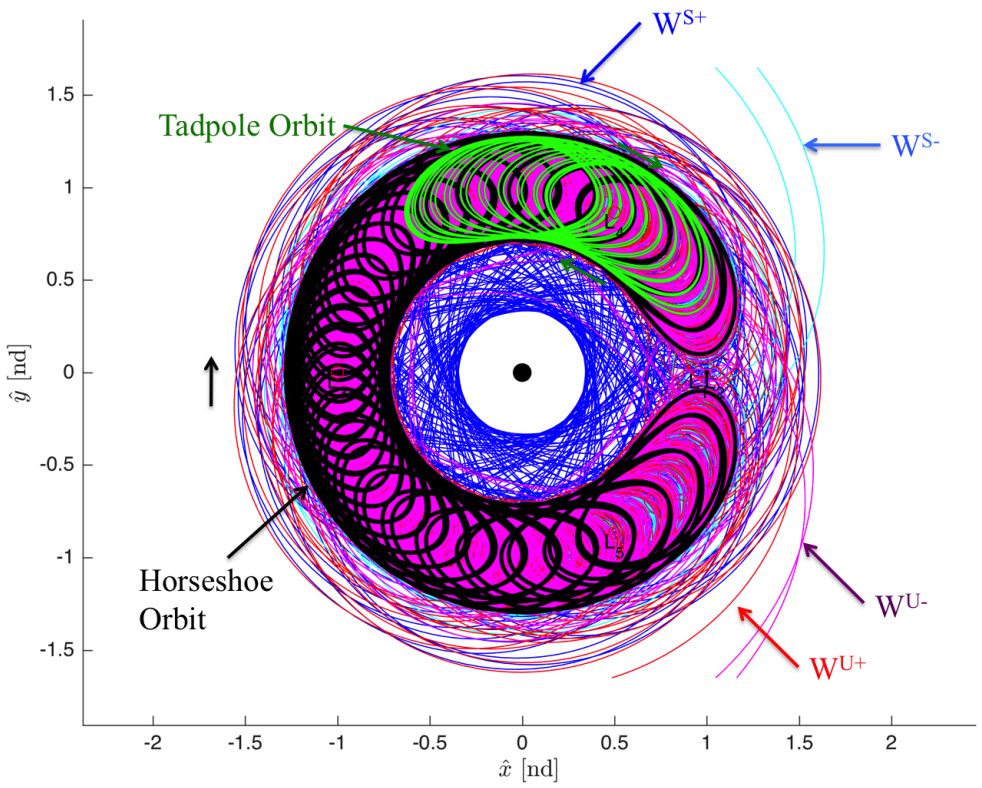

Figure 5.10. Tadpole and Horseshoe Orbit with Invariant Manifolds

and the tadpole orbit is difficult to analyze due to the complex looping motion, so a loop map is generated again, where r and θ are computed each time the trajectory changes direction, when $\dot{\theta} = 0$. In Figure 5.11, the loop map is plotted for the horseshoe manifold arcs and the tadpole orbit. Points corresponding to the condition $\dot{r} > 0$ are indicated by an asterisk and those for $\dot{r} < 0$ indicated by a triangle.

The manifolds circulate around the triangular points and L_3, providing a network of options connecting these regions. These manifold map intersections also pass much closer to the collinear point than those associated with the L_3 Lyapunov orbit, despite the resemblance of the motion for these manifolds. The tadpole orbit clearly overlaps

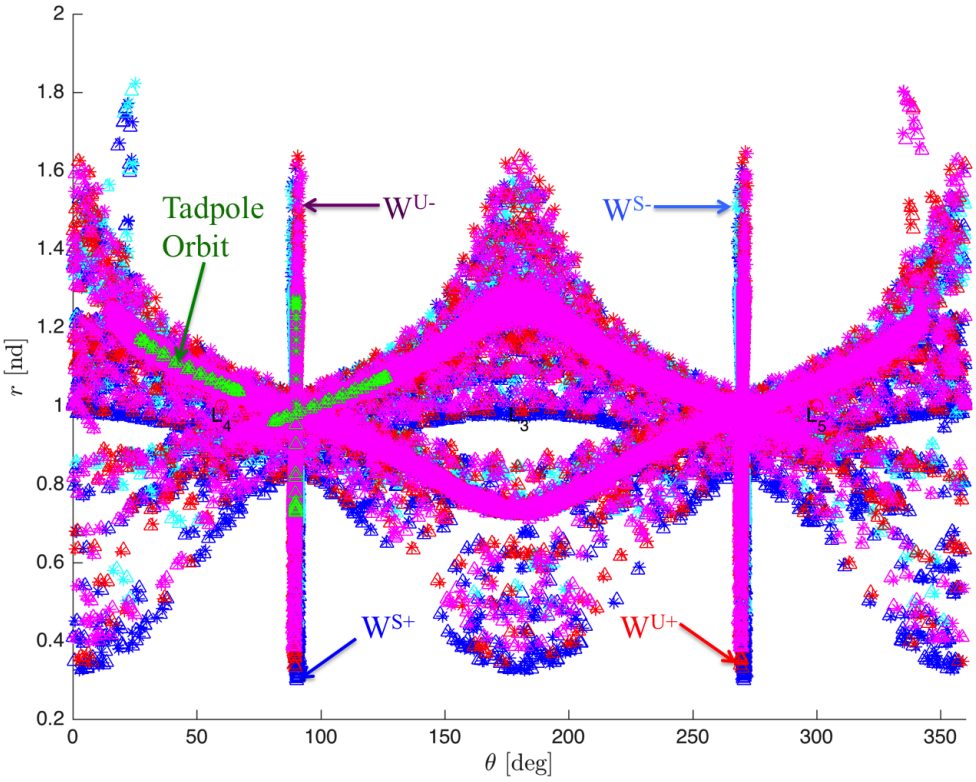

Figure 5.11. Tadpole and Horseshoe Orbit Manifolds Loop Map

the region where some of the manifold trajectories intersect the map, and a zoomed image is presented in Figure 5.12.

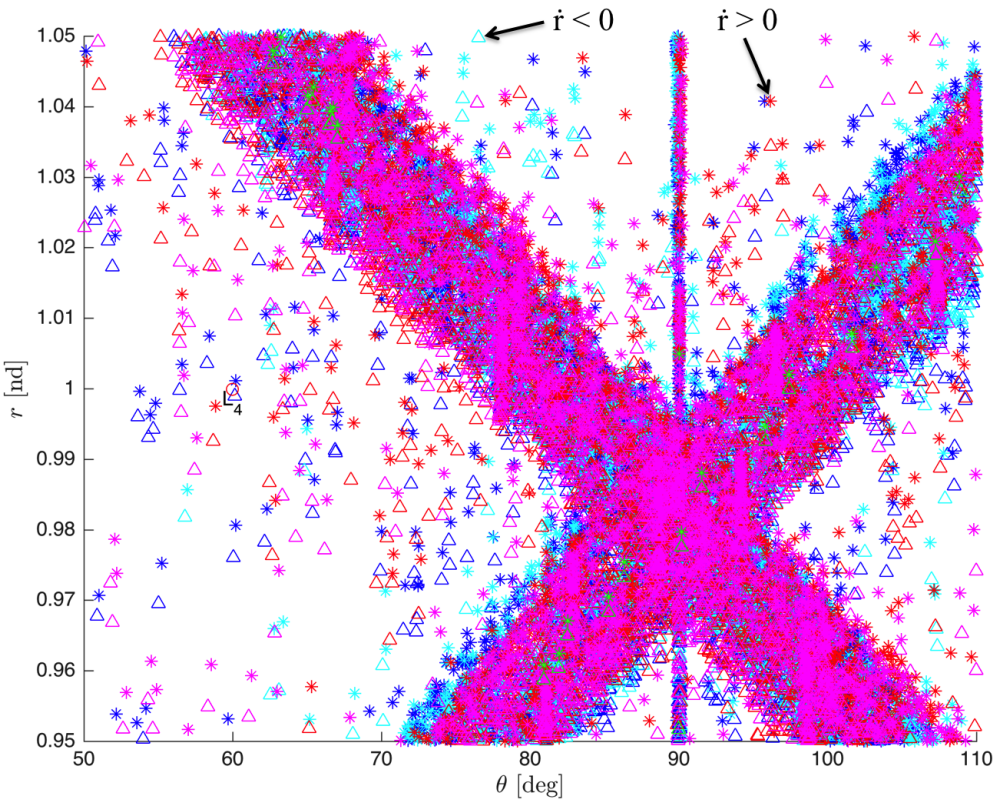

Figure 5.12. Tadpole and Horseshoe Orbit Manifolds Loop Map (Zoomed View)

5.1.4 Planar Resonant Orbits

Different type of planar resonant orbits can be related to the motion of tadpole orbits. Resonant orbits can be computed using the methods developed by Vaquero [30]. Although the mass ratio of the Saturn-Titan system is relatively small, it is large enough such that it can be difficult to find periodic solutions by supplying an initial guess from the two-body problem. Ephemeris data from Hyperion's orbit is used and corrected in the three-body problem to generate a 3:4 resonant orbit. This orbit completes approximately three periods of motion for every four revolutions of the Saturn-Titan system about its barycenter. Following, a family of 3:4 resonant orbits is computed using pseudo-arclength continuation. Because members of this resonant orbit family are unstable in the Saturn-Titan system, stable and unstable manifolds exist. Figure 5.14 shows the Jacobi constant of different members of the 3:4 resonant and tadpole orbit family members. From this plot, it is apparent that multiple resonant orbits with a matching Jacobi constant exists for all possible tadpole family members.

Tadpole family member 152 is selected so that the same orbit is used as the one in the L_3 Lyapunov and horseshoe orbit examples. The 3:4 resonant orbit family member with the closest Jacobi constant to this tadpole orbit is selected. This orbit is used as an initial guess in a Jacobi constant targeter such that the solution differs by 2×10^{-6} from the tadpole orbit, and a solution can be directly computed without a continuation method because the motion is much simpler than that of the horseshoe orbit. Table 5.3 shows the selected tadpole and 3:4 resonant orbit as well as characteristics defining these orbits.

Table 5.3. Selected Tadpole and 3:4 Resonant Orbit

Orbit	Jacobi Constant (nd)	Period (day)	System Resonance	ν
Tadpole	2.927436457	398.95604852	25.01841888	1
3:4 Resonant	2.927438457	65.915239747	4.133525697	7194.498955

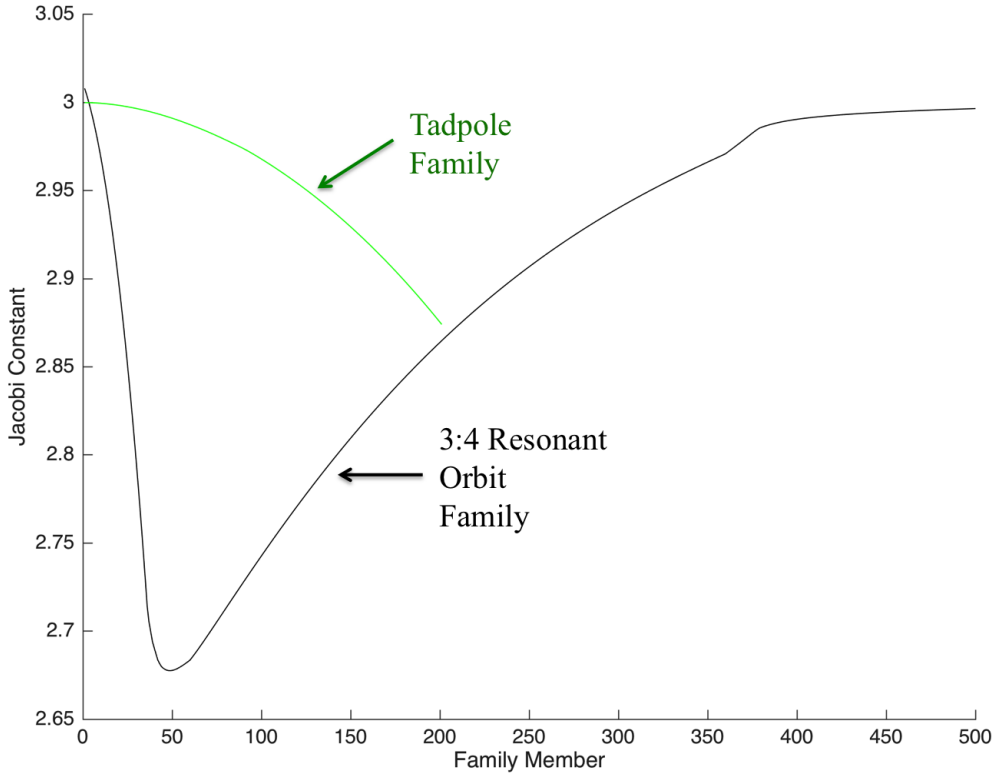

Figure 5.13. Tadpole and 3:4 Resonant Orbit Family Jacobi Constant

For the 3:4 resonant orbit, 150 manifold arcs are computed for each of the subsets of stable manifolds W^{S^+}, W^{S^-} and unstable manifolds W^{U^+}, W^{U^-}. These manifolds are computed by selecting a different hyperplane Σ across the entire orbit, such that each of these fixed points are evenly distributed in time for one period of the orbit. The step d is computed such that the manifold and tadpole orbit match in Jacobi constant, the trajectory is discarded if the step is more than 2000 km. These manifold arcs are propagated for 30 revolutions of the resonant orbit; however, propagation is stopped when the trajectories move far away from the system. In Figure 5.14, ten manifold arcs for each of the subsets of stable manifolds W^{S^+}, W^{S^-} and unstable manifolds W^{U^+}, W^{U^-} distributed across the orbit are plotted.

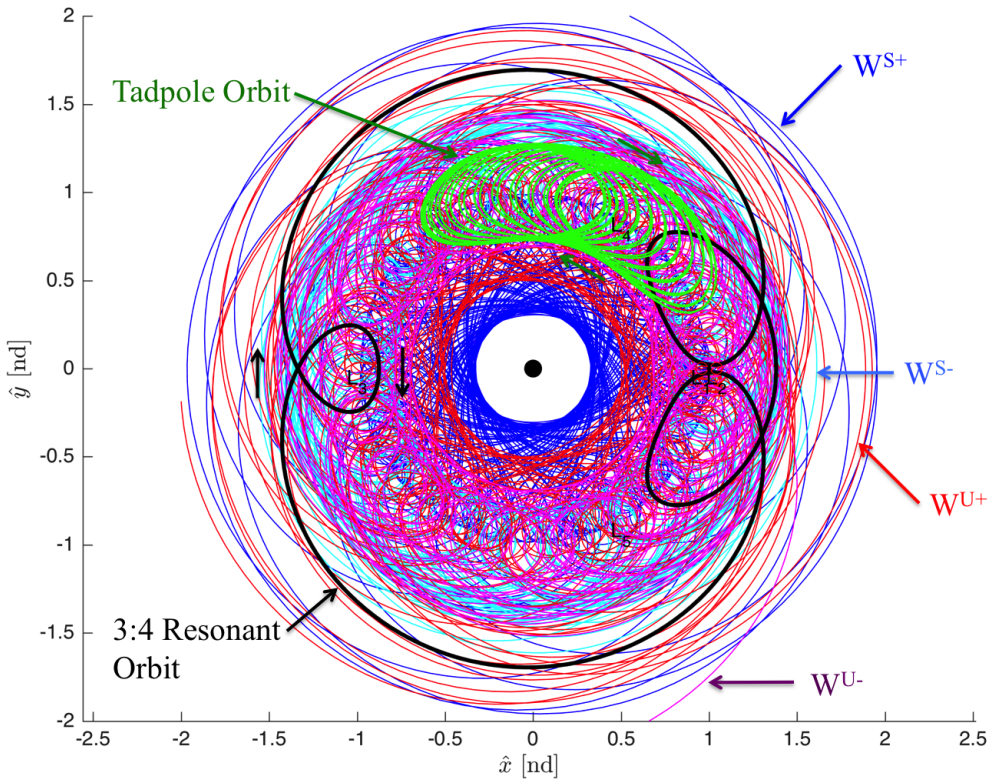

Figure 5.14. Tadpole and 3:4 Resonant Orbit with Invariant Manifolds

From Figure 5.14, the manifolds provide a variety of different trajectories, different than those computed for the L_3 Lyapunov and horseshoe orbits. A loop map is generated for these manifolds, where r and θ are computed each time the trajectory changes direction, when $\dot{\theta} = 0$. In Figure 5.15, the loop map is plotted for the 3:4 resonant orbit manifolds and the tadpole orbit. Points corresponding to the condition $\dot{r} > 0$ are indicated by an asterisk and those for $\dot{r} < 0$ indicated by a triangle.

The manifolds circulate around the triangular points and L_3, providing a network of options connecting these regions. These intersections densely populate the map, as a result of the variety of motion for the manifolds. The tadpole orbit clearly overlaps

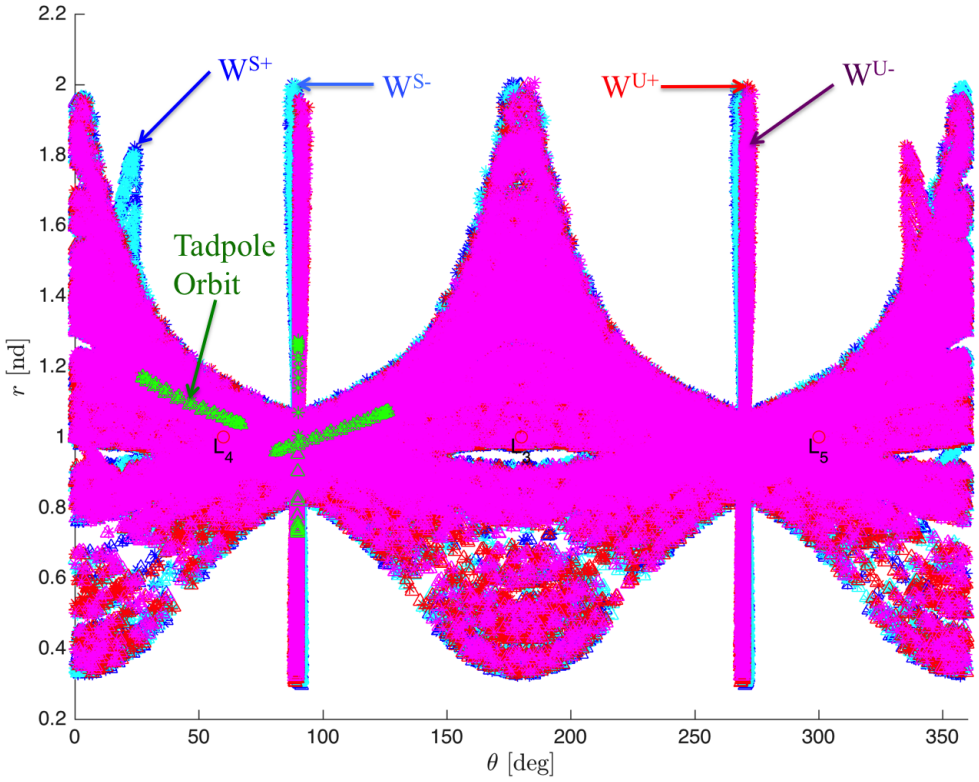

Figure 5.15. Tadpole and 3:4 Resonant Orbit Manifolds Loop Map

the region where some of the manifold arcs intersect the map, and a zoomed image is presented in Figure 5.16.

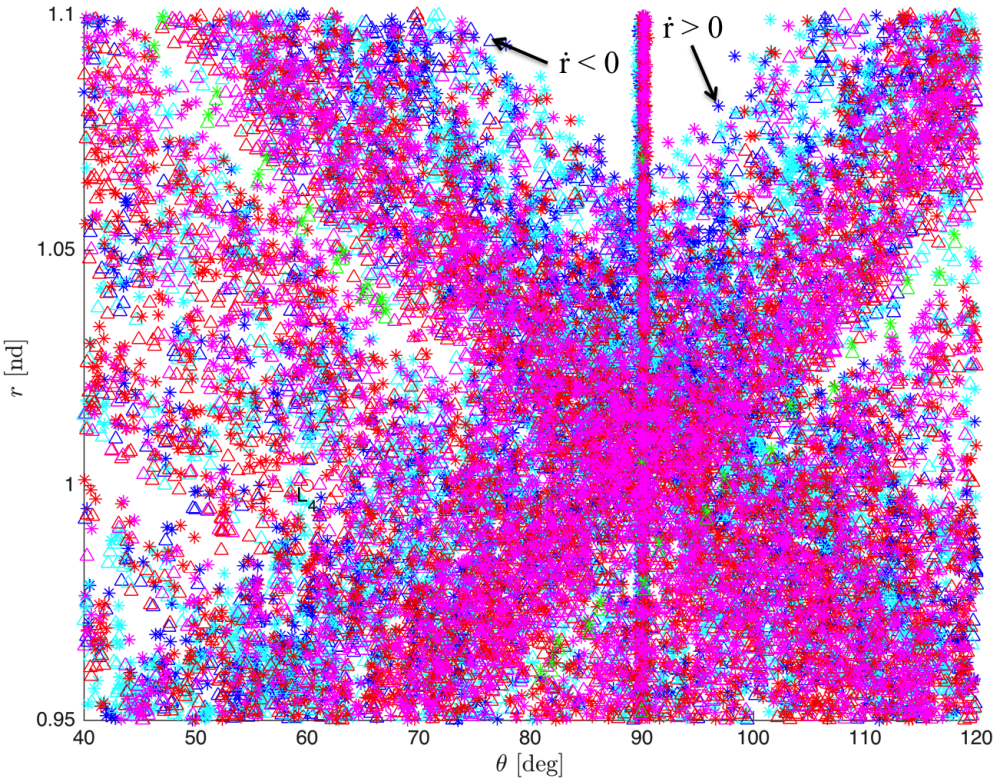

Figure 5.16. Tadpole and 3:4 Resonant Orbit Manifolds Loop Map (Zoomed View)

5.2 Natural Transfers to Tadpole Orbits in the Saturn-Titan System

Because the computed tadpole orbits are stable, natural motion will not arrive at or depart these orbits. In order to design low-cost transfer trajectories between tadpole and other orbits, the invariant manifolds of other unstable orbits may be used. A free heteroclinic connection will not be possible due to the stability of the tadpole orbits; however, low-cost transfers may be obtained. A subset of the stable manifolds W^{S^+}, W^{S^-} and unstable manifolds W^{U^+}, W^{U^-} with the same Jacobi constant as the tadpole orbit of interest can be propagated to see if any intersections in position exist. If intersections are found, an instantaneous ΔV maneuver can be applied to connect the tadpole orbit with a manifold arc.

5.2.1 Transfers to a L_4 Tadpole Orbit Using L_3 Lyapunov Orbit Unstable Manifolds

Transfers between tadpole orbits and unstable L_3 Lyapunov orbits can be designed by leveraging the stable and unstable manifolds associated with this orbit. By investigating the manifold arcs propagated previously, each of the intersections between these trajectories and the tadpole orbit can be found if they exist. Due to the complex looping motion of both the tadpole orbit and these manifolds, the states are converted to polar coordinates before computing the intersections. In Figure 5.17 an example of these intersections with the position expressed in polar coordinates is shown.

The velocity difference at these intersections can then be computed to determine the location along each manifold trajectory with the smallest required ΔV maneuver to insert in to the tadpole orbit. Because transfers to tadpole orbits are of interest in this section, intersections with the subset of unstable manifold arcs W^{U^+}, W^{U^-} are computed. These trajectories are assumed to depart the L_3 Lyapunov orbit for free, although they are a numerical approximation. For each of these manifolds arcs, the intersection with the smallest velocity difference is selected. Figures 5.18 - 5.19

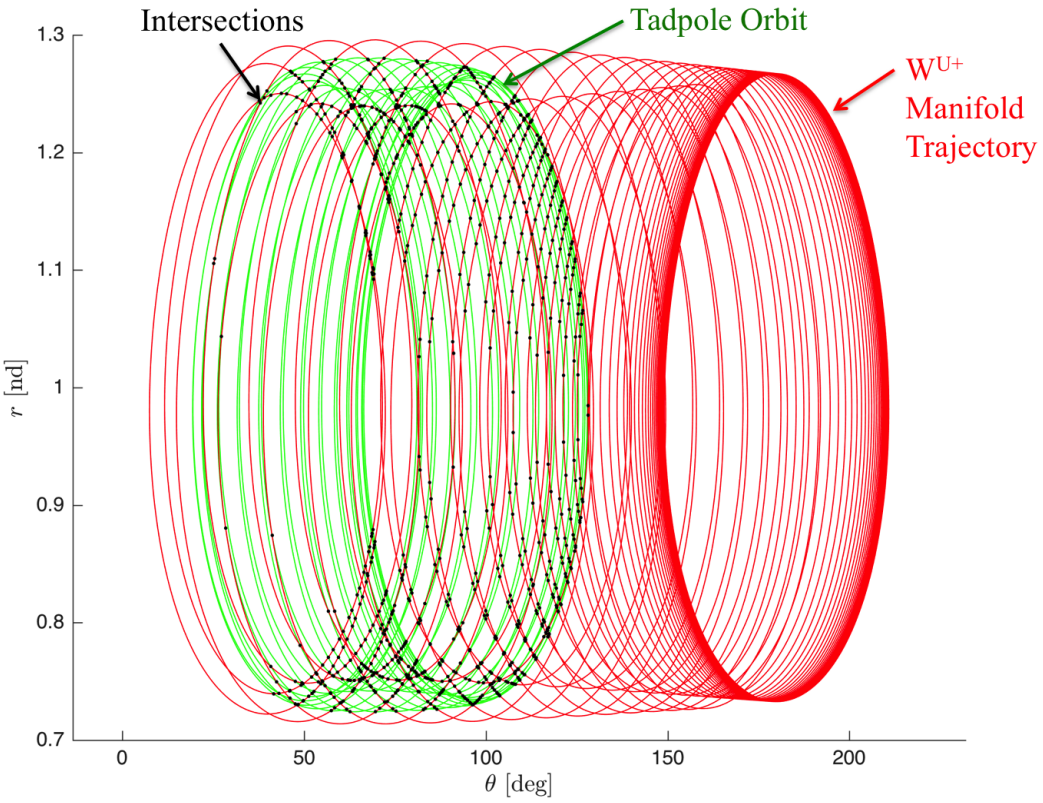

Figure 5.17. L_3 Lyapunov W^{U^+} Manifold Trajectory 73 and Tadpole Orbit Intersections

shows the ΔV and transfer time of flight (TOF) for the minimum ΔV case of each manifold arc for the subsets W^{U^+}, W^{U^-}. The color of each points indicates the step-off distance d from the Lyapunov orbit. It is important to acknowledge that numerical approximations of the manifolds are more accurate for smaller values of this step-off distance.

The information presented in Figures 5.18 - 5.19 provides a variety of low-cost transfers from the L_3 Lyapunov orbit to the tadpole orbit. The time of flight for all of these transfers is large because the manifolds take a long time to depart the L_3 Lyapunov orbit due to its small stability index. In Figure 5.20, the minimum

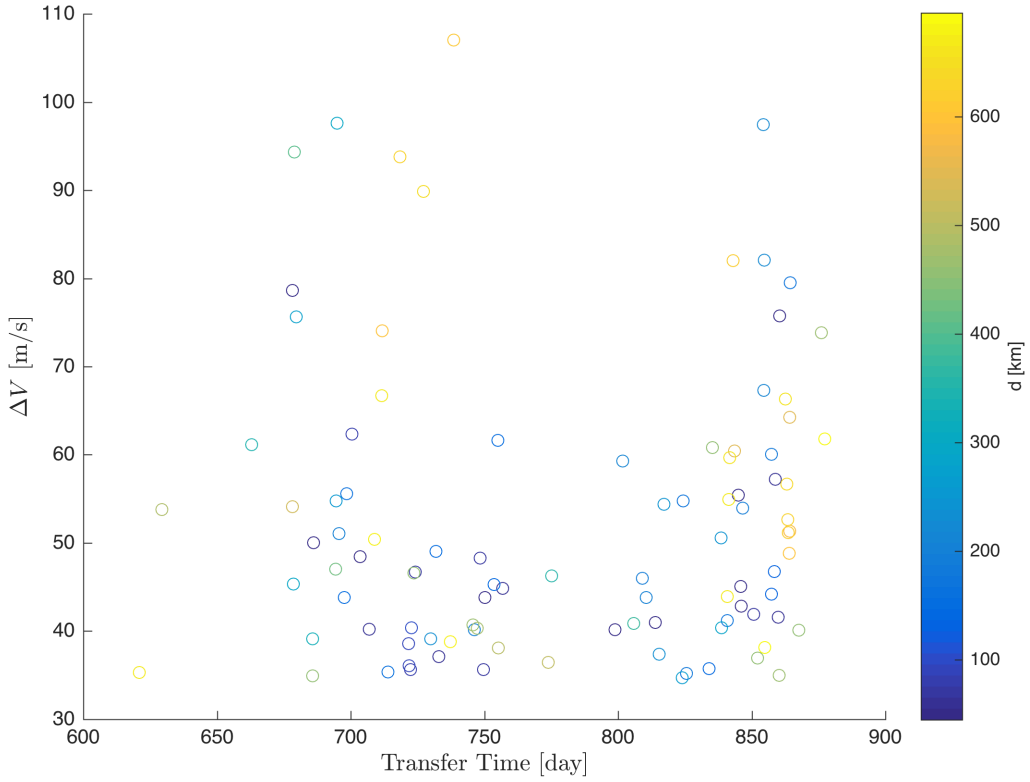

Figure 5.18. Maneuver Cost for L_3 Lyapunov W^{U+} Manifold Trajectories

ΔV transfer for manifold trajectory 73 in the W^{U+} subset is shown. The velocity change is applied at the intersection of the manifold and tadpole orbit with the smallest magnitude of this value, selected from all the options in Figure 5.17. A zoomed image near the insertion point is presented in 5.21, with the direction of the maneuver illustrated. At this point, the manifold trajectory and tadpole orbit are nearly aligned. The velocity is applied normal to the direction of motion, indicating that maneuver is changing the direction of motion to place P_3 in the tadpole orbit. The ΔV can be described in terms of its Cartesian velocity components in the rotating frame ΔV_x and ΔV_y or in terms of its magnitude and the angle Ψ defining the change in direction between the original direction of motion and the maneuver direction.

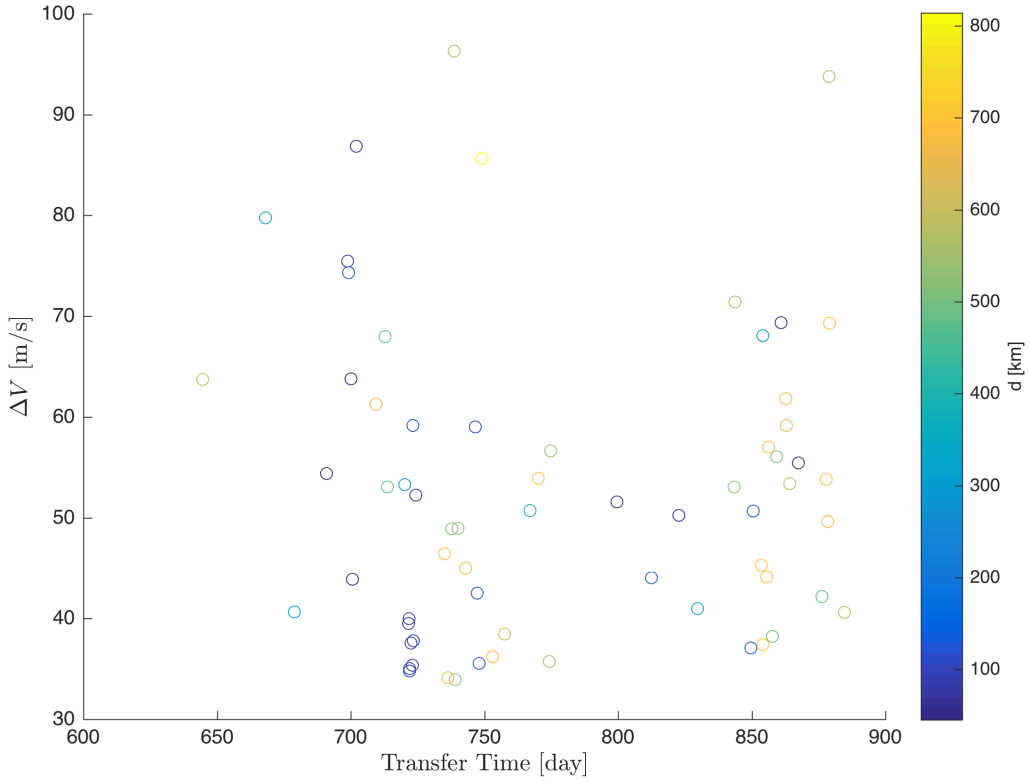

Figure 5.19. Maneuver Cost for L_3 Lyapunov W^{U^-} Manifold Trajectories

In Table 5.4, different transfers from the L_3 Lyapunov orbit to the tadpole orbit for the subset of unstable manifolds W^{U^+} are presented. Trajectories with the lowest ΔV cost for a range of transfer times are selected to provide a variety of options. The magnitude of the Jacobi constant difference between the manifold and tadpole orbit at the maneuver location during arrival $\Delta C_a = \|C_{Manifold} - C_{Tadpole}\|$ is computed. The maneuver ΔV magnitude and components as well as the transfer time of flight (TOF) are also listed, which are the important criteria for mission constraints.

For the subset of manifold trajectories W^{U^+}, the magnitude of the ΔV cost is similar across all options, and all of the options require a relatively large time of flight. The maneuvers are always applied normal to the direction of motion along the

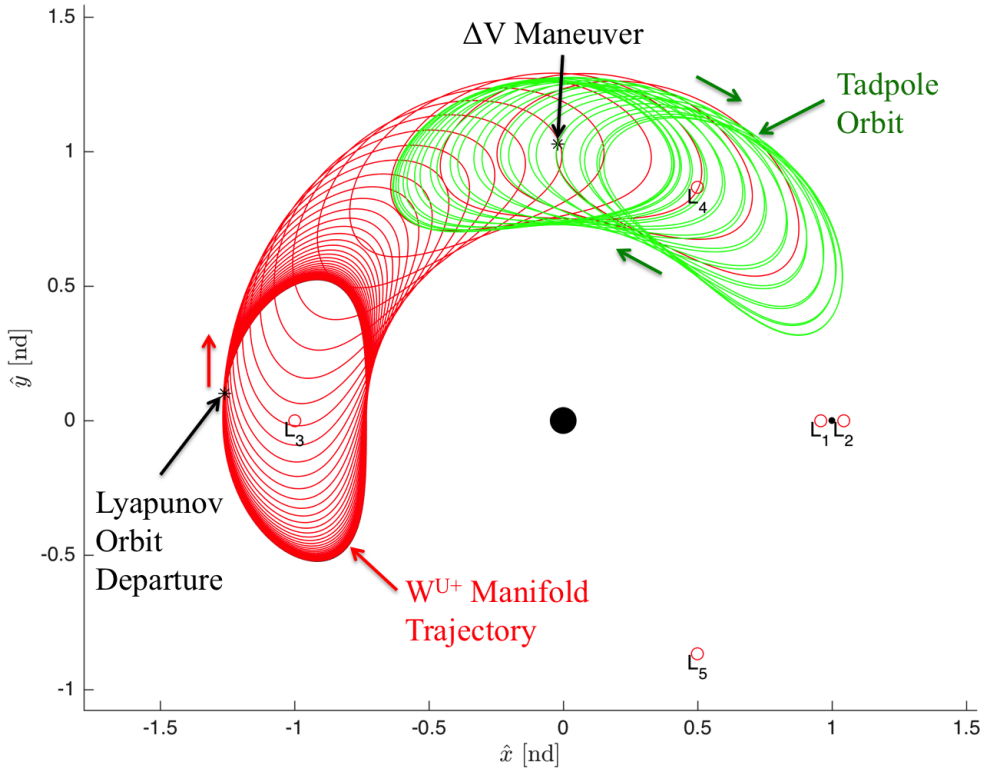

Figure 5.20. Transfer for L_3 Lyapunov W^{U+} Manifold Trajectory 73

manifold at the insertion location. A value of $\Psi \approx 90°$ indicates that the maneuver is applied in a direction 90 degrees clockwise from the initial direction of motion. For cases with this value of Ψ, the spacecraft is to the left of the larger primary P_1 with the maneuver applied inwards, as seen in Figures 5.22(d) and 5.23(d) (which is the minimum transfer time of flight case). A value of $\Psi \approx -90°$ indicates that the maneuver is applied in a direction 90 degrees counterclockwise from the initial direction of motion. For cases with this value of Ψ, the maneuver is applied outwards, as seen in Figures 5.22(b), 5.22(f), and 5.23(f). A value of $\Psi \approx -270°$ indicates that the maneuver is applied in a direction 270 degrees counterclockwise from the initial direction of motion. For cases with this value of Ψ, the spacecraft is to the right of

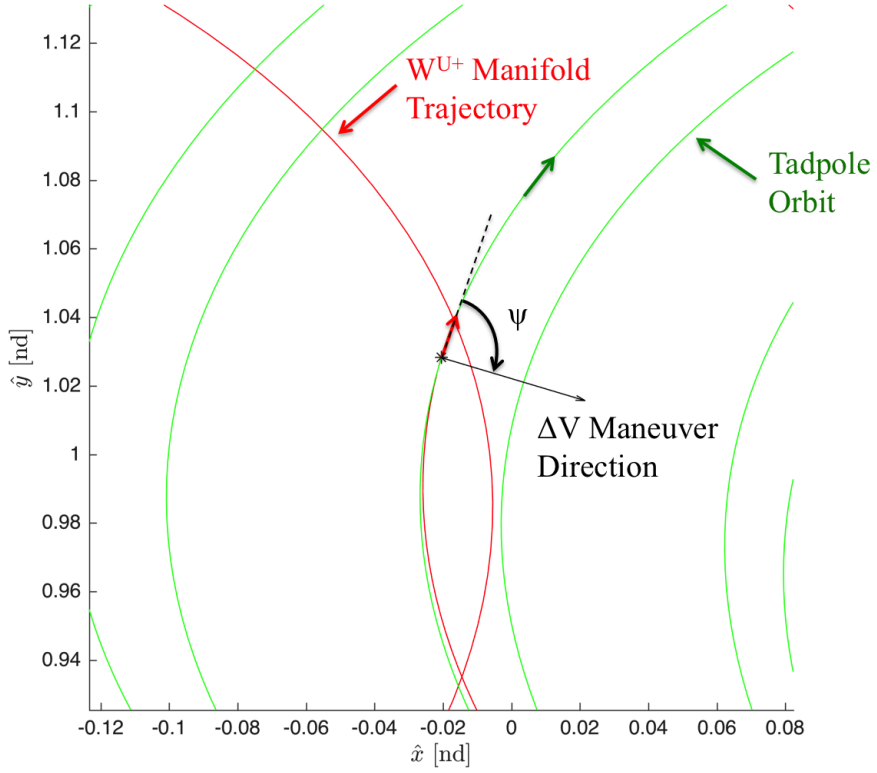

Figure 5.21. Insertion ΔV for L_3 Lyapunov W^{U^+} Manifold Trajectory 73

the larger primary P_1 with the maneuver applied inwards, as seen in Figure 5.23(b) (which is the minimum ΔV case).

For the subset of manifold trajectories W^{U^-}, the magnitude of the ΔV cost is similar across all options, and all of the options require a relatively large time of flight. A transfer is found with a smaller ΔV cost than the minimum case in the subset W^{U^+}, but it is not significantly different. This minimum ΔV case can be seen in Figure 5.25(e), and the case with the shortest time of flight is shown in Figure 5.24(a). Again, the maneuvers are always applied normal to the direction of motion along the manifold at the insertion location. The direction of the ΔV applied can again be characterized in the same manner by the angle Ψ. A value of $\Psi \approx 270°$

Table 5.4. L_3 Lyapunov to Tadpole Orbit Transfer Characteristics for W^{U^+} Trajectories

Num.	d (km)	ΔC_a	ΔV_x (m/s)	ΔV_y (m/s)	ΔV (m/s)	Ψ (deg)	TOF (day)
13	60	1×10^{-12}	35.62	-10.32	37.09	-90.64	733
17	67	1×10^{-12}	22.37	-27.76	35.66	-90.67	750
20	80	7×10^{-13}	32.46	14.67	35.62	90.67	722
27	140	4×10^{-14}	-34.71	8.55	35.74	-90.66	834
35	164	5×10^{-14}	30.57	-17.75	35.35	-90.68	714
39	180	1×10^{-13}	-26.73	22.89	35.19	-269.33	826
59	265	6×10^{-13}	-22.27	26.64	34.72	-269.35	824
73	452	9×10^{-13}	33.49	-9.99	34.95	90.65	686
77	674	3×10^{-13}	35.33	0.40	35.33	90.67	621
78	506	6×10^{-13}	26.79	-24.72	36.45	-90.67	774
80	469	7×10^{-13}	-34.55	5.40	34.97	-90.66	860
87	458	8×10^{-13}	-33.17	16.23	36.93	-269.32	852

indicates that the maneuver is applied in a direction 270 degrees clockwise from the initial direction of motion. For cases with this value of Ψ, the spacecraft is to the left of the larger primary P_1 with the maneuver applied outwards, as seen in Figure 5.24(f).

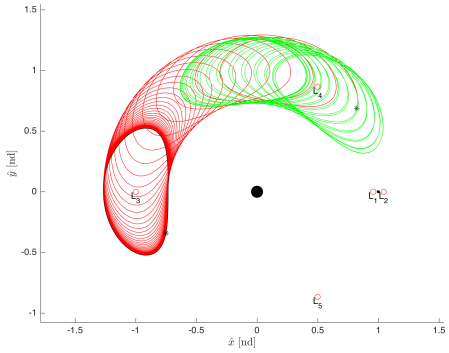

(a) W^{U^+} Trajectory 13

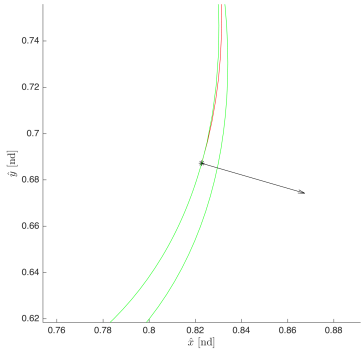

(b) W^{U^+} 13 ΔV Direction

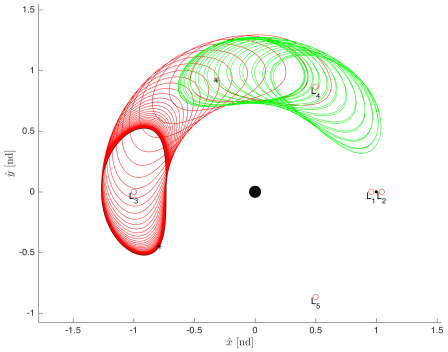

(c) W^{U^+} Trajectory 20

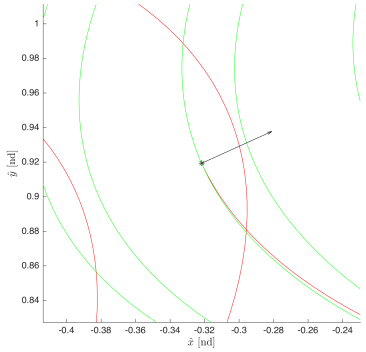

(d) W^{U^+} 20 ΔV Direction

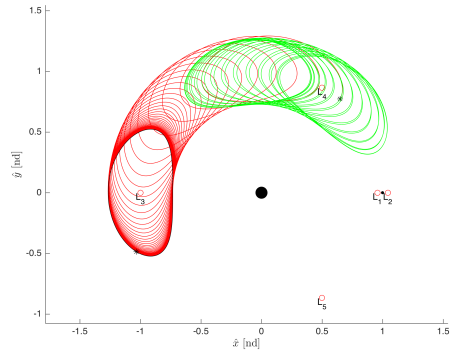

(e) W^{U^+} Trajectory 35

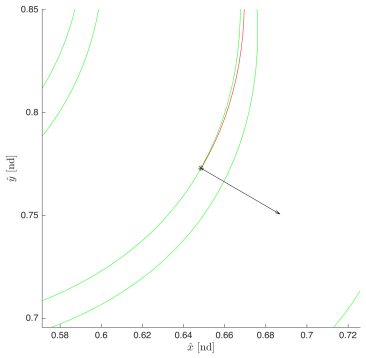

(f) W^{U^+} 35 ΔV Direction

Figure 5.22. Transfers for L_3 Lyapunov W^{U^+} Manifold Trajectories

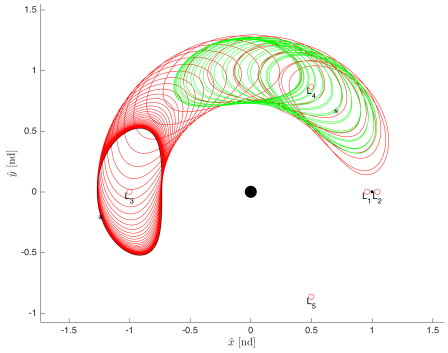

(a) W^{U^+} Trajectory 59

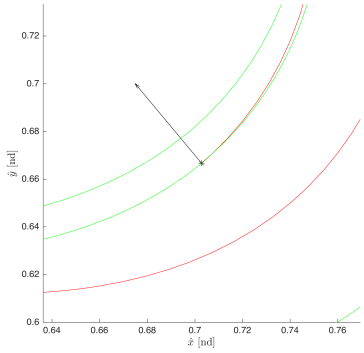

(b) W^{U^+} 59 ΔV Direction

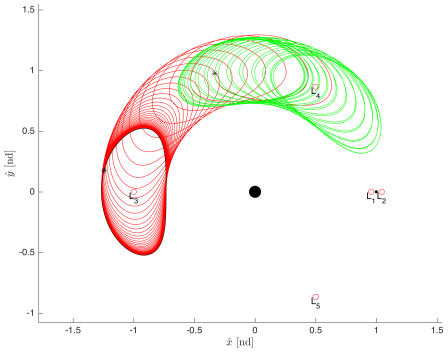

(c) W^{U^+} Trajectory 77

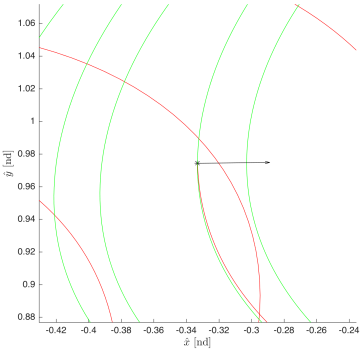

(d) W^{U^+} 77 ΔV Direction

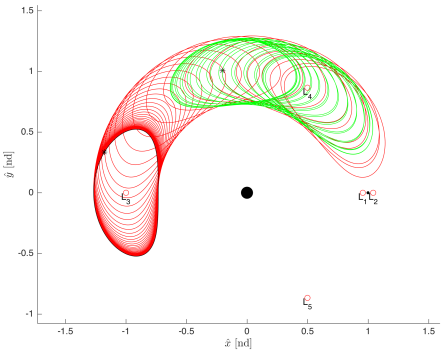

(e) W^{U^+} Trajectory 80

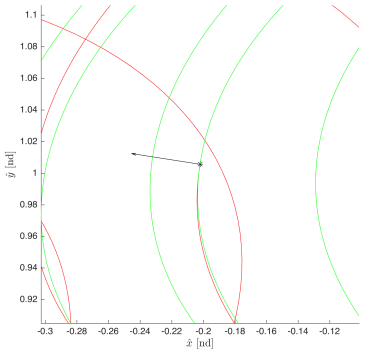

(f) W^{U^+} 80 ΔV Direction

Figure 5.23. Transfers for L_3 Lyapunov W^{U^+} Manifold Trajectories

Table 5.5. L_3 Lyapunov to Tadpole Orbit Transfer Characteristics for W^{U^-} Trajectories

Num.	d (km)	ΔC_a	ΔV_x (m/s)	ΔV_y (m/s)	ΔV (m/s)	Ψ (deg)	TOF (day)
11	77	2×10^{-12}	35.36	0.46	35.36	90.66	723
15	97	5×10^{-13}	33.09	11.53	35.04	90.66	722
16	98	4×10^{-13}	34.29	5.70	34.76	90.66	722
22	119	9×10^{-15}	21.31	-28.47	35.56	-90.68	748
24	125	6×10^{-14}	-37.01	-2.43	37.09	269.30	850
30	315	1×10^{-11}	35.27	-20.20	40.64	-90.78	679
38	541	5×10^{-11}	23.05	-27.29	35.72	-90.67	774
46	491	4×10^{-11}	-34.32	-16.83	38.23	269.30	858
51	521	4×10^{-11}	28.08	-19.03	33.92	-90.64	739
63	682	3×10^{-14}	29.43	-17.31	34.14	-90.64	736
68	694	5×10^{-14}	11.04	-34.51	36.23	-90.65	753
70	696	2×10^{-15}	-34.81	-13.72	37.42	269.30	854

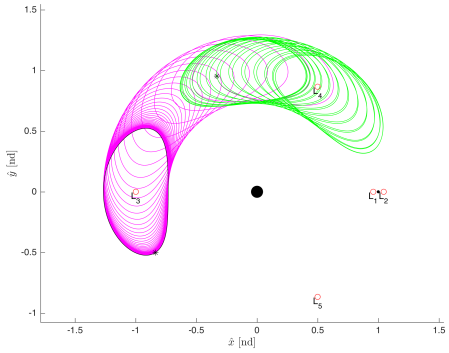

(a) W^{U^-} Trajectory 16

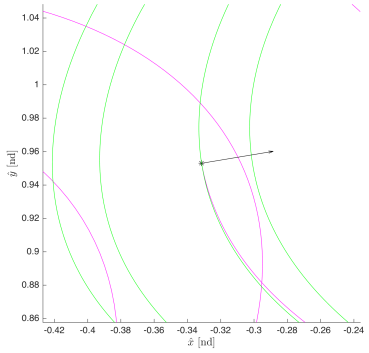

(b) W^{U^-} 16 ΔV Direction

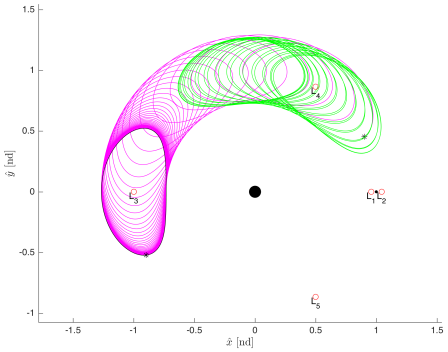

(c) W^{U^-} Trajectory 22

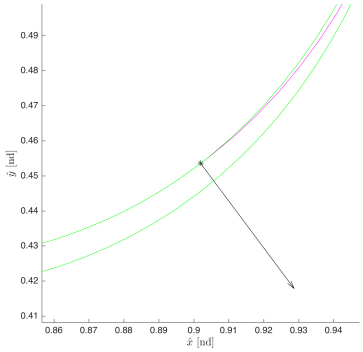

(d) W^{U^-} 22 ΔV Direction

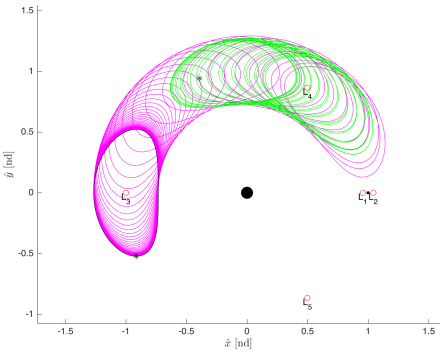

(e) W^{U^-} Trajectory 24

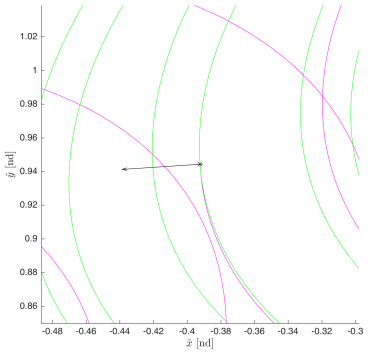

(f) W^{U^-} 24 ΔV Direction

Figure 5.24. Transfers for L_3 Lyapunov W^{U^-} Manifold Trajectories

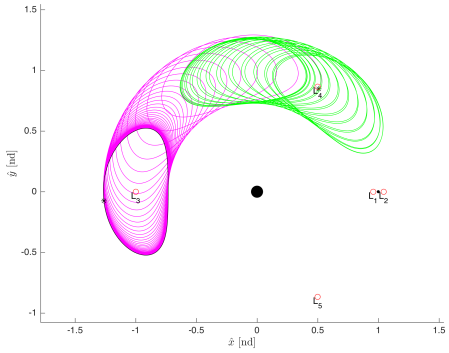

(a) W^{U^-} Trajectory 30

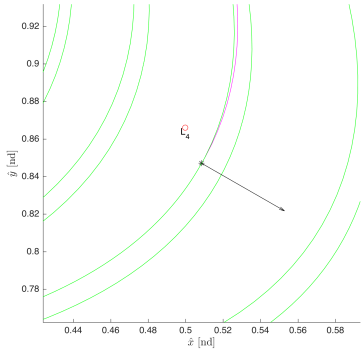

(b) W^{U^-} 30 ΔV Direction

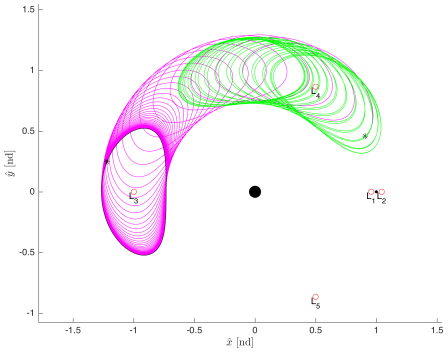

(c) W^{U^-} Trajectory 38

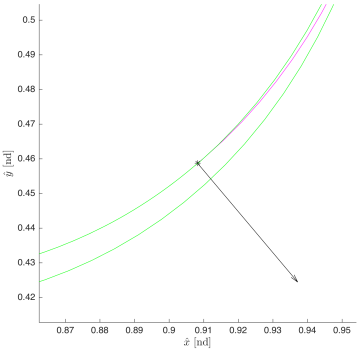

(d) W^{U^-} 38 ΔV Direction

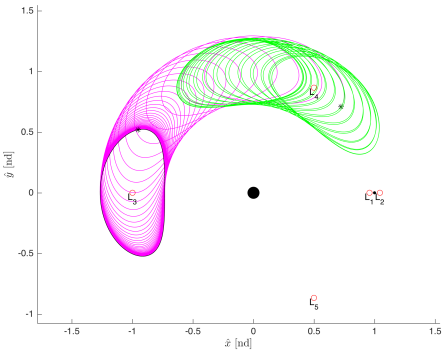

(e) W^{U^-} Trajectory 51

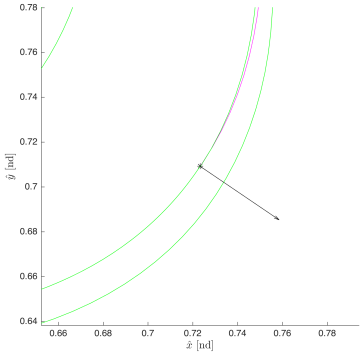

(f) W^{U^-} 51 ΔV Direction

Figure 5.25. Transfers for L_3 Lyapunov W^{U^-} Manifold Trajectories

5.2.2 Transfers to a L_4 Tadpole Orbit Using Horseshoe Orbit Unstable Manifolds

Transfers between tadpole orbits and unstable horseshoe orbits can be designed by leveraging the stable and unstable manifolds associated with this orbit. By investigating the manifold trajectories propagated previously for the selected horseshoe orbit, each of the intersections between these trajectories and the tadpole orbit can be found if they exist. Due to the complex motion of both the tadpole orbit and these manifolds, the states are converted to polar coordinates before computing the intersections. The subset of unstable manifold arcs W^{U^+}, W^{U^-} are computed, and these trajectories are assumed to depart the horseshoe orbit for free. For each of these manifolds arcs, the intersection with the smallest velocity difference is selected. Figures 5.26 - 5.27 shows the ΔV and transfer time of flight (TOF) for the minimum ΔV case of each manifold arc for the subsets W^{U^+}, W^{U^-}, where the numerical approximations of the manifolds are more accurate for smaller values of the step-off distance d.

The information presented in Figures 5.26 - 5.27 provides a variety of low-cost transfers from the horseshoe orbit to the tadpole orbit. Overall, these transfers are similar in cost to those associated with the L_3 Lyapunov orbit, which may be a result of the similar structure of the Lyapunov orbit manifolds and the horseshoe orbit. The time of flight has a variety of options because the horseshoe orbit extends much further than the Lyapunov orbit, providing transfers that depart from the orbit at different locations which are closer to or farther from the tadpole orbit. The ΔV can be described in terms of its Cartesian velocity components in the rotating frame ΔV_x and ΔV_y or in terms of its magnitude and the angle Ψ defining the change in direction between the original direction of motion and the maneuver direction. In Table 5.6, different transfers from the horseshoe orbit to the tadpole orbit for the subset of unstable manifolds W^{U^+} are presented. The magnitude of the Jacobi constant difference between the manifold and tadpole orbit at the maneuver location

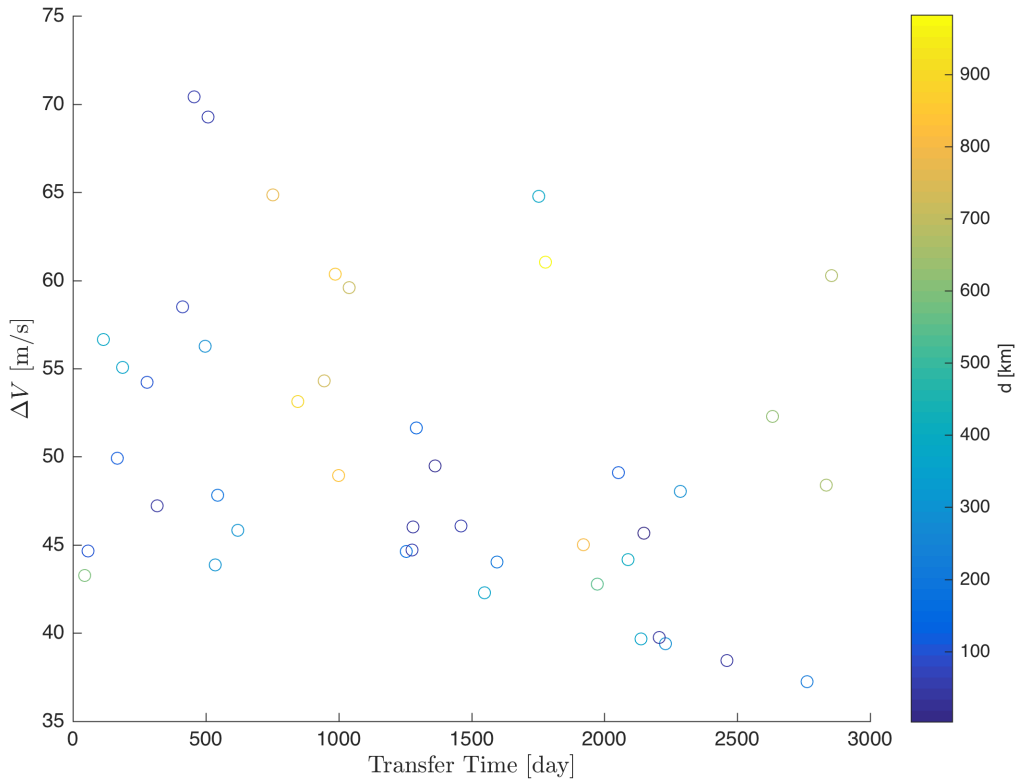

Figure 5.26. Maneuver Cost for Horseshoe Orbit W^{U^+} Manifold Trajectories

during arrival $\Delta C_a = \|C_{Manifold} - C_{Tadpole}\|$ is computed. Some of the manifold arcs have a difference in Jacobi constant that is greater than others, resulting from the computational technique used to compute the required step-off distance being unable to find a value that improves this error. The maneuver ΔV magnitude and components as well as the transfer time of flight (TOF) are also listed.

For the subset of manifold trajectories W^{U^+}, the magnitude of the ΔV cost is similar across all options. Differing from the transfers associated with the L_3 Lyapunov orbit, some of these transfers have a very short time of flight. The maneuvers are always applied normal to the direction of motion along the manifold at the insertion location. The direction of the ΔV applied can be characterized in the same manner as

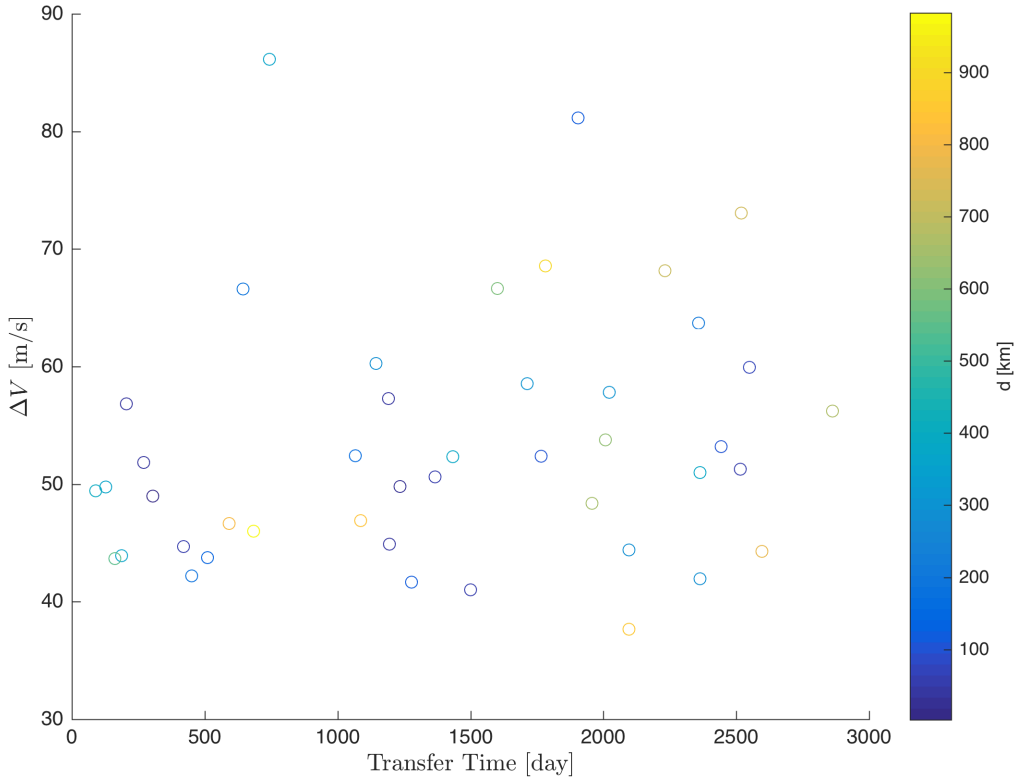

Figure 5.27. Maneuver Cost for Horseshoe Orbit W^{U^-} Manifold Trajectories

the transfers associated with the L_3 Lyapunov orbit manifolds by the angle Ψ. These transfers are all very similar in appearance, as the manifold arcs follow the motion of the horseshoe orbit. For transfers with a short time of flight, the trajectories are nearly indistinguishable from the horseshoe orbit. Figure 5.28(e) shows the case for the shortest time of flight for the transfers investigated. The spacecraft departs the manifold in a region overlapping the tadpole orbit, but the cheapest insertion point for this manifold arc is on the other end of the tadpole orbit. The minimum ΔV case can be seen in Figure 5.29(c), and this transfer takes a very long time to complete.

For the subset of manifold trajectories W^{U^-}, the magnitude of the ΔV cost is similar across all options, and the time of flight again varies. The minimum ΔV case

Table 5.6. Horseshoe to Tadpole Orbit Transfer Characteristics for W^{U^+} Trajectories

Num.	d (km)	ΔC_a	ΔV_x (m/s)	ΔV_y (m/s)	ΔV (m/s)	Ψ (deg)	TOF (day)
1	46	7×10^{-14}	-37.95	-6.20	38.46	269.27	2461
3	157	5×10^{-14}	-20.17	39.82	44.63	-269.20	1254
4	290	5×10^{-13}	35.60	-16.87	39.40	-90.75	2229
5	109	3×10^{-11}	-44.24	6.07	44.65	-90.83	57
6	590	3×10^{-11}	-43.26	0.18	43.26	-90.82	44
20	305	2×10^{-6}	37.04	-23.52	43.88	-90.81	535
21	215	2×10^{-6}	34.70	13.51	37.24	90.67	2762
36	357	4×10^{-6}	-34.31	19.92	39.67	-269.31	2137
40	544	4×10^{-6}	39.87	-15.49	42.77	-90.70	1973
57	367	2×10^{-6}	41.95	5.26	42.28	90.77	1549
64	59	2×10^{-6}	15.53	-41.93	44.71	-90.81	1276
66	37	2×10^{-6}	39.69	-2.40	39.76	90.73	2206

can be seen in Figure 5.31(a), and the case with the shortest time of flight is shown in Figure 5.30(e). Again, the maneuvers are always applied normal to the direction of motion along the manifold at the insertion location.

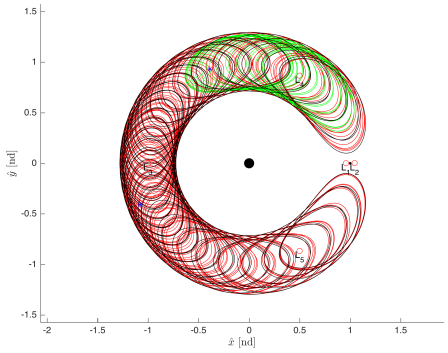

(a) W^{U^+} Trajectory 1

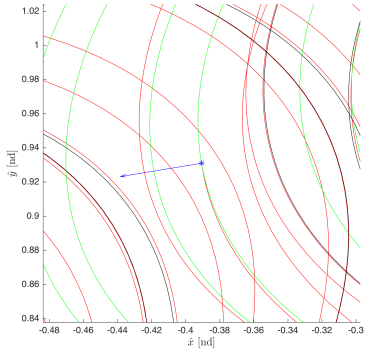

(b) W^{U^+} 1 ΔV Direction

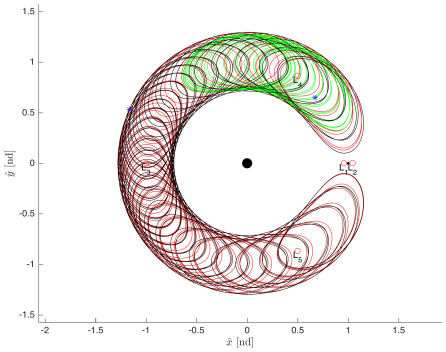

(c) W^{U^+} Trajectory 3

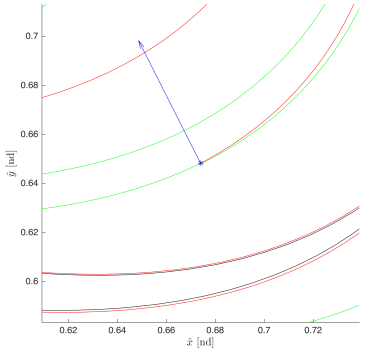

(d) W^{U^+} 3 ΔV Direction

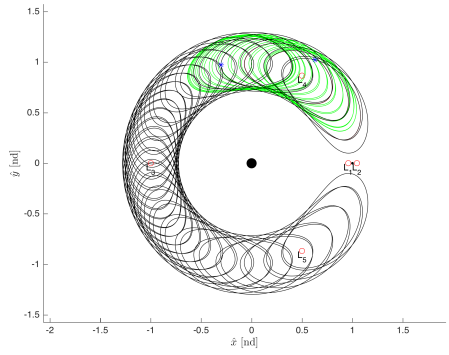

(e) W^{U^+} Trajectory 6

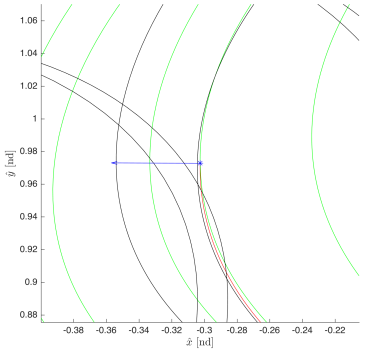

(f) W^{U^+} 6 ΔV Direction

Figure 5.28. Transfers for Horseshoe Orbit W^{U^+} Manifold Trajectories

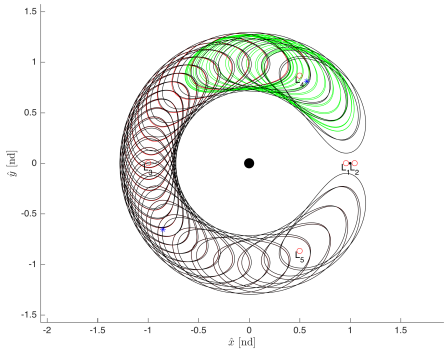

(a) W^{U^+} Trajectory 20

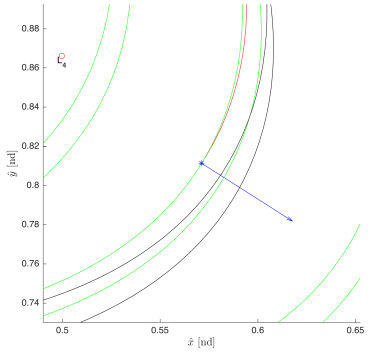

(b) W^{U^+} 20 ΔV Direction

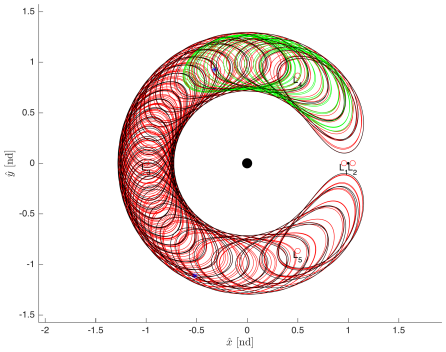

(c) W^{U^+} Trajectory 21

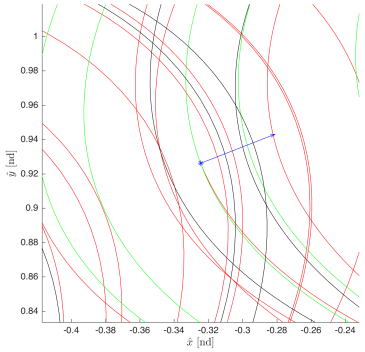

(d) W^{U^+} 21 ΔV Direction

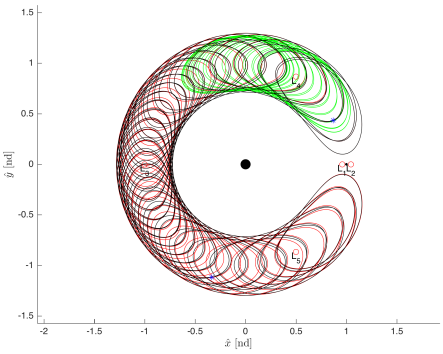

(e) W^{U^+} Trajectory 64

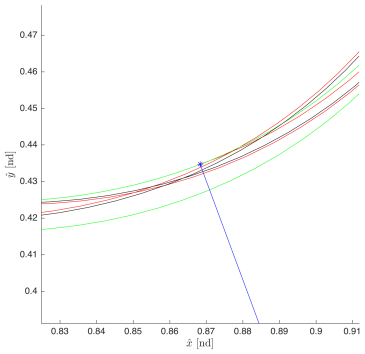

(f) W^{U^+} 64 ΔV Direction

Figure 5.29. Transfers for Horseshoe Orbit W^{U^+} Manifold Trajectories

Table 5.7. Horseshoe to Tadpole Orbit Transfer Characteristics for W^{U^-} Trajectories

Num.	d (km)	ΔC_a	ΔV_x (m/s)	ΔV_y (m/s)	ΔV (m/s)	Ψ (deg)	TOF (day)
2	110	4×10^{-13}	-40.22	10.85	41.66	-269.22	1278
5	358	3×10^{-11}	-43.80	3.35	43.93	-90.83	187
6	386	7×10^{-11}	1.78	-49.41	49.44	-90.85	89
7	544	2×10^{-10}	-43.61	2.12	43.66	-90.82	161
12	839	3×10^{-10}	-40.38	23.88	46.91	-90.87	1087
14	850	7×10^{-10}	37.64	-1.07	37.65	90.72	2096
22	768	2×10^{-6}	-21.79	38.57	44.30	-269.19	2597
26	173	2×10^{-6}	29.62	-30.05	42.20	-90.76	451
50	806	2×10^{-6}	11.07	-45.33	46.67	-90.77	591
56	290	2×10^{-6}	25.36	-33.41	41.94	-90.76	2364
65	40	2×10^{-6}	44.83	-2.59	44.91	90.83	1194

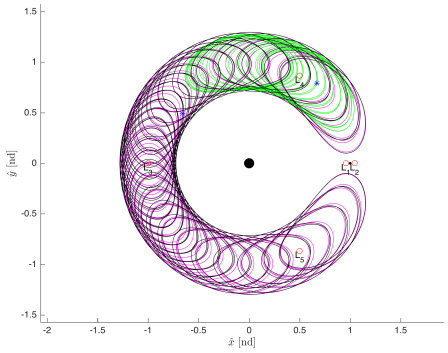

(a) W^{U^-} Trajectory 2

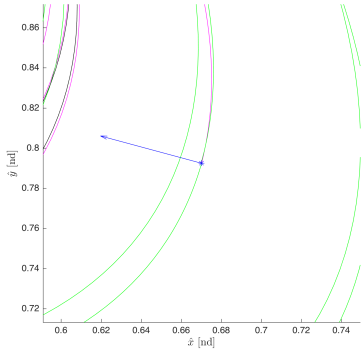

(b) W^{U^-} 2 ΔV Direction

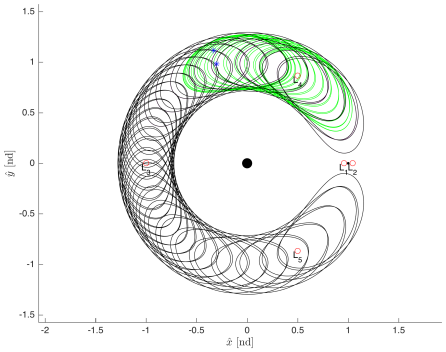

(c) W^{U^-} Trajectory 5

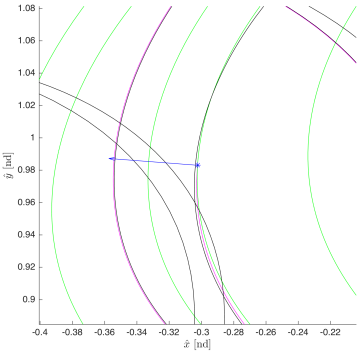

(d) W^{U^-} 5 ΔV Direction

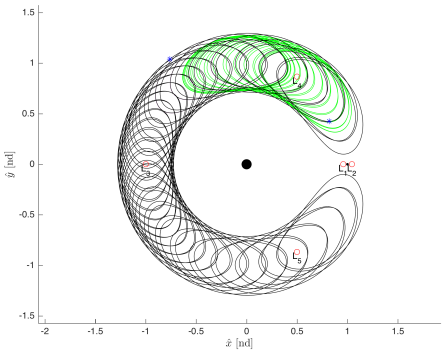

(e) W^{U^-} Trajectory 6

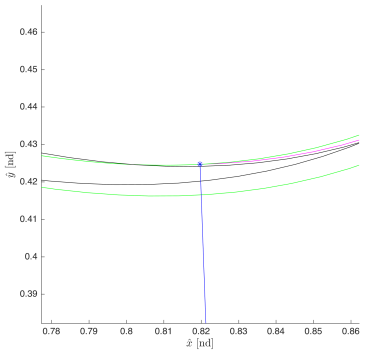

(f) W^{U^-} 6 ΔV Direction

Figure 5.30. Transfers for Horseshoe Orbit W^{U^-} Manifold Trajectories

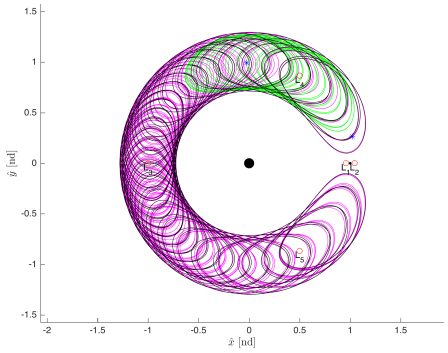

(a) W^{U^-} Trajectory 14

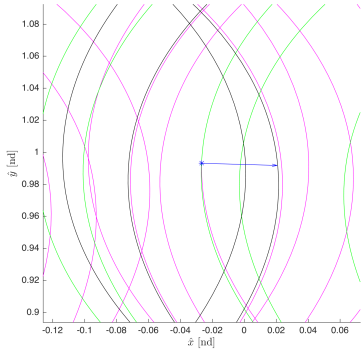

(b) W^{U^-} 14 ΔV Direction

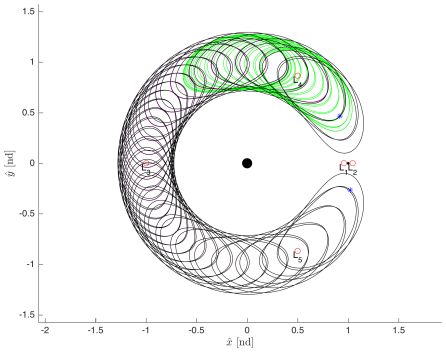

(c) W^{U^-} Trajectory 26

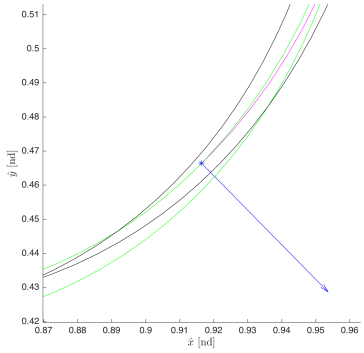

(d) W^{U^-} 26 ΔV Direction

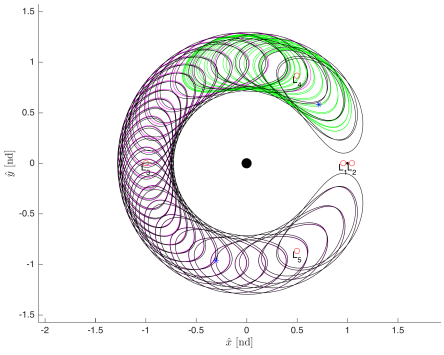

(e) W^{U^-} Trajectory 50

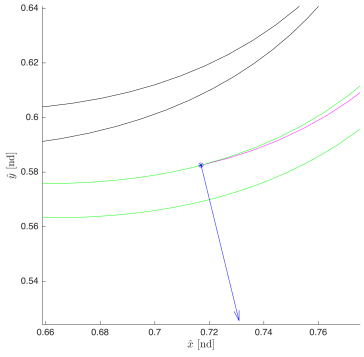

(f) W^{U^-} 50 ΔV Direction

Figure 5.31. Transfers for Horseshoe Orbit W^{U^-} Manifold Trajectories

5.2.3 Transfers to a L_4 Tadpole Orbit Using Planar Resonant Orbit Unstable Manifolds

Transfers between tadpole orbits and unstable resonant orbits can be designed by leveraging the stable and unstable manifolds associated with this orbit. By investigating the manifold trajectories propagated previously for the selected 3:4 resonant orbit, each of the intersections between these trajectories and the tadpole orbit can be found if they exist. Due to the complex motion of both the tadpole orbit and these manifolds, the states are converted to polar coordinates before computing the intersections. The subset of unstable manifold arcs W^{U^+}, W^{U^-} are computed, and these trajectories are assumed to depart the resonant orbit for free. For each of these manifolds arcs, the intersection with the smallest velocity difference is selected. Figures 5.32 - 5.33 shows the ΔV and transfer time of flight (TOF) for the minimum ΔV case of each manifold arc for the subsets W^{U^+}, W^{U^-}, where the numerical approximations of the manifolds are more accurate for smaller values of the step-off distance d.

The information presented in Figures 5.32 - 5.33 provides a variety of low-cost transfers from the resonant orbit to the tadpole orbit. Overall, these transfers are slightly more expensive than those associated with the L_3 Lyapunov orbit and horseshoe orbit, which may be a result of the manifolds of these other orbits having motion that is closer to that of the tadpole orbit. The time of flight has a variety of options because the manifold arcs vary much more than those of the other orbits investigated, providing transfers that take a very short or long amount of time. The ΔV can be described in terms of its Cartesian velocity components in the rotating frame ΔV_x and ΔV_y or in terms of its magnitude and the angle Ψ defining the change in direction between the original direction of motion and the maneuver direction. In Table 5.8, different transfers from the resonant orbit to the tadpole orbit for the subset of unstable manifolds W^{U^+} are presented. The magnitude of the Jacobi constant difference between the manifold arc and tadpole orbit at the maneuver location during arrival $\Delta C_a = \|C_{Manifold} - C_{Tadpole}\|$ is computed. Some of the manifolds have a difference in

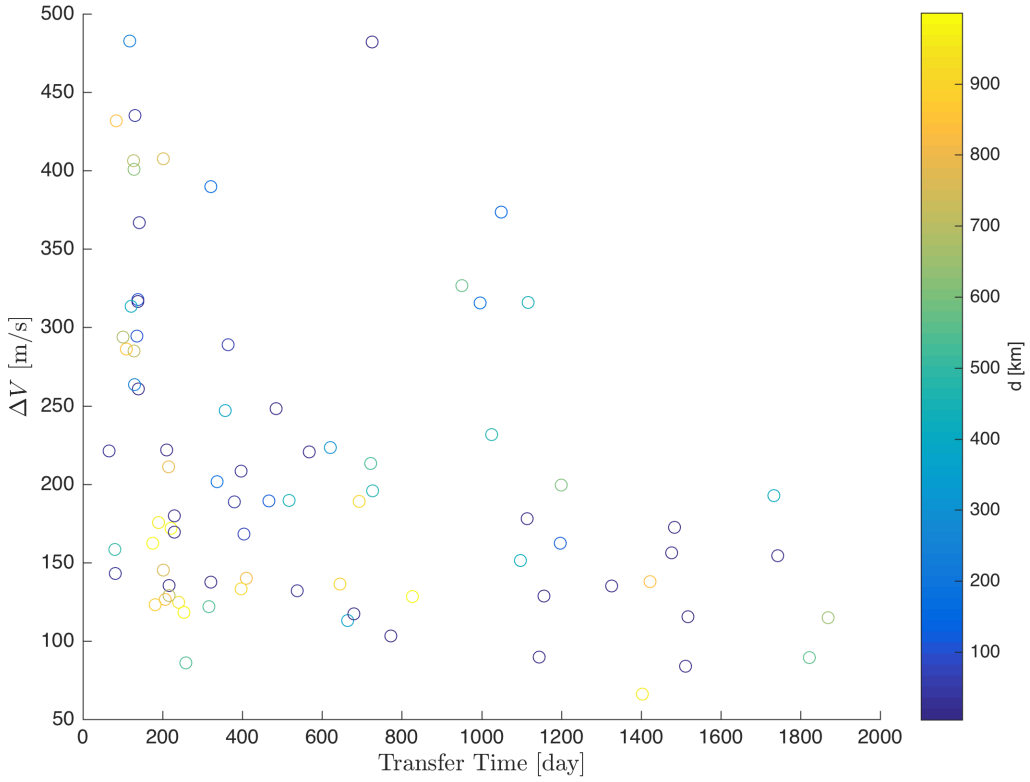

Figure 5.32. Maneuver Cost for 3:4 Resonant W^{U+} Manifold Trajectories

Jacobi constant that is greater than others, resulting from the numerical method used to compute the required step-off distance being unable to find a value that improves this error. The maneuver ΔV magnitude and components as well as the transfer time of flight (TOF) are also listed.

For the subset of manifold trajectories W^{U+}, the magnitude of the ΔV cost varies greatly across all options. Similar to the transfers associated with the horseshoe orbit, some of these transfers have a very short time of flight and the transfer times vary. The maneuvers are always applied normal to the direction of motion along the manifold at the insertion location; however, this angle is slightly more offset than the previous transfers examined for the L_3 Lyapunov and horseshoe orbits. This difference likely

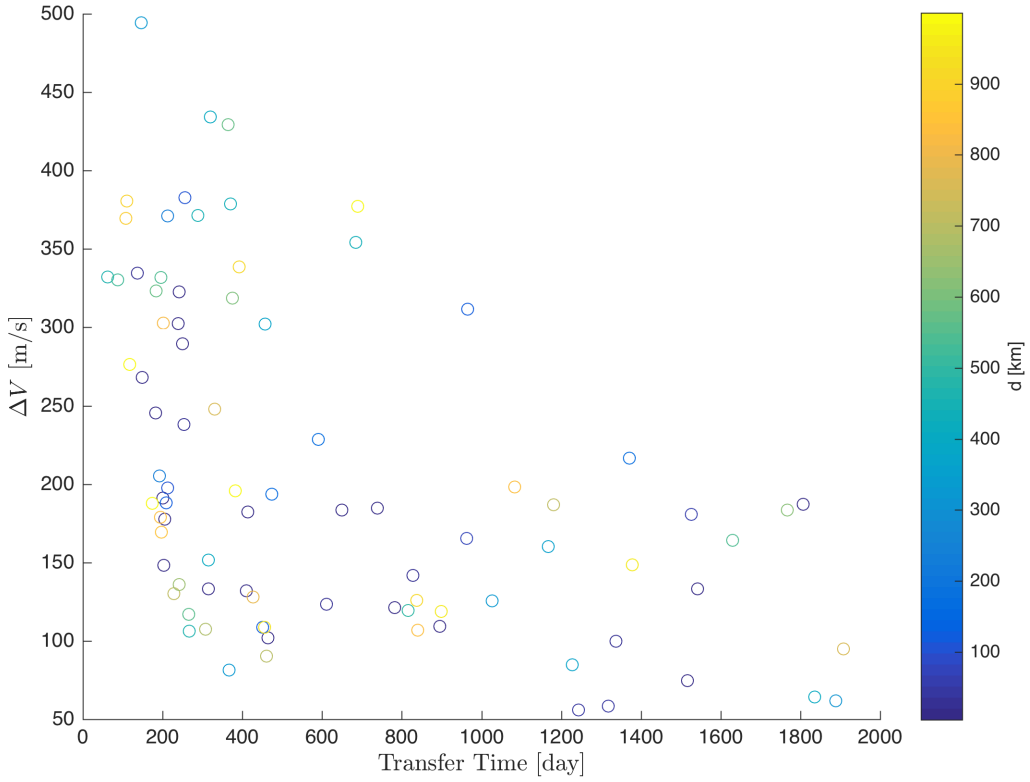

Figure 5.33. Maneuver Cost for 3:4 Resonant W^{U^-} Manifold Trajectories

results from the manifolds associated with the resonant orbit not always aligning as well with the tadpole orbit as the previous cases. The direction of the ΔV applied can be characterized in the same manner as the transfers associated with the L_3 Lyapunov and horseshoe orbit manifolds by the angle Ψ. These transfers have a similar structure to those investigated previously; however, the motion occasionally circulates the entire system, passing by the secondary body. For transfers with a short time of flight, the trajectories do not complete an entire revolution of the system before they insert in to the tadpole orbit, as seen in Figures 5.34(e) and 5.35(a) (which is the minimum transfer time case). In this case with the shortest time of flight, the manifold begins to form loops similar to that of the tadpole orbit, but the motion is different enough

Table 5.8. 3:4 Resonant to Tadpole Orbit Transfer Characteristics for W^{U^+} Trajectories

Num.	d (km)	ΔC_a	ΔV_x (m/s)	ΔV_y (m/s)	ΔV (m/s)	Ψ (deg)	TOF (day)
14	14	4×10^{-12}	40.96	-79.69	89.60	-91.38	1145
20	363	2×10^{-11}	37.47	106.63	113.02	91.75	664
32	830	2×10^{-6}	58.49	-112.26	126.58	-92.21	206
33	544	2×10^{-6}	73.59	44.51	86.00	91.58	258
65	28	2×10^{-6}	-127.98	63.89	143.04	-92.53	81
81	15	4×10^{-6}	94.78	-40.95	103.25	-91.95	772
93	535	4×10^{-6}	121.97	3.05	122.01	-92.08	316
97	990	4×10^{-6}	-115.64	23.90	118.09	-268.13	253
105	917	3×10^{-6}	131.60	20.06	133.12	92.52	397
119	1000	3×10^{-6}	-127.85	-11.86	128.40	267.72	827
130	24	2×10^{-6}	114.20	66.26	132.03	91.32	538
132	13	2×10^{-6}	80.51	23.43	83.85	91.53	1512

that a relatively large ΔV maneuver is still required. The minimum ΔV case can be seen in Figure 5.35(e), and this transfer takes the longest time to complete out of all the available options.

For the subset of manifold trajectories W^{U^-}, the magnitude of the ΔV cost and time of flight again varies across all options; however, more low-cost options are found. The minimum ΔV case can be seen in Figure 5.36(c), and the case with the shortest time of flight is shown in Figure 5.36(a). Again, the maneuvers are always applied nearly normal to the direction of motion along the manifold at the insertion location.

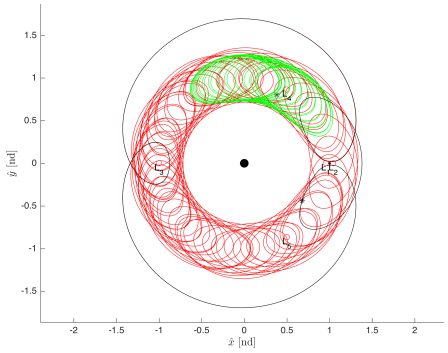

(a) W^{U^+} Trajectory 14

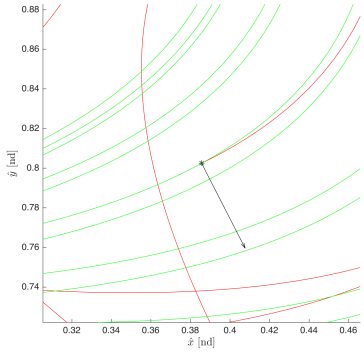

(b) W^{U^+} 14 ΔV Direction

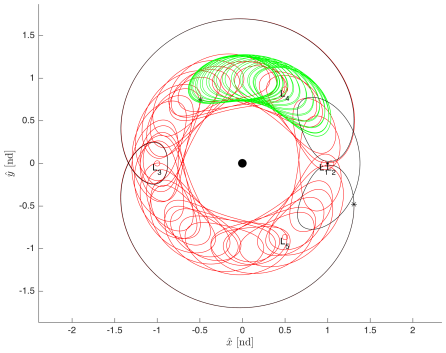

(c) W^{U^+} Trajectory 20

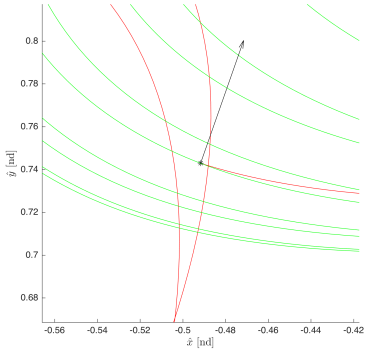

(d) W^{U^+} 20 ΔV Direction

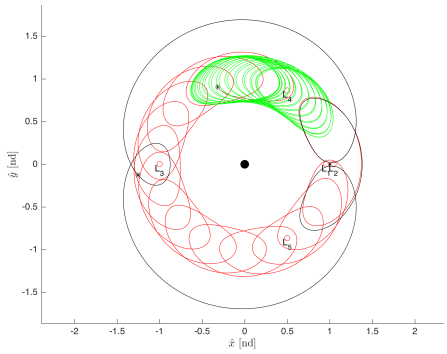

(e) W^{U^+} Trajectory 33

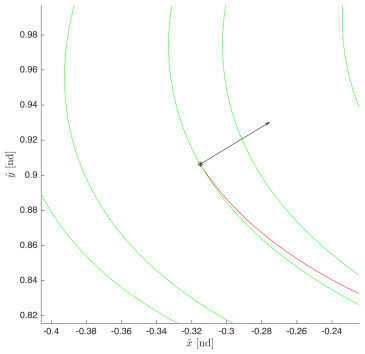

(f) W^{U^+} 33 ΔV Direction

Figure 5.34. Transfers for 3:4 Resonant W^{U^+} Manifold Trajectories

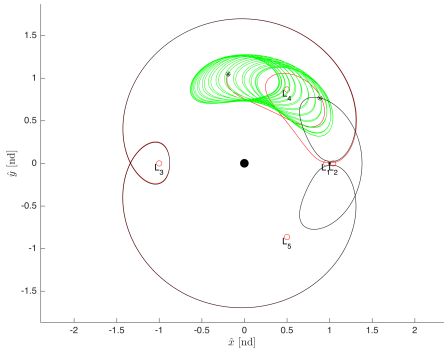

(a) W^{U^+} Trajectory 65

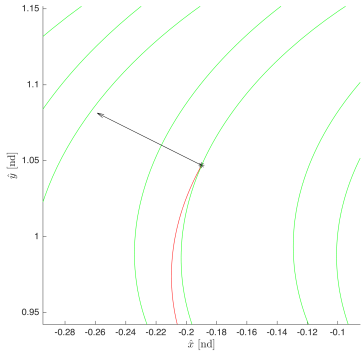

(b) W^{U^+} 65 ΔV Direction

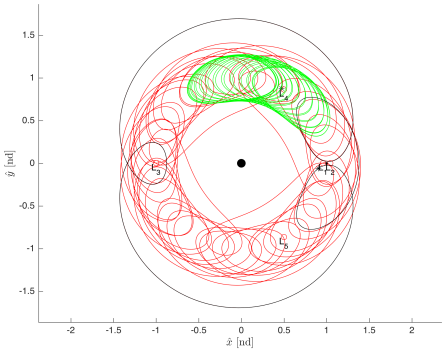

(c) W^{U^+} Trajectory 81

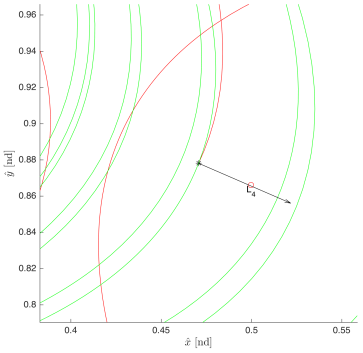

(d) W^{U^+} 81 ΔV Direction

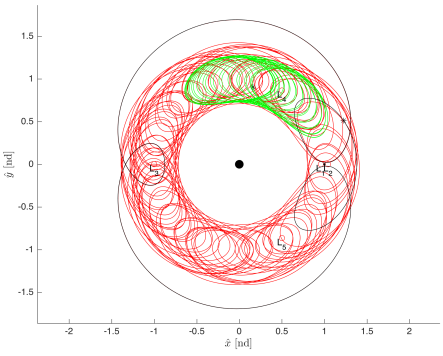

(e) W^{U^+} Trajectory 132

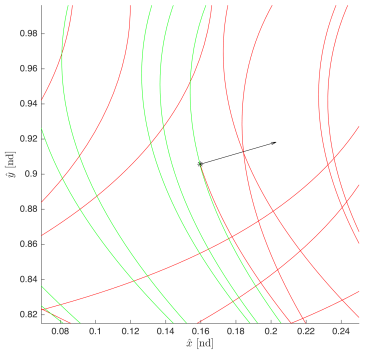

(f) W^{U^+} 132 ΔV Direction

Figure 5.35. Transfers for 3:4 Resonant W^{U^+} Manifold Trajectories

Table 5.9. 3:4 Resonant to Tadpole Orbit Transfer Characteristics for W^{U^-} Trajectories

Num.	d (km)	ΔC_a	ΔV_x (m/s)	ΔV_y (m/s)	ΔV (m/s)	Ψ (deg)	TOF (day)
6	15	3×10^{-14}	114.95	-93.50	148.17	-92.83	202
12	44	6×10^{-14}	-50.14	-24.81	55.94	268.97	1243
16	49	8×10^{-14}	-50.39	29.81	58.55	-91.00	1318
20	303	2×10^{-14}	46.63	40.57	61.81	92.91	1888
21	368	1×10^{-13}	-84.78	-0.98	84.79	91.50	1227
36	695	2×10^{-6}	86.50	25.66	90.22	91.70	460
37	397	2×10^{-6}	-48.41	42.16	64.19	-91.07	1836
63	5	2×10^{-6}	-39.41	101.89	109.25	-268.05	895
87	465	2×10^{-6}	66.97	82.46	106.23	91.70	267
95	830	3×10^{-6}	-92.85	52.77	106.79	-267.80	840
116	496	2×10^{-6}	72.65	-94.73	119.39	-92.20	816
121	319	2×10^{-6}	-80.78	9.14	81.30	-268.60	367

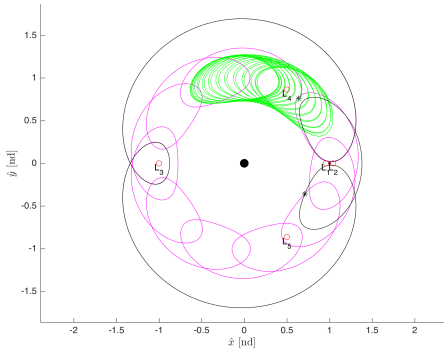

(a) W^{U^-} Trajectory 6

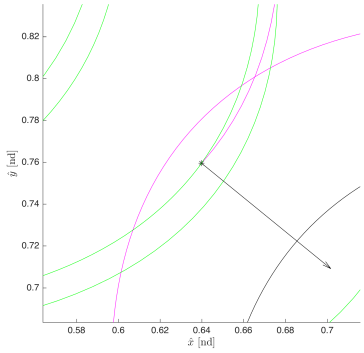

(b) W^{U^-} 6 ΔV Direction

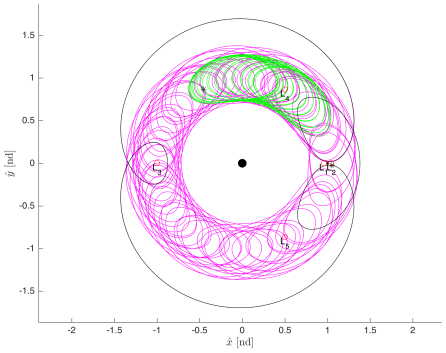

(c) W^{U^-} Trajectory 12

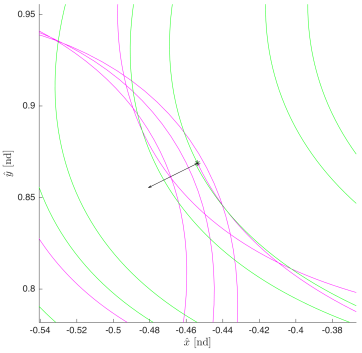

(d) W^{U^-} 12 ΔV Direction

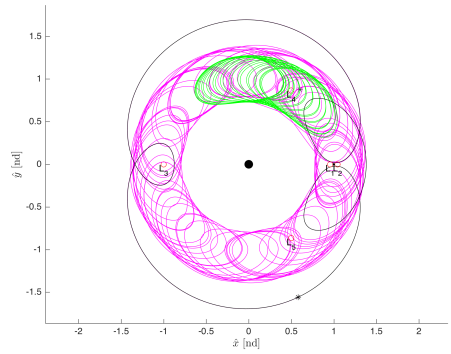

(e) W^{U^-} Trajectory 21

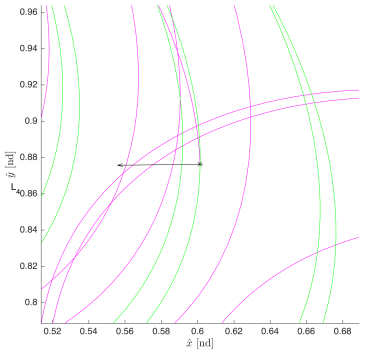

(f) W^{U^-} 21 ΔV Direction

Figure 5.36. Transfers for 3:4 Resonant W^{U^-} Manifold Trajectories

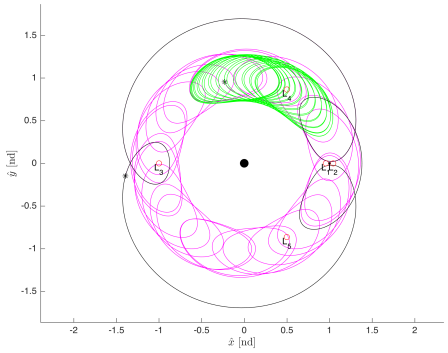

(a) W^{U^-} Trajectory 36

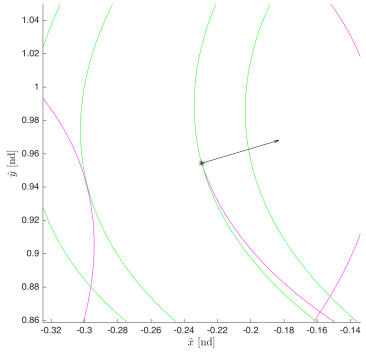

(b) W^{U^-} 36 ΔV Direction

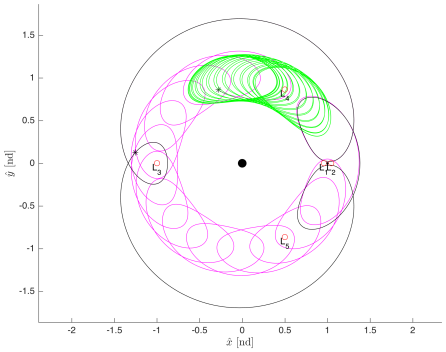

(c) W^{U^-} Trajectory 87

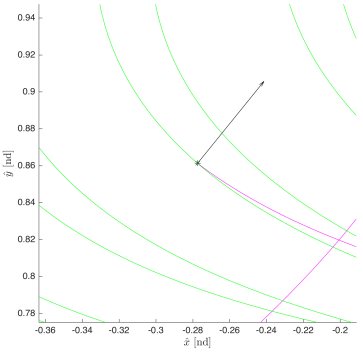

(d) W^{U^-} 87 ΔV Direction

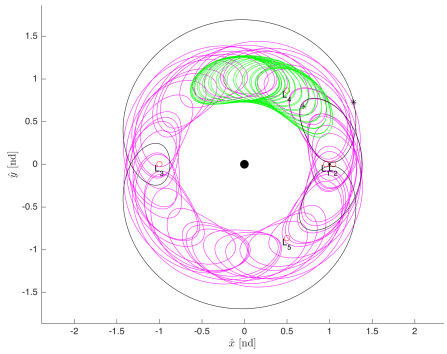

(e) W^{U^-} Trajectory 116

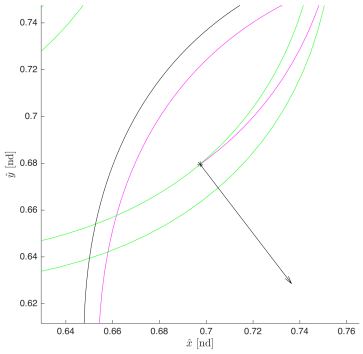

(f) W^{U^-} 116 ΔV Direction

Figure 5.37. Transfers for 3:4 Resonant W^{U^-} Manifold Trajectories

5.3 Natural Transfers from Tadpole Orbits in the Saturn-Titan System

For some mission design scenarios, consider that a spacecraft is already in a tadpole orbit. In this section, the L_5 partner of the L_4 tadpole orbit previously investigated is the initial starting orbit. This L_5 tadpole orbit seen in Figure 5.38 has the same value of Jacobi constant and period and is generated as a result of the *Mirror Theorem*. Because this L_5 tadpole orbit is also stable, natural motion will not arrive at or depart this orbit. In order to design low-cost transfer trajectories from this tadpole orbit to other orbits, the invariant manifolds of other unstable orbits may be used. A subset of the stable manifolds W^{S^+}, W^{S^-} with the same Jacobi constant as the tadpole orbit of interest can be propagated to see if any intersections in position exist. If intersections are found, an instantaneous ΔV maneuver can be applied to design a transfer trajectory from the tadpole orbit to another periodic orbit.

5.3.1 Transfers from a L_5 Tadpole Orbit Using L_3 Lyapunov Orbit Stable Manifolds

Transfers from tadpole orbits to unstable L_3 Lyapunov orbits can be designed by leveraging the stable manifolds associated with this orbit. By investigating the manifold arcs propagated previously, each of the intersections between these trajectories and the tadpole orbit can be found if they exist. Due to the complex looping motion of both the tadpole orbit and these manifolds, the states are converted to polar coordinates before computing the intersections. In Figure 5.39 an example of the positions at intersections in terms of their polar coordinates is shown.

The velocity difference at these intersections can then be computed to determine the location along each manifold trajectory with the smallest required ΔV maneuver to depart from the tadpole orbit. Because transfers from tadpole orbits are of interest in this section, intersections with the subset of stable manifold arcs W^{S^+}, W^{S^-} are computed. These trajectories are assumed to naturally arrive at the L_3 Lyapunov orbit for free, although they are a numerical approximation. For each of these man-

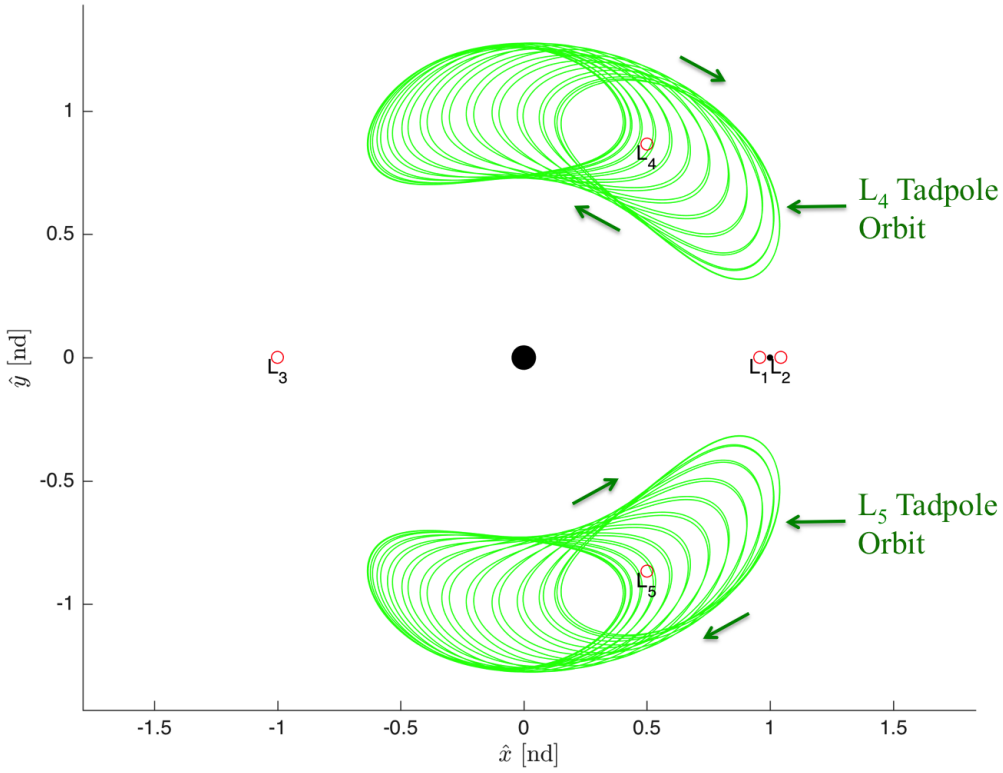

Figure 5.38. L_4 and L_5 Partner Tadpole Orbits

ifolds arcs, the intersection with the smallest velocity difference is selected. Figures 5.40 - 5.41 shows the ΔV and transfer time of flight (TOF) for the minimum ΔV case of each manifold arc for the subsets W^{S^+}, W^{S^-}. The stable manifolds can be approximated by taking a step-off d from the Lyapunov orbit; however, these trajectories depart the Lyapunov orbit in backwards time. If the correct ΔV maneuver is computed to depart the tadpole orbit and place the spacecraft along the stable manifold, these trajectories will flow towards the Lyapunov orbit in forwards time.

The information presented in Figures 5.40 - 5.41 provides a variety of low-cost transfers from the tadpole orbit to the L_3 Lyapunov orbit. The time of flight for all of these transfers is large and comparable to the time of flight for the transfers from

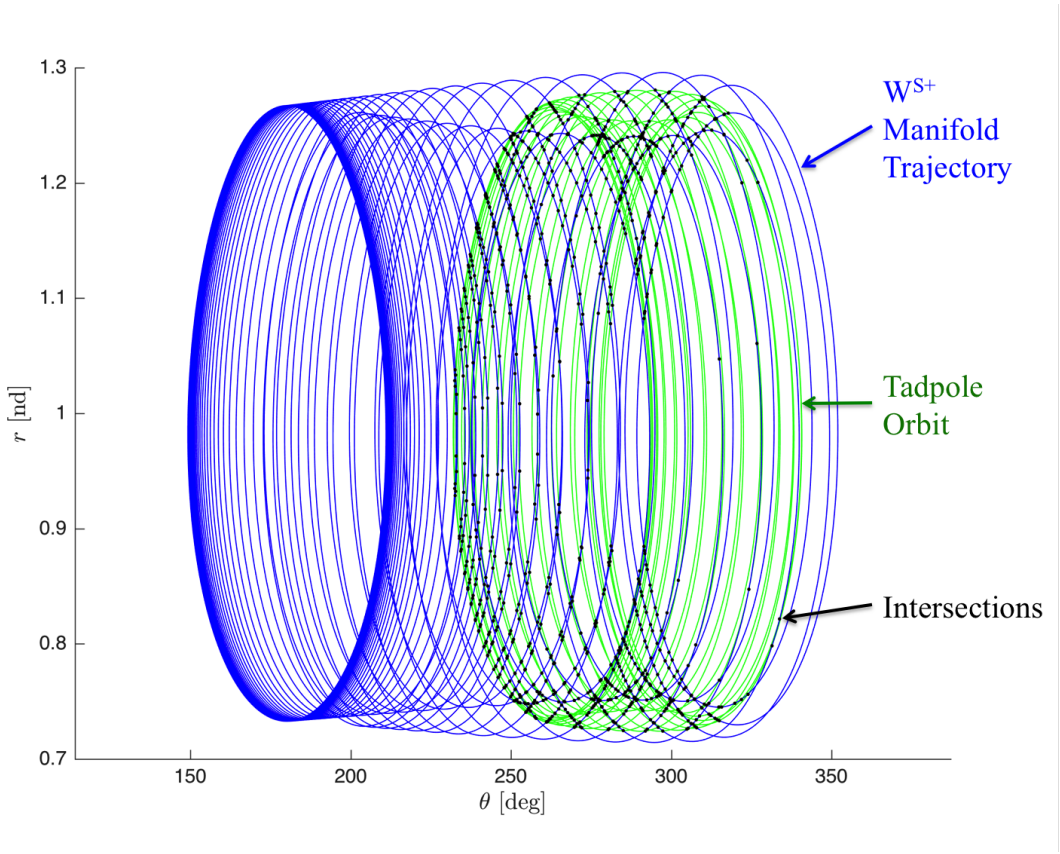

Figure 5.39. L_3 Lyapunov W^{S+} Manifold Trajectory 134 and Tadpole Orbit Intersections

the L_3 Lyapunov orbit to the L_4 tadpole orbit because the manifolds take a long time to depart the L_3 Lyapunov orbit in backwards time due to its small stability index. In Figure 5.42, the minimum ΔV transfer for manifold trajectory 134 in the W^{S+} subset is shown. The velocity change is applied at the intersection of the manifold and tadpole orbit with the smallest magnitude of this value, selected from all the options in Figure 5.39. This transfer trajectory is representative of the minimum ΔV case for all of the computed manifold arcs in this subset. A zoomed image near the departure point is presented in Figure 5.43, with the direction of the maneuver illustrated. At this point, the manifold trajectory and tadpole orbit are nearly aligned, and the velocity is applied normal to the direction of motion, following the same trend for the

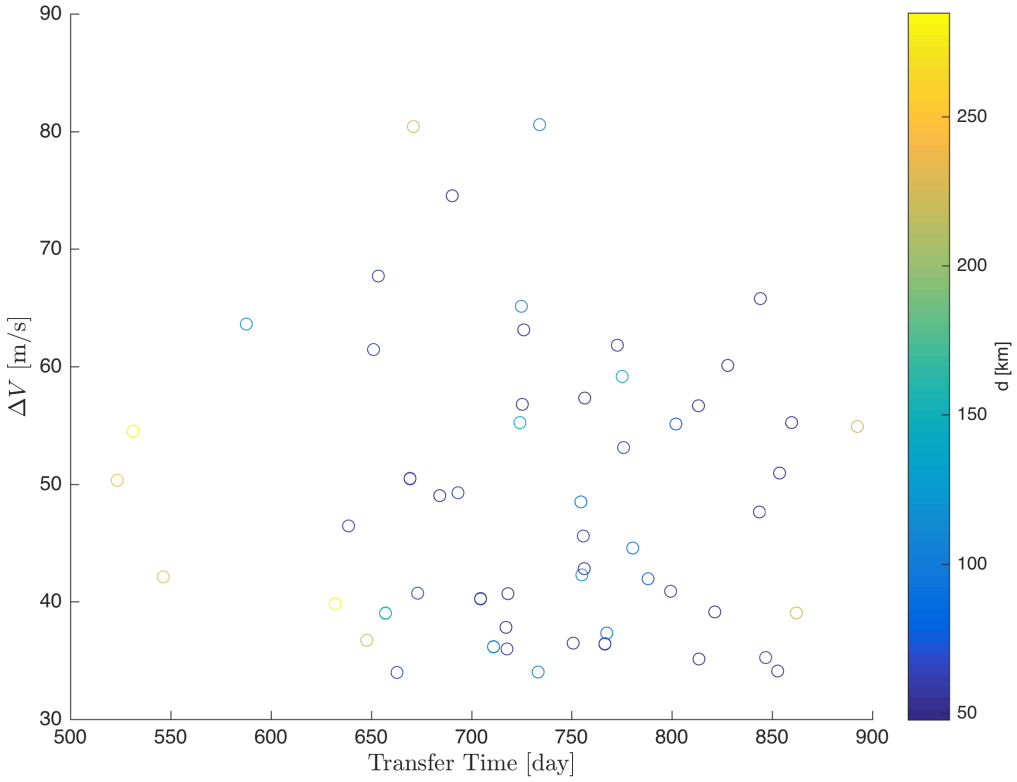

Figure 5.40. Maneuver Cost for L_3 Lyapunov W^{S+} Manifold Trajectories

unstable manifold transfers investigated previously. The angle Ψ defines the change in direction between the original direction of motion and the maneuver direction, where the spacecraft is initially moving along the tadpole orbit.

In Table 5.10, different transfers from the L_5 tadpole orbit to the L_3 Lyapunov orbit for the subset of stable manifolds W^{S+} are presented. Trajectories with the lowest ΔV cost for a range of transfer times are selected to provide a variety of options. The magnitude of the Jacobi constant difference between the manifold and tadpole orbit at the maneuver location during departure $\Delta C_d = \|C_{Manifold} - C_{Tadpole}\|$ is computed. The maneuver ΔV magnitude and components as well as the transfer time of flight (TOF) are also listed.

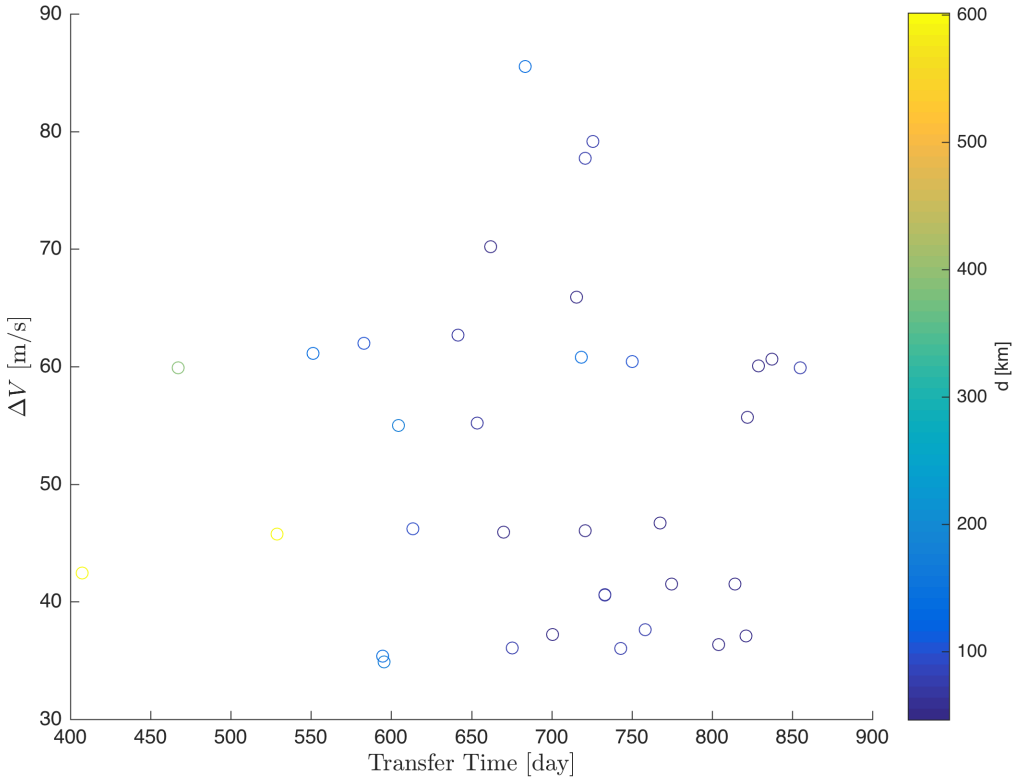

Figure 5.41. Maneuver Cost for L_3 Lyapunov W^{S^-} Manifold Trajectories

For the subset of manifold trajectories W^{S^+}, the magnitude of the ΔV cost is relatively similar across all options. Although transfers with a longer time of flight tend to have a smaller ΔV cost, this relationship does not hold for all cases. The maneuvers are always applied normal to the direction of motion along the manifold at the departure location. A value of $\Psi \approx 90°$ indicates that the maneuver is applied in a direction 90 degrees clockwise from the initial direction of motion. For cases with this value of Ψ, the maneuver is applied inwards, as seen in Figures 5.44(b), 5.44(f), and 5.45(d). A value of $\Psi \approx -90°$ indicates that the maneuver is applied in a direction 90 degrees counterclockwise from the initial direction of motion. For cases

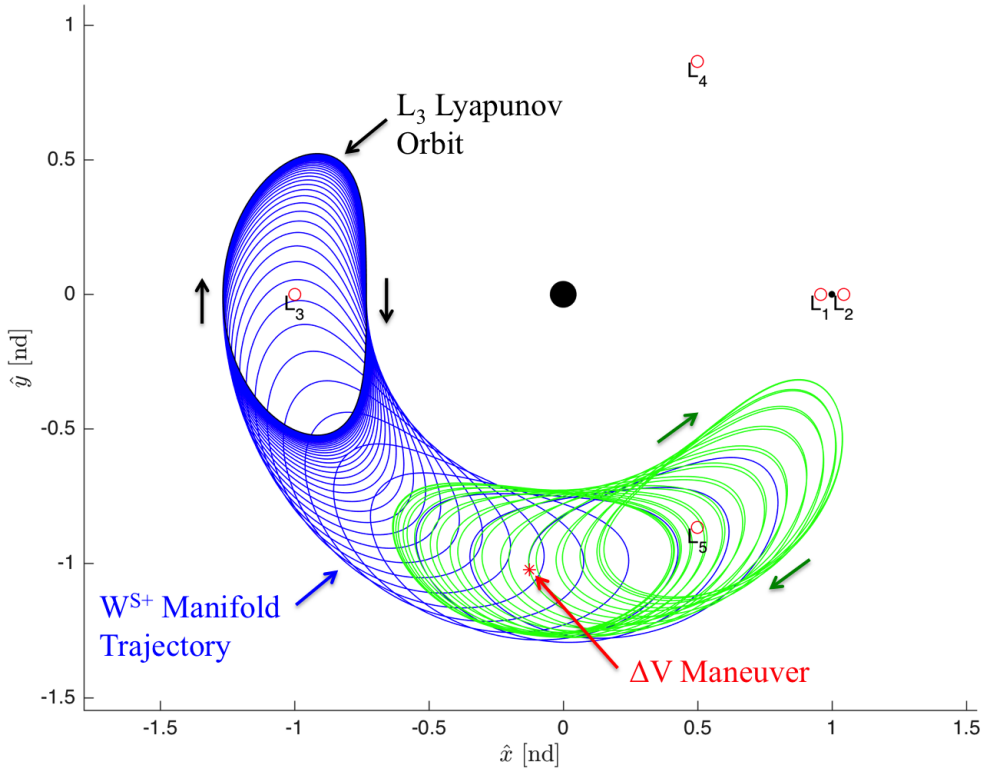

Figure 5.42. Transfer for L_3 Lyapunov W^{S^+} Manifold Trajectory 134

with this value of Ψ, the maneuver is applied outwards, as seen in Figures 5.44(d), 5.45(b) (minimum TOF case), and 5.45(f).

For the subset of manifold trajectories W^{S^-}, the magnitude of the ΔV cost is similar across all options, and all of the options require a relatively large time of flight. No transfer is found with a smaller ΔV cost than the minimum case in the subset W^{S^+}, but these minimum cases are very similar. This minimum ΔV case can be seen in Figure 5.46(c), and the case with the shortest time of flight is shown in Figure 5.46(a). Again, the maneuvers are always applied normal to the direction of motion along the manifold at the insertion location and the direction of the ΔV applied can again be characterized in the same manner by the angle Ψ.

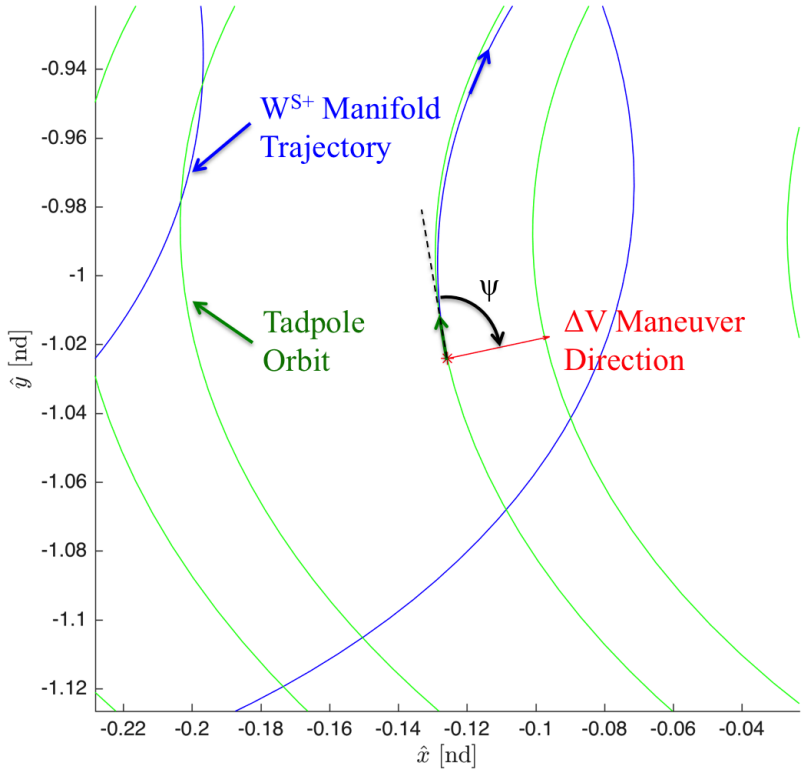

Figure 5.43. Departure ΔV for L_3 Lyapunov W^{S+} Manifold Trajectory 134

Table 5.10. Tadpole Orbit to L_3 Lyapunov Transfer Characteristics for W^{S+} Trajectories

Num.	d (km)	ΔC_d	ΔV_x (m/s)	ΔV_y (m/s)	ΔV (m/s)	Ψ (deg)	TOF (day)
103	243	1×10^{-12}	31.35	-28.09	42.10	90.69	546
110	57	6×10^{-14}	24.96	25.94	36.00	-90.68	718
111	52	8×10^{-14}	-24.62	-25.07	35.14	90.67	813
118	49	5×10^{-13}	10.63	34.90	36.48	-90.66	751
122	61	4×10^{-12}	-14.26	-32.24	35.25	90.66	847
134	68	2×10^{-12}	33.25	7.09	34.00	90.64	663
137	226	6×10^{-14}	-36.55	3.39	36.71	-90.70	648
232	243	7×10^{-12}	48.45	-13.64	50.34	-90.81	523
234	101	4×10^{-13}	-19.50	-27.88	34.02	90.65	733
239	57	5×10^{-14}	24.95	25.93	35.99	-90.67	718
249	55	3×10^{-12}	-33.90	3.58	34.08	-90.65	853
250	57	4×10^{-12}	26.84	24.61	36.41	-90.67	767

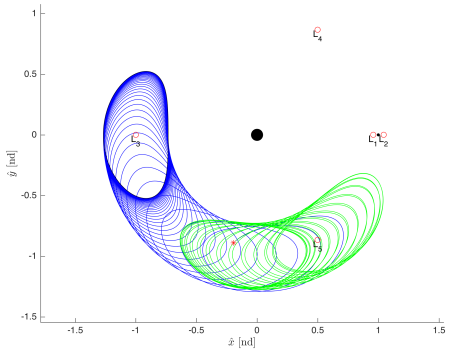

(a) W^{S^+} Trajectory 103

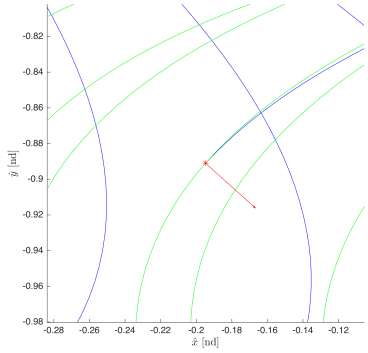

(b) W^{S^+} 103 ΔV Direction

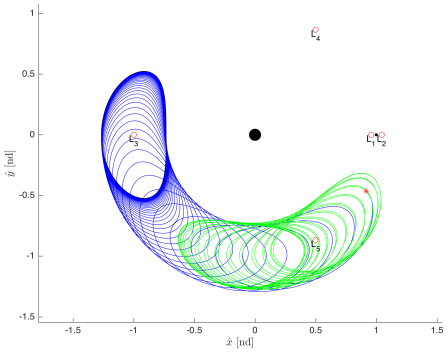

(c) W^{S^+} Trajectory 110

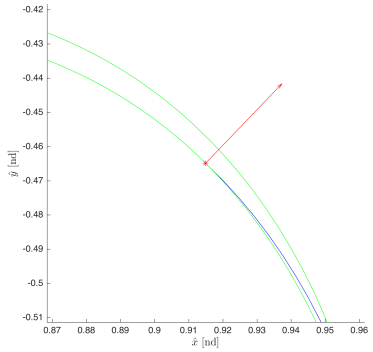

(d) W^{S^+} 110 ΔV Direction

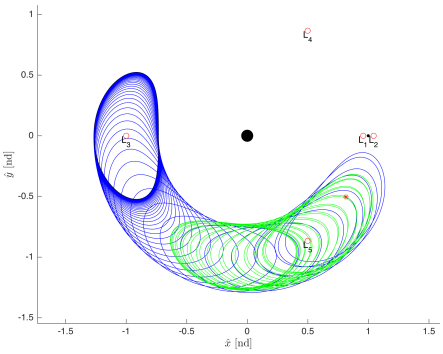

(e) W^{S^+} Trajectory 122

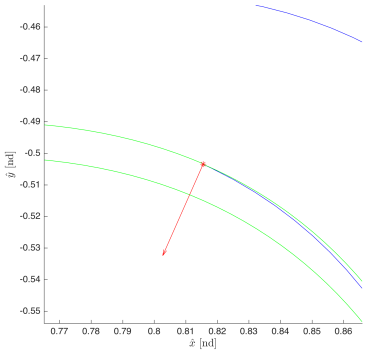

(f) W^{S^+} 122 ΔV Direction

Figure 5.44. Transfers for L_3 Lyapunov W^{S^+} Manifold Trajectories

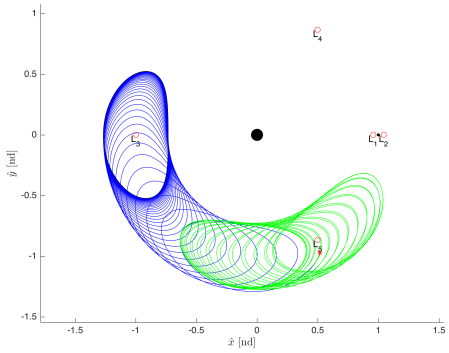

(a) W^{S^+} Trajectory 232

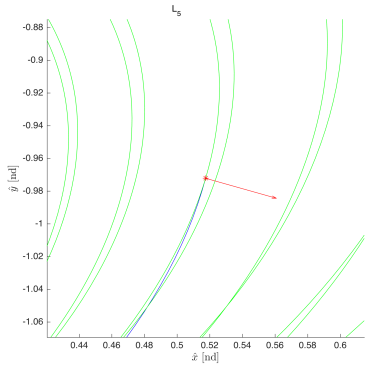

(b) W^{S^+} 232 ΔV Direction

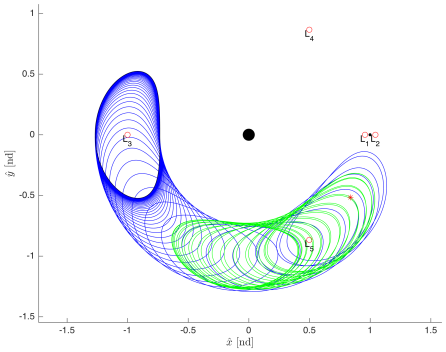

(c) W^{S^+} Trajectory 234

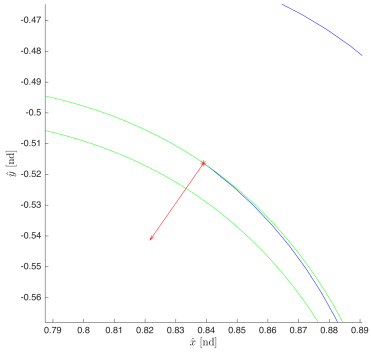

(d) W^{S^+} 234 ΔV Direction

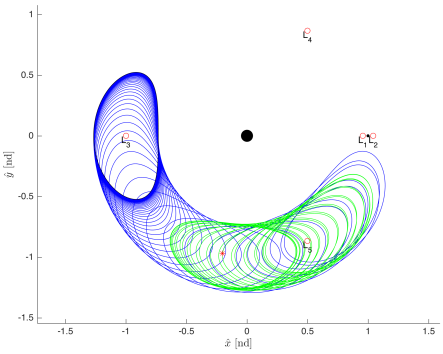

(e) W^{S^+} Trajectory 249

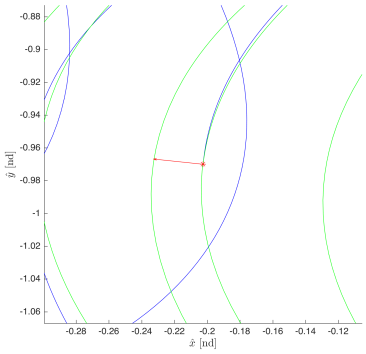

(f) W^{S^+} 249 ΔV Direction

Figure 5.45. Transfers for L_3 Lyapunov W^{S^+} Manifold Trajectories

Table 5.11. Tadpole Orbit to L_3 Lyapunov Transfer Characteristics for W^{S^-} Trajectories

Num.	d (km)	ΔC_d	ΔV_x (m/s)	ΔV_y (m/s)	ΔV (m/s)	Ψ (deg)	TOF (day)
11	602	4×10^{-14}	37.88	-19.11	42.43	90.81	407
64	176	3×10^{-12}	34.81	-1.90	34.86	90.66	596
65	141	1×10^{-12}	32.73	-13.41	35.37	90.67	595
68	54	5×10^{-14}	36.38	7.87	37.22	-90.64	701
70	67	1×10^{-11}	40.51	2.94	40.62	-90.74	733
72	47	3×10^{-14}	-33.22	16.49	37.09	-90.69	821
77	76	2×10^{-12}	-35.50	6.01	36.00	-90.67	743
78	81	2×10^{-12}	-32.67	18.65	37.62	-90.70	758
82	602	9×10^{-12}	-45.48	-5.09	45.77	90.71	529
137	80	1×10^{-13}	35.40	-6.95	36.08	90.67	675
139	54	8×10^{-14}	-35.58	7.49	36.36	-90.67	804
141	67	6×10^{-12}	40.46	2.92	40.57	-90.72	733

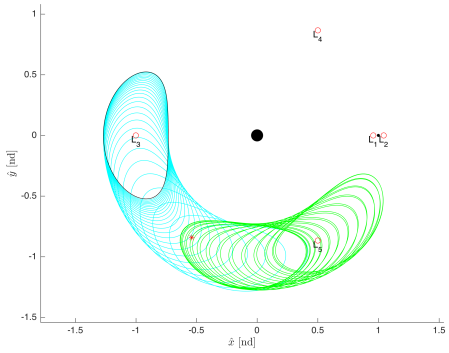

(a) W^{S^-} Trajectory 11

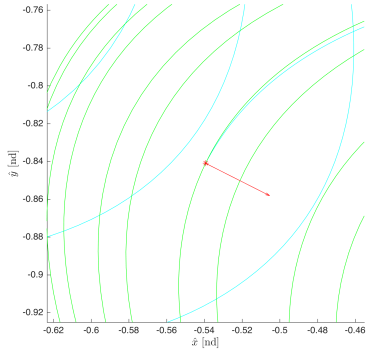

(b) W^{S^-} 11 ΔV Direction

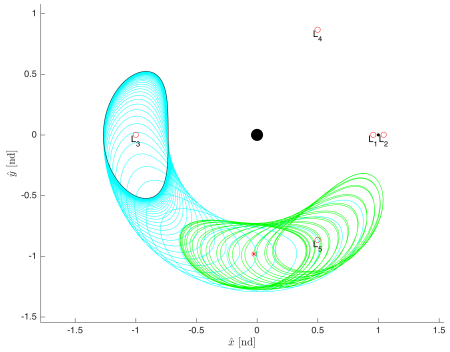

(c) W^{S^-} Trajectory 64

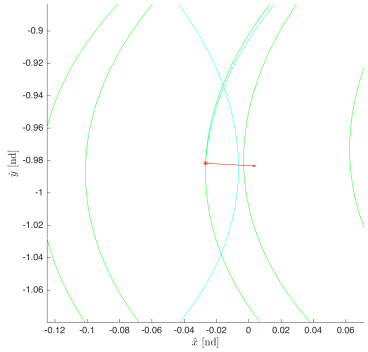

(d) W^{S^-} 64 ΔV Direction

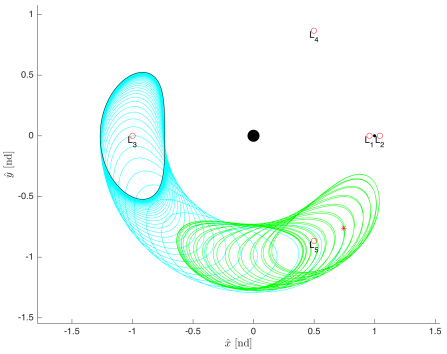

(e) W^{S^-} Trajectory 68

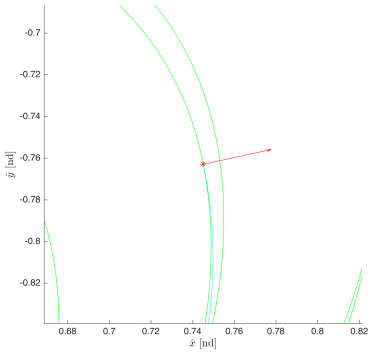

(f) W^{S^-} 68 ΔV Direction

Figure 5.46. Transfers for L_3 Lyapunov W^{S^-} Manifold Trajectories

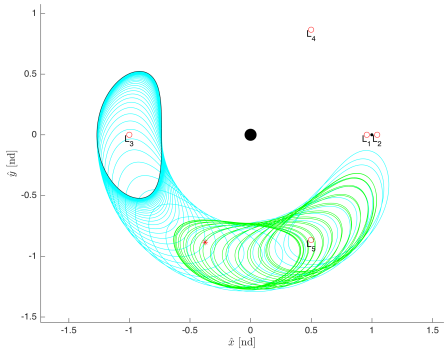

(a) W^{S^-} Trajectory 78

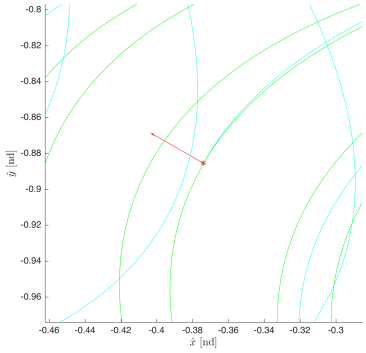

(b) W^{S^-} 78 ΔV Direction

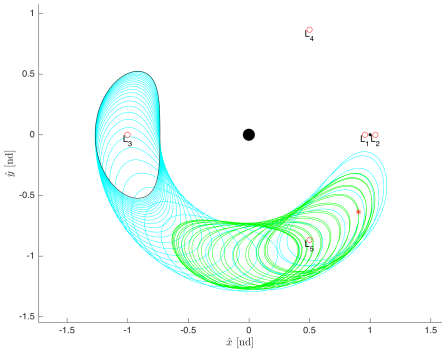

(c) W^{S^-} Trajectory 82

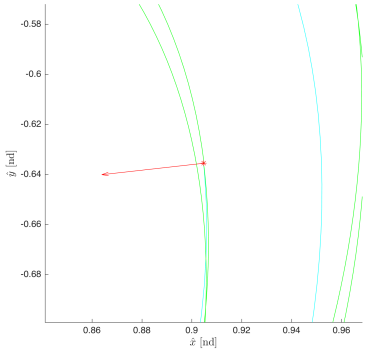

(d) W^{S^-} 82 ΔV Direction

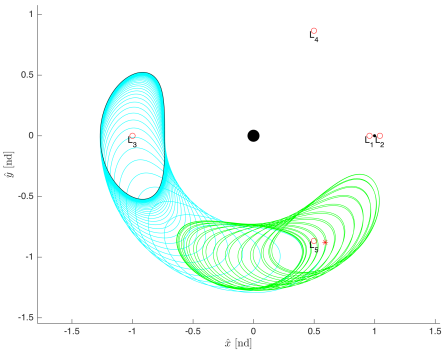

(e) W^{S^-} Trajectory 141

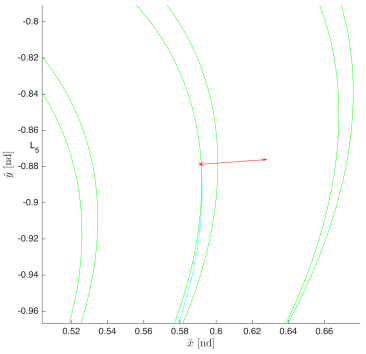

(f) W^{S^-} 141 ΔV Direction

Figure 5.47. Transfers for L_3 Lyapunov W^{S^-} Manifold Trajectories

5.3.2 Transfers from a L_5 Tadpole Orbit Using Horseshoe Orbit Stable Manifolds

Transfers from tadpole orbits to unstable horseshoe orbits can be designed by leveraging the stable manifolds associated with this orbit. By investigating the manifold arcs propagated previously for the selected horseshoe orbit, each of the intersections between these trajectories and the L_5 tadpole orbit can be found if they exist. The subset of unstable manifold arcs W^{S^+}, W^{S^-} are computed, and these trajectories are assumed to arrive at the horseshoe orbit for free in forwards time. For each of these manifolds arcs, the intersection with the smallest velocity difference is selected. Figures 5.48 - 5.49 shows the ΔV and transfer time of flight (TOF) for the minimum ΔV case of each manifold arc for the subsets W^{S^+}, W^{S^-}.

The information presented in Figures 5.48 - 5.49 provides a variety of low-cost transfers from the L_5 tadpole orbit to the resonant orbit. These transfers are similar in cost to those associated with the L_3 Lyapunov orbit, comparable to the results for the unstable manifold transfer trajectories investigated previously. The time of flight has a variety of options because the horseshoe orbit extends much further than the Lyapunov orbit, providing transfers that depart from the orbit at different locations which are closer to or farther from the tadpole orbit. It is important to note that although the transfer time of flight may be short, it may take a long time for the spacecraft to reach a desired location along the horseshoe orbit due to the long period of this orbit. In Table 5.12, different transfers from the tadpole orbit to the horseshoe orbit for the subset of stable manifolds W^{S^+} are presented.

For the subset of manifold trajectories W^{S^+}, the magnitude of the ΔV cost is similar across all options. Differing from the transfers associated with the L_3 Lyapunov orbit, some of these transfers have a very short time of flight. The maneuvers are always applied normal to the direction of motion along the manifold at the insertion location, with the direction of the ΔV applied characterized in the same manner as the transfers associated with the L_3 Lyapunov orbit manifolds by the angle Ψ.

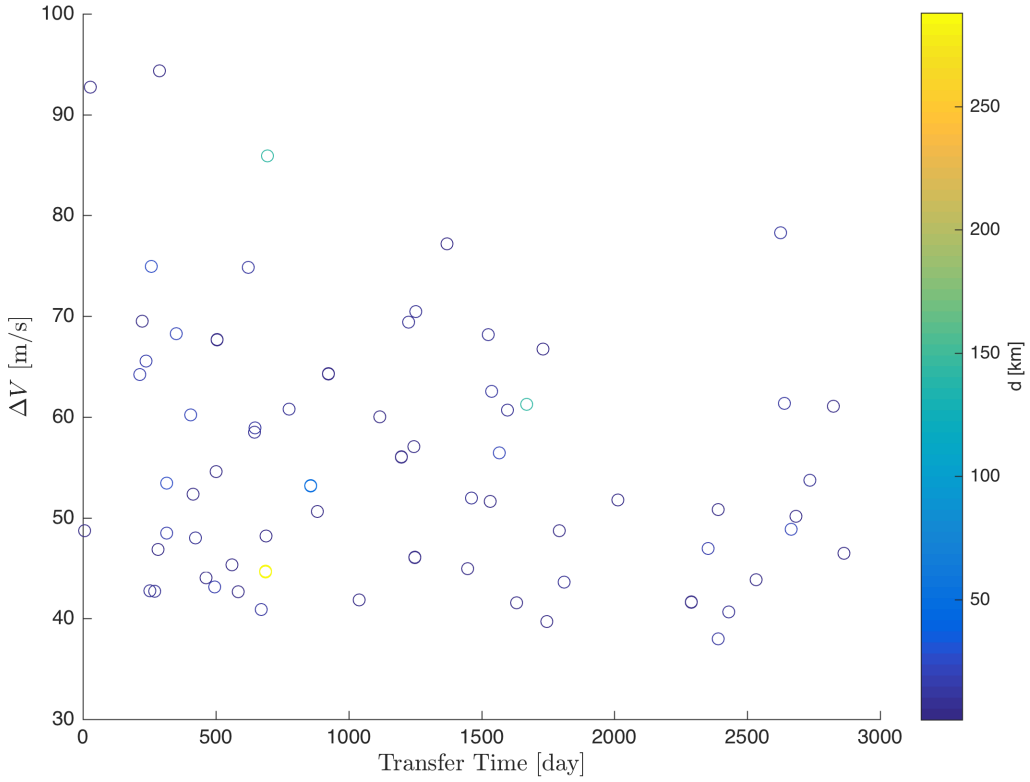

Figure 5.48. Maneuver Cost for Horseshoe Orbit W^{S+} Manifold Trajectories

When the value of $\Psi \approx 270°$, the maneuver is applied in a direction 270 degrees counterclockwise from the initial direction of motion. For cases with this value of Ψ, the maneuver is applied outwards, as seen in Figure 5.51(e) (which is the minimum transfer time case). These transfers are all very similar in appearance, as the manifold arcs follow the motion of the horseshoe orbit. For transfers with a short time of flight, the trajectories are nearly indistinguishable from the horseshoe orbit. The minimum ΔV case can be seen in Figure 5.51(a), and this transfer takes a very long time to complete.

For the subset of manifold trajectories W^{S-}, the magnitude of the ΔV cost is similar across all options, and the time of flight again varies. The minimum ΔV case

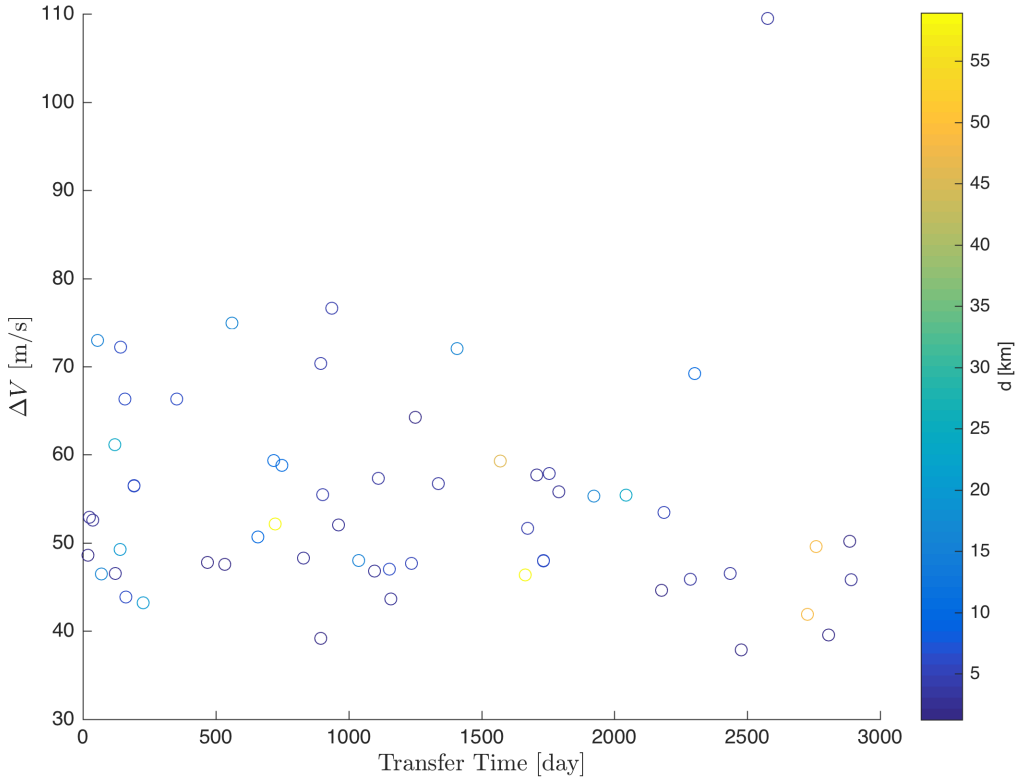

Figure 5.49. Maneuver Cost for Horseshoe Orbit W^{S^-} Manifold Trajectories

is slightly smaller than the one computed for the subset W^{S^+}, and it can be seen in Figure 5.52(a). The case with the shortest time of flight is shown in Figure 5.53(c). Again, the maneuvers are always applied normal to the direction of motion along the manifold at the insertion location. Although the minimum ΔV case has a very small ΔV_y component, it is important to note that the cases with the smallest total ΔV do not necessarily follow this trend.

Table 5.12. Tadpole to Horseshoe Orbit Transfer Characteristics for W^{S^+} Trajectories

Num.	d (km)	ΔC_d	ΔV_x (m/s)	ΔV_y (m/s)	ΔV (m/s)	Ψ (deg)	TOF (day)
17	3	5×10^{-14}	-43.04	8.44	43.86	-90.84	2533
22	4	6×10^{-14}	-12.48	-37.71	39.72	90.71	1746
25	4	8×10^{-14}	-38.51	-15.62	41.55	269.22	1633
27	12	2×10^{-14}	40.41	-6.16	40.88	90.78	671
39	2	1×10^{-14}	27.58	31.46	41.84	-90.80	1039
41	6	2×10^{-14}	-34.90	-20.88	40.67	90.78	2431
42	15	9×10^{-14}	-22.93	-30.25	37.96	90.71	2390
46	6	1×10^{-14}	15.23	39.89	42.70	-90.80	270
56	18	8×10^{-14}	-41.83	10.53	43.13	-90.77	495
66	1	5×10^{-14}	38.81	17.72	42.66	90.75	584
78	3	4×10^{-15}	-45.81	-16.63	48.73	269.14	6
81	3	7×10^{-14}	-37.46	-18.12	41.61	90.79	2289

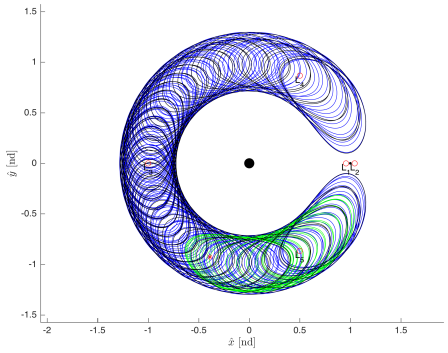

(a) W^{S^+} Trajectory 17

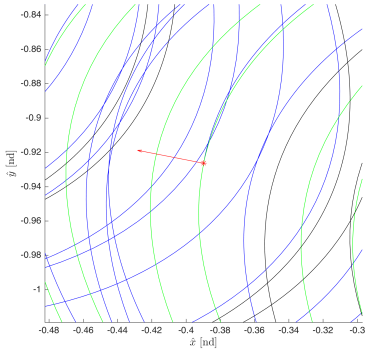

(b) W^{S^+} 17 ΔV Direction

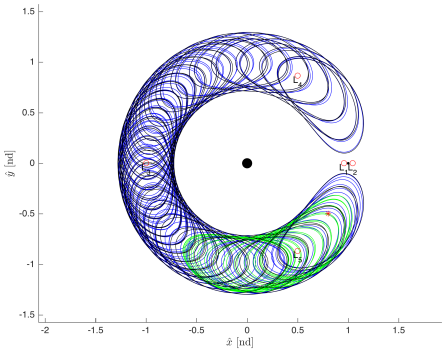

(c) W^{S^+} Trajectory 22

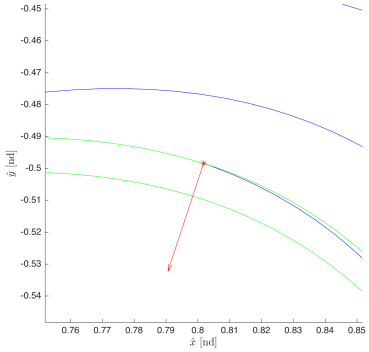

(d) W^{S^+} 22 ΔV Direction

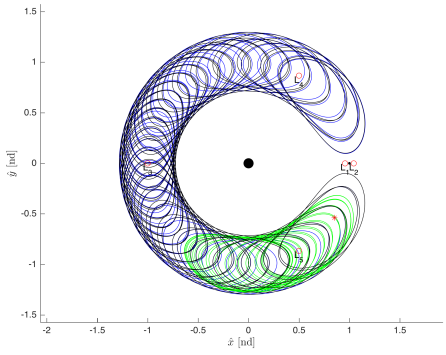

(e) W^{S^+} Trajectory 39

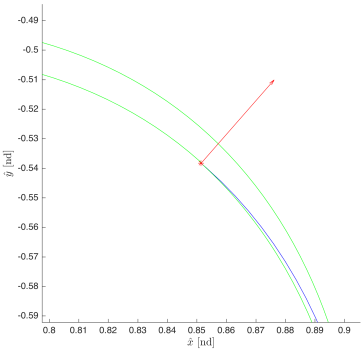

(f) W^{S^+} 39 ΔV Direction

Figure 5.50. Transfers for Horseshoe Orbit W^{S^+} Manifold Trajectories

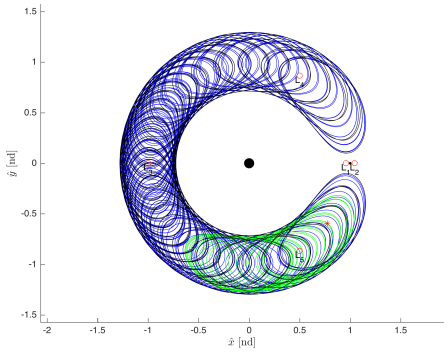

(a) W^{S^+} Trajectory 42

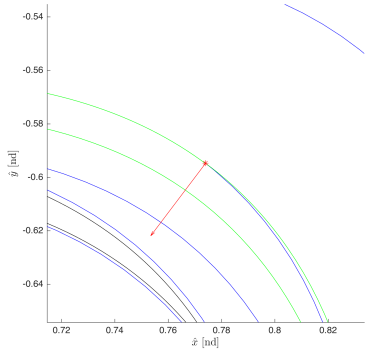

(b) W^{S^+} 42 ΔV Direction

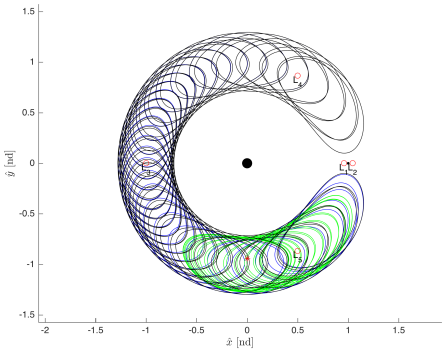

(c) W^{S^+} Trajectory 56

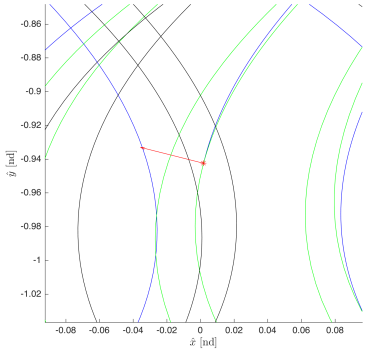

(d) W^{S^+} 56 ΔV Direction

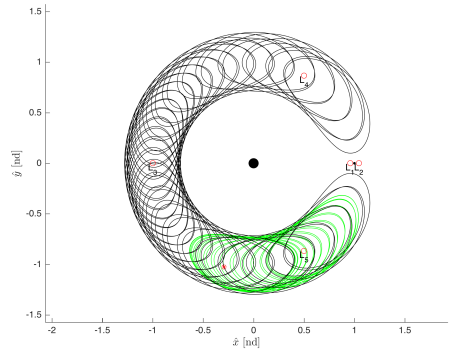

(e) W^{S^+} Trajectory 78

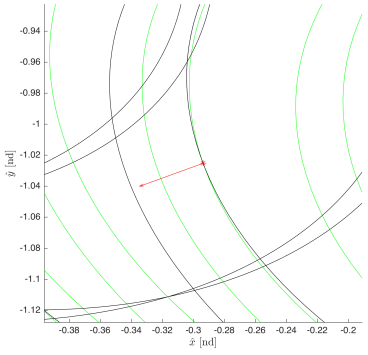

(f) W^{S^+} 78 ΔV Direction

Figure 5.51. Transfers for Horseshoe Orbit W^{S^+} Manifold Trajectories

Table 5.13. Tadpole to Horseshoe Orbit Transfer Characteristics for W^{S^-} Trajectories

Num.	d (km)	ΔC_d	ΔV_x (m/s)	ΔV_y (m/s)	ΔV (m/s)	Ψ (deg)	TOF (day)
3	2	6×10^{-14}	-37.87	0.27	37.87	-90.72	2477
10	59	2×10^{-13}	-39.09	24.94	46.37	-90.83	1664
18	1	1×10^{-14}	38.65	-6.42	39.18	90.75	895
27	6	2×10^{-14}	-43.74	-3.01	43.84	269.18	161
29	20	4×10^{-15}	-43.19	0.29	43.19	-90.82	226
36	2	1×10^{-13}	34.56	28.25	44.63	-90.85	2177
39	48	1×10^{-13}	40.92	9.15	41.93	90.75	2726
50	1	3×10^{-15}	-45.79	-16.34	48.62	269.15	19
53	16	4×10^{-15}	-45.05	-11.35	46.46	269.16	70
54	2	2×10^{-14}	23.16	32.09	39.57	-90.76	2806
57	3	1×10^{-14}	-45.10	-11.48	46.54	269.16	122
65	3	2×10^{-6}	39.23	19.19	43.67	-90.86	1158

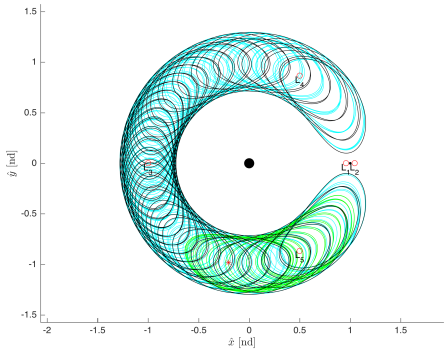

(a) W^{S^-} Trajectory 3

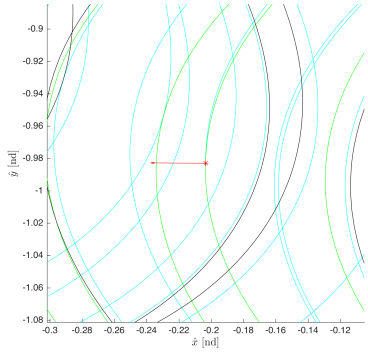

(b) W^{S^-} 3 ΔV Direction

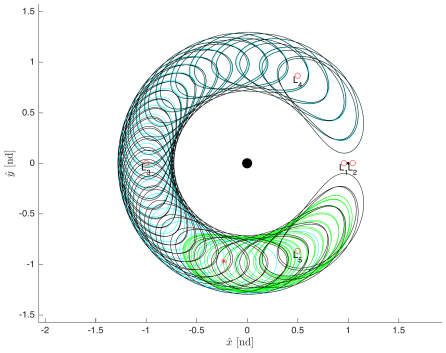

(c) W^{S^-} Trajectory 18

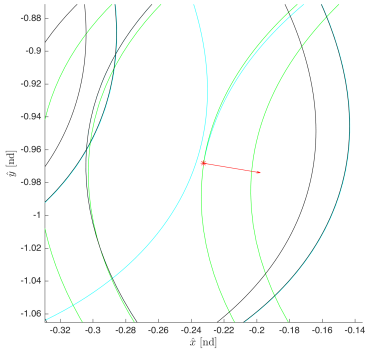

(d) W^{S^-} 18 ΔV Direction

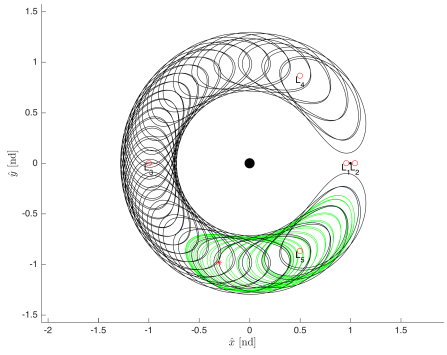

(e) W^{S^-} Trajectory 27

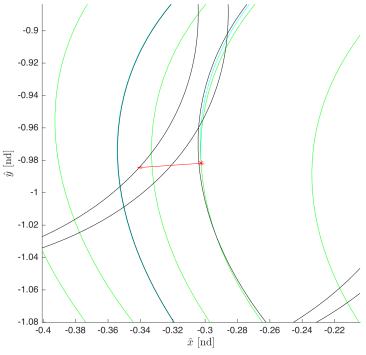

(f) W^{S^-} 27 ΔV Direction

Figure 5.52. Transfers for Horseshoe Orbit W^{S^-} Manifold Trajectories

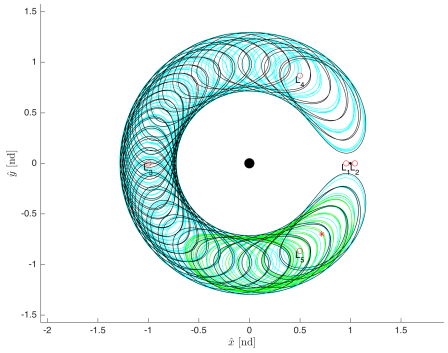

(a) W^{S^-} Trajectory 36

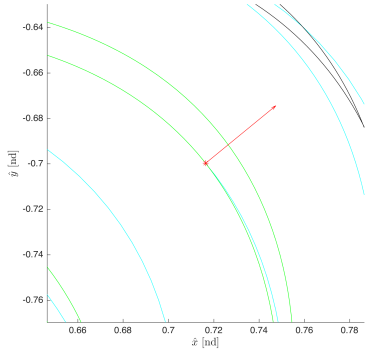

(b) W^{S^-} 36 ΔV Direction

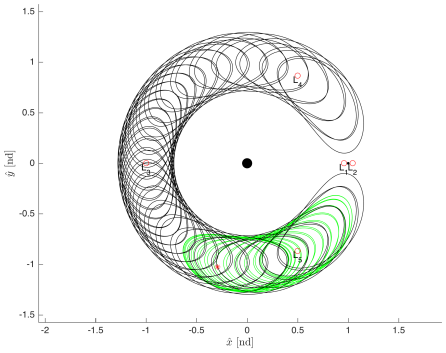

(c) W^{U^-} Trajectory 50

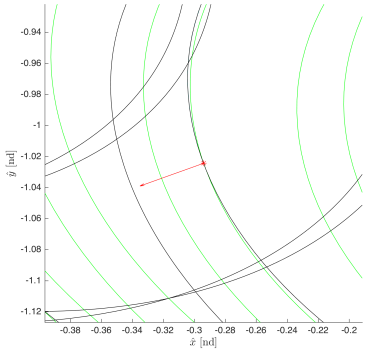

(d) W^{S^-} 50 ΔV Direction

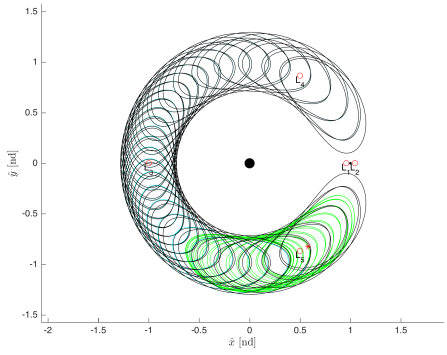

(e) W^{S^-} Trajectory 65

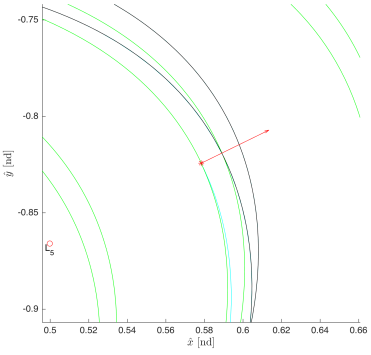

(f) W^{S^-} 65 ΔV Direction

Figure 5.53. Transfers for Horseshoe Orbit W^{S^-} Manifold Trajectories

5.3.3 Transfers from a L_5 Tadpole Orbit Using Planar Resonant Orbit Stable Manifolds

Transfers from tadpole orbits to unstable resonant orbits can be designed by leveraging the stable manifolds associated with this orbit. By investigating the manifold arcs propagated previously for the selected 3:4 resonant orbit, each of the intersections between these trajectories and the L_5 tadpole orbit can be found if they exist. The subset of unstable manifold arcs W^{S^+}, W^{S^-} are computed, and these trajectories are assumed to depart the resonant orbit for free, and the intersection with the smallest velocity difference is selected for each of these manifold arcs. Figures 5.54 - 5.55 shows the ΔV and transfer time of flight (TOF) for the minimum ΔV case of each manifold arc for the subsets W^{S^+}, W^{S^-}.

The information presented in Figures 5.54 - 5.55 provides a variety of seemingly low-cost transfers from the L_4 tadpole orbit to the 3:4 resonant orbit. Overall, these transfers are much more expensive than those associated with the L_3 Lyapunov and horseshoe orbits. These manifold trajectories have motion that is not as close to that of the tadpole orbit as those associated with the other orbits investigated. In Figure 5.54, it appears that some cheaper transfers should exist. For these cases, the trajectory does flow into the resonant orbit after applying the departure maneuver and integrating the state, so a viable transfer trajectory does not exist and these cases are discarded. This error may be a result of the intersection between the tadpole orbit and stable manifold trajectory to be an exact match in position, when some error does exist. In Table 5.14, different transfers from the resonant orbit to the tadpole orbit for the subset of unstable manifolds W^{S^+} are presented.

For the subset of manifold trajectories W^{S^+}, the magnitude of the ΔV cost and the time of flight varies greatly across all options. The maneuvers are always applied normal to the direction of motion along the manifold at the insertion location; however, this angle is offset more than the previous transfers examined for the L_3 Lyapunov and horseshoe orbits. This difference in the angle Ψ from the normal di-

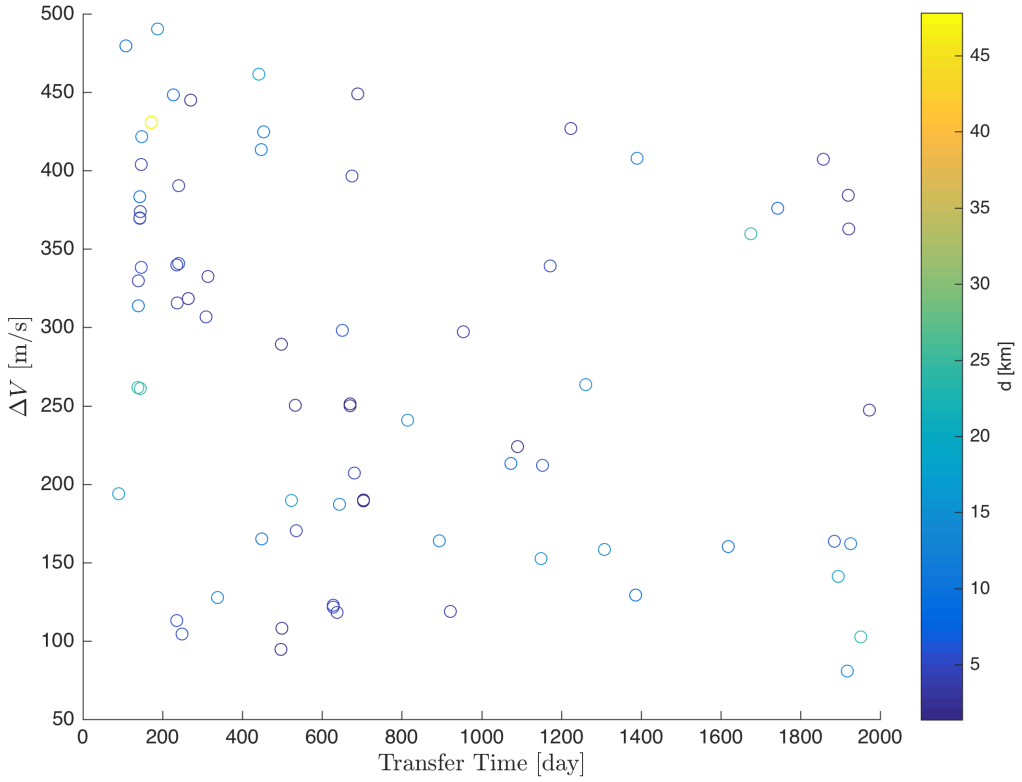

Figure 5.54. Maneuver Cost for 3:4 Resonant W^{S+} Manifold Trajectories

rection correlates directly with these maneuvers costing more than those for the other orbits investigated. The case with the shortest time of flight is not the most expensive case in terms of ΔV cost, and it can be seen in Figure 5.57(e). The minimum ΔV case can be seen in Figure 5.57(a), and this transfer does not take the longest time to complete out of all the available options.

For the subset of manifold trajectories W^{S-}, the magnitude of the ΔV cost and time of flight again varies across all options; however, a cheaper option is found than the minimum case in the subset W^{S+}. This minimum ΔV case can be seen in Figure 5.58(c), and the case with the shortest time of flight is shown in Figure 5.59(c). Again,

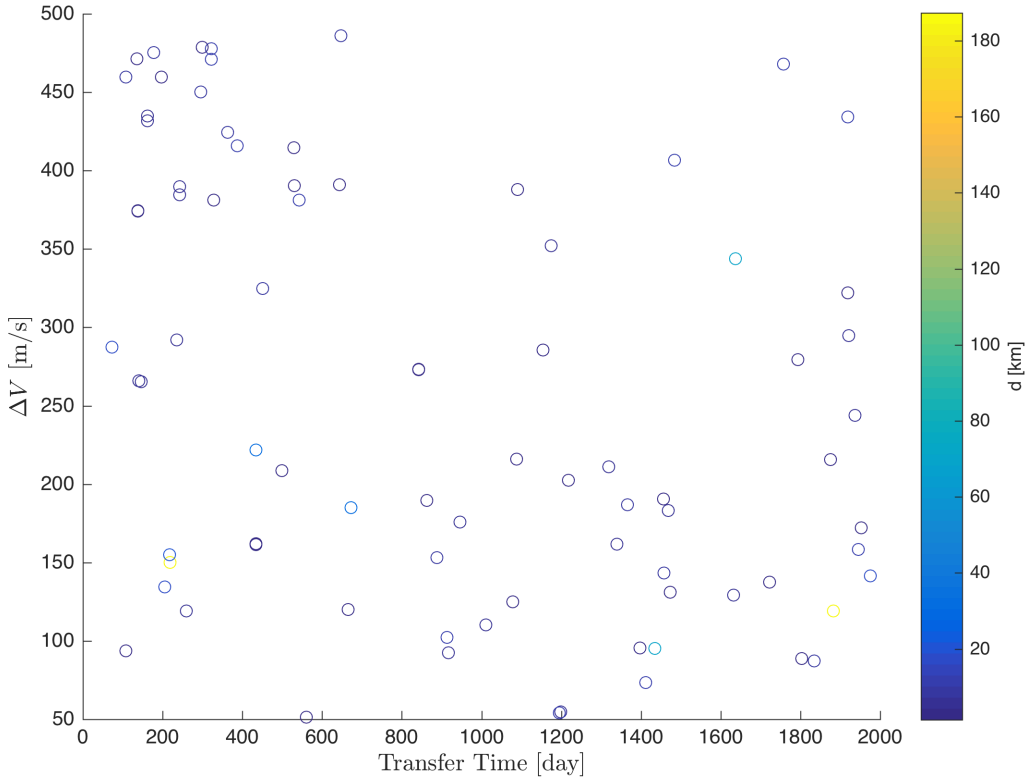

Figure 5.55. Maneuver Cost for 3:4 Resonant W^{S^-} Manifold Trajectories

the maneuvers are applied with a slight deviation from the normal to the direction of motion along the tadpole orbit at the departure location.

Table 5.14. Tadpole to 3:4 Resonant Orbit Transfer Characteristics for W^{S^+} Trajectories

Num.	d (km)	ΔC_d	ΔV_x (m/s)	ΔV_y (m/s)	ΔV (m/s)	Ψ (deg)	TOF (day)
31	10	9×10^{-15}	130.97	100.46	165.06	-93.01	448
41	6	5×10^{-12}	-4.00	-112.84	112.91	91.63	236
63	4	1×10^{-15}	115.58	-41.06	122.66	-92.00	628
65	24	3×10^{-11}	256.31	49.22	260.99	94.93	143
68	4	9×10^{-15}	97.54	-66.88	118.27	92.25	638
115	6	7×10^{-15}	-102.58	18.95	104.32	-268.20	249
137	4	1×10^{-14}	115.13	-38.85	121.51	-91.99	628
139	24	6×10^{-14}	212.53	152.70	261.70	-95.00	137
142	4	3×10^{-14}	97.53	-66.90	118.27	92.25	638
149	17	9×10^{-16}	-124.95	148.19	193.83	-93.06	90

Table 5.15. Tadpole to 3:4 Resonant Orbit Transfer Characteristics for W^{S^-} Trajectories

Num.	d (km)	ΔC_d	ΔV_x (m/s)	ΔV_y (m/s)	ΔV (m/s)	Ψ (deg)	TOF (day)
6	4	3×10^{-15}	174.32	74.64	189.63	93.52	862
16	3	1×10^{-14}	-76.14	54.74	93.77	-91.45	107
23	1	3×10^{-14}	208.54	3.64	208.57	-93.59	499
63	5	4×10^{-15}	142.20	255.17	292.12	-95.55	236
74	31	3×10^{-14}	-156.57	-98.55	185.00	93.44	672
83	16	2×10^{-11}	-222.09	-182.60	287.52	264.75	72
118	187	4×10^{-13}	-135.29	64.59	149.92	-92.74	219
137	16	2×10^{-11}	129.71	-35.66	134.52	92.56	205
138	19	2×10^{-11}	14.36	154.33	155.00	-92.74	218
151	5	2×10^{-6}	48.36	108.73	119.00	-92.04	259

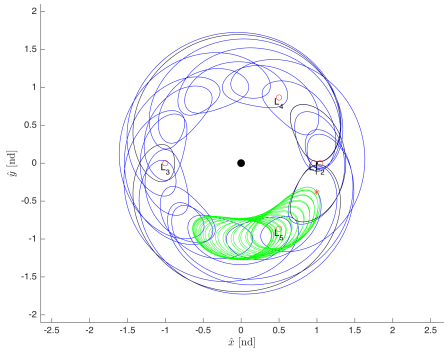

(a) W^{S^+} Trajectory 31

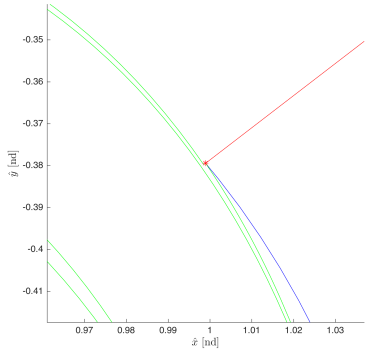

(b) W^{S^+} 31 ΔV Direction

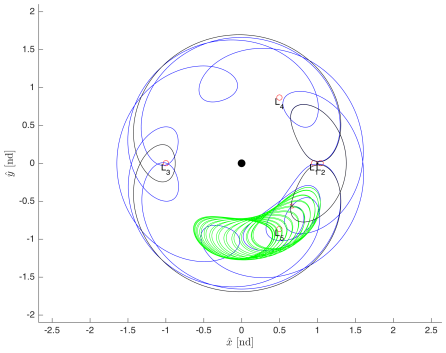

(c) W^{S^+} Trajectory 41

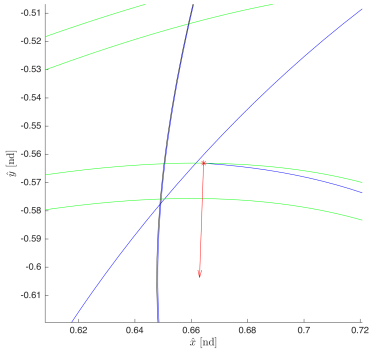

(d) W^{S^+} 41 ΔV Direction

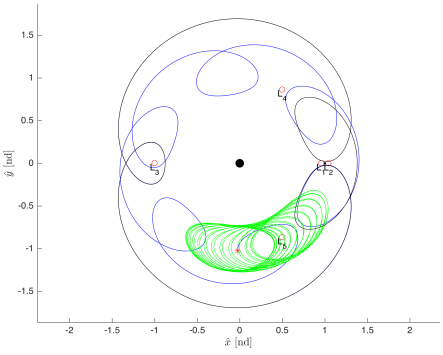

(e) W^{S^+} Trajectory 65

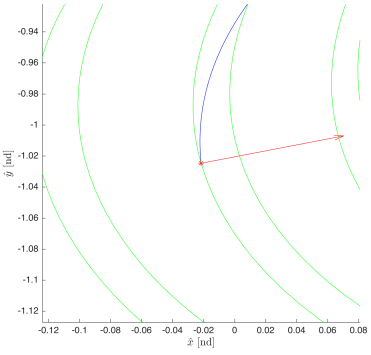

(f) W^{S^+} 65 ΔV Direction

Figure 5.56. Transfers for 3:4 Resonant W^{S^+} Manifold Trajectories

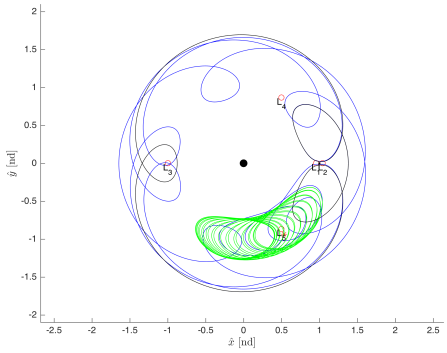

(a) W^{S^+} Trajectory 115

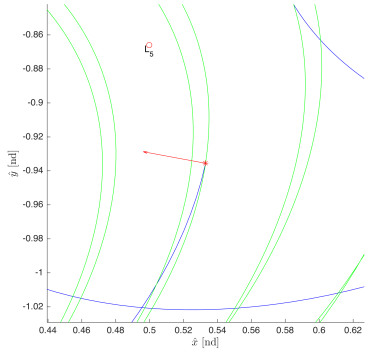

(b) W^{S^+} 115 ΔV Direction

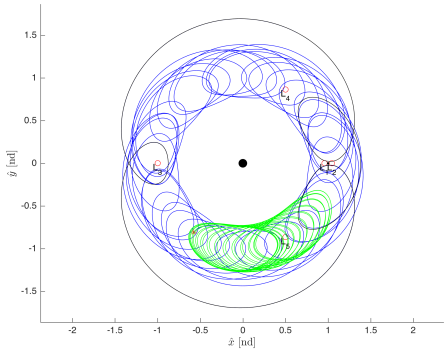

(c) W^{S^+} Trajectory 142

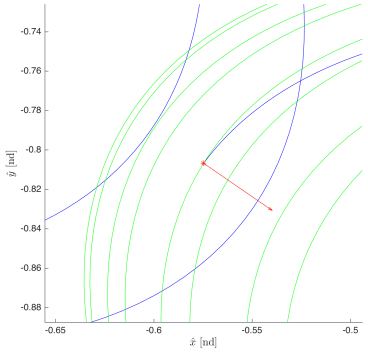

(d) W^{S^+} 142 ΔV Direction

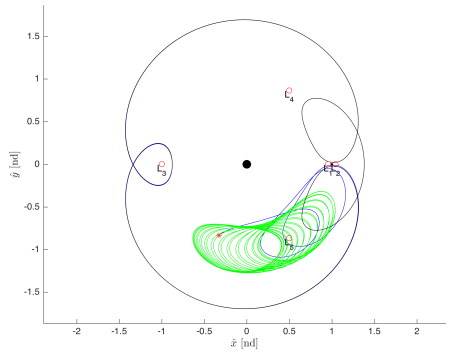

(e) W^{S^+} Trajectory 149

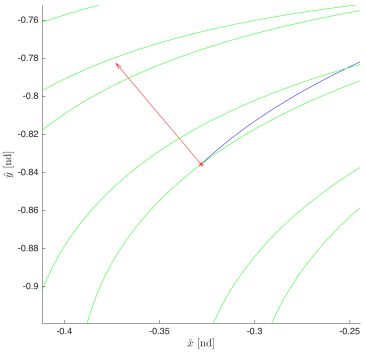

(f) W^{S^+} 149 ΔV Direction

Figure 5.57. Transfers for 3:4 Resonant W^{S^+} Manifold Trajectories

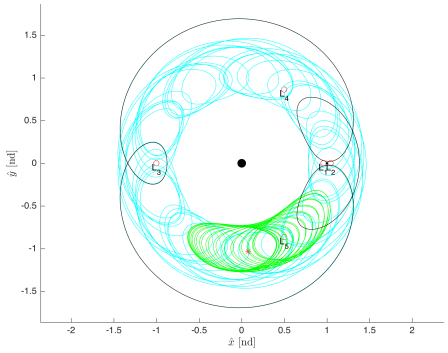

(a) W^{S^-} Trajectory 6

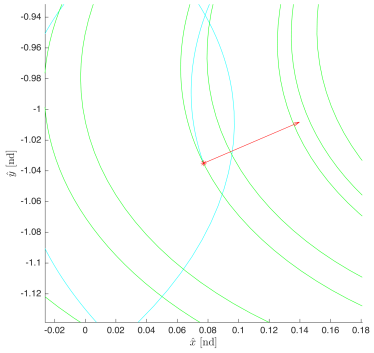

(b) W^{S^-} 6 ΔV Direction

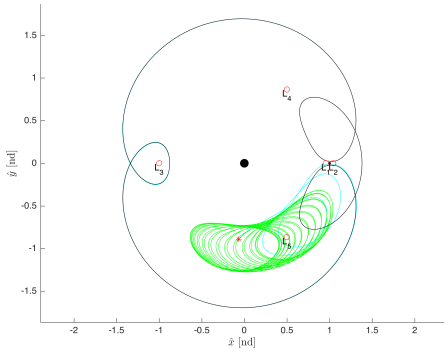

(c) W^{S^-} Trajectory 16

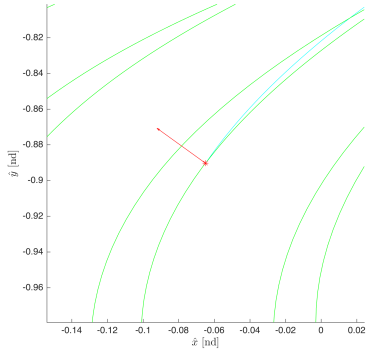

(d) W^{S^-} 16 ΔV Direction

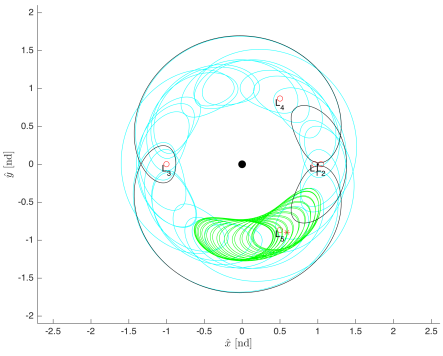

(e) W^{S^-} Trajectory 23

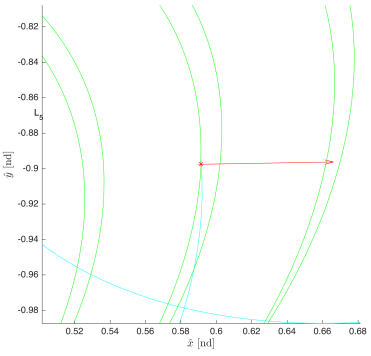

(f) W^{S^-} 23 ΔV Direction

Figure 5.58. Transfer for 3:4 Resonant W^{S^-} Manifold Trajectories

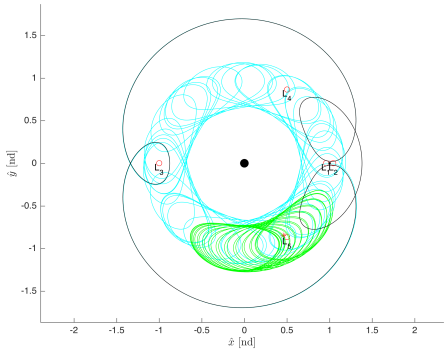

(a) W^{S^-} Trajectory 74

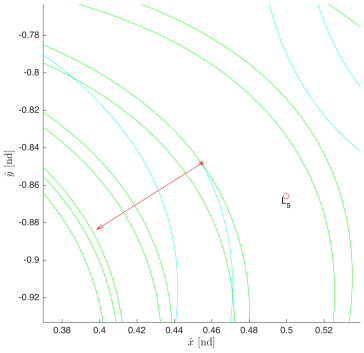

(b) W^{S^-} 74 ΔV Direction

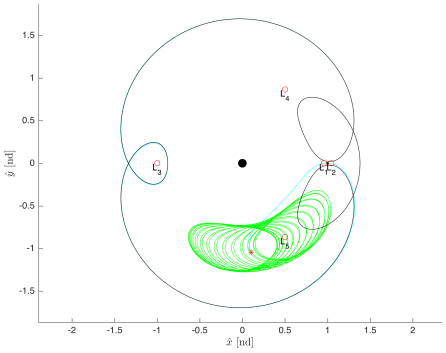

(c) W^{S^-} Trajectory 83

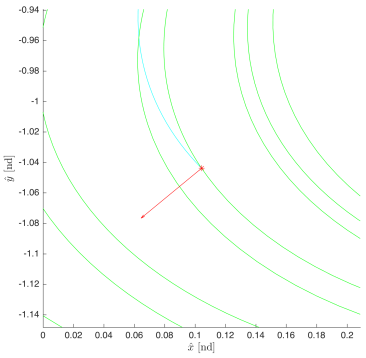

(d) W^{S^-} 83 ΔV Direction

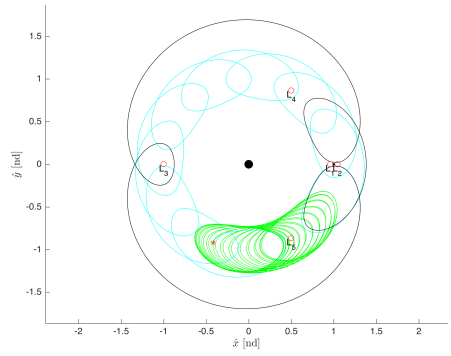

(e) W^{S^-} Trajectory 137

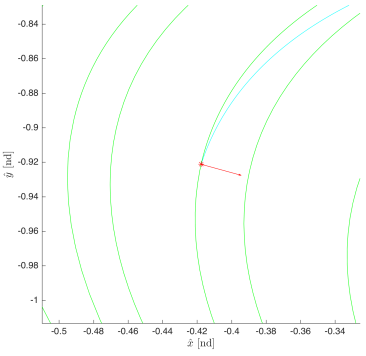

(f) W^{S^-} 137 ΔV Direction

Figure 5.59. Transfer for 3:4 Resonant W^{S^-} Manifold Trajectories

5.4 Transport Between the Triangular Points

For some mission design scenarios, it may be desirable to move from a stable orbit around one of the triangular points to a stable orbit around the other. Because the tadpole orbits being investigated are stable, they do not have natural motion departing or arriving at them. The invariant manifolds from other orbits can be used to design transfers between these equilateral points, with the goal of reducing ΔV cost by leveraging the natural dynamics. The invariant manifolds of these associated orbits may also help explain the natural transfer of some Trojan asteroids from a tadpole orbit around one of the triangular points to a tadpole orbit around the other. For this investigation, transfer trajectories are designed for different mission scenarios where the required perturbation to transition the motion between these invariant manifolds and a tadpole orbit is performed by inserting an instantaneous ΔV maneuver.

5.4.1 Planar Transfers from L_5 to L_4 Using Invariant Manifolds

Transfers from one of the triangular points to another orbit by inserting on to a stable manifold trajectory can provide an intermediate step in reaching the other triangular point. After the spacecraft reaches this intermediate orbit, it can depart on an unstable manifold trajectory to reach the other Lagrange point. The stable manifolds of the L_3 Lyapunov orbit and other orbits previously investigated can be used to design the first part of one of these transfers, departing from an L_5 tadpole orbit. In order to design the remainder of the transfer, the associated unstable manifolds can then be used to send the spacecraft to the final L_4 tadpole orbit. Table 5.16 presents all combination of the minimum ΔV and minimum time of flight cases for the maneuvers computed earlier, using the L_3 Lyapunov orbit invariant manifolds. The subsets in which the manifold trajectories exist W_1 and W_2 as well as the number of the computed manifold trajectory are listed for the first and second transfer arcs, respectively. The value of ΔV_1 gives the magnitude of the maneuver required to depart the initial L_5 tadpole orbit, and ΔV_2 refers to the L_4 tadpole orbit insertion

maneuver. The time of flight for these transfer trajectory legs are defined by T_1 and T_2. Because the spacecraft will not reach the intermediate orbit in the same location as the unstable manifold departs towards the L_4 tadpole orbit, it must coast along this orbit for the time ΔT. This geometry will repeat for every period of the intermediate orbit, so the spacecraft can wait in this intermediate orbit if it is beneficial to a mission. Finally, the total cost for the L_5 to L_4 transfer ΔV_t and total flight time T_t are listed. The minimum ΔV case can be seen in Figure 5.60. This transfer takes almost four years to complete; however, it is completed with a small ΔV cost. The minimum transfer time case can be seen in Figure 5.61. This transfer is completed in a year shorter than the minimum ΔV case for only a small penalty in ΔV cost.

Table 5.17 presents all combination of the minimum ΔV and minimum time of flight cases for the maneuvers computed earlier, using the horseshoe orbit invariant manifolds. The minimum ΔV case can be seen in Figure 5.62. This transfer takes almost 16 years to complete, which is likely too long for most mission design scenarios. The minimum transfer time case can be seen in Figure 5.63, and it is completed in less than two years. It is difficult to see the manifold arcs used in this transfer because they follow the path of the horseshoe orbit with only a very slight divergence. The ΔV penalty is relatively small when considering how much shorter the time of flight is for this transfer when comparing to the minimum ΔV case.

Table 5.18 presents all combination of the minimum ΔV and minimum time of flight cases for the maneuvers computed earlier, using the 3:4 resonant orbit invariant manifolds. The minimum ΔV case can be seen in Figure 5.64. This transfer takes about the same time as the minimum ΔV case for the transfers using the L_3 Lyapunov orbit manifolds, but it is much more costly. The minimum transfer time case can be seen in Figure 5.65, and it is completed in less than one year. This transfer is very costly in terms of ΔV, and transfers using the manifolds of the other orbits investigated would likely be used instead of this resonant orbit.

Table 5.16. Transfer from L_5 to L_4 Tadpole Orbit through L_3 Lyapunov Orbit and Associated Invariant Manifolds

W_1	Num.	W_2	Num.	ΔV_1 (m/s)	ΔV_2 (m/s)	ΔV_t (m/s)	T_1 (day)	ΔT (day)	T_2 (day)	T_t (day)
W^{S^+}	134	W^{U^+}	59	34.00	34.72	68.72	663	6	824	1493
W^{S^+}	134	W^{U^+}	77	34.00	35.33	69.33	663	8	621	1292
W^{S^+}	134	W^{U^-}	51	34.00	33.92	67.92	663	11	739	1413
W^{S^+}	134	W^{U^-}	16	34.00	34.76	68.76	663	2	722	1387
W^{S^+}	232	W^{U^+}	59	50.34	34.72	85.06	523	10	824	1357
W^{S^+}	232	W^{U^+}	77	50.34	35.33	85.67	523	12	621	1156
W^{S^+}	232	W^{U^-}	51	50.34	33.92	84.26	523	15	739	1277
W^{S^+}	232	W^{U^-}	16	50.34	34.76	85.10	523	6	722	1251
W^{S^-}	11	W^{U^+}	59	42.43	34.72	77.15	407	5	824	1237
W^{S^-}	11	W^{U^+}	77	42.43	35.33	77.76	407	7	621	1035
W^{S^-}	11	W^{U^-}	51	42.43	33.92	76.35	407	10	739	1156
W^{S^-}	11	W^{U^-}	16	42.43	34.76	77.19	407	1	722	1131
W^{S^-}	64	W^{U^+}	59	34.86	34.72	69.59	596	10	824	1429
W^{S^-}	64	W^{U^+}	77	34.86	35.33	70.19	596	12	621	1228
W^{S^-}	64	W^{U^-}	51	34.86	33.92	68.78	596	15	739	1349
W^{S^-}	64	W^{U^-}	16	34.86	34.76	69.63	596	6	722	1323

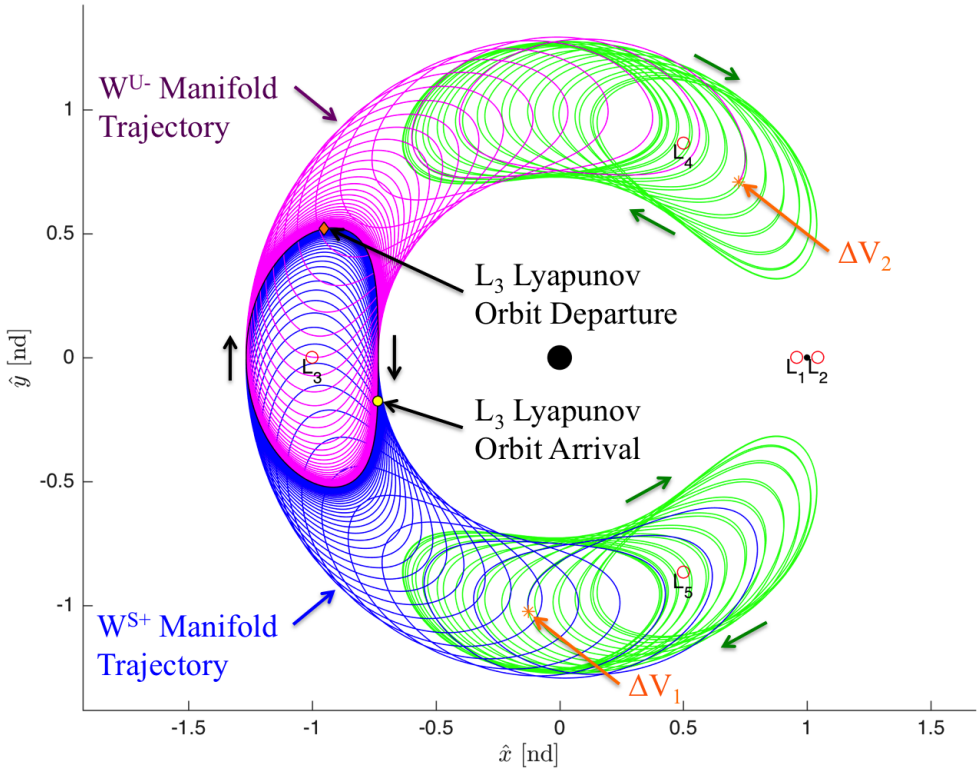

Figure 5.60. Minimum ΔV Transfer from L_5 to L_4 Tadpole Orbit Using L_3 Lyapunov Orbit Manifold Trajectories W^{S+} 134 and W^{U-} 51

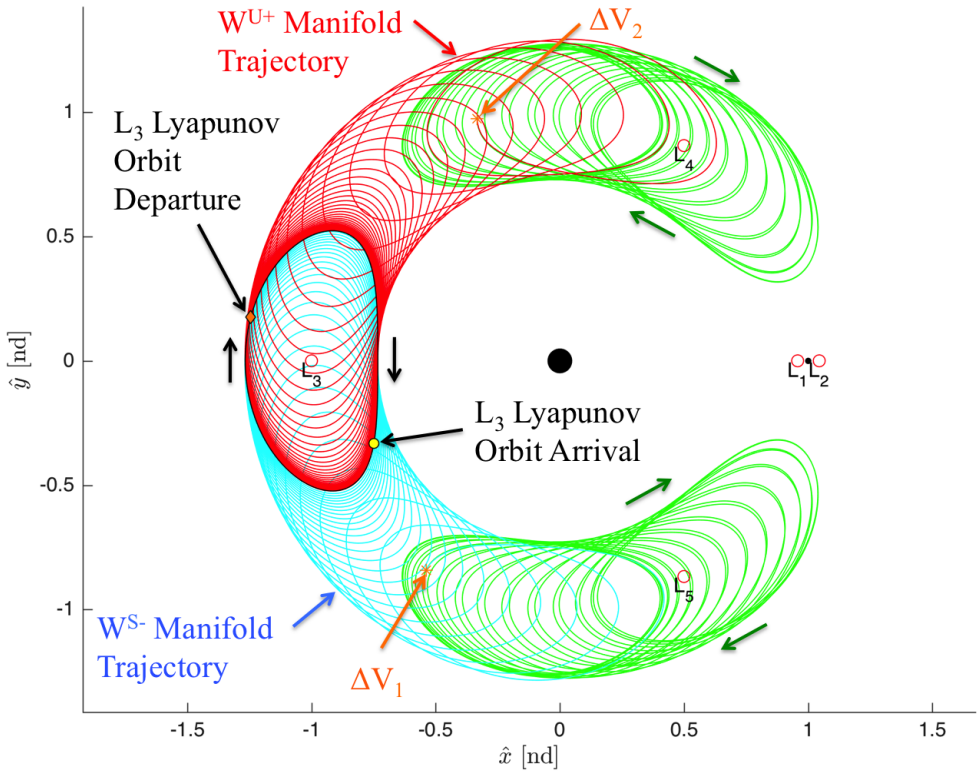

Figure 5.61. Minimum Time of Flight Transfer from L_5 to L_4 Tadpole Orbit Using L_3 Lyapunov Orbit Manifold Trajectories W^{S-} 11 and W^{U+} 77

Table 5.17. Transfer from L_5 to L_4 Tadpole Orbit through Horseshoe Orbit and Associated Invariant Manifolds

W_1	Num.	W_2	Num.	ΔV_1 (m/s)	ΔV_2 (m/s)	ΔV_t (m/s)	T_1 (day)	ΔT (day)	T_2 (day)	T_t (day)
W^{S^+}	42	W^{U^+}	21	37.96	37.24	75.20	2390	649	2762	5802
W^{S^+}	42	W^{U^+}	6	37.96	43.26	81.22	2390	273	44	2707
W^{S^+}	42	W^{U^-}	14	37.96	37.65	75.62	2390	247	2096	4733
W^{S^+}	42	W^{U^-}	6	37.96	49.44	87.41	2390	143	89	2622
W^{S^+}	78	W^{U^+}	21	48.73	37.24	85.98	6	935	2762	3702
W^{S^+}	78	W^{U^+}	6	48.73	43.26	91.99	6	558	44	608
W^{S^+}	78	W^{U^-}	14	48.73	37.65	86.39	6	532	2096	2634
W^{S^+}	78	W^{U^-}	6	48.73	49.44	98.18	6	428	89	523
W^{S^-}	3	W^{U^+}	21	37.87	37.24	75.12	2477	441	2762	5681
W^{S^-}	3	W^{U^+}	6	37.87	43.26	81.13	2477	65	44	2586
W^{S^-}	3	W^{U^-}	14	37.87	37.65	75.53	2477	39	2096	4613
W^{S^-}	3	W^{U^-}	6	37.87	49.44	87.32	2477	909	89	3475
W^{S^-}	50	W^{U^+}	21	48.62	37.24	85.86	19	922	2762	3702
W^{S^-}	50	W^{U^+}	6	48.62	43.26	91.88	19	545	44	608
W^{S^-}	50	W^{U^-}	14	48.62	37.65	86.28	19	519	2096	2634
W^{S^-}	50	W^{U^-}	6	48.62	49.44	98.07	19	415	89	523

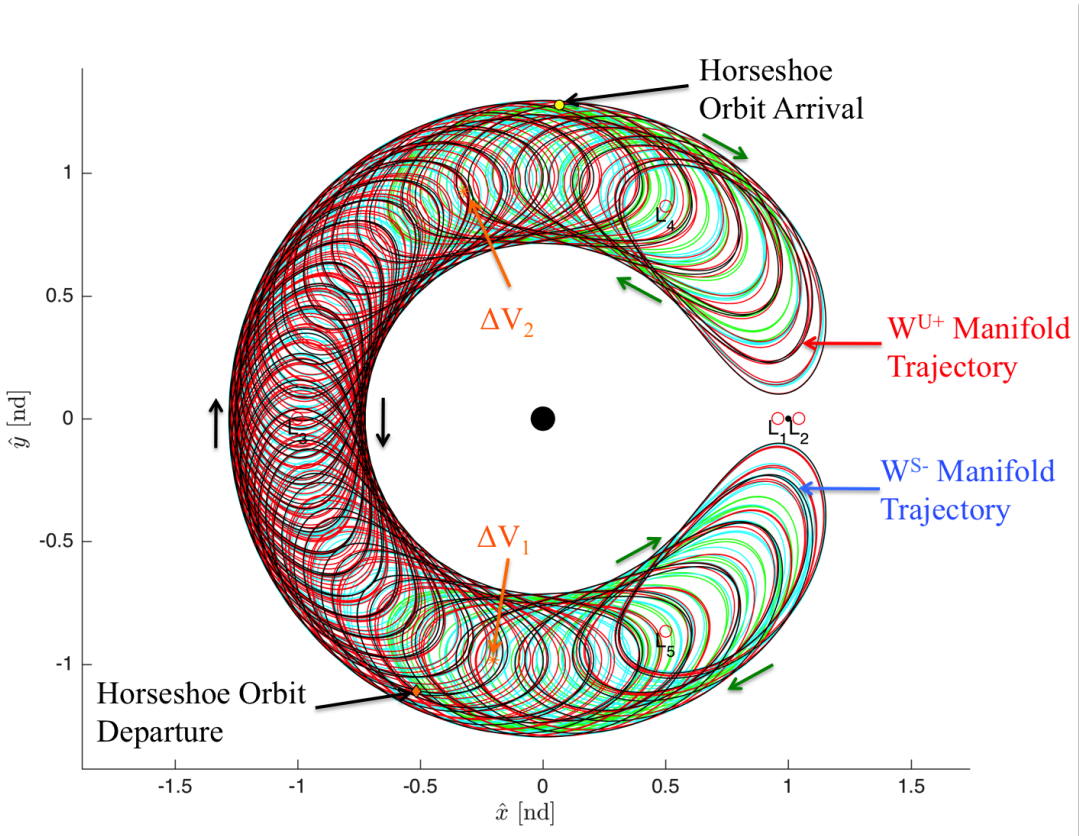

Figure 5.62. Minimum ΔV Transfer from L_5 to L_4 Tadpole Orbit Using Horseshoe Orbit Manifold Trajectories W^{S-} 3 and W^{U+} 21

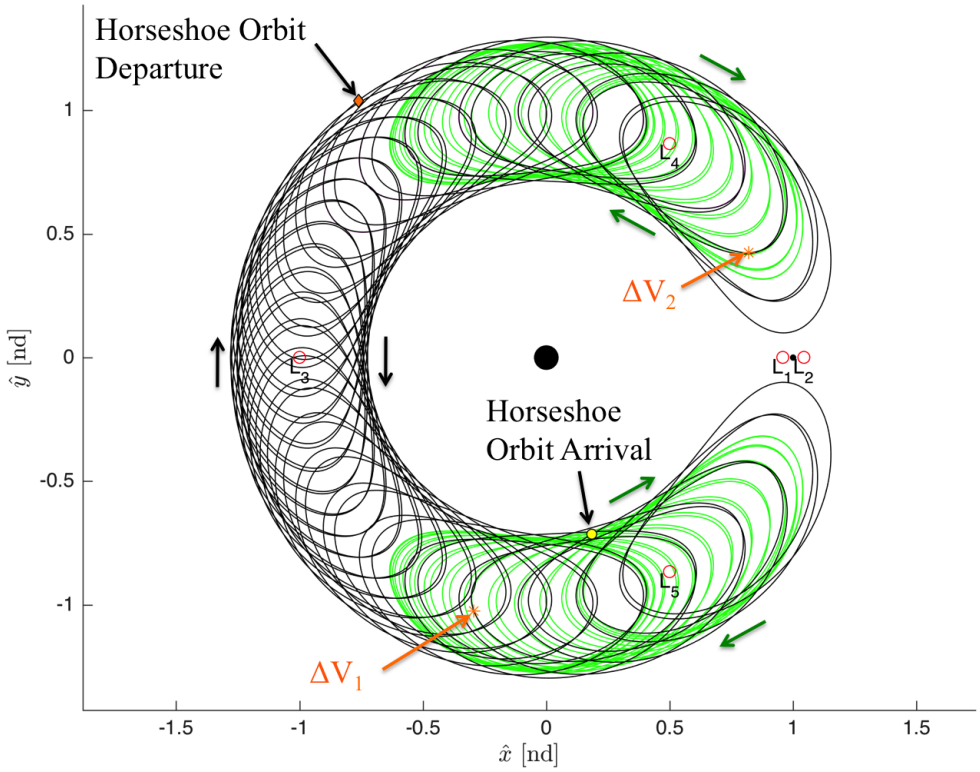

Figure 5.63. Minimum Time of Flight Transfer from L_5 to L_4 Tadpole Orbit Using Horseshoe Orbit Manifold Trajectories W^{S^-} 50 and W^{U^-} 6

Table 5.18. Transfer from L_5 to L_4 Tadpole Orbit through 3:4 Resonant Orbit and Associated Invariant Manifolds

W_1	Num.	W_2	Num.	ΔV_1 (m/s)	ΔV_2 (m/s)	ΔV_t (m/s)	T_1 (day)	ΔT (day)	T_2 (day)	T_t (day)
W^{S^+}	115	W^{U^+}	132	104.32	83.85	188.17	249	25	1512	1785
W^{S^+}	115	W^{U^+}	65	104.32	143.04	247.36	249	22	81	352
W^{S^+}	115	W^{U^-}	12	104.32	55.94	160.26	249	39	1243	1531
W^{S^+}	115	W^{U^-}	6	104.32	148.17	252.49	249	36	202	487
W^{S^+}	149	W^{U^+}	132	193.83	83.85	277.68	90	65	1512	1666
W^{S^+}	149	W^{U^+}	65	193.83	143.04	336.88	90	62	81	233
W^{S^+}	149	W^{U^-}	12	193.83	55.94	249.77	90	13	1243	1346
W^{S^+}	149	W^{U^-}	6	193.83	148.17	342.01	90	10	202	302
W^{S^-}	16	W^{U^+}	132	93.77	83.85	177.62	107	47	1512	1666
W^{S^-}	16	W^{U^+}	65	93.77	143.04	236.82	107	45	81	233
W^{S^-}	16	W^{U^-}	12	93.77	55.94	149.72	107	62	1243	1412
W^{S^-}	16	W^{U^-}	6	93.77	148.17	241.95	107	58	202	368
W^{S^-}	83	W^{U^+}	132	287.52	83.85	371.37	72	53	1512	1637
W^{S^-}	83	W^{U^+}	65	287.52	143.04	430.56	72	51	81	204
W^{S^-}	83	W^{U^-}	12	287.52	55.94	343.46	72	2	1243	1317
W^{S^-}	83	W^{U^-}	6	287.52	148.17	435.69	72	64	202	339

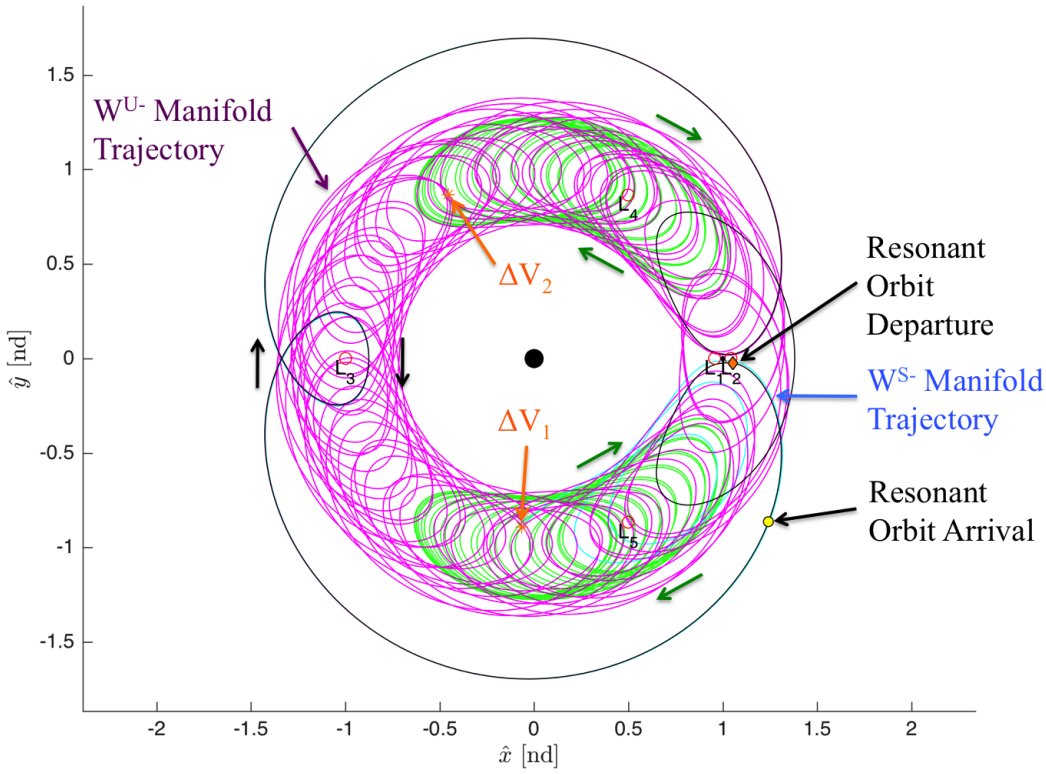

Figure 5.64. Minimum ΔV Transfer from L_5 to L_4 Tadpole Orbit Using 3:4 Resonant Orbit Manifold Trajectories W^{S-} 16 and W^{U-} 12

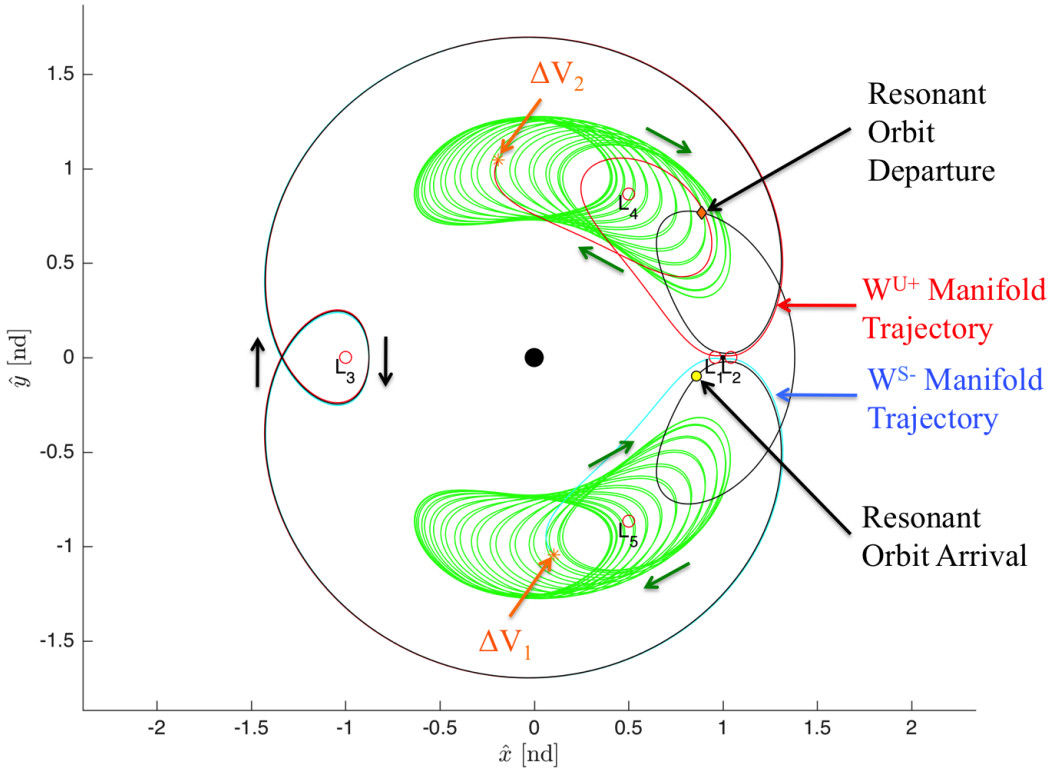

Figure 5.65. Minimum Time of Flight Transfer from L_5 to L_4 Tadpole Orbit Using 3:4 Resonant Orbit Manifold Trajectories W^{S-} 83 and W^{U+} 65

6. Summary and Recommendations

6.1 Summary

This investigation culminates with a better understanding of the dynamical structures and flow associated with tadpole orbits and other related motion that passes through the vicinity of the triangular equilibrium points. This information is applied to a preliminary low-cost transfer trajectory strategy to tadpole orbits, which is developed by means of the invariant manifolds associated with other periodic orbits. First, a strategy to construct periodic tadpole orbits numerically must be developed. The existence of Trojan asteroids in the Sun-Jupiter system spawned extensive research on the long-term stability of these natural bodies; however, exploring the relationship of tadpole orbits with flow associated with other nearby dynamical structures is a recent topic. Different numerical strategies are developed to compute periodic tadpole orbits by formulating the problem in terms of the Circular Restricted Three-Body Problem. The development of a robust formulations allows for the construction of tadpole orbits in systems of different mass ratios, and is not limited to the Sun-Jupiter system. Given a family of periodic tadpole orbits, a relationship with other periodic solutions in the region is investigated. The characteristics of the families and the dynamical structures in their vicinity offer a framework to explain the natural flow in the tadpole region. Connections between these orbits and tadpole orbits are determined by leveraging the natural dynamics of invariant manifolds associated with the other periodic orbits. Finally, transfers from one equilateral point to the opposite triangular point are developed by also using these manifolds.

Example transfer trajectories from other periodic orbits to a specific tadpole orbit in the Saturn-Titan system are computed. A L_3 Lyapunov orbit and horeshoe orbit are investigated because of the structural similarity between their invariant manifolds

and a tadpole orbit with the same value of Jacobi constant. A 3:4 resonant orbit is also investigated to provide another example that is expected to have natural flow associated with it that does not as closely resemble tadpole motion. The transfer trajectories depart these other periodic orbits without a maneuver on an unstable manifold arc and a ΔV maneuver is performed at arrival in the vicinity of the triangular point to insert the spacecraft into the periodic tadpole orbit. Transfers from a tadpole orbit to these other orbits can also be computed by using the stable manifolds and applying a ΔV maneuver to depart the tadpole orbit. Because the motion of the invariant manifolds associated with the L_3 Lyapunov orbit and horeshoe orbit closely resembles that of the tadpole orbit, these transfers require a small ΔV maneuver; however, they take a long time to complete. A larger variety of options exist for the 3:4 resonant orbit in terms of time of flight, but these transfers are typically more expensive. Transport between the triangular points can be designed by combining a transfer from one tadpole orbit using a stable manifold arc and one that arrives at the opposite triangular point by means of the unstable manifold.

6.2 Recommendations for Future Work

This current work provides a beginning understanding of the dynamical flow associated with tadpole orbits. This knowledge can be used to explain the motion of natural objects, such as the transport of Trojan asteroids in the Sun-Jupiter system with motion that initially follows a tadpole orbit in the vicinity of one of the triangular points to the opposite point. The ephemeris data of additional bodies can be investigated to search for this type of behavior. Additionally, an attempt to facilitate this transport can be made by adding the perturbations of other bodies in the vicinity of a tadpole orbit in the circular restricted three-body problem. A better understanding of these mechanisms can help lead to more intuitive mission design choices by fully leveraging the natural dynamics in the tadpole region. These dynamical structures and the relationship between tadpole orbits and other periodic orbits can be further

explored by computing more Poincaré maps and selecting different surfaces of section. The transfer trajectories presented in this work give a preliminary set of options that connect different periodic orbits with tadpole orbits. In future work, an optimizer can be used to minimize the ΔV cost. Additionally, the transfers that are cheapest in terms of ΔV may not arrive at the desired location along a tadpole orbit for a certain mission scenario. Because the periods of tadpole orbits are typically long for the systems of interest, it may be undesirable to wait until the spacecraft reaches this location. A strategy can be developed to move a spacecraft between different points within a tadpole orbit by applying maneuvers. Finally, direct transfers to tadpole orbits from a parking orbit around one of the primaries can be investigated which may be applicable to more general mission scenarios. With future work, a dynamical network forming a connection with the triangular points can be leveraged to better understand the surrounding flow and intuitively design transfers by strategically applying this information.

REFERENCES

REFERENCES

[1] B. Érdi, E. Forgács-Dajka, and A. Süli. On Some Long Time Dynamical Features of the Trojan Asteroids of Jupiter. *Celestial Mechanics and Dynamical Astronomy*, 117(1):3–16, 2013.

[2] S. F. Dermott and C. D. Murray. The Dynamics of Tadpole and Horseshoe Orbits: I. Theory. *Icarus*, 48(1):1–11, 1981.

[3] F. Marzari, H. Scholl, C. Murray, and C. Lagerkvist. Origin and Evolution of Trojan Asteroids. *Asteroids III*, 1:725–738, 2002.

[4] P. Robutel and J. Souchay. An Introduction to the Dynamics of Trojan Asteroids. In *Dynamics of Small Solar System Bodies and Exoplanets*, pages 195–227. Springer, 2010.

[5] K. Oshima and T. Yanao. Jumping Mechanisms of Trojan Asteroids in the Planar Restricted Three-and Four-Body Problems. *Celestial Mechanics and Dynamical Astronomy*, 122(1):53–74, 2015.

[6] E. Barrabés and M. Ollé. Invariant Manifolds of L3 and Horseshoe Motion in the Restricted Three-Body Problem. *Nonlinearity*, 19(9):2065, 2006.

[7] C. D. Murray and S. F. Dermott. *Solar System Dynamics*. Cambridge University Press, Cambridge, Great Britain, 1999.

[8] F. Salazar, C. de Melo, E. Macau, and O. Winter. Three-Body Problem, its Lagrangian Points and How to Exploit Them Using an Alternative Transfer to L4 and L5. *Celestial Mechanics and Dynamical Astronomy*, 114(1-2):201–213, 2012.

[9] L. R. Irrgang. Investigation of Transfer Trajectories to and From the Equilateral Libration Points L4 and L5 in the Earth-Moon System. Master's thesis, Purdue University, 2008.

[10] P. J. Llanos, G. R. Hintz, M. W. Lo, and J. K. Miller. Powered Heteroclinic, Homoclinic Connections Between the Sun-Earth Triangular Points and Quasi-Satellite Orbits for Solar Observations. In *AAS/AIAA Astrodynamics Specialist Conference, AAS*, pages 13–786, 2013.

[11] M. Vaquero and K. C. Howell. Transfer Design Exploiting Resonant Orbits and Manifolds in the Saturn–Titan System. *Journal of Spacecraft and Rockets*, 50(5):1069–1085, 2013.

[12] C. H. Yam, D. C. Davis, J. M. Longuski, and K. C. Howell. Saturn Impact Trajectories for Cassini End-of-Life. *Paper No. AAS*, pages 07–257, 2007.

[13] I. Newton. The Principia: Mathematical Principles of Natural Philosophy (IB Cohen & A. Whitman, Trans.). Berkeley, 1999.

[14] J. Barrow-Green. *Poincaré and the Three Body Problem*. The American Mathematical Society, Providence, Rhode Island,, 1997.

[15] D. B. Taylor. Horseshoe Periodic Orbits in the Restricted Problem of Three Bodies for a Sun-Jupiter Mass Ratio. *Astronomy and Astrophysics*, 103:288–294, 1981.

[16] G. W. Darwin. Periodic Orbits. *Acta Mathematica*, 21(1):99–242, 1897.

[17] E. W. Brown. On a New Family of Periodic Orbits in the Problem of Three Bodies. *Monthly Notices of the Royal Astronomical Society*, 71:438–454, 1911.

[18] E. Rabe. Determination and Survey of Periodic Trojan Orbits in the Restricted Problem of Three Bodies. *The Astronomical Journal*, 66:500, 1961.

[19] E. Rabe. Third-Order Stability of the Long-Period Trojan Librations. *The Astronomical Journal*, 72:10, 1967.

[20] L. A. D'Amario and T. N. Edelbaum. Minimum Impulse Three-Body Trajectories. *AIAA Journal*, 12(4):455–462, 1974.

[21] R. Broucke. Traveling Between the Lagrange Points and the Moon. *Journal of Guidance, Control, and Dynamics*, 2(4):257–263, 1979.

[22] J. R. Stuart and K. C. Howell. Autonomously Generated Optimal Low-thrust Rendezvous Tours of the Sun-Jupiter Trojan Asteroids. In *23rd International Symposium on Space Flight Dynamics (ISSFD), Jet Propulsion Laboratory, Pasadena, California*, 2012.

[23] J. R. Stuart, K. C. Howell, and R. S. Wilson. Automated Design of Propellant-Optimal, End-to-End, Low-Thrust Trajectories for Trojan Asteroid Tours. In *AAS/AIAA 23rd Space Flight Mechanics Meeting, Kauai, Hawaii*, pages 989–1005, 2013.

[24] A. E. Roy and M. W. Ovenden. On the Occurrence of Commensurable Mean Motions in the Solar System: The Mirror Theorem. *Monthly Notices of the Royal Astronomical Society*, 115(3):296–309, 1955.

[25] J. M. Howsman. Investigation of Transfer Trajectories to Periodic Horseshoe Orbits. Master's thesis, Purdue University, 2011.

[26] A. F. Schanzle. Horseshoe-Shaped Orbits in the Jupiter-Sun Restricted Problem. *The Astronomical Journal*, 72:149, 1967.

[27] W. Schlei, K. C. Howell, X. Tricoche, and C. Garth. Enhanced Visualization and Autonomous Extraction of Poincare Map Topology. *The Journal of the Astronautical Sciences*, 61(2):170–197, 2014.

[28] Solar System Dynamics Group. *HORIZONS System*, 2015 (accessed November 5, 2015). `http://ssd.jpl.nasa.gov/?horizons`.

[29] Navigation and Ancillary Information Facility (NAIF). *NAIF Planetary Data System Navigation Node*, 2015 (accessed November 5, 2015). `http://naif.jpl.nasa.gov/naif/`.

[30] M. Vaquero. Poincare Sections and Resonant Orbits in the Restricted Three-Body Problem. Master's thesis, Purdue University, 2010.

[31] B. Érdi, I. Nagy, Z. Sándor, A. Süli, and G. Fröhlich. Secondary Resonances of Co-Orbital Motions. *Monthly Notices of the Royal Astronomical Society*, 381(1):33–40, 2007.

[32] N. Bosanac. Exploring the Influence of a Three-Body Interaction Added to the Gravitational Potential Function in the Circular Restricted Three-Body Problem: a Numerical Frequency Analysis. Master's thesis, Purdue University, 2012.

[33] T. A. Pavlak. *Trajectory Design and Orbit Maintenance Strategies in Multi-Body Dynamical Regimes*. PhD thesis, Purdue University, 2013.

[34] M. Vaquero. *Spacecraft Transfer Trajectory Design Exploiting Resonant Orbits in Multi-Body Environments*. PhD thesis, Purdue University, 2013.

[35] P. E. Verrier and C. R. McInnes. Periodic Orbits for Three and Four Co-Orbital Bodies. *Monthly Notices of the Royal Astronomical Society*, 442(4):3179–3191, 2014.

[36] M. Vaquero and K. C. Howell. Leveraging Resonant-Orbit Manifolds to Design Transfers Between Libration-Point Orbits. *Journal of Guidance, Control, and Dynamics*, 37(4):1143–1157, 2014.

[37] M. Vaquero and K. C. Howell. Design of Transfer Trajectories Between Resonant Orbits in the Earth–Moon Restricted Problem. *Acta Astronautica*, 94(1):302–317, 2014.

[38] J. R. Stuart, K. C. Howell, and R. S. Wilson. Design of End-To-End Trojan Asteroid Rendezvous Tours Incorporating Potential Scientific Value. In *AAS/AIAA 24th Space Flight Mechanics Meeting, Santa Fe, New Mexico*, 2014.

[39] M. Tantardini, E. Fantino, Y. Ren, P. Pergola, G. Gómez, and J. J. Masdemont. Spacecraft Trajectories to the L3 Point of the Sun–Earth Three-Body Problem. *Celestial Mechanics and Dynamical Astronomy*, 108(3):215–232, 2010.

[40] K. Uesugi. Results of the MUSES-A HITEN mission. *Advances in Space Research*, 18(11):69–72, 1996.

[41] W. S. Koon, M. W. Lo, J.E. Marsden, and S.D. Ross. Dynamical Systems, the Three-Body Problem and Space Mission Design. 2000.

[42] V. Szebehely. *Theory of Orbits: The Restricted Problem of Three Bodies*. Academic Press Inc., New York, New York, 1967.

[43] F. Diacu. The Solution of the n-body Problem. *The Mathematical Intelligencer*, 18(3):66–70, 1996.

[44] K. C. Howell et al. Families of Orbits in the Vicinity of the Collinear Libration Points. *Journal of the Astronautical Sciences*, 49(1):107–126, 2001.

[45] W. H. Press. *Numerical Recipes 3rd Edition: The art of Scientific Computing*. Cambridge university press, 2007.

[46] V. Markellos and A. Halioulias. Numerical Determination of Asymmetric Periodic Solutions. *Astrophysics and Space Science*, 46(1):183–193, 1977.

[47] T. S. Parker and L. Chua. *Practical Numerical Algorithms for Chaotic Systems*. Springer Science & Business Media, 2012.

[48] K. E. Davis, R. L. Anderson, D. J. Scheeres, and G. H. Born. The Use of Invariant Manifolds for Transfers Between Unstable Periodic Orbits of Different Energies. *Celestial Mechanics and Dynamical Astronomy*, 107(4):471–485, 2010.

[49] D. W. Jordan and P. Smith. *Nonlinear Ordinary Differential Equations: An Introduction to Dynamical Systems*, volume 2. Oxford University Press, USA, 1999.

[50] J. D. Hadjidemetriou. Symmetric and Asymmetric Librations in Extrasolar Planetary Systems: A Global View. *Celestial Mechanics and Dynamical Astronomy*, 95(1-4):225–244, 2006.

[51] L. Perko. *Differential Equations and Dynamical Systems*, volume 7. Springer Science & Business Media, 2013.

[52] V. A. Chobotov et al. Orbital Mechanics, American Institute of Aeronautics and Astronautics. *Inc., Reston, VA*, page 20, 2002.

[53] W. Qiu-Dong. The Global Solution of the n-body Problem. *Celestial Mechanics and Dynamical Astronomy*, 50(1):73–88, 1990.

[54] B. T. Barden. Using Stable Manifolds to Generate Transfers in the Circular Restricted Problem of Three Bodies. Master's thesis, Purdue University, 1994.

[55] P.E. Robutel, F. Gabern, and A. Jorba. The Observed Trojans and the Global Dynamics Around the Lagrangian Points of the Sun-Jupiter system. In *A Comparison of the Dynamical Evolution of Planetary Systems*, pages 53–69. Springer, 2005.

[56] P. Robutel and F. Gabern. The Resonant Structure of Jupiter's Trojan Asteroids–I. Long-Term Stability and Diffusion. *Monthly Notices of the Royal Astronomical Society*, 372(4):1463–1482, 2006.

[57] R. Schwarz and R. Dvorak. Trojan Capture by Terrestrial Planets. *Celestial Mechanics and Dynamical Astronomy*, 113(1):23–34, 2012.

[58] S. D. Ross and D. J. Scheeres. Multiple Gravity Assists, Capture, and escape in the Restricted Three-Body Problem. *SIAM Journal on Applied Dynamical Systems*, 6(3):576–596, 2007.

[59] R. L. Anderson and M. W. Lo. Flyby Design Using Heteroclinic and Homoclinic Connections of Unstable Resonant Orbits. 2011.

[60] Y. Ren, J. J. Masdemont, G. Gómez, and E. Fantino. Two Mechanisms of Natural Transport in the Solar System. *Communications in Nonlinear Science and Numerical Simulation*, 17(2):844–853, 2012.

[61] K. C. Howell, B. T. Barden, R. S. Wilson, and M. W. Lo. Trajectory Design Using a Dynamical Systems Approach with Application to GENESIS. *Astrodynamics 1997*, pages 1665–1684, 1997.

[62] D. C. Folta, M. Woodard, K. C. Howell, C. Patterson, and W. Schlei. Applications of Multi-Body Dynamical Environments: the ARTEMIS Transfer Trajectory Design. *Acta Astronautica*, 73:237–249, 2012.

[63] M. Connors, P. Wiegert, and C. Veillet. Earths Trojan Asteroid. *Nature*, 475(7357):481–483, 2011.